THE FLORIDA STATE UNIVERSITY

COLLEGE OF ARTS AND SCIENCES

PREFERENTIAL FLOW PATHS IN SOLUBLE POROUS MEDIA AND CONDUIT SYSTEM DEVELOPMENT IN CARBONATES OF THE WOODVILLE KARST PLAIN, FLORIDA

By

CHRISTOPHER L. WERNER

A Thesis submitted to the
Department of Geological Sciences
in partial fulfillment of the
requirements for the degree of
Master of Science

Degree Awarded:
Spring Semester, 2001

The members of the Committee approve the

thesis of Christopher L. Werner defended on March 20, 2001.

_____
David J. Furbish
Professor Directing Thesis

_____
James B. Cowart
Committee Member

_____
David E. Loper
Committee Member

Approved:

_____
David J. Furbish, Chair, Department of Geological Sciences

For Leano and Mary

ACKNOWLEDGMENTS

I would like to thank my major professor, Dr. David J. Furbish, for his guidance and encouragement in this research. His enthusiasm and excitement provided me with the motivation I needed to complete this thesis. I would also like to thank my committee members, Dr. James Cowart and Dr. David Loper for their comments and suggestions, as well as their emphasis on good writing and communication skills.

Many thanks to the members of the Woodville Karst Plain Project, especially project director George Irvine III, without whose involvement and mentorship, none of this would have been possible. Special thanks to Brent Scarabin and Rick Sankey for their contributions to my diving education and longevity. I also am indebted to my fellow explorers, John Rose, Ted Cole, Barry Miller, Scott Landon and Jesse Armantrout, with whom I have had the pleasure to experience first hand the unique environment of the underwater caves south of Tallahassee.

Additionally, I would like to thanks the employees of the Florida Geological Survey; particularly, Jon Arthur for his patience, professionalism and assistance. Finally, I would like to thank my parents Beverly and Lee, for their tolerance and my wife, Leslie, for her patience, encouragement and understanding during the writing of this thesis.

TABLE OF CONTENTS

LIST OF TABLES

LIST OF FIGURES

ABSTRACT

It is proposed that the underwater caves of the Woodville Karst Plain (WKP) exhibit at least three, and possibly five, distinct horizontal levels of cave passage distribution indicative of a tiered system. The overall suggestion is that some of the caves within the WKP were air filled at various times during their development. The present situation of an elevated water table suggests that the caves have been submerged relative to their initial development. There appears to be considerable correlation between passage depth distribution and duration of sea level elevation, implying that these caves may have formed preferentially at or near the water table. Hence, it can be deduced that their development has been dependent on base level and supports the theory of 'water table' cave development. The timeline of formation for karstification and cave passage development found within the WKP is likely on the order of ~500 Ka, using sea level duration records indicating maximum correlation coefficients near 450 Ka BP. The results of a theoretical stability analysis suggest that initial dissolutional development does not occur in a phreatic setting; the system is unconditionally stable on a short time scale. The specific mechanism that produces preferential flow paths (PFP) is proposed to be 'mixing dispersion', while the subsequent rapid enlargement of the PFP is likely the transition from laminar to turbulent flow and is solely responsible for upstream porosity development. It is proposed that dissolution from 'mixing dispersion' may be the initial mechanism by which the PFP are formed.

CHAPTER 1

INTRODUCTION

Purpose and Scope

There are several extensive underwater caves systems developed within the carbonates of the Woodville Karst Plain (WKP), which is evident through the related karst features and topography. Many of the cave systems extend more than several kilometers and are as deep as 98 m below present water table and possibly deeper. Several distinct levels of conduit development appear to exist at various depths below the water table. This suggests a vertically tiered dissolution regime, which may have been the result of base level lowering of the water table. The cave passages may have formed due to preferential groundwater flow during sea level stands of the Quaternary.

The cave systems may be part of a larger groundwater flow pattern. This flow pattern may be influenced by localized groundwater flow-patterns operating in the WKP. In turn, the orientation of the cave passages and the flow direction through the passages may control the present flow patterns.

This research will attempt to determine which factors control and/or contribute to the observed cave passage development and the horizontal passage spacing (*e.g.* master conduit, *sensu.* White, 1999) within the WKP. Specifically, the degree to which elevational development may be the result of a base level control through fluctuating sea level will be determined. This information will be used to establish the most likely subsurface paleodrainage pattern at the onset of conduit formation, herein referred to as

preferential flow paths (PFP). Additionally, the question of whether there is an inherent instability leading to preferential flow paths in unfractured or homogeneously fractured soluble porous media will be investigated to determine the relevance in the development of observed cave passages of the Woodville Karst Plain.

There has been recent progress in developing a quantitative theory of conduit formation in soluble limestone terraines through numerical simulations of flow within fractured media (Groves & Howard, 1994b; Howard and Groves, 1995; Siemers and Dreybrodt, 1998; Gabrovsek and Dreybrodt, 2000). In this thesis, a theoretical approach examining dissolution of soluble porous media and an investigation of preferential instabilities leading to the formation of dissolutional conduits will be undertaken to further advance the understanding of preferential flow path growth initiated by groundwater flow in karstic aquifers.

This analysis is primarily concerned with phreatic flow conditions in soluble porous media and resultant conduit initiation and development. The present field conditions within the WKP are primarily indicative of phreatic and, to a much lesser degree, vadose conduit development. The investigation will concentrate on phreatic flow conditions and initiation of PFP and their development toward large-scale drainage conduits (*sensu.* White, 1999) presently observed within the WKP.

From this point forward, reference to the terms ‘conduit’ and ‘cave passage’ will denote slightly varied meanings. The term ‘conduit’ will be defined as a cave passage with specific reference to its initial formation and development with little geomorphic modification. The term ‘cave passage’ will be defined as the presently observed water-filled condition existing in the field, including any modification by terminal collapse, breakdown of the ceiling and/or walls, sediment deposition, secondary dissolution modification, etc. This difference is necessary for descriptive purposes and will provide a better understanding during the discussion of development of cave systems of the WKP.

Specific Problem

The questions to be addressed from this study are: (1) What mechanisms control and/or contribute to the apparent tiered conduit development of the WKP in the vertical extent and (2) what mechanisms produce and/or contribute to the apparent branchwork (*sensu.* Palmer, 1991) and/or master conduit drainage pattern (*sensu.* White, 1999) of the observed cave systems? Answers to these questions are essential for determining the dissolutional conduit development and its hydrologic drainage basin evolution within the carbonates in the WKP.

In order to answer these questions, a preliminary research plan was initiated to examine the cave system characteristics within the WKP. Upon obtaining survey data from the Woodville Karst Plain Project (Irving, 1997), a group dedicated to exploring and mapping the underwater caves of the WKP, relevant characteristics, including passage length, depth and orientation, of the cave systems were examined. The data was divided into appropriate categories with which certain aspects of the questions could be analyzed. This preliminary data set was then analyzed statistically to help identify specific issues to be addressed by this study and to propose the hypothesis that will be tested below.

Study Area

The Woodville Karst Plain, located in the Big Bend area of northern Florida, is characterized by a large sequence of carbonate deposits, 150-600 m thick, overlain by a layer of unconsolidated sediments, predominantly sands, with some clays and silts, approximately 8-20 m thick. The surface of this area has numerous sinkholes, karst windows, sinking streams, and large springs. Hydrologically, the area is part of the extensive Floridan aquifer system (FAS), which underlies southern Alabama, southern

Georgia, eastern South Carolina and the entire state of Florida (Miller, 1986). In the region north of the WKP, in southern Georgia and northern Florida, regional groundwater movement is south toward the WKP and ultimately to the Gulf of Mexico.

The study area encompasses the westernmost portion of the WKP just south of Tallahassee, FL (Figure 1.1). It extends from just west of U. S. Route 319 in the west, to north of Capital Circle Southwest and Capital Circle Southeast in the north, to the Woodville Hwy in the east, and to Apalachee Bay in the Gulf of Mexico in the south. There are over 48 km of surveyed underwater cave passages within the WKP. These include some well-known and explored springs and cave systems, such as Indian Springs Cave, Sally Ward Spring Cave, Wakulla Springs and Leon Sinks Cave System (Figure 1.2). All are included within this study. Figure 1.3 illustrates the locations of all sinks and springs used in this study.

The study area was chosen for several reasons. First, all caves and cave systems are completely submerged. This suggests that either the caves had formed in a subaqueous state (*i.e.* below the water table) or that they were formed near or above the water table and subsequently drowned by sea level rise. Second, the WKP, and hence the submerged caves within its borders, are within a few tens of kilometers of the present coastline of Apalachee Bay. The study area is relatively close to the Gulf of Mexico and is well suited for an examination of the effects of base level controls (*i.e.* fluctuating seas) on carbonate dissolution. Third, the WKP has relatively subdued topographic relief, with maximum elevations of approximately 20 m at the northernmost extent of the study area, and transgressing and regressing seas have shaped its geomorphology during the Quaternary. Finally, many of the caves of the WKP are amenable to advanced diving exploration and provide an easily accessible environment for explorers to face the challenges of the world's most extensive deep underwater caves. Because of the nearly 20-year continuous exploration effort within the WKP caves, many are well documented.

Underwater surveys and maps, that is available, provided significant information and data utilized in this study.

Hypothesis

A reasonable explanation of the observed features, discussed in Chapter 2 and Chapter 3, of the WKP cave systems can be made with some confidence. The existence of at least three, and as many as five, separate conduit levels suggests that base level fluctuations have played an important role in developing the observed tiered cave systems. This vertical development may have initiated during the extended sea level still-stands of the Gulf of Mexico during the Quaternary. The sea level still-stands may have allowed the initiation of PFP at several corresponding elevations within the sequence of carbonates. These PFP may have been enlarged at different times throughout their development while the water table was near the PFP elevation. The duration of time the water table was near the PFP elevation may have played a substantial role in developing a majority of the observed conduit levels.

In conjunction with the above hypothesis related to the vertical development, the subsurface drainage pattern of the cave passages and geomorphic features suggests that a natural horizontal spacing of conduits may have been imposed on the PFP. This spacing may have been caused by an intrinsic instability of karstic groundwater flow. Although the spacing may have developed the PFP at regularly spaced distances, competition between the PFP through time resulted in the development of large primary conduits. Hence, the primary cave passages now observed might be the PFP that effectively dominated all others.

The PFP capturing a majority of the aggressive groundwater, due to less hydraulic resistance, in turn dissolves more of the carbonate medium, increasing its

volume and decreasing its hydraulic resistance, allowing capture of even more flow than previously possible. This process can be described as a positive feedback loop. Therefore, the most efficient PFP of the past are essentially the large primary cave passages (*i. e*. master conduits) observed today.

Both mechanisms suggested above have led to the development of the cave systems observed today in the WKP. It is proposed that these mechanisms have been the dominant controls of conduit formation and development possibly eclipsing other mechanisms responsible for preferential dissolution, including structural, lithologic, and stratigraphic controls. It is reasoned that sea level fluctuation and its subsequent elevation duration, in conjunction with the development of PFP, has dominated development of solutional cave passages within the WKP.

Significance

Groundwater flow involving more that one type of porosity (*i. e.* multiple-porosity) has presented significant problems to researchers. Difficulties typically arise in mathematical and numerical models used to predict groundwater flow and transport. The inherent problems are exemplified by the complex interaction of both diffuse (intergranular) and conduit (cave passage) flow regimes. Prediction of groundwater flow, solute transport and aquifer resource management become exceedingly unreliable for large spatial and temporal scales. Karst hydrology represents an end member in groundwater flow through multiple-porosity geologic media.

This study will focus on advancing theoretical and statistical techniques in an attempt to develop a conceptual model of preferential flow path initiation and subsequent development of extensive conduit systems. The results will allow researchers to better model the groundwater flow conditions within the WKP. Subsequent studies in other

locations will be able to incorporate these findings to better understand and predict groundwater flow in coastal karst regions of Florida. This result will set a precedent for further theoretical and observational research and establish the Woodville Karst Plain as a subaqueous solutional conduit-system type locality.

Figure 1.1. Study area located within the Big Bend Area of Northern Florida, south of Tallahassee.

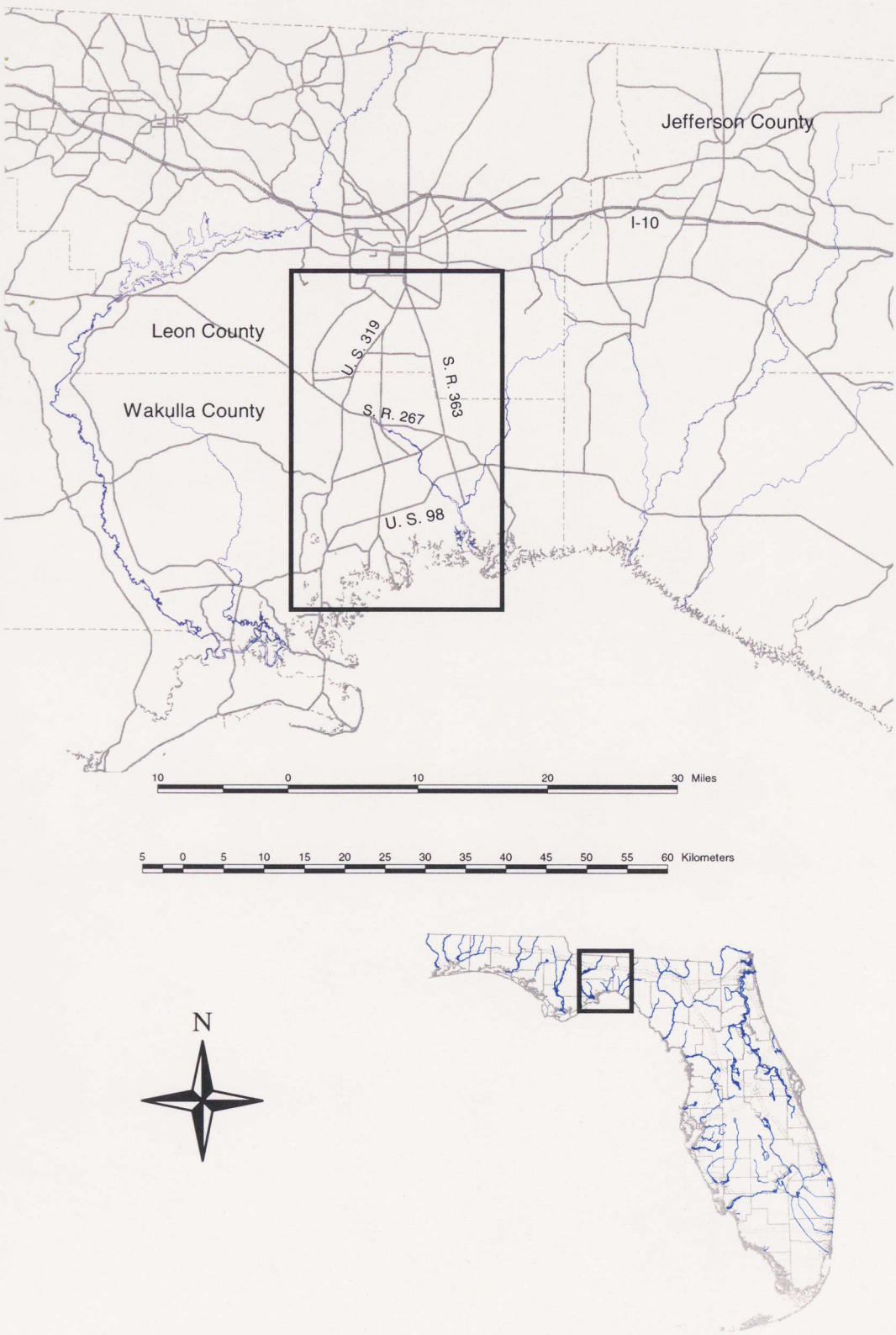
Jefferson County
I-10
Leon County
U. S. 319
S. R. 363
Wakulla County
S. R. 267
U. S. 98
10 0 10 20 30 Miles
5 0 5 10 15 20 25 30 35 40 45 50 55 60 Kilometers
N

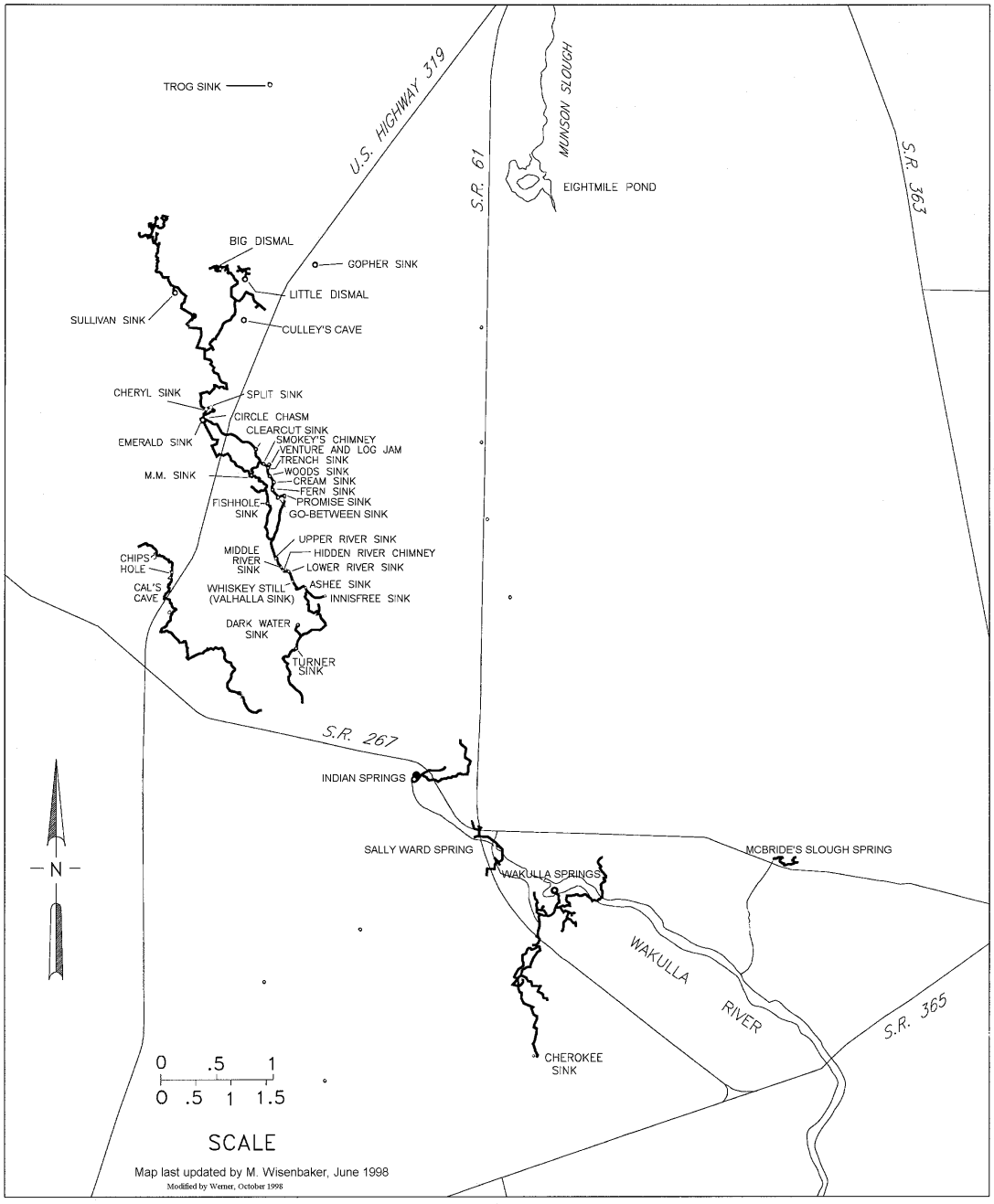

Figure 1.2. Map of significant caves of the WKP, modified from Wisenbaker (1998) and Werner (1998). Cave systems displayed include Leon Sinks Cave System, Chip's Hole Sink Cave, Indian Springs Cave, Sally Ward Cave, McBride's Slough Cave and Wakulla Springs Cave System. Note the large number of sinkholes that comprise the Leon Sinks Cave System. Unnamed sinks appear along State Route 61 and south of Indian Springs.

Figure 1.3. Sinkhole and spring locations used in this study. Cave surveys used in this study have corresponding circles with dots. Caves indicated with circles only, did not have surveys available for use but did provide important geomorphic passage and/or sediment deposit observations.

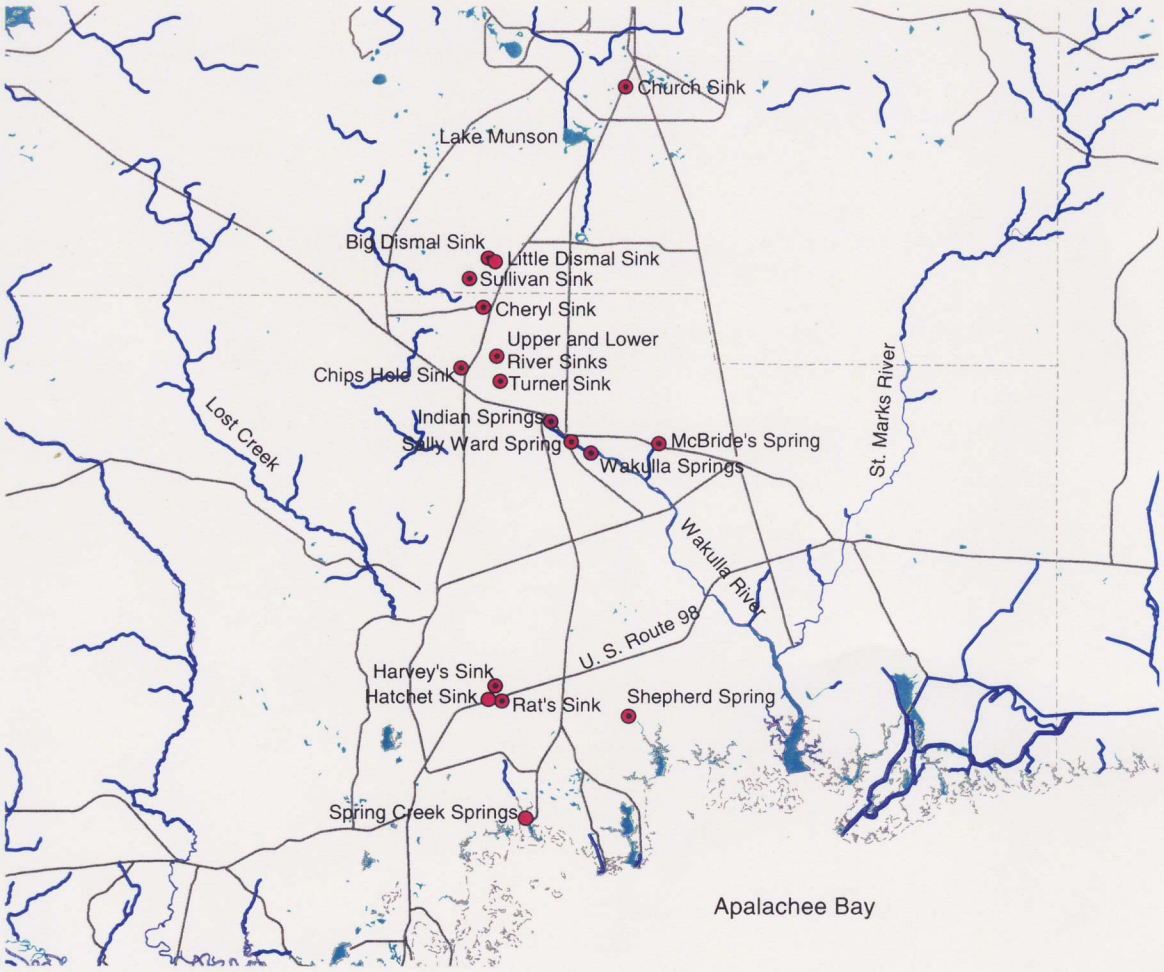
Church Sink
Lake Munson
Big Dismal Sink
Little Dismal Sink
Sullivan Sink
Cheryl Sink
Upper and Lower
River Sinks
Chips Hole Sink
Turner Sink
Lost Creek
Indian Springs
Sally Ward Spring
McBride's Spring
Wakulla Springs
St. Marks River
Wakulla River
U. S. Route 98
Harvey's Sink
Hatchet Sink
Rat's Sink
Shepherd Spring
Spring Creek Springs
Apalachee Bay
10 0 10 Miles
10 0 10 20 Kilometers
N
Jefferson County
I-10
Leon County
Wakulla County
U.S. 319
S. R. 363
S. R. 267
U. S. 98

CHAPTER 2

HYDROGEOLOGICAL SETTING

The Woodville Karst Plain

Physiography

The WKP lies in the Gulf Coastal Lowlands geomorphic province (Puri and Vernon, 1964) and was originally described by Hendry and Sproul (1966). It was defined as being surrounded by the Tallahassee Hills to the north, the Gulf of Mexico in the south, and the Apalachicola Coastal Lowlands in the west (Hendry and Sproul, 1966; Rupert and Spencer, 1988). To the east, the Jefferson County line formerly bound the WKP. Recently, however, its eastern border was extended to the Steinhatchee River (Scott, 2000). The Cody Scarp, an east-west trending escarpment, forms the boundary between the WKP and the Tallahassee Hills (Hendry and Sproul, 1966). The escarpment is the largest of several relict marine terraces (Rupert and Spencer, 1988) that include the Wicomico, Penholoway, Talbot, Palmetto and Silver Bluff terraces (see Rupert and Spencer (1988) for details). These terraces are nearshore erosional and depositional surfaces present within and/or surrounding the WKP and developed during the Pleistocene. All are features of the transgression and regression of the Gulf of Mexico.

The WKP is divided into four geomorphically distinct regions which include (1) the Coastal Marsh Belt (Rupert and Spencer, 1988, Fig. 5), (2) the River Valley Lowlands, which contains the Wakulla River and the St. Marks River lowlands (Rupert and Spencer, 1988, Fig. 5; Hendry and Sproul, 1966, Fig. 8), (3) the Lake Munson Hills (Hendry and Sproul, 1966, Fig. 8) and (4) the Wakulla Sand Hills (Hendry and Sproul, 1966, Fig. 8; Rupert and Spencer,

1988, Fig. 5). The entire WKP is characterized by low elevations not exceeding 20 m above mean sea level. There is a change in the surficial lithology between the distinct geomorphic regions. From the Cody Scarp to the Gulf of Mexico, the surficial sediments trend from a clay-rich sand, to silt- and sand-rich deposits and finally to mud- and silt-rich sediments.

Geomorphology

The climate of northern Florida is subtropical and is typically characterized by humid conditions. The summer season is warm with high temperatures ranging between 32° – 38°C. The winter season is mild with low temperatures falling below 0°C less than thirty times annually. The mean annual precipitation of northern Florida is approximately 135 cm with over half falling between June and September (Winsberg, 1990). Mean annual rainfall near Tallahassee from 1886 to 1965 was approximately 145 cm (Hughes, 1967). Winter precipitation is typically associated with atmospheric fronts from both the continental interior and Gulf of Mexico, while summer precipitation usually arises from late afternoon convective thundershowers.

Denudation rates of limestone have been used by several researchers to explain varying elevations of geologically related physiographic provinces. The denudation rate estimates vary considerably from 3.8 cm/Ka (Brooks, 1967) to 5.0 – 6.1 cm/Ka (Hendry and Sproul, 1966). While overall denudation rates of limestone are useful, the abundant surface streams flowing toward the perimeter of the WKP are much more significant in cave system development. These surface streams, upon entering the WKP, typically disappear into the subsurface through exposed limestone. The disappearing streams are point-source recharges to the groundwater flow system and mark significant locations of surface water/groundwater interaction.

Such surface water/groundwater interactions deliver CO_2-rich and organic-rich aggressive waters to the cave systems. The vegetative cover surrounding the WKP,

typically of a higher elevation and well drained, is primarily composed of pine, black-jack and oak trees (Hendry and Sproul, 1966). The WKP itself, of lower elevation and with poor surface drainage and/or moderately developed subsurface drainage, is comprised of pine, cypress and bay trees, as well as 30 species of shrubs and 109 species of herbs (Hendry and Sproul, 1966). The subtropical climate, high mean annual precipitation and dense vegetative cover contribute to high soil-CO_2 production rate. The input of CO_2-rich waters is enhanced by the entrainment of decaying vegetative matter within surface waters. The vegetative matter is easily transported into the cave systems and may form thick deposits, typically near sinkholes. The deposits typically contain abundant decaying tree trunks, branches and leaves. The deposits continually supply organic acids to the groundwater. The additive effect results in low-pH, high dissolved CO_2 waters in contact with soluble limestone.

Geology

Stratigraphy and Lithology. The WKP, as it has developed in Leon, Wakulla, and Jefferson Counties, Florida, is characterized by a thin veneer of unconsolidated and undifferentiated Pleistocene quartz sand and shell beds, overlying a thick sequence of relatively horizontal carbonates (Hendry and Sproul, 1966). The Avon Park Formation, Ocala and Suwannee Limestones and the St. Marks Formation underlie the unconsolidated sands, from depth, and comprise the upper FAS (Rupert and Spencer, 1988, Fig. 10; Davis, 1996, Fig. 3). These limestones, being very porous, permeable and soluble, have undergone considerable dissolution from groundwater movement (Hendry and Sproul, 1966). Consequently, the topography is karstic in nature, with numerous sinkholes, karst windows, sinking streams, and springs (Rupert, 1988).

The Ocala Limestone and Avon Park Formation overlie Lower Eocene limestones and underlie the Suwannee Limestone, respectively. Although important in the transport of deeper groundwater in the upper FAS, the Ocala Limestone has no known caves within the WKP. Therefore, neither formation will be considered in this study.

The Oligocene Suwannee Limestone reaches a maximum thickness of 160 m with the top approximately 30 m to 150 m below land surface within Leon and Wakulla Counties (Davis, 1996). The thickest portion of the Suwannee is found south of Tallahassee at the Gulf of Mexico and the thinnest is located near the Georgia border (Hendry and Sproul, 1966). It primarily consists of two types of permeable rock: (1) a crystalline tan, highly fossiliferous limestone and (2) a white to cream, finely crystalline limestone containing foraminifera with micritic limestone pellets (Davis, 1996). Occasionally, both limestones types may have dolostone present. The Suwannee Limestone is the principal lithology transporting much of the groundwater of the upper FAS within the WKP. The majority of dissolutional conduits within the WKP are primarily developed in the Suwannee Limestone.

The Miocene sediments include the St. Marks Formation and the Hawthorn Group. The Hawthorn Group is composed of several formations and members. It is primarily a siliciclastic unit, consisting of fine- to medium-grained sandy clays and silty, clayey sands, with variable amounts of carbonate (Rupert, 1988). These are usually interbedded and may contain minor amounts of dolomite and phosphate but are very rare within the WKP. The Tallahassee Hills, north of the Cody scarp and basally composed of Hawthorn Group sediments have limited permeability and act as a confining unit (Davis, 1996, Fig. 4).

The St. Marks Formation sediments are predominately fine- to medium-fine grained, partially recrystallized, silty to sandy limestones that have undergone varying

degrees of secondary dolomitization (Hendry and Sproul, 1966). Within the WKP, the St. Marks Formation comprises the top of the upper FAS (Rupert, 1988). It also contains extensive shallow conduits in portions of the Leon Sinks Cave System and Indian Springs Cave. It erosionally pinches out against the Suwannee Limestone in southwestern Jefferson County and reaches a maximum thickness of approximately 60 m in western Wakulla County.

The WKP is a gently sloping topographic region of low sand dunes and exposed carbonates rising from the Gulf of Mexico to approximately 20 m in elevation within Leon County, the northern terminus being the Cody scarp. The loosely consolidated Pleistocene sands are very porous and permeable and allow rapid infiltration of precipitation (Hendry and Sproul, 1966).

Structure. The regional structure of the area surrounding the WKP contains three major components: (1) the Apalachicola Embayment, (2) the Gulf Trough in southwestern Georgia and (3) the Ocala Platform. These three features have provided the necessary conditions predating the initiation of karst conduit development in the WKP (Rupert and Spencer, 1988, Fig. 21).

The Apalachicola Embayment, sometimes referred to as the Southwest Georgia Embayment, located west of the WKP, is a southwest-plunging syncline containing a thick sequence of predominantly siliciclastic material (Miller, 1986). It is thought that this feature is a Middle Mesozoic to Middle Cenozoic depositional basin (Schmidt, 1984; Huddlestun, 1993). In some instances, carbonate deposition spilled westward from the Florida platform into the embayment. The region has continued to subside and a downwarping of sediments is observed, as well as a thickening of the Ocala and Suwannee Limestones and St. Marks Formation to the west from the WKP.

The Gulf Trough is either a series of northeast-trending faults that bound a series of small grabens (Miller, 1986; Davis, 1996, Fig. 4) or more likely an erosional feature (Huddlestun, 1993). These grabens or post-erosional sediments are primarily low-permeability clastic rocks that abut with a thick sequence of carbonates on either side. This feature may have the effect of retarding the flow of groundwater from the north within the FAS (Miller, 1986).

The Ocala Platform is another northwest-trending feature paralleling the Peninsular Arch to the west. The Ocala Platform affects only sediments of Middle Eocene and younger, and is thought to be a buildup of Eocene carbonate sediments, or more likely, a compaction of Eocene material after deposition (Miller, 1986).

The regional structural features of the Apalachicola Embayment bounding the WKP in the west have been influential in its history by setting the stage for deposition of carbonates. The Eocene compaction of sediments from the Ocala Platform and the Gulf Trough have been the regional features responsible for creating the current exposure of Miocene and Oligocene carbonates seen at the surface (Miller, 1986, Fig. 6). These structural manifestations have allowed the overlying sediments of the Hawthorn Group, formerly overlying the WKP, to be subjected to physical and chemical erosion from the Gulf waters during the Quaternary. These influences have culminated in a geologic setting conducive to karst conduit formation.

It is important to note that the carbonate sequences within which karst development takes place in the WKP are nearly horizontal (<1°). There is little, if any, field evidence for structural controls influencing conduit orientation or morphology on either a local or regional scale. The St. Marks Formation appears to be a shallow near shore siliciclastic-rich sediment contained in a carbonate cement and the Suwannee Limestone is likely a thick platform reefal deposit that has undergone moderate

diagenesis. The contact between the Suwannee Limestone and the St. Marks Formation is moderately irregular and marks an unconformity that lacks bedding plane partings.

Hydrology

Regional hydrology. There are two distinct water-bearing units, the surficial aquifer system (SAS) and the FAS (Davis, 1996, Fig. 3). In most places surrounding the WKP low permeability rocks of the intermediate confining unit (ICU) of the FAS separate the SAS and FAS. The ICU is comprised of low-permeability siliciclastic rocks. The ICU is absent within the WKP. The SAS is commonly comprised of poorly consolidated to unconsolidated clastic rocks and sediments where water typically occurs in unconfined conditions (Miller, 1986). The upper FAS includes Tertiary carbonates formed during the Oligocene and Miocene Series and is overlain by deposits from the Pliocene, Pleistocene and Holocene (Hendry and Sproul, 1966). Specifically, within the WKP, the upper FAS is comprised of the Avon Park Formation, Suwannee and Ocala Limestons and the St. Marks Formation.

The regional recharge area for WKP includes the Florida counties of Leon, Jefferson and Wakulla, and extends north of the Georgia border for over 80 km and covers portions of over five Georgia counties (Davis, 1996). The regional groundwater flow pattern, taken from potentiometric contour maps, shows generally south trending flow lines (Scott *et. al.*, 1991; Davis, 1996). The potentiometric contour maps show a saddle or potentiometric low area extending well into the WKP (Scott *et. al.*, 1991, Fig. 32; Davis, 1996, Fig. 11). Here, as evidenced by the low topographic elevations, the ICU has been removed. This causes a convergent regional flow line pattern toward the south-central area of the karst plain. This convergence of flow is postulated to originate from the fact that the WKP ICU is absent. In conjunction with this observation, the potentiometric low is also the result of large conduits transporting significant volumes of

groundwater very efficiently to the coast. The lowered pressure gradient within the conduits serves to depress the potentiometric surface.

The absence of a confining unit allows groundwater to emerge at an elevation equivalent to the pressure produced by its hydraulic head. The result is commonly referred to as artesian flow. Thus, flow through Leon and Jefferson Counties, confined by the Miccosukee Formation and Hawthorn Group, converges in the WKP, where the lack of the ICU allows groundwater to result in artesian flow at the surface. In this area, there are several first-order magnitude springs including Wakulla Springs, the St. Marks Spring Group, the Spring Creek Spring Group and Wacissa Springs.

Most groundwater circulation is thought to take place within the upper FAS (Miller, 1986). The groundwater of the lower FAS is typically substantially mineralized compared with the upper FAS indicating much longer residence times (Sprinkle, 1985). Hence, the upper FAS is regarded as having strong circulation. This circulation is believed to be the result of high moldic and intergranular porosity, as well as secondary dissolution (Miller, 1986). This however, does not exclude the possibility that there is deep circulation or mixing of groundwater from the lower FAS.

Within the FAS, local low-permeability zones of Eocene sediments with varying elevations comprise the Middle confining unit (MCU). Specific to the WKP, there are three confining units described by Miller (1986) that may be regionally important in influencing groundwater flow. These MCUs (Miller, 1986, Figs. 15, 17 and 22) are referred to as Units III, IV, and VII (Miller, 1986). Unit III is considered to be a leaky confining bed and is seen as grading downward into clastic rocks of low permeability in places where its thickness is greater than 60 m (Miller, 1986). The portion of Unit III, which is less than 60 m thick, is believed to confine non-circulating waters of the lower FAS. These waters are seen as slow moving and are not considered in many regional flow models.

Unit IV is composed of thick calcareous sands and clays, which grade northwestward into clastic rocks. These rocks are Early to Middle Eocene and are associated with the Apalachicola Embayment. The upper FAS is very thick where it is underlain by Unit IV, and is considered to be relatively leaky in that it has the ability to transmit water vertically. The narrow band of Unit VII in west-central Georgia represents the base of the upper FAS. This bed of low permeability rocks is micritic to finely crystalline limestone, partially dolomitized and contains intergranular gypsum (Miller, 1986). This Eocene bed is associated with the Gulf Trough. Miller (1986) suggests that its location is adjacent to the Gulf Trough and that this juxtaposition creates a damming of groundwater flow.

The WKP, as stated earlier, is an area characterized by unconfined groundwater flow in the upper FAS. The ICU has been removed by erosion and the upper FAS is exposed, covered by only a thin veneer of permeable sands (Miller, 1986). Observed individually, the MCUs may not be of great importance in studying the regional groundwater flow, but considered as a whole they appear to confine the regions adjacent to the WKP. The cumulative effect of the MCUs may be to preferentially influence groundwater flow between the lower and upper FAS. In the context concerning the lack of the ICU in the upper FAS within the WKP, the MCUs may serve as ceilings to groundwater flow in the lower FAS and may be involved in movement of this water laterally toward the WKP. This water, moving laterally under the MCU, may then move vertically into the upper FAS and ultimately toward base level within the WKP (and/or the Gulf of Mexico). This may be achieved, in the WKP, via the lack of the ICU, in addition to the lack of a MCU.

Local Hydrology. There are several extensive underwater caves systems developed within the WKP (Fig. 1.2). As stated earlier, the loosely consolidated very porous and permeable sands, allow rapid infiltration of precipitation. Likewise, several

surface streams disappear below land surface upon entering the WKP. Some streams are intermittent, with the ability to transport water only when the infiltration rate is exceeded and surface runoff is initiated through excessive precipitation with respect to volume and/or time. In some places within the Leon Sinks Geological Site (*e.g.* Fisher Creek and Natural Bridge), groundwater emerges and flows in a surface stream and within a few tens of meters, diappear below ground once again.

The upper FAS has very high transmissivity, high permeability and porosity, and is the principal route of local groundwater flow. Much of the drainage is subsurface within the WKP, through large open cave passages developed in the St. Marks Formation and Suwannee Limestone. Cave divers of the Woodville Karst Plain Project (WKPP) have conducted surveys of many of the underwater caves and have established the existence of a large network of interconnecting passages. Over 48 km of passage has been mapped to date. Approximately 33.5 km of passage have been connected to establish the Leon Sinks Cave System (Irvine, 1999), the largest and deepest underwater cave system within the United States (Fig. A.19, A.20). Appendix A contains maps of each underwater cave used in this study in both plan and profile view.

Cave Systems

The cave systems used in this study include the Leon Sinks Cave System, which comprises Sullivan Sink Cave, Big Dismal Sink Cave, Cheryl Sink Cave, Emerald Sink Cave and Turner Sink Cave. The others include Wakulla Springs Cave System, Sally Ward Spring Cave, Indian Springs Cave, Harvey's Sink Cave, Chip's Hole Sink Cave, McBride's Slough Cave, Church Sink Cave, Shepherd Spring Cave and Rat's Sink Cave (Appendix A). Caves within the study area that were not included, due to poor survey data, accessibility, and/or water visibility conditions include Little Dismal (Hammock)

Sink Cave and Hatchet Sink Cave (Figure 1.3). Other caves not included in this study, Bird Sink Cave and caves in the vicinity of Woodville, were outside the study area boundaries or did not have surveys available. These caves are likely important in the overall hydrogeology on the WKP and St. Marks River basin, but fall significantly northeast and east, respectively, of the study area and were, therefore, not included in this study.

Two features of the caves pertinent to this study of formation and development are the flow routes and cross-sectional passage morphology. In general, the present flow routes of groundwater within the submerged caves in the study area is from north to south along the cave passages. This is consistent with the regional hydraulic gradient. Two exceptions to this general trend were discussed by Werner (1998). Namely, northward (opposite the hydraulic gradient) cave passage flow directions within both Indian Springs Cave and Wakulla Springs Cave System. These inconsistencies appear to be caused by modification of cave passage by collapse resulting in alternative flow paths on a limited local scale (Werner, 1998).

The cross-sectional passage morphology is important for several reasons. First, several morphologies have been identified as indicative of either phreatic or vadose development (Palmer, 1981; White, 1988; Ford and Williams, 1989). Phreatic passages tend to be tube-like and are thought to be formed at or below the water table. Examples of typical phreatic passages from dry caves can be found in Palmer, 1981, Fig. 53, White, 1988, Fig. 3.5 and Fig. 3.7a, 3.7b, and Ford and Williams, 1989, Fig. 7.33. Vadose passages typically have canyon cross-sections and are considered to form only above the water table by cave streams with a free surface, much like a downcutting surface stream. Examples from dry caves can be found in Palmer, 1981, Fig. 12, and Ford and Williams, 1989, Fig. 7.36. Vertical solution pits are also indicative of vadose entrenchment (Palmer, 1981, Fig. 16).

Second, modification of original cross-sectional morphologies can be indicative of the change of development mechanism for passage enlargement. While most morphological modifications are very difficult to distinguish, the transition from phreatic-dominated to vadose-dominated development is usually easily identified (Palmer, 1981, Fig. 15). The characteristic key-hole passage indicates that the conditions forming the original phreatic tube, were modified by a lowering of base level or regional uplift of carbonate strata, producing cave streams with a free surface where erosion occurs in the floor and/or bed of the cave stream.

The caves of the WKP, where identifiable, are generally dominated by phreatic cross-sectional cave passage morphologies. Nearly 60 percent exhibit the typical elliptical tube, while approximately 25 percent are indicative of a rectangular modified-tube (*sensu.* White, 1988, Fig. 3.5). There are some passages that are vadose dominated but they amount to less than 5 percent of the total. The remaining 10 percent are indicative of transitional morphologies. The most striking example is the upstream passage from the Black Abyss, in Cheryl Sink Cave, to the Bitter End passage (Figures A.23 and A.24). This 850 meter long passage, formed at approximately 60 m below the present water table, has a dominant keyhole cross-section. The upper phreatic tube has a mean width of 5 m and height of 3 m, whereas the entrenched vadose canyon below it is approximately 2 meters deep and 1.5 m wide. This observational field evidence suggests that this section of the Leon Sinks Cave System was for some significant time an air-filled cave stream passage.

Additionally, two very large vertical solution pits have recently been discovered in Harvey's Sink Cave and Hatchet Sink Cave (Figure 1.3). The solution pit, resembling a large cylindrical shaft, in Harvey's Sink Cave (Figure A.5 and A.6) begins at 24 m and drops to 82 m below the present water table, while in Hatchet Sink Cave the solution pit begins at 9 m and drops to 67 m below the present water table. While not

uniquely indicative of vadose conditions, this field evidence with relation to the keyhole passage in Cheryl Sink Cave suggests that a significant portion of the WKP caves were air-filled during their history. The air-filled history is likely attributable to extended periods of low sea level.

CHAPTER 3

CAVE PASSAGE DEVELOPMENT AND SEA LEVEL

Introduction

In this chapter the first question of the problem will be addressed. Namely, what mechanisms control and/or contribute to the development of the vertical distribution of conduits in the WKP. To begin, earlier research concerning vertical conduit development will be discussed and relevant studies will be examined. Second, several working assumptions will be introduced as well as relevant background material pertinent to the specific problem. Next, the water table elevation, conduit elevation and conduit depth below water table will be examined and discussed. Subsequently, the distribution of total passage length versus depth below present water table, as well as several running mean distributions, will be determined. Moreover, the concept of tiered passages will be examined within the WKP. Next, sea level fluctuation records will be considered and a methodology for establishing correlation with the passage length distribution will be established. Furthermore, a timeline of formation will be established using the longest sea level elevation duration records by determining the highest correlation coefficients for a given time before present conditions. Finally, the results of the analysis will be presented and discussed.

Previous Research

Historically, there have been three primary theories concerning the origin of cave passages. These include the vadose theory, the deep phreatic theory and the water table cave theory (White, 1988). The origin of cave passages by vadose theory involves the infiltration of surface waters percolating through the unsaturated zone invoking dissolution of carbonate rock above the water table. This movement downward by chemically aggressive waters produces easily recognizable dissolution features such as surface stream capture by vertical dissolution pits, dissolving sinkhole drains, and prominent solution canyons which terminate at the top of the saturated zone (White, 1988). While there are many variations on the theme of vadose cave passage formation, many of the elements remain the same. There must be (1) a hydraulic gradient sufficient to drive flow, (2) a developing surface or underground drainage pattern, (3) some relief of carbonate strata above the water table, and (4) a change in base level of the watershed to initiate the process of dissolution through vadose entrenchment. It is reasoned that initial movement of surface waters into the carbonate strata begins through highly permeable joints and/or fractures. The joints and/or fractures are widened over time, developing vertical dissolution features. After a sufficient time has elapsed, the conduit system produced is one in which evolution of passages has been through dissolution by streams with a free surface (Dreybrodt, 1988).

The theory of deep phreatic conduit evolution has its early origins in the alpine karst of Europe. Later championed by Davis (1930), the deep phreatic theory involves a hydrostatic head which drives flow deep into the phreatic zone along flow lines (White, 1988). The theory involves uniform dissolution throughout the flow lines leading to base level. With this in mind, many proponents of the deep phreatic theory believed this dissolution would take place tens to hundreds of meters below a stable water table. This

stable water table was usually thought to coincide with a peneplain geomorphology, while subsequently being preserved for a sufficiently long period of time (Dreybrodt, 1988). White (1988) mentions that upon careful examination of both the Davis (1930) and the Bretz (1955) hypotheses the reader is left with "the distinct impression that Bretz's deep phreatic was nowhere near as deep as Davis' deep phreatic."

The water table theory of karst conduit development was advanced primarily by Swinnerton (1932). Upon observation of primarily horizontally oriented cave passages throughout the world, Swinnerton (1932) hypothesized that passage development must take place near the water table surface and specifically in the region of vertical fluctuations of the water table from periodic seasonal variations (White, 1988). Infiltrating water moves vertically through the vadose zone to the water table, where it is theorized that the water proceeds down gradient horizontally along the water table to base level. The largest fluid movement occurs in the shallow phreatic zone near the water table surface (Dreybrodt, 1988). With large fluid mass transport occurring in such a limited location, the majority of dissolution will thus occur in this horizontal plane, eventually developing a conduit system. Dissolution is further strengthened by a stable water table, in which flow is allowed to migrate along the hydraulic gradient toward base level over a period of time.

The water table theory is also supported by the observations of tiered caves. A tiered cave is one in which there are several distinct elevation levels of nearly horizontal cave passages. White (1988) suggests a causal relationship between the coincidence of passage level elevation and river terrace elevation. He suggests there is a correlation between the position of local base level and the position of the water table in the evolution of the drainage system. Davies (1960) came to much the same conclusions in his theory of shallow phreatic conduit development, in which the cave levels are formed at the water table surface of the maturing river valley base level. Davies (1960) and

White and White (1974) related river terraces to caves found in the Potomac River Valley. Others, such as Sweeting (1950) and Droppa (1957), have also found the same type of correlation in Yorkshire, England and in Demanova Valley, Czechoslovakia, respectively.

Perhaps the most compelling observations for water table cave development came from Miotke and Palmer (1972) and Palmer (1981) concerning the Flint Ridge-Mammoth Cave System in central Kentucky. Palmer systematically distinguished six distinct cave levels and correlated their development to periods of stable levels of the Green River. He commented that each of these major levels formed at progressively lower altitudes, and that they can be considered time horizons or markers (Palmer, 1981). The interesting point to note is that the younger, more recent levels of passage development are the ones at the lower elevation. Many of these lower levels still function as part of the drainage system, whereas the older, higher elevation conduits are primarily relict cave stream passages. Tiered caves form when new drainage routes are formed below the older routes as flow is captured by the lower passages, which in turn leave the older, higher elevation passages dry (White, 1988). This type of development is one in which discontinuous downcutting within the drainage basin is dependent on base level lowering (White, 1988).

Background

In order to further clarify the problem and test the first part of the hypothesis, namely, the determination of a control mechanism responsible for conduit development in the WKP, several working assumptions will need to be employed. First, it will be assumed that base level of the WKP during the Quaternary has been the Gulf of Mexico. Second, due to the close proximity of the WKP and its cave systems to the Gulf, it will be

assumed that sea level height (elevation) fluctuations obtained for the Quaternary may be used as an accurate record of base level lowering for the caves of the WKP. Third, from work completed by Palmer (1981) at the Flint Ridge-Mammoth Cave System, it appears reasonable to correlate past sea level fluctuations with conduit development. A representative sea level height (elevation) record (Imbrie *et. al.*, 1984) is provided in Figure 3.1.

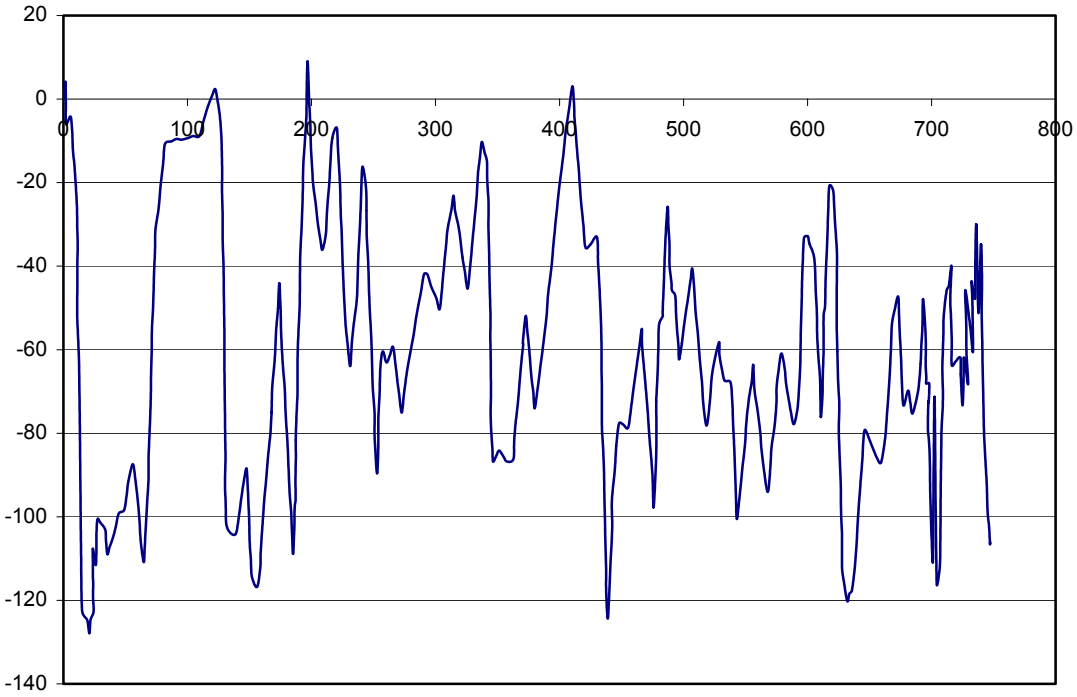

Figure 3.1. $\delta^{18}O$ record of Core DSDP 502b modified from Imbrie *et. al.* (1984, fig. 5), with ordinate in meters derived from the $\delta^{18}O‰$ variations in *Globigerinoides sacculifer* and abscissa the time in Ka BP.

In order to use sea level fluctuations as an accurate record for base level elevation, two other assumptions must be employed: (1) the carbonate platform of Florida has been relatively stable in recent geologic time (*i.e.* the Quaternary) and (2) the predominant regional groundwater flow patterns have not been significantly altered from their present orientation. Similarly, there is nothing present (*i. e.* aquitards) within the carbonates of the WKP that would disrupt the sea level / water table relationship. In

other words, the water table is free to rise and fall with sea level. An estimate of the time necessary to generate the conduit dimensions observed in the WKP is on the order of ~10^5 years (White, 1988, Fig. 9.12). Both of these assumptions appear reasonable given that initial conduit formation likely occurred less than 1 Ma BP, approximately Middle Pleistocene. This approximation is compatible with the maximum development time for the Mammoth-Flint Ridge Cave System of ~ 2 Ma BP (Schmidt, 1982).

Based on the discussion above and the previous research reviewed in the last section, a correlation between the specific conduit levels and base level should exist. However, due to sea level fluctuations, there has not been a continuous base level lowering at the Gulf of Mexico. This fact complicates the simple continuous base level lowering models discussed previously. In order to compensate for sea level fluctuation, an alternate approach is taken.

Water table elevation

Based on descriptions of the local and regional hydrology of the WKP in Chapter 2, some simplifying assumptions were attempted in order to reconcile the conduit depth below the water table with mean sea level. The survey data obtained for this study (Irvine, 1999) involve depth measurements of cave passages below the present water table. To determine the actual elevation at each survey point, application of the Dupuit approximation was employed. This approach was attempted in order to directly correlate each cave survey within the study area to mean sea level.

Since the slope of the water table within the WKP is relatively small, as confirmed through potentiometric maps of Florida (Mahon et. al., 1997; Scott et. al., 1991, Fig. 32; Healy, 1982), changes in the height of the water table, denoted by the quantity ∂h, is very small compared with the total length L, along the direction of flow

(*i.e.* north to south) of the unconfined Floridan aquifer in the study area: $h << L$. Finally, it was assumed that the lower boundary of the upper FAS beneath the WKP is horizontal. As mentioned previously, the upper FAS is not entirely separated from the lower FAS. Significant portions of the MCU are absent within and surrounding the WKP and these beds do not correspond to a working horizontal datum.

An attempt was made to mathematically model the water table of the study area using the Dupuit approximation (Bear, 1972). This approximation neglects the vertical flow components and reduces the number of independent variables of interest (*x, z*) from two to one, no longer employing the vertical elevation *z* (Bear, 1972, Fig. 8.1.1). This approach considers the flow as a single streamtube by assuming that the vertical cross-sections are equipotential surfaces to the water table elevation *h*. Forchheimer used a variation of the original Dupuit approximation, which predicts an ellipsoidal shape to the water table described by the equation

$$h = \left[h_0^{\,2} - \frac{h_0^{\,2} - h_L^{\,2}}{L} x + \frac{p}{k}(L - x)x \right]^{\frac{1}{2}},$$

where h is the height of the water table at some distance x from the Gulf coast, $h(0) = h_0$ = depth of the datum at mean sea level, $h(L) = h_L$ is the height of the water table above the datum at the northern most point of the WKP, p is the precipitation rate minus the evapotranspiration rate and k is the hydraulic conductivity (after Bear, 1972, Fig. 8.2.2).

It should be noted that the ratio $\frac{p}{k}$ in the above equation determines the shape of the potentiometric surface. If $\frac{p}{k} < 0$, the equation describes a hyperbola, whereas $\frac{p}{k} > 0$ describes an ellipse. This approximation is also complicated by the fact that the

discharge into the WKP from the Tallahassee Hills Q_{in} and the discharge at the coast Q_{out} are unknowns (Figure 3.2). It was assumed that $Q_{in} = Q_{out}$ and therefore, would not enter into the equation.

The first derivative of the Dupuit-Forchheimer equation above with respect to x may be expressed as

$$\frac{\partial h}{\partial x} \cong \frac{1}{2h}\left[\frac{h_0^{\,2} - h_L^{\,2}}{L} + \frac{p}{k}(L - 2x)\right],$$

which is the equation for a straight line with slope p/hk. This formulation shows that the water table can be projected as a straight line of negligible slope within the unconfined WKP.

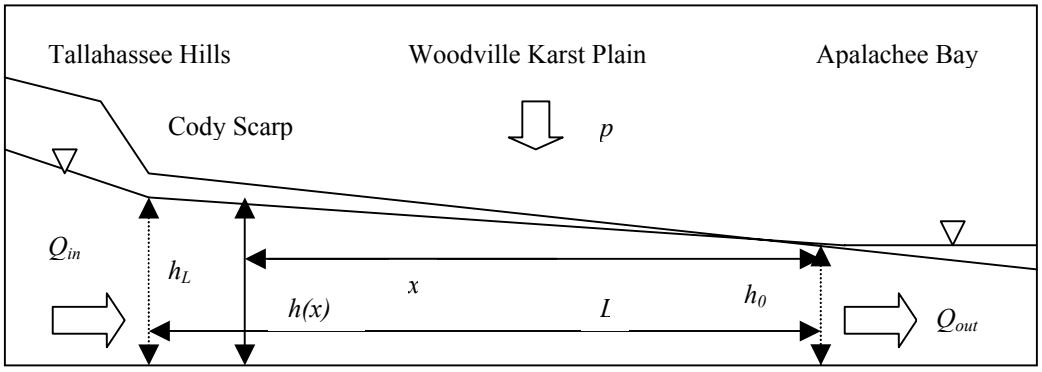

Figure 3.2. Simple N-S cross-section through the WKP (not to scale) showing water table, land surface and inputs and outputs, p, Q_{in} and Q_{out}, which contribute to the water table elevation.

Although the Dupuit-Forchheimer equation describes a parabolic/elliptic $h(x)$, to good approximation, this is straight over the horizontal length L, therefore the analysis is simplified to this approximation. Therefore, another approach needed to be taken. Namely, the actual survey data using the measured depths below the water table was employed. In this approach the water table is assumed to retain its same shape and approximate slope, rising and falling with the fluctuations of sea level. This assumption

is not unreasonable given the slope of the present water table (Figure 3.3). The field evidence of keyhole cross-sectional passage morphologies from Cheryl Sink Cave and the solution pits of Hatchet Sink Cave and Harvey's Sink Cave suggest that the water table experienced fluctuations on the order of those of sea level.

These field observations suggest that many of the cave passages of the Leon Sinks Cave System were likely dry (air filled) during periods of substantial base level lowering. In fact, the geomorphic features discussed in Chapter 2 are likely the result of extensive base level lowering events in which free surface cave stream beds experienced

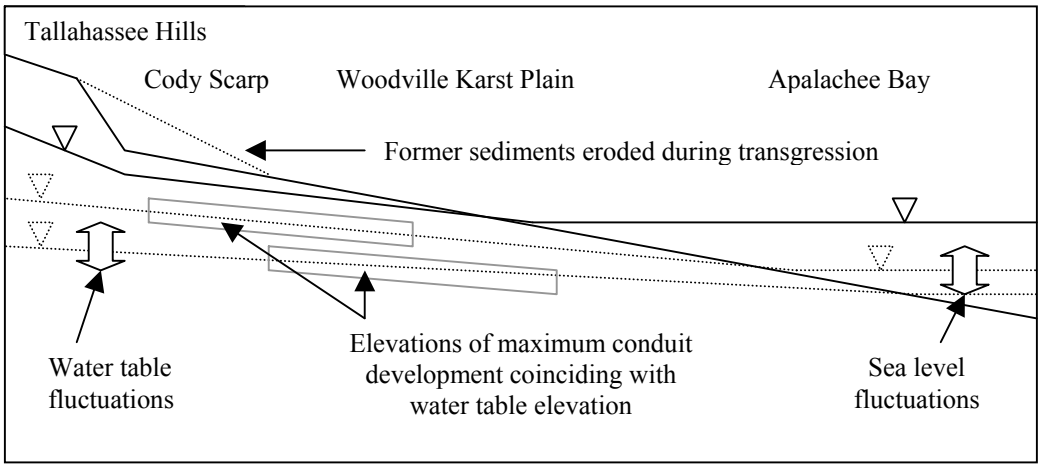

Figure 3.3. Simple N-S cross-section through WKP suggesting that water table fluctuations (not to scale) coincided with sea level fluctuations. Here the shape of the water table surface is proposed to remain essentially constant while it moves vertically depending on sea level height.

erosional downcutting. These findings appear to be consistent with other documented cases of base level lowering (Palmer, 1981) and the transition from phreatic to vadose dominated erosional regimes (White, 1988). In order to utilize the conduit depth below water table and the elevation of sea level during fluctuations, it is necessary to compare the error of both the water table elevations and the survey data. The maximum elevation of the water table relative to mean sea level at the northern most cave used in this study, Church Sink Cave, is approximately 6.1 m. The maximum error of the survey

data is ± 2.36 m (discussed in the next section) implying an error range of 4.72 m. Hence, the survey error is the same magnitude as the height of the average water table above mean sea level. If the water table rises and falls consistently with fluctuations of sea level, then the depth of maximum conduit development below the water table should be coincident with sea level fluctuations in elevation. This allows the depth of maximum conduit development below the water table to be correlated directly to sea level fluctuations.

Conduit tiering

In order to establish whether the caves of the WKP are tiered, the cave passage lengths were measured and totaled at certain mean depths below present sea level. Due to the lack of extremely accurate instruments for underwater surveys, in particular depth gauges available to the WKPP divers, a certain degree of error exists in these surveys. Additionally, the surveys were completed over the course of several years and at varying water table elevations dependent on seasonal precipitation. There are also slight tidal variations in many springs in close proximity to the Gulf. Very few of these variations, including fluctuations of magnetic declination, were corrected for during the survey process. Therefore, it was necessary to calculate the maximum error of the instruments and water table height. Recalculation of survey bearings for declination and averaging of several cave surveys, where possible, decreased the maximum error. Additionally, the algorithm used to generate the cave maps and profiles in Appendix A allowed for minimization of closed-loop survey triangulation error. These techniques, along with the maximum fluctuations due to both tidal influence and seasonal water table height, obtained from both Wakulla Springs Basin and a gauged sink near the coast, were used to calculate a maximum error in surveying of ± 2.36 m. The maximum error is additive:

$E_{MAX} = \left(g_{MAX} + s_{MAX} + f_{MAX} \right)$, where g_{MAX} is the maximum gauge or instrument error, s_{MAX} is the maximum survey error after loop closure and f_{MAX} is the maximum seasonal and tidal water table fluctuations during clear visibility conditions.

Taking the maximum error into consideration while constructing the cave passage depth below water table distribution for the WKP, has suggested the creation of several alternatively plausible distributions. Several passage distributions were constructed by summing the total passage lengths over various depth intervals of 1/3 m, 1 m, 2 m, 3 m and 4 m. Additionally, these distributions were also plotted using several running means over the varying intervals, producing four additional sets of distributions for each interval. These included the straight running-three and –five mean and weighted running-three and –five mean figures. All subsequent figures can be found in Appendix D. A representative figure is illustrated in Figure 3.4.

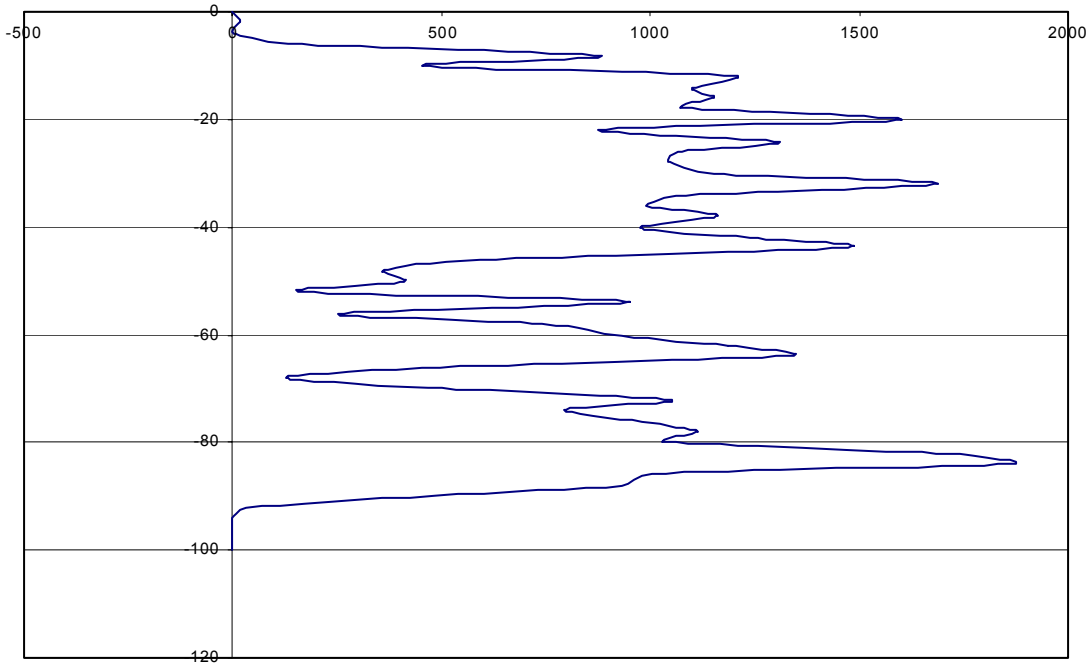

Figure 3.4. Depth below water table over 2 m interval vs. Total passage length, with surveyed maximum error of ± 2.36 m. Ordinate axis in meters below water table and abscissa axis in meters of total passage length.

With the surveyed cave passage likely being a small subset of the entire cave passage within the WKP, it is reasonable to suggest that a running mean distribution is a more appropriate and accurate representation of the entire cave passage present. Assuming the sample population represents the actual distribution on all cave passage within the WKP, three qualitative observations can be made.

First, there appears to be evidence of cave passage tiering. Figure 3.4 shows at least three elevation ranges where cave passage development was maximum. The most apparent maximized development elevation occurs at ~ -83 m, with an effective range of ~ -75 m to -88 m. The second highly defined peak of maximized passage development occurs at ~ -63 m. Although not as pronounced as the peak at -83 m, it appears to be quite significant. A larger and broader maximized development occurs at the elevation range of ~ -15 m to -45 m, with a central peak of ~ -32 m below the water table.

Second, the large broad distribution from ~ -15 m to -45 m may suggest that there are several distinct elevations of maximized passage development, which may be subdivided into three separate levels where maxima occur at ~ -20 m, -32 m and -42 m. This would effectively create five separate elevation levels of maximum passage development.

Third, Figure 3.4 can be compared with the figures of Appendix D to discern the effectiveness of smoothing this distribution over the 1 m, 2 m, 3 m and 4 m intervals. The three, as well as the five, maximized passage development levels can be distinctly seen in the 2 m and 3 m intervals as well as the 1m interval. The 4 m interval experienced unrealistic smoothing, resulting from the large interval. This suggests, qualitatively, that these maximum passage development levels warrant the description of a tiered cave distribution. As was noted by Palmer (1981), passage level tiering of the Flint Ridge-Mammoth Cave System appeared to be correlated to base level lowering of the Green River. Here, within the WKP, the apparent passage level tiering may also be

attributable to base level lowering and/or fluctuations. To investigate this possibility, an examination of sea level elevation records were used to determine a correlation between the tiered passage distribution and the duration of sea level elevation at the Gulf of Mexico.

Sea level elevation records

It was necessary to select several representative sea level elevation records to successfully determine the correlation of sea level elevation duration and the passage length distributions. The criteria for selecting sea level elevation records include (1) the time scale over which the record was valid, (2) the age dating technique used to determine sea level elevation, (3) a detailed comparison of the record to other sea level records in the literature, and (4) the geographic location of the study. These criteria are discussed below in the context of their selection for this study.

First, the sea level height record must be of significant duration for it to be applicable to this study. The records chosen all extend to more than 50 Ka BP. This was a requirement based on the time needed for formation of the surveyed passages (White, 1988, Fig. 9.12). A relatively short duration, on the order of several thousand years, is likely insufficient to have produced the observed cross-sectional dimensions of the surveyed passages in the WKP. A variety of differing time length records were chosen, ranging from ~ 70 Ka to ~ 800 Ka BP.

Second, several studies involving various age dating techniques were also chosen. A large number of studies involved measured variations in $\delta^{18}O$ ratios obtained from several species of both planktonic and benthonic foraminifera from deep sea cores (Imbrie *et. al.*, 1984; Chappell & Shackleton, 1986; Laberie *et. al.*, 1987). Other studies effectively compared variations in $\delta^{18}O$ ratios from cores to isotopic ratios ($^{230}Th/^{234}U$

and $^{87}Sr/^{86}Sr$) and elevations of raised coral terraces (Dodge *et. al.*, 1983; Shackleton, 1987; Bard *et. al.*, 1990a; Bard *et. al.*, 1990b; Dia *et. al.*, 1992). For additional details concerning the sampling techniques, measurement criteria and sea level records obtained, the reader may wish to consult the above studies. The comparison studies provide constraints on many of the $\delta^{18}O$ records. The comparison studies, while less complete than the $\delta^{18}O$ records, were chosen to provide a diverse data set with which cave passage length distributions and sea level elevation duration could be compared.

Finally, there is a considerable lack of detailed records in the vicinity of the study area, namely the Gulf of Mexico. In considering the type of records that these studies provide, it is reasonable to suggest that the sea level fluctuations were most likely global in extent and that local variations differed only slightly. This reasoning is used extensively in the above mentioned studies and appears to be consistent with global climatic and glacio-eustatic theories (Hays *et. al.*, 1976; Imbrie *et. al.*, 1984; Imbrie *et. al.*, 1989).

Methodology

Fourteen sea level elevation records were chosen (Dodge *et. al.*, 1983; Imbrie *et. al.*, 1984; Chappell & Shackleton, 1986; Laberie *et. al.*, 1987; Shackleton, 1987; Bard *et. al.*, 1990; Dia *et. al.*, 1992), each in graphical representation. The sea level elevation records were digitized using CAD software. The process of digitizing each curve is prone to an introduction of error. The digitizing process was tested statistically for root-mean-square error, standard deviation and largest residual and the results of each record are contained in Table 3.1. Each error calculation was based on the four initial digitized points corresponding to the four corners of the sea level duration record. The root-mean-

square was calculated using $RMS = \sqrt{\frac{(X_i - \overline{X_i})^2}{N}}$, where $(X_i - \overline{X_i})^2$ is the sum of squares and N is the number of degrees of freedom; the standard deviation was calculated using $s = \sqrt{\frac{1}{n-1}\sum (X_i - \overline{X_i})^2}$, where n is the number of digitized points; the largest residual was calculated using $R_i = X_i - \overline{X_i}$, where X_i is the digitized corner point and $\overline{X_i}$ represents the true corner point. The digitized points were extracted in an x-y coordinate plane and entered into a spreadsheet. The curve was then plotted and smoothed to produce the sea level elevation records found in Appendix B.

Due to the nature of the original sea level elevation records, each abscissa was expressed in Ka BP, but unfortunately the ordinate axis was expressed in depth below present mean sea level, $\delta^{18}O$ ratios, $^{230}Th/^{234}U$ and/or $^{87}Sr/^{86}Sr$ ratios. In order to effectively compare the sea level elevation records with the depth of maximum passage formation presented earlier, it was necessary to express each ordinate axis as depth in meters below present mean sea level. This was done for the $\delta^{18}O$ records by using a conversion factor for the fraction per million per meter of sea level change. Typical values of this factor range from 0.011 to 0.7. This is a linear scaling factor which appropriately adjusts the magnitude of the sea level elevation record to that typically accepted in the literature from comparison record studies (*i. e.* Imbrie *et. al.*, 1984; Chappell & Shackleton, 1986; Laberie *et. al.*, 1987, etc.). For the purpose of this study, the scaling factor simply adjusts the maximum relative sea level fluctuations to certain bounds consistent with other sea level records. It is used to compensate for the influences of water temperature, regional geographic variations, species specific variations, dissolution, sedimentation rates, and stratigraphic sequences (Imbrie *et. al.*, 1984).

Following conversion of the ordinate axis to depth in meters below present mean sea level, each sea level record was then analyzed for the duration at which it was at a particular depth below present mean sea level. To present the most plausible representation, each sea level record was summed over 1 m, 2 m, 3 m and 4 m intervals, hence smoothing the duration distribution. It should be noted that two records, namely the Barbados raised coral reef $^{230}Th/^{234}U$ isotope ratio record (Bard *et. al.*, 1990b) and the Sr isotope ratio record (Dia *et. al.*, 1992), contained too few data point resulting in a skewed distribution. These skewed records were eliminated from the set of possible sea level records. The remaining twelve sea level duration records were smoothed by summing over 2 m, 3 m and 4 m intervals and are contained in Appendix C.

The twelve sea level duration records and the total passage length distributions, including the actual passage distance, straight running-three and –five mean and weighted running-three and –five mean, were then used to calculate correlation coefficients for the 1 m, 2 m, 3 m and 4 m intervals. The correlation coefficient data are presented in Tables 3.2, 3.3, 3.4 and 3.5.

Correlation

In a preliminary study, sea level elevation records obtained from Bard *et. al.* (1990b), Shackleton (1987), Chappell and Shackleton (1986), and Labeyrie *et. al.* (1987) were selected. The corresponding data sets of the four sea level duration records were systematically summed over a 3 m interval to produce a smoothed stack duration record. The duration records were summed and not averaged because they are equivalent graphs differing only by a scaling factor. The cumulative smooth stacked duration record was created to represent a eustatic sea level curve. The total passage length records on a 3 m interval were adjusted by a three, six and nine meter interval to better fit the cumulative

sea level duration record. This correlation procedure was employed in the preliminary study for several reasons: (1) to account for the gradual elevation change of the potentiometric surface with distance from the Gulf, (2) to factor in possible effects from subsidence, and (3) to better approximate passage development in relation to the water table. The highest correlation coefficients calculated were for the straight running-five mean, where a 3 m adjustment in passage length distribution produced a coefficient of 0.814, a 6 m adjustment, 0.821, and a 9 m adjustment, 0.810. The distribution with no smoothing of the total passage length produced a correlation coefficient of 0.456 for the smooth stacked duration record.

In this study, the surveyed passage distribution was directly correlated, both direct distances and smoothed running means, with the twelve sea level duration records. The correlation coefficients were calculated from the *x* and *y* data (see Methodology in this Chapter), produced during the digitizing process, using $r = \frac{1}{n-1}\sum\left(\frac{x-\bar{x}}{s_x}\right)\left(\frac{y-\bar{y}}{s_y}\right)$, where *n* is the number of data points, $\bar{x}$ is the mean of the *x* data, $\bar{y}$ is the mean of the *y* data, s_x and s_y are the standard deviations of the *x* and *y* data, respectively. Selected figures illustrating correlations of the passage length distributions and the sea level duration records are contained in Appendix E.

For the 1 m interval, the maximum correlation coefficient calculated was 0.341 for the $\delta^{18}O$ record of Core V19-29 on the actual passage distance distribution (Figure E.1). For the 2 m interval, the three highest coefficients calculated were for the $\delta^{18}O$ record of Core RC17-177. Coefficients of 0.455, 0.398, and 0.389 were found to correspond to the straight running-five, straight running-three and weighted running-three means, respectively. For the 3 m interval, the first and third highest coefficients calculated were 0.527 and 0.484 for the $\delta^{18}O$ record of Core V30-40 (Figure E.5 and

E.6), for the straight running-three and –five mean, respectively. The second highest coefficient calculated was 0.520 for the $\delta^{18}O$ record of Core V28-238 for the straight running-five mean (Figure E.7). For the 4 m interval, the highest correlation coefficients calculated were 0.654 and 0.677 for the $\delta^{18}O$ record of Core RC17-177 corresponding to a straight running-three mean (Figure E.11) and the $\delta^{18}O$ record of Core V30-40 corresponding to the straight running-five mean (Figure E.12), respectively.

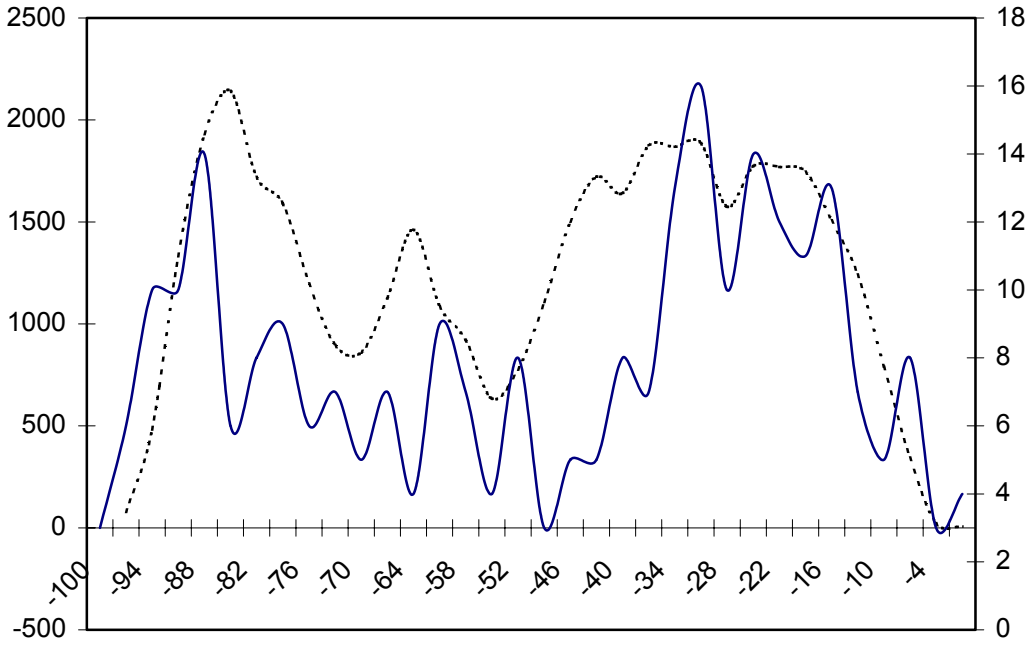

Figure 3.5. Straight running three-mean of passage distance (dotted line), left ordinate in meters, and duration of sea level height, right ordinate in frequency, for Core V30-40 (solid line) summed over 3 m interval, abscissa in meters below mean sea level.

It is apparent from Tables 3.2, 3.3, 3.4 and 3.5 and the discussion above that the correlation coefficient increases as the size of the interval over which they are summed increases. This finding suggests the 4 m interval is a better approximation than the 1 m, 2 m, or 3 m interval for the overall correlation of mean sea level duration and the maximum passage development distribution (Figures E.10, E.11, E.12 and E.13). In examining the overall correlation, the results appear mixed. Higher correlation coefficients resulted

from a direct comparison of the actual passage length distribution and sea level duration record in the present study than the preliminary study: a correlation of approximately 22.7% (3 m interval) and 35.4% (4 m interval) for this study versus 21.0% (3 m interval) for the preliminary study. Even with this slight improvement the results are far less than the correlation of approximately 67.4% for the adjusted distributions of the preliminary study.

Timeline of formation

The concern that the time scale in the selection criteria be of considerable length, on the order of 10^5 years, may have been an erroneous prerequisite. It appears as though there may be an optimal time scale over which the correlation is greatest. In the 2 m interval, the highest correlation, Core RC17-177 has a time scale of 140 Ka BP. In the 3 m interval, the highest correlation, Core V30-40 has a time scale of ~ 300 Ka BP. This may suggest that the longer time scale records, Core DSDP 502b and the smoothed stack SPECMAP, may show little correlation because conduit development was not operating over ~ 700 – 800 Ka, but rather over a shorter time scale of approximately 300 - 500 Ka.

Table 3.1. Digitizing inaccuracies for each sea level record displaying root-mean-square error, standard deviation, and largest residual.

Digitizing Error	RMS Error	Standard Deviation	Residual
Barbados Corals	0.237	0.078	0.332
DSDP502b $\delta^{18}O$	1.015	0.616	1.860
SPECMAP $\delta^{18}O$	0.854	0.979	0.894
V28-238 Sr	0.379	0.189	0.582
V28-238 $\delta^{18}O$	0.343	0.176	0.600
Labeyrie $\delta^{18}O$	0.402	0.073	0.462
Huon & V19-30 $\delta^{18}O$	0.325	0.168	0.286
Meteor 12392	0.124	0.730	0.260
V19-29 $\delta^{18}O$	0.119	0.076	0.228
New Guinea Terrace	0.337	0.157	0.530
RC17-177 $\delta^{18}O$	0.183	0.132	0.412
V19-30 benthic $\delta^{18}O$	0.180	0.125	0.381
V19-30 planktonic & benthonic $\delta^{18}O$	0.186	0.253	0.512
V30-40 $\delta^{18}O$	1.496	0.979	2.48

With this in mind, a subsequent investigation to determine the maximum correlation coefficient on a shortened time scale was initiated. The correlation could only involve two of the twelve sea level duration records, namely Core DSDP 502b and the smoothed stack SPECMAP. Both of these cores contain a sufficient record spanning ~750 Ka to ~800 Ka BP. The two records were utilized with 25 Ka intervals spanning 400 to 500 Ka.

Table 3.2. Correlation coefficients over 1 m interval for sea level duration record listed in rows and maximum passage development distribution in columns.

1m Interval	Actual Passage Length	Running three mean	Running three weighted mean	Running five mean	Running five weighted mean
DSDP 502b $\delta^{18}O$	0.103	0.125	0.089	0.023	0.035
SPECMAP $\delta^{18}O$	-0.130	-0.085	-0.181	-0.156	-0.173
V28-238 $\delta^{18}O$	0.097	0.217	0.225	0.235	0.199
Labeyrie $\delta^{18}O$	0.100	0.175	0.108	0.076	0.052
Huon & V19-30 $\delta^{18}O$	0.182	0.203	0.200	0.158	0.164
Meteor 12392	0.157	0.106	0.133	0.103	0.123
V19-29 $\delta^{18}O$	0.341	0.238	0.309	0.244	0.284
New Guinea Terrace	0.139	0.171	0.244	0.233	0.238
RC17-177 $\delta^{18}O$	0.007	-0.011	0.031	0.055	0.035
V19-30 benthic $\delta^{18}O$	0.014	0.029	0.004	0.028	0.013
V19-30 planktonic & benthonic $\delta^{18}O$	0.243	0.309	0.273	0.319	0.288
V30-40 $\delta^{18}O$	0.221	0.219	0.208	0.185	0.203

The five time intervals produced, 400 Ka, 425 Ka, 450 Ka, 475 Ka and 500 Ka BP, were directly correlated to the five passage length distributions over 2 m, 3 m and 4 m intervals. The results are displayed in Tables 3.6, 3.7 and 3.8. Selected figures illustrating correlations of the passage length distributions and the sea level duration records are contained in Appendix F.

Table 3.3. Correlation coefficients over 2 m interval for sea level duration record listed in rows and maximum passage development distribution in columns.

2m Interval	Actual Passage Length	Running three mean	Running three weighted mean	Running five mean	Running five weighted mean
DSDP 502b $\delta^{18}O$	0.153	0.135	0.087	0.032	-0.034
SPECMAP $\delta^{18}O$	-0.105	-0.052	-0.133	-0.220	-0.271
V28-238 $\delta^{18}O$	0.338	0.307	0.354	0.349	0.309
Labeyrie R$\delta^{18}O$	0.188	0.166	0.160	0.133	0.076
Huon & V19-30 $\delta^{18}O$	0.240	0.241	0.212	0.217	0.172
Meteor 12392	0.110	0.201	0.121	0.146	0.110
V19-29 $\delta^{18}O$	0.371	0.344	0.326	0.301	0.306
New Guinea Terrace	0.376	0.326	0.371	0.338	0.338
RC17-177 $\delta^{18}O$	0.300	0.398	0.389	0.455	0.300
V19-30 benthic $\delta^{18}O$	0.035	-0.004	0.076	0.091	0.016
V19-30 planktonic & benthonic $\delta^{18}O$	0.329	0.306	0.388	0.410	0.348
V30-40 $\delta^{18}O$	0.361	0.374	0.331	0.348	0.315

The results of this analysis for the 2 m interval show significant increases in the correlation coefficients from a maximum of the actual passage length distribution for the entire record from 0.153 to 0.184 on the 475 Ka record for Core DSDP 502b and a maximum of the running-three mean for the entire record from –0.052 to 0.155 on the 450 Ka record for the smoothed stack SPECMAP.

Table 3.4. Correlation coefficients over 3 m interval for sea level duration record listed in rows and maximum passage development distribution in columns.

3m Interval	Actual Passage Length	Running three mean	Running three weighted mean	Running five mean	Running five weighted mean
DSDP 502b $\delta^{18}O$	0.124	0.125	0.054	0.032	0.019
SPECMAP $\delta^{18}O$	-0.155	-0.105	-0.174	-0.203	-0.150
V28-238 $\delta^{18}O$	0.405	0.438	0.445	0.520	0.439
Labeyrie R$\delta^{18}O$	0.233	0.141	0.196	0.299	0.135
Huon & V19-30 $\delta^{18}O$	0.356	0.315	0.327	0.386	0.319
Meteor 12392	0.101	0.227	0.131	0.156	0.178
V19-29 $\delta^{18}O$	0.370	0.406	0.359	0.290	0.288
New Guinea Terraces	0.319	0.292	0.290	0.264	0.252
RC17-177 $\delta^{18}O$	0.422	0.445	0.427	0.409	0.478
V19-30 benthic $\delta^{18}O$	0.080	-0.032	0.044	0.093	-0.014
V19-30 planktonic & benthonic $\delta^{18}O$	0.408	0.292	0.429	0.413	0.399
V30-40 $\delta^{18}O$	0.477	0.527	0.456	0.484	0.477

The 3 m interval correlation coefficients increase from a maximum for the running-three mean distribution of the entire record from 0.125 to 0.469 on the 450 Ka record for Core DSDP 502b and a maximum for the running-three mean of the entire record from –0.105 to 0.401 for the running-three mean on the 400 Ka record for the smoothed stack SPECMAP.

Table 3.5. Correlation coefficients over 4 m interval for sea level duration record listed in rows and maximum passage development distribution in columns.

4m Interval	Actual Passage Length	Running three mean	Running three weighted mean	Running five mean	Running five weighted mean
DSDP 502b $\delta^{18}O$	0.418	0.481	0.472	0.477	0.367
SPECMAP $\delta^{18}O$	0.203	0.277	0.261	0.362	0.191
V28-238 $\delta^{18}O$	0.573	0.623	0.620	0.639	0.592
Labeyrie R$\delta^{18}O$	0.359	0.426	0.414	0.510	0.399
Huon & V19-30 $\delta^{18}O$	0.409	0.498	0.482	0.540	0.460
Meteor 12392	0.268	0.343	0.328	0.404	0.328
V19-29 $\delta^{18}O$	0.410	0.445	0.444	0.408	0.414
New Guinea Terraces	0.454	0.415	0.434	0.438	0.439
RC17-177 $\delta^{18}O$	0.591	0.654	0.648	0.617	0.609
V19-30 benthic $\delta^{18}O$	0.040	0.116	0.096	0.187	0.125
V19-30 planktonic & benthonic $\delta^{18}O$	0.333	0.439	0.417	0.441	0.424
V30-40 $\delta^{18}O$	0.595	0.662	0.655	0.677	0.633

The 4 m interval correlation coefficients increase for the maximum for the running-three mean distribution of the entire record from 0.481 to 0.566 on the 425 Ka record for Core DSDP 502b. Likewise, for the running-five mean of the entire record from 0.477 to 0.653 on the 425 Ka record for Core DSDP 502b. Increases were also observed for the maximum for the running-five mean of the entire record from 0.362 to 0.466 on the 450 Ka record for the smoothed stack SPECMAP.

Table 3.6. Timeline of formation correlation coefficients over 2 m interval for sea level duration record listed in rows and maximum passage development distribution in columns.

2m Interval	Actual Passage Length	Running three mean	Running three weighted mean	Running five mean	Running five weighted mean
DSDP 502b $\delta^{18}O$					
400 Ka	0.087	0.000	0.077	0.047	-0.001
425 Ka	0.077	-0.070	0.036	-0.005	-0.031
450 Ka	0.182	0.087	0.147	0.120	0.082
475 Ka	0.184	0.101	0.152	0.128	0.086
500 Ka	0.175	0.076	0.133	0.102	0.059
SPECMAP $\delta^{18}O$					
400 Ka	-0.005	0.136	0.010	0.012	-0.058
425 Ka	0.015	0.140	0.060	0.047	-0.023
450 Ka	0.000	0.155	0.040	0.037	-0.042
475 Ka	-0.024	0.119	0.019	0.009	-0.070
500 Ka	-0.017	0.131	0.022	0.011	-0.067

The results of the analysis to determine a timeline of formation for the caves of the WKP suggest that initial conduit formation took place approximately 450 Ka BP. Both Core DSDP502b and the smoothed stack SPECMAP sea level duration records show maximum correlation coefficients near 450 Ka BP. In particular, Core DSDP 502b shows maximum correlation coefficients for the 2m interval at 475 Ka, the 3 m interval at 450 Ka and the 4 m interval at 425 Ka BP. The smoothed stack SPECMAP shows maximum correlation coefficients for the 2m interval at 450 Ka, the 3 m interval at 400 Ka and the 4 m interval at 450 Ka BP. These results are illustrated in Appendix G.

The results for Core DSDP 502b may show greater correlation coefficients due to the fact the core is from the Gulf of Mexico and may be the best single indicator for sea

level fluctuations influencing the Woodville Karst Plain. The SPECMAP record may not show the same improvements in correlation coefficient due to the fact it is a composite from several cores sampled in different ocean basins.

The results of this subsequent analysis strongly suggest that the caves of the WKP show a maximum in correlation coefficients for sea levels records on the order of approximately 425 Ka to 475 Ka BP. This is strongly dependent on the assumption that maximum cave passage development within the WKP primarily took place near the water table. This assumption is reinforced by the observations of multiple cave passage tiering demonstrated earlier in this Chapter and the cave passage geomorphology of upstream Cheryl Sink Cave, Harvey's Sink Cave and Hatchet Sink Cave discussed in Chapter 2.

Table 3.7. Timeline of formation correlation coefficients over 3 m interval for sea level duration record listed in rows and maximum passage development distribution in columns.

3m Interval	Actual Passage Length	Running three mean	Running three weighted mean	Running five mean	Running five weighted mean
DSDP 502b $\delta^{18}O$					
400 Ka	0.041	0.114	0.046	0.083	0.064
425 Ka	0.409	0.469	0.396	0.463	0.440
450 Ka	0.434	0.469	0.411	0.465	0.451
475 Ka	0.148	0.137	0.116	0.112	0.122
500 Ka	0.177	0.154	0.154	0.144	0.157
SPECMAP $\delta^{18}O$					
400 Ka	0.031	0.401	0.057	0.104	0.076
425 Ka	0.026	0.380	0.052	0.085	0.065
450 Ka	0.021	0.367	0.050	0.082	0.062
475 Ka	0.022	0.383	0.055	0.093	0.069
500 Ka	0.022	0.381	0.053	0.092	0.069

Table 3.8. Timeline of formation correlation coefficients over 4 m interval for sea level duration record listed in rows and maximum passage development distribution in columns.

4m Interval	Actual Passage Length	Running three mean	Running three weighted mean	Running five mean	Running five weighted mean
DSDP 502b $\delta^{18}O$					
400 Ka	0.386	0.394	0.399	0.337	0.261
425 Ka	0.510	0.566	0.560	0.653	0.547
450 Ka	0.422	0.434	0.439	0.407	0.317
475 Ka	0.441	0.467	0.468	0.437	0.348
500 Ka	0.418	0.481	0.472	0.477	0.367
SPECMAP $\delta^{18}O$					
400 Ka	0.227	0.308	0.290	0.388	0.227
425 Ka	0.288	0.381	0.361	0.462	0.303
450 Ka	0.295	0.385	0.366	0.466	0.311
475 Ka	0.279	0.362	0.345	0.440	0.284
500 Ka	0.203	0.277	0.261	0.362	0.191

CHAPTER 4

STABILITY ANALYSIS

Introduction

This section will investigate the initialization of preferential flow paths (PFP). The focus of the basic problem, including its initial and boundary conditions, will be in the context of primary subsurface phreatic conduit development in the WKP. A thin slab of porous media in two-dimensional Cartesian coordinates will approximate the regional groundwater flow discussed in Chapter 2. An attempt will be made to derive a characteristic horizontal spacing (wavelength of separation) of initial formation and temporal growth rate that may have dominated the early development of the phreatic conduits. A two-dimensional linear analysis will be performed to determine the stability of aggressive phreatic groundwater flow through a soluble porous media.

Previous work

The question of conduit formation controls has been addressed largely through qualitative reasoning (Davis, 1930; Ewers, 1982; Ford, 1968, 1971, 1989; Ford and Ewers, 1978, Ford and Williams, 1989; Swinnerton, 1932; Sweeting, 1950; White, 1988; White and White, 1974, 1989). Similar problems have been addressed for the distribution of overland flow channels of dendritic stream systems (Smith and Bretherton, 1972; Loewenherz, 1991; Izumi & Parker, 1995) and bed forms in steep streams

(Furbish, 1998). Substantial progress has been made through quantitative analyses, allowing new insights of the characteristic scaling of discrete channels in stream basin evolution. There has also been progress in coupled flow-reaction systems in porous media through reactive infiltration instabilities for saturated (phreatic) systems (Chadam *et. al.*, 1986; Hoefner and Fogler, 1988), as well as for unsaturated (vadose) wetting fronts (Parlange and Hill, 1976, Diment and Watson, 1983, Diment and Watson, 1985; Glass *et. al.*, 1989a, 1989b). Recently, these concepts have been applied to upwelling magma at mid-ocean ridges. (Aharanov *et. al.*, 1995, 1997).

Formulation of the problem

Consider a thin slab of porous material initially having homogeneous and isotropic porosity and permeability. A Cartesian xy-coordinate system will be used with the x-axis parallel and horizontal to the mean flow direction (Figure 4.1). The input and output boundaries of the porous slab are positioned at $x = 0$ and $x = L$. The y-axis is also horizontal with impervious boundaries at $y = \pm b/2$. The slab is completed saturated (immersed) with fluid simulating phreatic conditions and all pore space contains fluid. Aggressive fluid is driven from left to right along increasing x by a constant pressure gradient ∇P. There is assumed to be no initial chemically reactive propagating front. The solid medium is assumed to be rigid (non-deformable) and completely reactive to the fluid. Fluid flow is assumed to be uniform initially. We are interested in a steady state condition on a reasonable time scale for initialization of PFP.

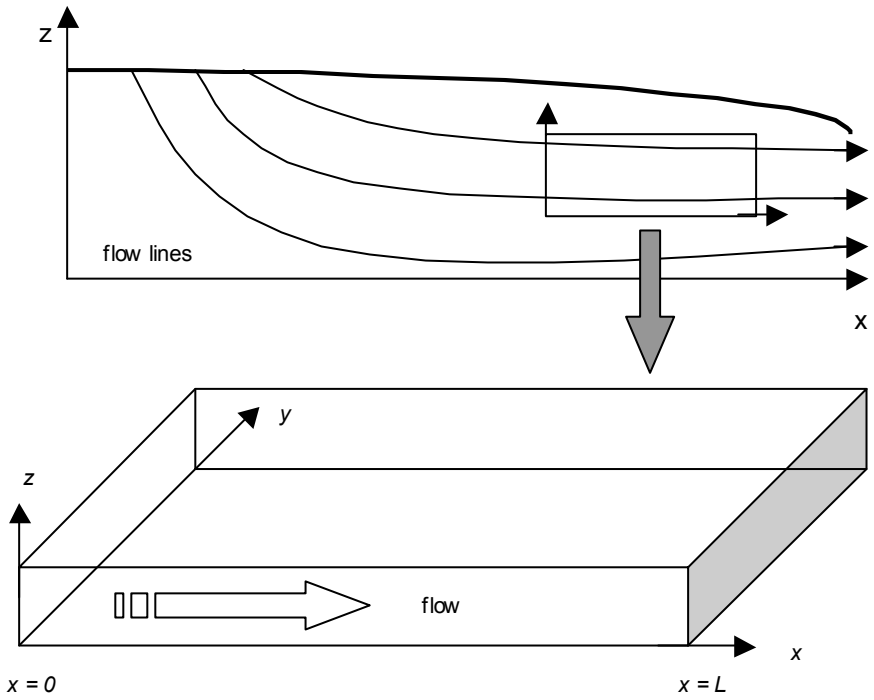

Figure 4.1. Diagram outlining geometry of thin slab used in linear analysis.

Governing Equations

Conservation of mass

It will be assumed that the solid matrix is of constant density, whereas the fluid density is non-constant, due to a dissolved solid content. This additional dissolved solid density within the fluid is very small compared to the fluid density. A suitable equation of state for the fluid density is

$$\rho = \rho_0 \left[1 + \gamma \left(c_0 - c \right) \right], \tag{1}$$

where ρ_0 is the density of the fluid at the equilibrium concentration c_0 and γ is a coefficient of compositional density variation defined by

$$\gamma = \frac{1}{\rho_0} \frac{\partial \rho}{\partial c} \tag{2}$$

for isothermal conditions. At low concentrations c, (1) is exact in the limit of isovolumetric reaction for either dissolution or precipitation such that $\gamma\rho_0 = \partial\rho/\partial c = 1$. In this problem, interest lies in small perturbations about the zeroth-order state, where the fluid is saturated with respect to the solid matrix. Thus, the zeroth-order state represents equilibrium conditions between the fluid and the solid matrix.

The coordinate system will be affixed to the solid matrix, so that the velocity $\vec{U} = \{U, V\}$ of the solid will vanish. The conservation of the non-deformable solid phase can be represented as a function of the porosity and concentration by

$$\rho_s \frac{\partial \phi}{\partial t} = f(\phi, c).$$

Specifically, the conservation of solid mass will be written as

$$\rho_s \frac{\partial \phi}{\partial t} - \frac{R(1-\phi)}{1-\delta(\phi-\Phi)}(c_0 - c) = 0, \tag{3}$$

where ρ_s is density of the solid phase, ϕ is the porosity, c is the concentration of dissolved solid with dimensions [M L^{-3}], c_0 is the equilibrium concentration [M L^{-3}] and t is time. The quantity δ of order unity is defined by

$$\delta = -\frac{1}{S_0}\frac{\partial S}{\partial \phi}, \tag{4}$$

where S is the specific surface area and S_0 is a reference value of the specific surface area [L^{-1}] associated with the reference porosity Φ. The reaction rate constant R, with dimensions of [T^{-1}], may vary with the ratio $\left|\frac{c}{c_0}\right|$. For diffusion-limited dissolution or precipitation, it can be demonstrated on dimensional and physical grounds that the rate of change in solid mass m_s [M] is

$$\frac{\partial m_s}{\partial t} = -ND_m r c_0 \left(1 - \frac{c}{c_0}\right) \tag{5}$$

where D_m is the molecular diffusion coefficient and r is an average characteristic grain size (Furbish, 1997). With $m_s = \rho_s (1-\phi) V$ and $r = 3(1-\phi)/S$, (5) becomes

$$\rho_s \frac{\partial \phi}{\partial t} = \frac{3N_v D_m (1-\phi) c_0}{S}\left(1 - \frac{c}{c_0}\right), \tag{6}$$

where $N_v = N/V$ is a fixed quantity for a volume V containing N spherical grains. It is not possible to express S solely in terms of ϕ without also specifying r. Therefore, we assume that for small variations in porosity

$$S = S_0 \left[1 - \delta(\phi - \Phi)\right]. \tag{7}$$

With close packing of non-spherical grains, the geometric details of (6) becomes uncertain, but this formulation remains valid on dimensional grounds. Furthermore, it has been proposed that for concentrations c far from the equilibrium concentration c_0, carbonate dissolution follows a first-order reaction described in (6), but for concentrations near c_0, dissolution may involve a high-order reaction (Palmer, 1991; Svensson and Dreybrodt, 1992). Substituting (7) into (6) and specifying the reaction order by $l + 1$ leads to

$$\rho_s \frac{\partial \phi}{\partial t} - \frac{R_1 (1-\phi) c_0}{1 - \delta(\phi - \Phi)}\left|\left(1 - \frac{c}{c_0}\right)^l\right|\left(1 - \frac{c}{c_0}\right) = 0, \tag{8}$$

where $R_1 \sim N_v D_m / S_0$ [T^{-1}] is a reaction rate constant specific to conditions near S_0 and Φ. When $l = 0$, (8) reduces to a first-order kinetic reaction.

The first-order reaction, represented by the last parenthetical quantity in (8), is modulated by the l-order factor (a small quantity) for c close to c_0. Thus, the order of the

reaction influences the rate of response of the system to small perturbations in concentration, but does not contribute to the stability (negative or positive feedback) of the system. For numerical reasons, we can choose a value $c = c_s$, arbitrarily close to c_0, and rewrite (8) as (3), in which the reaction rate constant *R* is

$$R = R_1 \left| \left(1 - \frac{c_s}{c_0} \right)^l \right| \approx \frac{N_v D_m}{S_0} \left| \left(1 - \frac{c_s}{c_0} \right)^l \right|. \tag{9}$$

Conservation of the fluid phase is governed by

$$\nabla \cdot \left(\rho \vec{u} \phi \right) + \frac{\partial}{\partial t} \left(\rho \phi \right) - \rho_s \frac{\partial \phi}{\partial t} = 0 \tag{10}$$

where $\vec{u} = \{u, v\}$ is the velocity of the fluid and $\nabla = \mathbf{i} \frac{\partial}{\partial x} + \mathbf{j} \frac{\partial}{\partial y}$. Equation (10) maintains that when the fluid velocity $\vec{u} = 0$, there must be a balance between the change in fluid density and the change in porosity.

Conservation of momentum

The momentum balance will follow Darcy's Law by relating the pressure field and the velocity of the fluid at low Reynolds number:

$$\phi \vec{u} = -\frac{k}{\mu} \nabla p \tag{11}$$

where

$$k = \frac{B \phi^n}{\left[1 - \delta \left(\phi - \Phi \right) \right]^2} \tag{12}$$

is the permeability which is a power law function described by Bear (1988), B is a constant of proportionality that represents a typical grain size distribution,

$n = \{n : n > 0\}$, ∇p is the pressure gradient and μ the dynamic viscosity of the fluid. On dimensional and physical grounds the permeability *k* is given by

$$k = \frac{a\Phi^3}{S^2} \tag{13}$$

where *a* is a constant. Using (7), the above equation becomes (12), in which $B = \frac{a}{S^2}$.

Advection-Dispersion relation

The flow of dissolved solid in porous media is described by the advection-dispersion equation. This equation treats the transport of a conservative solute in porous media and takes into account the diffusion and mechanical dispersion of that solute (Furbish, 1997). We will use the general form with a source term to represent the dissolution of solid mass:

$$\nabla \cdot \left(\phi \vec{u} c\right) - \nabla \cdot \left(\phi \overline{D} \nabla c\right) + \frac{\partial}{\partial t}\left(\phi c\right) - \rho_s \frac{\partial \phi}{\partial t} = 0 \tag{14}$$

where $\overline{D}$, the two-dimensional tensor coefficient of hydrodynamic dispersion with elements:

$$D_{xx} = \left(\alpha u^2 + \beta v^2\right) / \left|\vec{u}\right|, D_{xy} = D_{yx} = \left(\alpha - \beta\right) uv / \left|\vec{u}\right|, D_{yy} = \left(\beta u^2 + \alpha v^2\right) / \left|\vec{u}\right|. \tag{15}$$

Here, α and β are the longitudinal and transverse dispersivities, respectively.

Scaling and Stability Analysis

For constant density ρ_s, substitution of (1), (11), (12), and (15) into (10) and (14) leads to three equations in ϕ, *p* and *c*. Namely, conservation of solid mass

$$\rho_s \frac{\partial \phi}{\partial t} - \frac{R(1-\phi)}{1-\delta(\phi-\Phi)}(c_0 - c) = 0, \tag{16}$$

conservation of fluid mass

$$\begin{gathered} -\frac{\rho k}{\mu}\frac{\partial^2 p}{\partial x^2} - \frac{\rho}{\mu}\frac{\partial p}{\partial x}\frac{\partial k}{\partial x} - \frac{k}{\mu}\frac{\partial p}{\partial x}\frac{\partial \rho}{\partial x} - \frac{\rho k}{\mu}\frac{\partial^2 p}{\partial y^2} - \frac{\rho}{\mu}\frac{\partial p}{\partial y}\frac{\partial k}{\partial y} \\ -\frac{k}{\mu}\frac{\partial p}{\partial y}\frac{\partial \rho}{\partial y} + \rho\frac{\partial \phi}{\partial t} + \phi\frac{\partial \rho}{\partial t} - \rho_s\frac{\partial \phi}{\partial t} = 0 \end{gathered} \tag{17}$$

and conservation of dissolved solid

$$-\frac{k}{\mu}\frac{\partial c}{\partial x}\frac{\partial p}{\partial x} - \frac{ck}{\mu}\frac{\partial^2 p}{\partial x^2} - \frac{c}{\mu}\frac{\partial k}{\partial x}\frac{\partial p}{\partial x} - \frac{k}{\mu}\frac{\partial c}{\partial y}\frac{\partial p}{\partial y} - \frac{ck}{\mu}\frac{\partial^2 p}{\partial y^2} - \frac{c}{\mu}\frac{\partial k}{\partial y}\frac{\partial p}{\partial y} = 0. \tag{18}$$

Non-dimensionalization

In order to scale the problem with respect to quantities characteristic of the zeroth-order (basic) state, the following dimensionless quantities are introduced and denoted by a caret:

$$\begin{aligned} \phi &= \Phi\hat{\phi}, \\ p &= P\hat{p}, \\ c &= c_0\hat{c}, \\ x &= L\hat{x}, \\ y &= b\hat{y} \end{aligned} \tag{19}$$

where Φ denotes the zeroth-order porosity and P denotes the zeroth-order pressure drop over the distance L. Substituting (19) into (3) yields two characteristic time scales inherent in the problem. Namely,

$$\begin{aligned} \tau &= \frac{1}{R}, \\ \mathrm{T} &= \frac{\rho_s \Phi}{c_0 R}. \end{aligned} \tag{20}$$

The first, τ, is a 'short' reaction-rate time scale explicit to dissolution or precipitation of the solid phase. In our case, it represents the time with which aggressive (chemically under saturated) waters become saturated with respect to calcium carbonate. Here, it is used to set

$$t = \frac{1}{R}\hat{t}\,. \tag{21}$$

The second, T, is a 'long' time scale representing a measure of the period required for significant change in porosity of the solid, due to dissolution or precipitation. This time scale can be envisaged as the 'hydrogeomorphic' time on which conduit formation operates. The ratio of these time scales produces a scaling factor

$$\varepsilon \equiv \frac{\tau}{\mathrm{T}} = \frac{c_0}{\rho_s \Phi}\,. \tag{22}$$

Note that $\varepsilon \ll 1$.

Expanding $\hat{\phi}$, $\hat{p}$ and $\hat{c}$ about a zeroth-order state with small perturbations of the scaling factor ε produces

$$\hat{\phi} = 1 + \varepsilon\hat{\phi}_1 + \varepsilon^2\hat{\phi}_2 + \ldots\,, \tag{23}$$

$$\hat{p} = \hat{p}_0 + \varepsilon\hat{p}_1 + \varepsilon^2\hat{p}_2 + \ldots\,, \tag{24}$$

$$\hat{c} = 1 + \varepsilon\hat{c}_1 + \varepsilon^2\hat{c}_2 + \ldots \tag{25}$$

where the subscripts on $\hat{\phi}$, $\hat{p}$ and $\hat{c}$ denote orders of terms. Substituting (23)-(25) into (16), (17) and (18) and expanding, the fluid mass equation (17) yields at lowest order

$$\frac{\partial^2 \hat{p}_0}{\partial \hat{x}^2} = 0 \tag{26}$$

which when integrated equals the uniform pressure gradient associated with the zeroth-order state. At first-order ε, (16) and (18) yield

$$\varepsilon \frac{\partial \hat{\phi}_1}{\partial \hat{t}} = 0\,, \tag{27}$$

which suggests that the porosity does not change significantly over the reaction-rate time scale τ. Substituting (27) into (17) also yields

$$\varepsilon \frac{\partial^2 \hat{p}_1}{\partial \hat{x}^2} - \varepsilon \left(n + 2\delta\Phi\right) \frac{\partial \hat{\phi}_1}{\partial \hat{x}} + \varepsilon \frac{L^2}{b^2} \frac{\partial^2 \hat{p}_1}{\partial \hat{y}^2} = 0 \tag{28}$$

which indicates a steady-state flow condition operating over the reaction time-scale τ.

At second-order ε^2, substituting (27) and (28) into (17) and (18), respectively yield

$$\varepsilon^2 \frac{\partial \hat{\phi}_2}{\partial \hat{t}} + \varepsilon^2 \left(1 - \Phi\right) \hat{c}_1 = 0 \tag{29}$$

$$\begin{aligned} -\varepsilon^2 \frac{\partial \hat{c}_1}{\partial \hat{x}} \frac{\partial \hat{p}_0}{\partial \hat{x}} - \varepsilon^2 \frac{\alpha}{L} \frac{\partial^2 \hat{c}_1}{\partial \hat{x}^2} \left| \frac{\partial \hat{p}_0}{\partial \hat{x}} \right| - \varepsilon^2 \frac{\beta}{L} \frac{L^2}{b^2} \frac{\partial^2 \hat{c}_1}{\partial \hat{y}^2} \left| \frac{\partial \hat{p}_0}{\partial \hat{x}} \right| \\ + \varepsilon^2 \frac{L^2 R \mu \Phi}{PB\Phi^n} \frac{\partial \hat{c}_1}{\partial \hat{t}} - \varepsilon^2 \frac{L^2 R \mu}{PB\Phi^n} \frac{\partial \hat{\phi}_2}{\partial \hat{t}} = 0 \end{aligned} \tag{30}$$

Integrating (26) and substituting the result and (29) into (30), yields

$$\frac{\partial \hat{c}_1}{\partial \hat{x}} - \frac{\alpha}{L} \frac{\partial^2 \hat{c}_1}{\partial \hat{x}^2} - \frac{\beta}{L} \frac{L^2}{b^2} \frac{\partial^2 \hat{c}_1}{\partial \hat{y}^2} + \frac{L^2 R \mu \Phi}{PB\Phi^n} \frac{\partial \hat{c}_1}{\partial \hat{t}} + \frac{L^2 R \mu \left(1 - \Phi\right)}{PB\Phi^n} c_1 = 0\,. \tag{31}$$

It is assumed that the solution of equation (31) will have the form

$$\hat{c}_1 = \hat{C}_1 e^{j(\omega \hat{x} + j\psi \hat{y}) + \sigma t} \tag{32}$$

where $\hat{C}_1$ is a complex amplitude, j is a dimensionless wave number in the transverse direction and σ is a dimensionless quantity whose real part represents a growth rate while the imaginary part represents a waveform speed of the perturbation. Additionally, $\omega = \frac{2\pi}{L}$ and $\psi = \frac{2\pi}{b}$, whereas the dimensionless forms are represented by $\hat{\omega} = \omega L$

and $\hat{\psi} = \psi b$. Substituting (32) into (31) and differentiating with respect to $\hat{x}$, $\hat{y}$ and $\hat{t}$ results in

$$\sigma = -\frac{(1-\Phi)}{\Phi} - \frac{4\pi^2 PB\Phi^{n-1}}{L^3 R\mu}\left[\alpha + \frac{\beta L^2}{b^2}\right] - i\frac{2\pi PB\Phi^{n-1}}{L^2 R\mu}. \tag{33}$$

It is clear from (33) that both the real and imaginary parts of σ will are always negative. This implies that there will be no growing instability with time and hence, no positive feedback.

Two controlling parameters emerge in this problem and are apparent in the solution of the growth rate equation (33):

$$Da = \frac{L}{L_{eq}} \tag{34}$$

$$T_A \equiv \frac{L}{u} = -\frac{\mu L}{B\Phi^{n-1}P}. \tag{35}$$

The Damkhöler number *Da* defines the ratio between the size of the system in the mean flow direction *L* and the chemical equilibrium length, $L_{eq} = \frac{\Phi u}{R}$. The advective time-scale T_A defines the ratio of the size of the system *L* to its mean velocity *u*. In this sense, (34) and (35) can be substituted into (33) producing two equations in the context of an equilibrium length for both the chemical reaction and the advective time-scale:

$$\sigma = -\frac{(1-\Phi)}{\Phi} - \frac{4\pi^2}{\Phi L^2}\frac{1}{Da}\left[\alpha + \frac{\beta L^2}{b^2}\right] - i\frac{2\pi}{\Phi L}\frac{1}{Da} \tag{36}$$

$$\sigma = -\frac{(1-\Phi)}{\Phi} - \frac{4\pi^2}{RL^2}T_A\left[\alpha + \frac{\beta L^2}{b^2}\right] - i\frac{2\pi}{RL}T_A. \tag{37}$$

Results

In the context of the problem, the result of (36) and (37) suggests that the system is unconditionally stable for any perturbation. This implies that there will be no initiation of PFPs in the phreatic zone. This finding appears intuitive in the sense that the aggressive waters will become saturated with respect to the soluble media in a very short time (reaction-rate time scale). If the aggressive waters become saturated shortly after entering a soluble porous media, they will be unable to dissolve material farther down their flow line.

Consequently, there are several wide reaching implications for the previous mentioned theories presented in Chapter 3 concerning conduit formation below the water table. This analysis suggests that the either conduit formation cannot take place within the phreatic zone or that the mechanism regarding carbonate dissolution by higher-order chemical kinetics is incorrect for cave development. This analysis does not necessarily mean deep phreatic does not occur, only that another mechanism is required.

One such possible mechanism, originally suggested by Bogli (1964), is that of 'mixing corrosion'. Bogli's 'mixing corrosion' theory states that the physical mixing of two saturated waters, each at different points along the carbonate saturation curve, will yield an undersaturated product (Figure 4.2). This undersaturated product (Fig. 2, Bogli, 1964) is capable of dissolving carbonate, forming solution pockets and conduits. Bogli's theory is highly dependent on the CO_2 differential of the two waters. White (1988) points out that mixing corrosion provides a possible mechanism for high intensity dissolution occurring near the water table, but can be complicated by other effects that can lead to changes in the saturation state of mixed waters.

One significant problem with Bogli's 'mixing corrosion' mechanism is the fact that the differing saturated waters must be transported through previously existing joints

and fractures. This predisposition to fracture flow becomes inherently constrained within the carbonates of the WKP where a lack of such extensive fracturing becomes problematic. Although it has been shown that significant development may have been produced near the water table, a suitable mechanism for deep phreatic development remains elusive. Building on the conceptual framework introduced by Bogli (1964) and Rhodes and Sinacori (1941), a new model for extensive phreatic carbonate dissolution capable of creating large-scale conduits will be introduced.

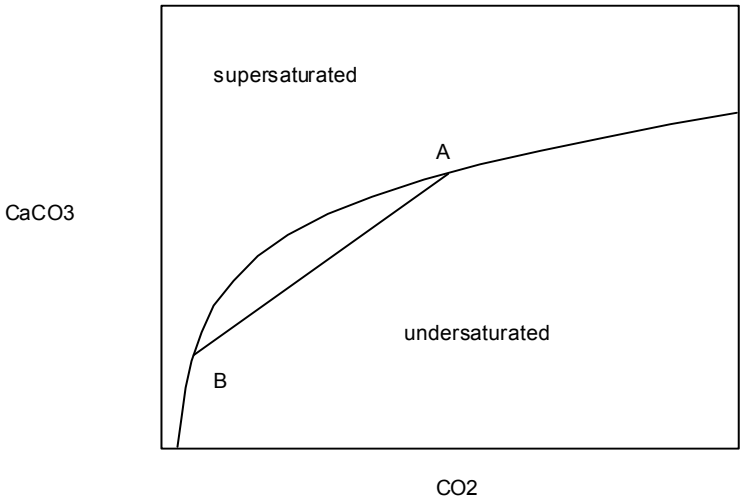

Figure 4.2. Diagram modified from Bogli (1964) demonstrating the quantitative relationship between the equilibrium concentrations of calcium carbonate and carbon dioxide. When waters A and B, both at equilibrium along the saturation curve, are mixed the product is an undersaturated water along the straight line connecting A and B.

Conceptual model

Background

Rhoades and Sinacori (1941) showed theoretically that there could be significant dissolution near a point discharge. With time, the point discharge would enlarge preferentially and cut back forming a master conduit. This master conduit would develop

at the water table along the convergent flow lines. This headward dissolution would modify the flow lines so that deeper seated waters would become less important while the shallow waters would become much more important. This has the affect of allowing flow lines to terminate at the head of the master conduit and not at the discharge point. There was no significant contribution by Rhoades and Sinacori (1941) as to the nature of the actual mechanism that triggered the dissolution.

Bogli's (1964) mechanism provides for significant dissolution at depth where only non-aggressive waters would be found. The origin of most karst cavities in carbonate rock cannot be fully explained based on the prevailing information. Many inconsistencies remain; namely, the exceedingly long time scales necessary to produce observed dimensions of conduits. Therefore, it is necessary to establish the mechanism by which preferential flow paths develop. This will involve the model proposed in the 'mixing corrosion' suggested by Bogli (1964). The basis of the 'mixing corrosion' mechanism is dissolved carbon dioxide limited.

A previously unanswered aspect of this portion of the cave forming process, the chemical interpretation of CO_2 enhanced carbonate dissolution by 'deep phreatic' water, was shown above to be incapable of creating PFPs in homogeneously fractured or unfractured terraines. This oversight shows how problematic the chemical equilibrium equation describing dissolution is and why it alone cannot account for the development of large cave systems. This way the 'deep phreatic' zone is completely sequestered to aggressive waters. The analysis above also included the aspect of higher-order chemical kinetics suggested by Palmer (1981) and Dreybrodt (1996). There, an attempt was made to incorporate the higher-order chemical kinetics suggested by Plummer and Wigley (1976) and Plummer, Wigley and Parkhurst (1978). The conceptual framework using these findings was White's (1988) 'kinetic trigger'.

With the large length scales observed in extensive cave systems, low-order kinetic reactions (dissolution) are incapable of dissolving carbonate material along the entire flow line or preferential flow path. The aggressive water entering the boundary equilibrates over very short distances for typical flow velocities. This reaction distance is much smaller by several orders of magnitude than the observed length scales. A higher-order kinetic reaction, the perceived solution by White (1988), provides for slightly undersaturated waters to penetrate the PFP or fractures for greater distances. Here the rate of reaction is dramatically reduced but unfortunately the time required to produce the dimensions of observed cave systems is greater than tens of millions of years.

Mixing dispersion

In examining the stability analysis above for parallel flow lines, it becomes clear that convergent geometries will introduce mixing of different saturated waters. The convergent geometry enhances mixing through transverse and longitudinal dispersion, producing a significant consequence. The geometrical convergence within the flow space (subsurface drainage basin) is proposed to be an enhancement of 'mixing dispersion'. The effect of the transition to turbulence and the propagation of solution porosity cause an overall growth of the PFP upstream producing a positive feedback loop. The preferential flow path grows upstream along the flow lines.

Most of the dissolution occurs near the water table or halocline in coastal terraines. This indicates that the problem is likely a boundary problem and dissolution is controlled by physicochemical phenomena occurring near this boundary. The mixing of slightly varying concentrations of carbonate-saturated waters under a pressure head locally obeys Darcy's Law and the Advection-Dispersion equation. It is proposed that dissolution from 'mixing dispersion' is the initial mechanism by which the PFP are formed. The PFPs are enlarged subsequently by 'mixing dispersion' or enhancements

through ‘mixing corrosion’ spelled out by Bogli (1964) and, when of significant cross-sectional area, appear to develop rapidly when the size of the PFP begins to allow transition from laminar to turbulent flow.

The development and growth of the PFPs is tightly controlled by the geometry of the basin and subsequently by the flow patterns resulting from that geometry. Essentially this hypothesis is a combination of the conceptual model and quantitative results obtained by Rhoades and Sinacori (1941) and ‘mixing corrosion’ proposed by Bogli (1964). The specific mechanism that produces the PFPs is proposed to be ‘mixing dispersion’, while the subsequent rapid enlargement of the PFP is the transition to turbulence and is solely responsible for upstream porosity development.

Proof of Concept

Upon further examination of the stability analysis presented above, it becomes apparent that this problem involves both multiple time and length scales. To fully address these possibilities, it is necessary to use the method of multiple scales to solve the problem. In order to account for the time scales, the expansion in (23) - (25) will need to be modified. As an example, the porosity can be written

$$\phi\left(\underline{x},t\right)=\Phi\hat{\phi}\left(\hat{\underline{x}},\hat{t},\hat{T}\right) \tag{38}$$

where $\hat{\underline{x}}$ represents the non-dimensional spatial vector and $\hat{t}$ the non-dimensional short time scale follows from (21). It follows from (20) and (22) that the non-dimensional long time scale

$$\hat{T}=\frac{t}{T}=\varepsilon Rt \tag{39}$$

can be obtained from

$$T = \frac{\tau}{\varepsilon} = \frac{1}{\varepsilon R}. \tag{40}$$

Rewriting (23) and expanding produces

$$\begin{aligned}
\frac{\partial \phi}{\partial t} &= \Phi \frac{\partial \hat{\phi}}{\partial \hat{t}} \frac{\partial \hat{t}}{\partial t} + \Phi \frac{\partial \hat{\phi}}{\partial \hat{T}} \frac{\partial \hat{T}}{\partial t} \\
&= R\Phi \left[\frac{\partial \hat{\phi}}{\partial \hat{t}} + \varepsilon \frac{\partial \hat{\phi}}{\partial \hat{T}} \right] \\
&= R\Phi \left[\begin{array}{l} \dfrac{\partial \widehat{\phi_0}}{\partial \hat{t}} + \varepsilon \dfrac{\partial \widehat{\phi_1}}{\partial \hat{t}} + \varepsilon^2 \dfrac{\partial \widehat{\phi_2}}{\partial \hat{t}} + ... \\ ... + \varepsilon \dfrac{\partial \widehat{\phi_0}}{\partial \hat{T}} + \varepsilon^2 \dfrac{\partial \widehat{\phi_0}}{\partial \hat{T}} + \varepsilon^3 \dfrac{\partial \widehat{\phi_0}}{\partial \hat{T}} + ... \end{array} \right]
\end{aligned} \tag{41}$$

In this equation, it can be seen that both the long and the short time scales are operative. The first term in the second expansion of the right-hand side indicates that changes in porosity over the long time scale occur are zeroth-order. This is the term of interest.

To test the conceptual model several assumptions will be employed. First, it will be assumed that there is a constant flux *Q*. Second, the concentration *c* is small, indicating weak solubility. Third, the reaction rate constant *R* will be a constant written as *R(c)*. Last, the concentration *c* will be a function of *x*, written *c(x)* which will be allowed to increase linearly downstream.

A simplified version of the conservation of solid mass and fluid mass equations, (3) and (10) respectively, will be used. The fluid mass equation will be written

$$Q \frac{\partial c}{\partial x} + \left(\rho_w - \rho_s \right) \frac{\partial \phi}{\partial t} = 0 \tag{42}$$

and the solid mass equation written

$$\rho_s \frac{\partial \phi}{\partial t} = R\left(\phi, c \right)\left(c_0 - c \right). \tag{43}$$

A linear relation for the concentration will simulate the downstream ‘mixing dispersion’

$$c_0(x) = C + Mx \tag{44}$$

where C is a reference concentration and M is a constant representing the slope of the concentration line due to lateral dispersion (Figure 4.3). The initial condition $c(0)=B$ will be used where B represents some constant initial value of the system.

Substituting (43) into (42) yields a first order linear ordinary differential equation

$$\frac{\partial c}{\partial x} - \frac{\left(C + Mx - c\right)}{L} = 0 \tag{45}$$

where

$$L = \frac{Q\rho_s}{R\left(\rho_s - \rho_w\right)}. \tag{46}$$

Integrating (45), employing the method of undetermined coefficients and rewriting produces

$$c_0 - c = ML\left(e^{-\frac{x}{L}} - 1\right) + \left(B - C\right)e^{-\frac{x}{L}}. \tag{47}$$

The second term on the right-hand side is the short length scale represented in the stability analysis above. The first term on the right-hand side, however, represents the long length scale of the problem. This terms importance will be demonstrated below.

Substituting (47) into (43) and integrating produces

$$\phi = \Phi + \frac{RML}{B}t. \tag{48}$$

This equation shows that as time increases the porosity ϕ grows without bound. In equation (47) if $M=0$, the first term vanishes and the short length scale dominates, whereas if x becomes large the second term becomes insignificant and the concentration difference approaches $-ML$.

This simple analysis suggests that ‘mixing dispersion’ may be a viable

mechanism given the above assumptions. Equation (48) suggests that deep phreatic conduit development can grow without bound and that the proposed mechanism of 'mixing dispersion' appears to coincide with the short reaction rate dissolution according to (47). The conceptual model will need to be tested more rigorously by establishing a more realistic reaction rate R, a formal check of the solution of the advection-dispersion relation and an equation of state for $c_0(x, y)$ from physical chemistry.

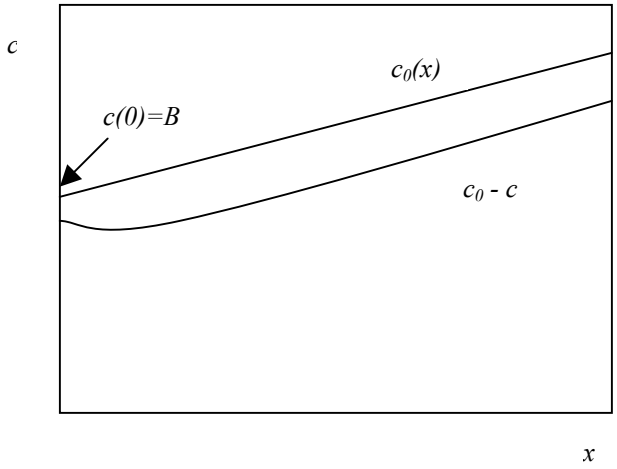

Figure 4.3. Diagram outlining the linear growth of the concentration downstream representing the lateral 'mixing dispersion'. The concentration difference $(c_0 - c)$ is proposed to approach $c(x)$ and represents the unbounded solution of (48).

CHAPTER 5

DISCUSSION AND CONCLUSIONS

Passage depth and sea level correlation

The statistical analysis involving the distribution of passage depth presented in Chapter 2 suggests that the caves of the WKP are tiered. This result was obtained from averaging the passage depth below the water table on 1 m, 2 m, 3 m and 4 m intervals versus the total length of the cave passage. It is clear from Figures D.8, D.12, D.14 and D.21 that there are at least three primary levels of development below the present water table. Figures D.9, D.11, D.13 and D.15 suggests that there may be additional levels of development that were either indicative of secondary or modified-primary origin.

Secondary origin is less pronounced conduit development than primary development conduit. These secondary (tributary) passages are formed in conjunction with the primary (master) conduits, but appear to be consequential to the primary development. Modified-primary origin may be the result of subsequent erosion following development of the primary and secondary conduits at various levels. This may occur due to local variations in hydrology, stratigraphy, lithology or structure. The three pronounced peaks on Figures D.10, D.11 and D.14 between –15 m and –45 m may indicate three distinct primary levels. However, the limited geomorphic detail of the caves within the sample population hinder any definite classification.

Geomorphic observation of vadose cave development present within Cheryl Sink Cave, Harvey's Sink Cave and Hatchet Sink Cave suggest that the possible above

mentioned levels may be indicative of vadose modification. These finding provide additional evidence that the water table resided at severely depressed elevations during lower stands of sea level at the Gulf of Mexico. These finding are consistent with other studies suggesting that eustatic sea level was depressed during several periods of the Quaternary (Dodge *et. al.*, 1983; Imbrie *et. al.*, 1984; Shackleton, 1987; Bard *et. al.*, 1990a; Bard *et. al.*, 1990b; Dia *et. al.*, 1992). The overall suggestion is that some of the caves within the WKP were air filled at various times during their development. The present situation of an elevated water table suggests that the caves have been submerged relative to their initial development.

The suggestion that the caves of the WKP are tiered also implies that development was dependent on base level lowering (Palmer, 1981; White, 1988). While sea level elevation (height) has fluctuated during the Quaternary (Appendix B), there appears to be a correlation between the passage depth distribution and the duration of sea level elevation. This correlation is complicated by the fact that the fluctuation of sea level may have produced episodic conduit development at various elevations. Likewise, the time scale of formation in which base level lowering has operated, makes correlation of the water table elevation to passage depth difficult. The findings of Chapter 3 and the figures of Appendices E and F suggest that there is a substantial correlation. Although the correlation coefficients of Tables 3.2 – 3.5 do not exceed 0.662, it is clear that a considerable correlation does exist.

The inaccuracies within the surveys, the uncertainty in the maximum age of development and modification of the original conduits to the present cave passages all complicated the statistical correlation. However, given these difficulties, employment of smoothing (averaging) techniques for both the passage depth distribution and the sea level elevation duration, there appears to be substantial correlation. This correlation can be seen most clearly in Figures E.5, E.6, E.12 and E.13. Contained within the above

statements and figures are the implication that these caves may have formed preferentially at or near the water table. Hence, it can be inferred that their development has been dependent on base level and supports the theory of 'water table' cave development. It should also be noted that the 'water table' cave development may have been influenced by subtle variations in hydrology, both surface and subsurface flow patterns, lithology, stratigraphy and non-uniform erosion of the confining layers above the St. Marks Limestone.

Erosional history

It is clear from Figure B.2 that there have been several episodes where sea level elevation has been greater than the present. These elevated sea levels were likely responsible for the erosion of the confining units above the St. Marks Limestone within the WKP. The geomorphic conditions that existed at that time were likely similar to the present Tallahassee Hills north of the Cody Scarp. Presently, the geomorphology of the Tallahassee Hills includes closed surface drainage basins, episodically draining sinkhole lakes, stream-dominated surface drainage and denudation through overland surface flow during large precipitation events. Typical mean elevations are between 35 m (115 ft) and 55 m (175 ft), more than 30 m above the mean elevation of the WKP. The high sea level stands of Figures B.2 and B.14 suggests that extensive erosion of the confining units of the WKP probably took place within the past 450 Ka BP. These high still-stands of sea level are likely represented by the paleoshoreline deposits discussed in Chapter 2 and referred to by Rupert and Spencer (1988).

Although preferential flow paths may have begun to form along the water table due to fluctuating sea level, extensive dissolution and enlargement of the conduits would likely not take place until aggressive waters could penetrate the largest flow paths.

Infiltration of surface waters through breaches in the confining layer (*i.e.* sinkholes and closed depressions) may have triggered the first occurrences of extensive conduit development. Taking the mean elevation difference between the Tallahassee Hills and the WKP and dividing it by 450 Ka, produced average denudation rates of the confining unit at 0.067 mm/yr or 6.7 cm/Ka. This figure appears reasonable for typical denudation rates of sediments and the estimates for limestones of Florida (Hendry and Sproul, 1966; Brooks, 1967).

Timeline of formation

Cores DSDP 502b and the smoothed stack SPECMAP contained a sufficient record spanning 400 to 500 Ka and were utilized to determine a timeline of formation for the caves of the WKP. The results of the analysis suggest that initial conduit formation took place approximately 450 Ka BP. Both Core DSDP502b and the smoothed stack SPECMAP sea level duration records show maximum correlation coefficients near 450 Ka BP. Selected figures illustrating the correlations of the passage length distributions and the sea level duration records are contained in Appendix F.

The results for Core DSDP 502b may show greater correlation coefficients possibly due to the fact it is from the Gulf of Mexico. It may be the best single indicator for sea level fluctuations influencing the Woodville Karst Plain. It is suggested here, that the timeline of formation for the extensive karstification and cave passage development found within the WKP are likely on the order of ~500 Ka. This is also consistent with estimates for submerged conduit dimensions (White, 1988, Fig. 9.12) and the estimates of erosional rates employed in the discussion above.

While this timeline may be short compared to cave systems such as the 2 Ma Mammoth-Flint Ridge Cave System (Schmidt, 1982), it appears reasonable given the

extensive fluctuations of base level and the fact that many of the deepest (largest) passages have likely been active flow routes during a majority of the conduits developmental history.

Stability analysis

The results of the stability analysis of Chapter 4 suggests that the problem of initial dissolutional development in a phreatic (hydrologically saturated) setting is not an intrinsic instability for the short time scale. The problem examined resulted in the system being unconditionally stable for all solutions (Equation (36) and (37) of chapter 4). There are damped waveforms that propagate in the mean direction of flow resulting from the introduction of small perturbations; however, they do not trigger dissolution (precipitation) on the short time scale.

Two important time scales emerge within the problem. The first is a 'short' timescale, Equation (20) which can be interpreted as specific to the chemical reactions involved with dissolution or precipitation of carbonate. The second is a 'long' timescale, Equation (20) that can be interpreted as the period required for significant change porosity of the limestones and the eventual development of karst landforms. Additionally, one can speak of an advective timescale, Equation (35), in which the fluid parcels travel in the mean flow direction over the length of the system on the short time scale.

A single nondimensional quantity that emerges within the analysis is the Damkhöler number, Equation (34), that defines the ratio between the size of the system in the mean flow direction L and the chemical equilibrium length. It is apparent from Equation (36) that the value of the Damkhöler number is inconsequential to producing PFP in this problem. While it has been relevant to other dissolution-reaction problems

(Hoefner and Fogler, 1988; Aharanov *et. al.*, 1995, 1997) it does not play any significant role in this problem as related to the short time scale.

The importance of this analysis to initial karst development is significant with respect to the water table. The overall results suggest that there cannot be PFP (conduit) development below the water table (phreatic) in a parallel flow model for the short time scale. This finding applies to solid as well as fractured media. Hence, this analysis casts doubt on the theories of both deep and shallow phreatic cave development discussed in Chapter 3. It does, however, support the theories of both water table cave development and vadose development.

This is significant to the WKP in two regards: First, it suggest that no initial development of conduits below the water table occur over the short time scale, implying that initial development occurred at or above the water table. Second, it strengthens the findings of Chapter 3 suggesting that the primary initiation and development is well correlated to the duration of the sea level (base level) elevation distribution.

Mixing Dispersion

The development and growth of the PFPs is tightly controlled by the geometry of the basin and subsequently by the resulting flow patterns. The specific mechanism that produces the PFPs is proposed to be 'mixing dispersion', while the subsequent rapid enlargement of the PFP is due to the transition to turbulent flow and is solely responsible for upstream porosity development. It is proposed that dissolution from 'mixing dispersion' is the initial mechanism by which the PFP are formed on the long time scale. The PFPs are enlarged subsequently by 'mixing dispersion' or enhancements through 'mixing corrosion' spelled out by Bogli (1964) and, when of significant cross-sectional area, appear to develop rapidly when the size of the PFP begins to allow transition from

laminar to turbulent flow. Essentially this hypothesis is a combination of the conceptual model and quantitative results obtained by Rhoades and Sinacori (1941) and 'mixing corrosion' proposed by Bogli (1964), utilizing 'mixing dispersion' as the initial mechanism by which the PFPs may be formed.

The proof of concept in Chapter 4 suggests that 'mixing corrosion' is a viable mechanism able to produce conduits of significant size over a long time scale. The porosity (48) suggests that dissolution producing conduits can grow without bound. Equation (47) suggests that both the short and long length scales can be represented in a single equation, unifying both concepts. This development leads o a comprehensive conceptual model of 'mixing dispersion' as the mechanism for significant conduit development in the phreatic zone.

APPENDIX A

This appendix contains cave plots of survey data used in this study. In order to limit the size of this appendix only the plan view and one directional profile view for each cave is shown. Several survey stations are labeled on each figure to aid the reader in identifying the passages that constitute the cave system. Each figure has a small scale in the lower right that gives the appropriate scale in meters/centimeter. Note that this scale may not match the original figures before printing and the reader is cautioned to use the small bar scale for appropriate comparison. Each profile view contains an appropriate vertical exaggeration with which the highlights of the cave passage could easily be seen. For some caves, there was the unavoidable clustering of various passages.

The Leon Sinks Cave System is presented last with an overview of the entire system in both plan and profile view followed by a breakdown of the system into its constituent parts. These include Sullivan Sink Cave, Big Dismal Sink Cave, Cheryl Sink Cave and Turner Sink Cave. Each figure shows the connecting survey stations. Note that there is survey data missing between the Big Dismal Sink Cave deep section and the Bitter End tunnel of Cheryl Sink Cave. The original survey for this part of the cave system has been irretrievably lost. A resurvey of this passage could not be undertaken before this report was completed.

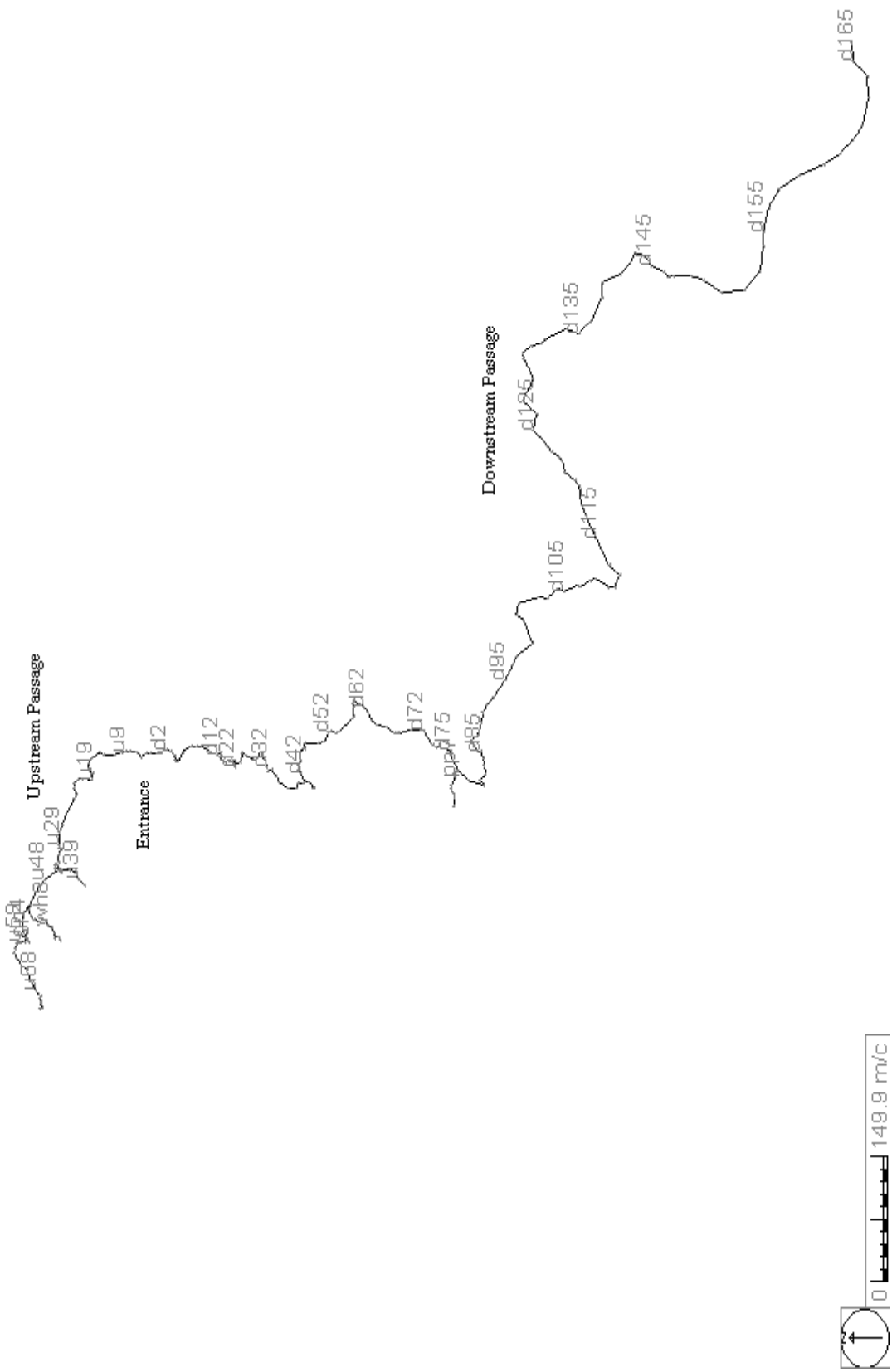

Figure A.1. Chips Hole Cave plan view. Horizontal scale is ~150 m/cm.

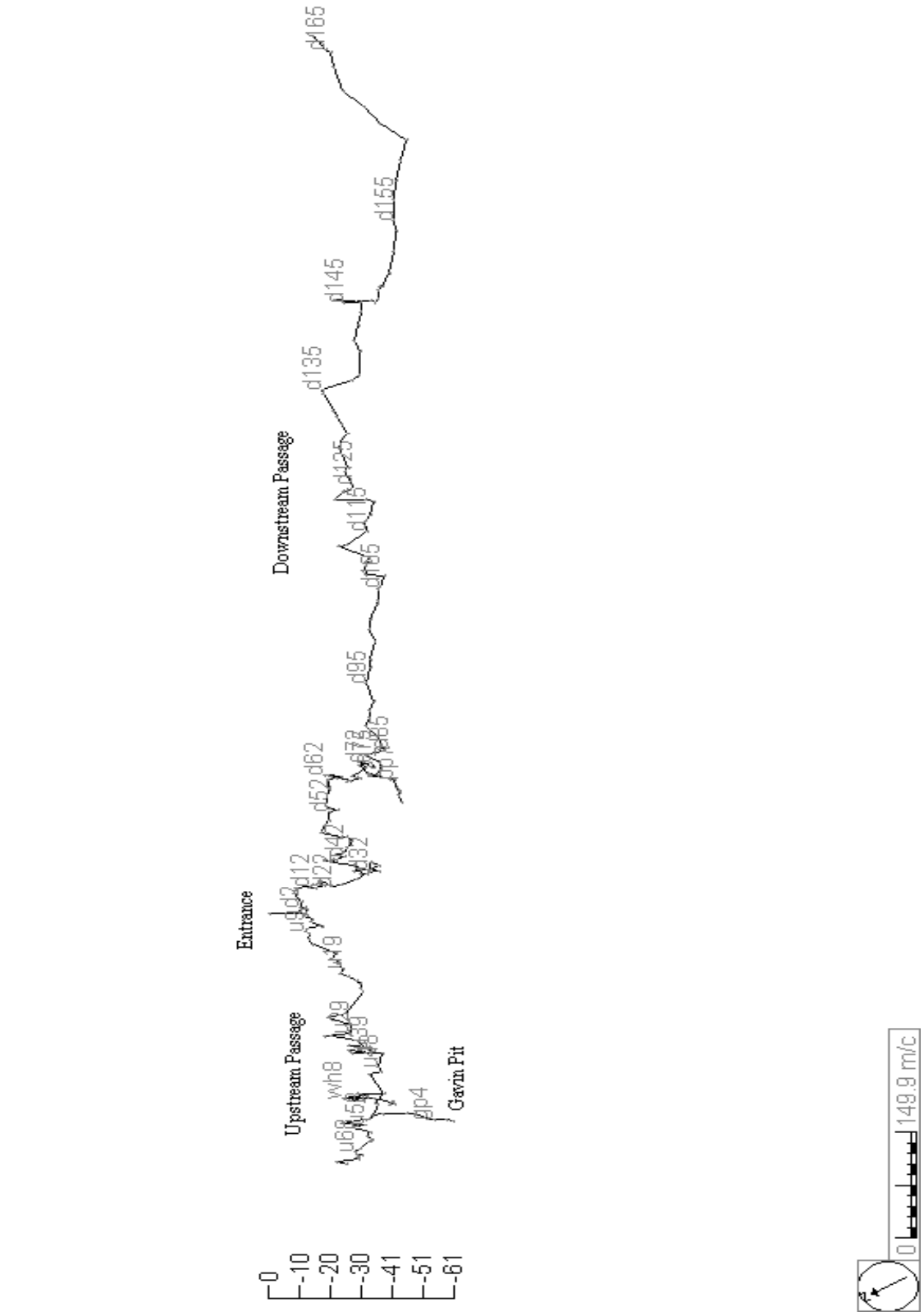

Figure A.2. Chips Hole Cave profile view. Horizontal scale is ~150 m/cm with depth in meters. The vertical exaggeration is 7X.

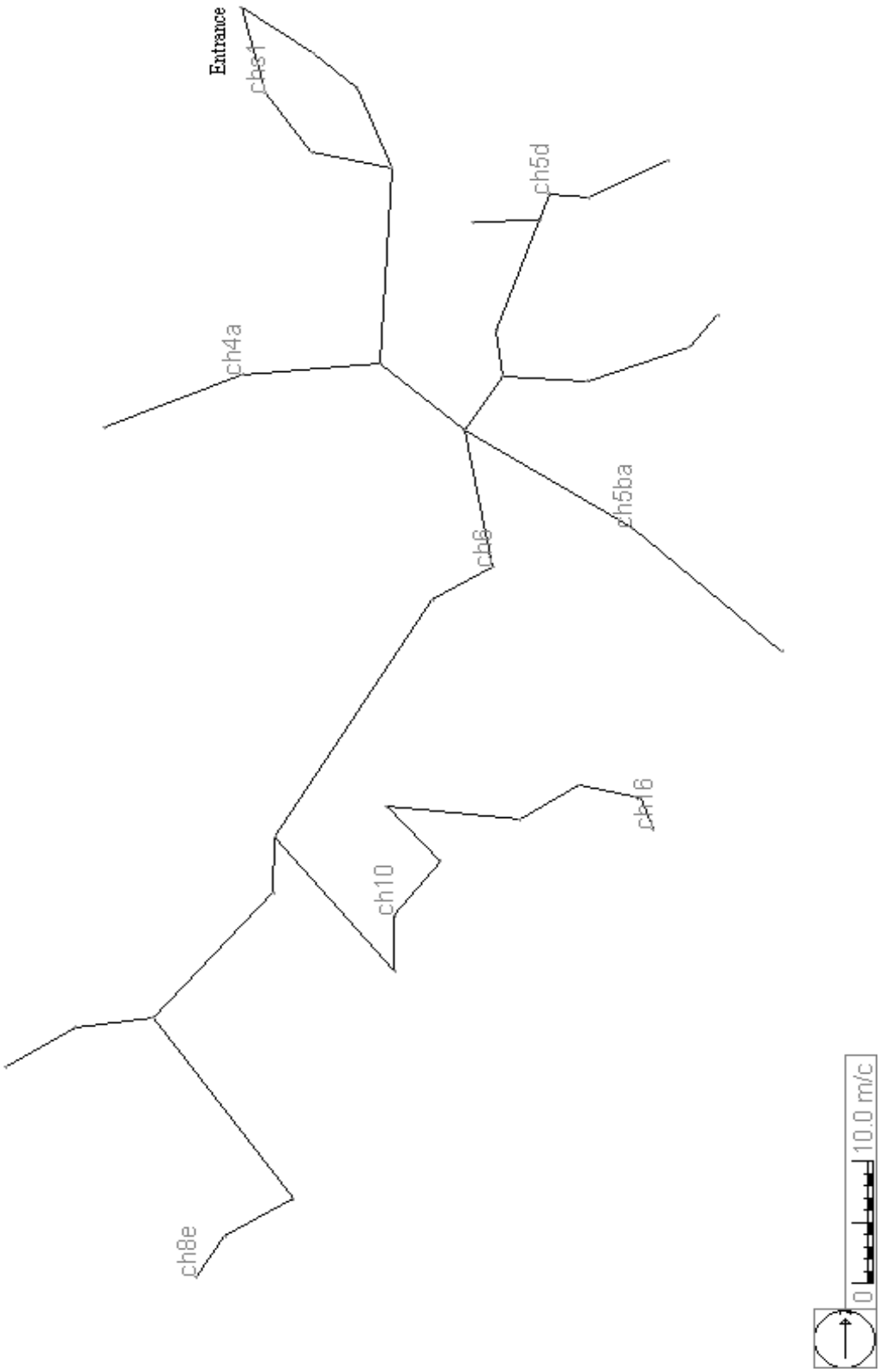

Figure A.3. Church Sink Cave. Horizontal scale is ~10.0 m/cm.

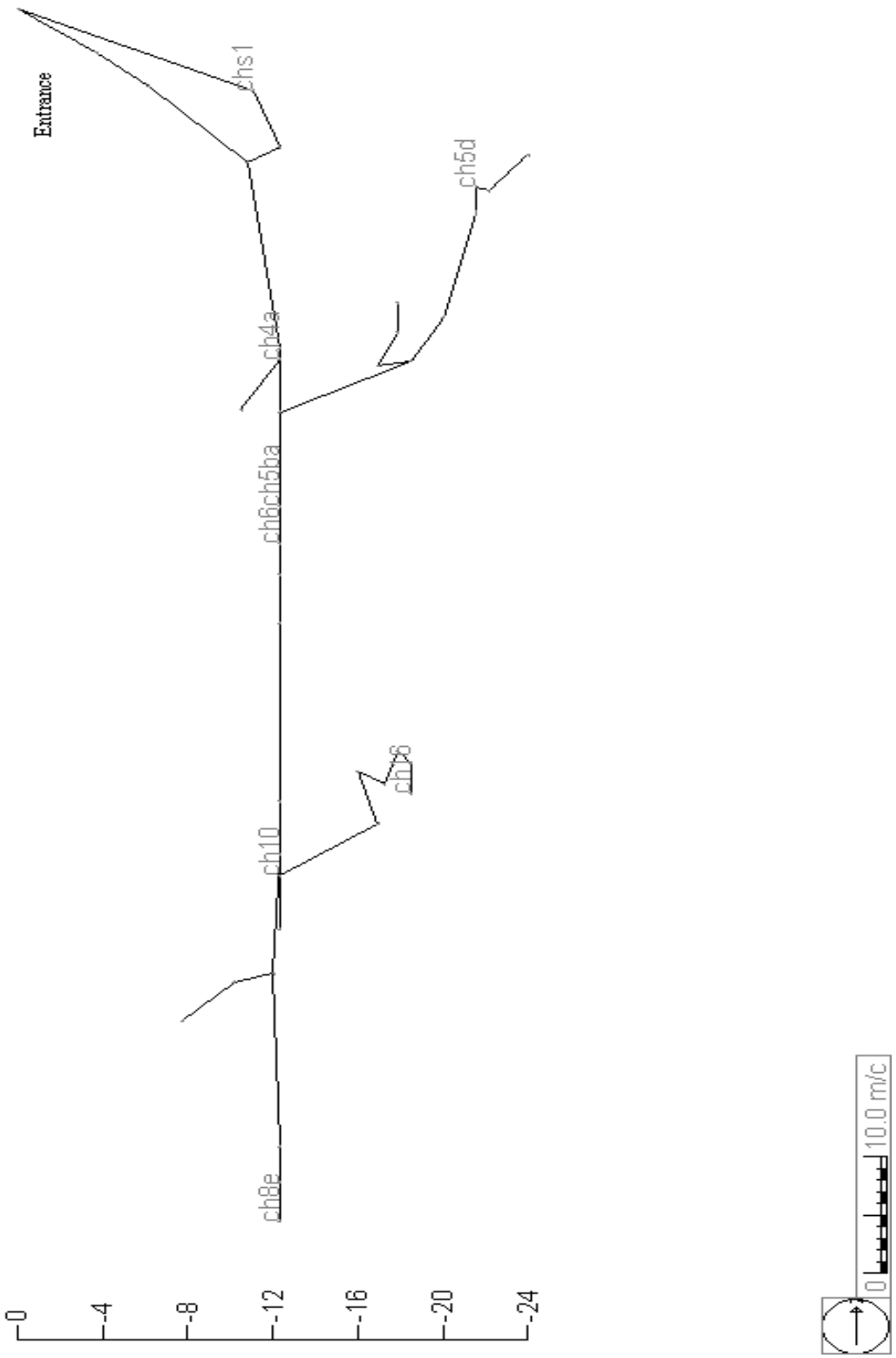

Figure A.4. Church Sink Cave. Horizontal scale is ~10.0 m/cm with depth in meters. The vertical exaggeration is 3X.

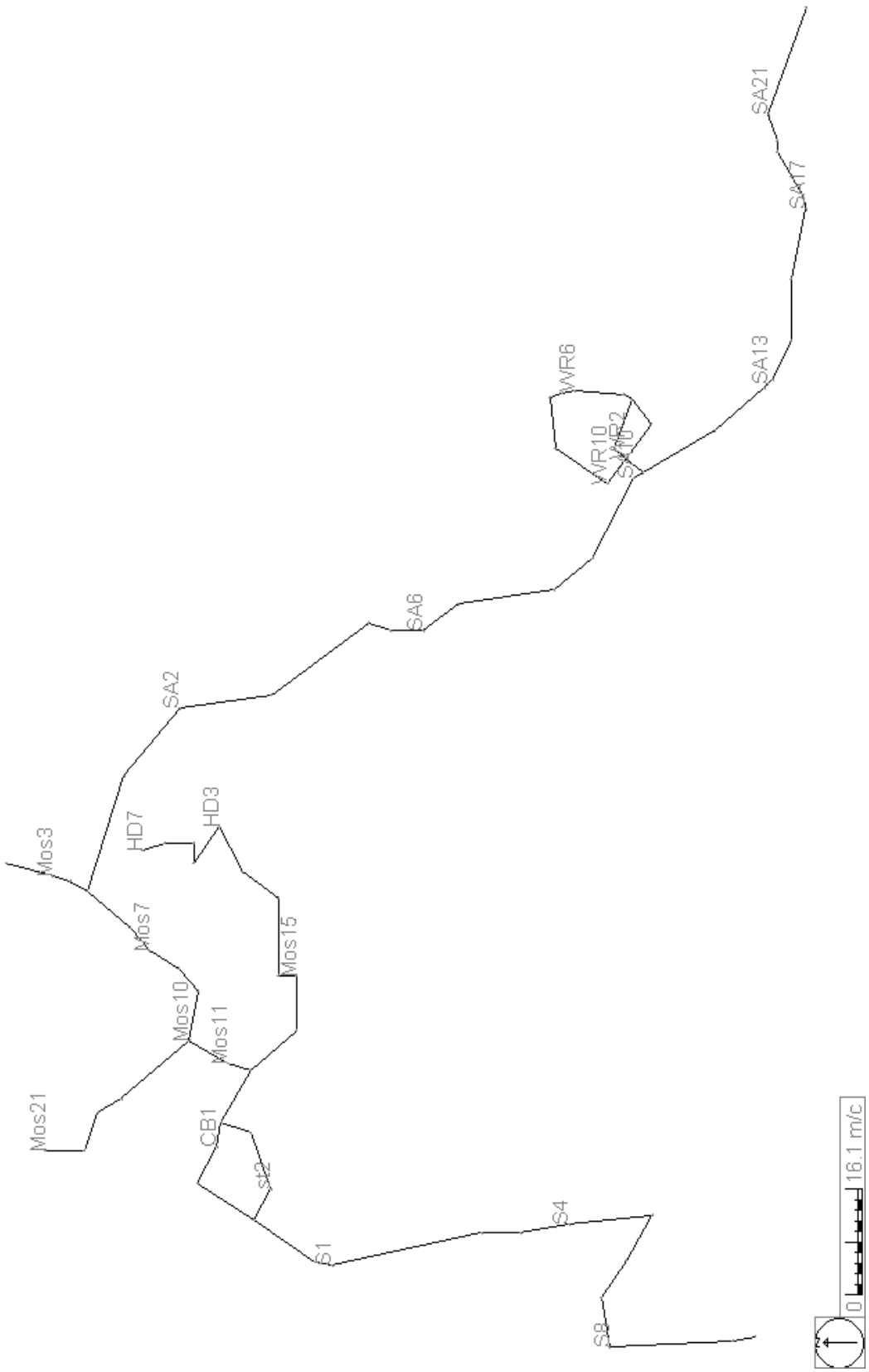

Figure A.5. Harvey's Sink Cave plan view. Horizontal scale is ~16 m/cm.

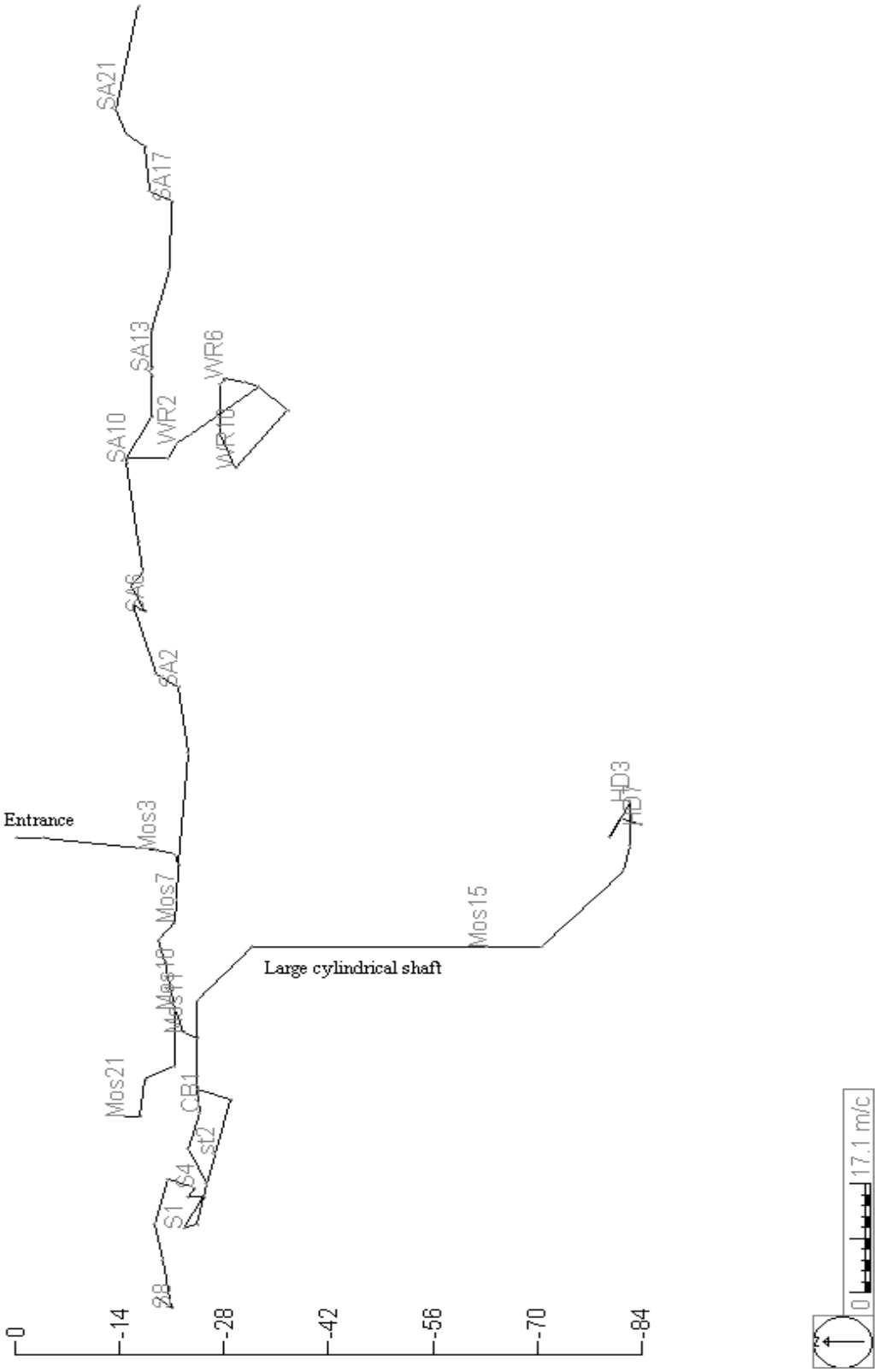

Figure A.6. Harvey's Sink Cave profile view. Horizontal scale is ~17 m/cm with depth in meters. The vertical exaggeration is 2X.

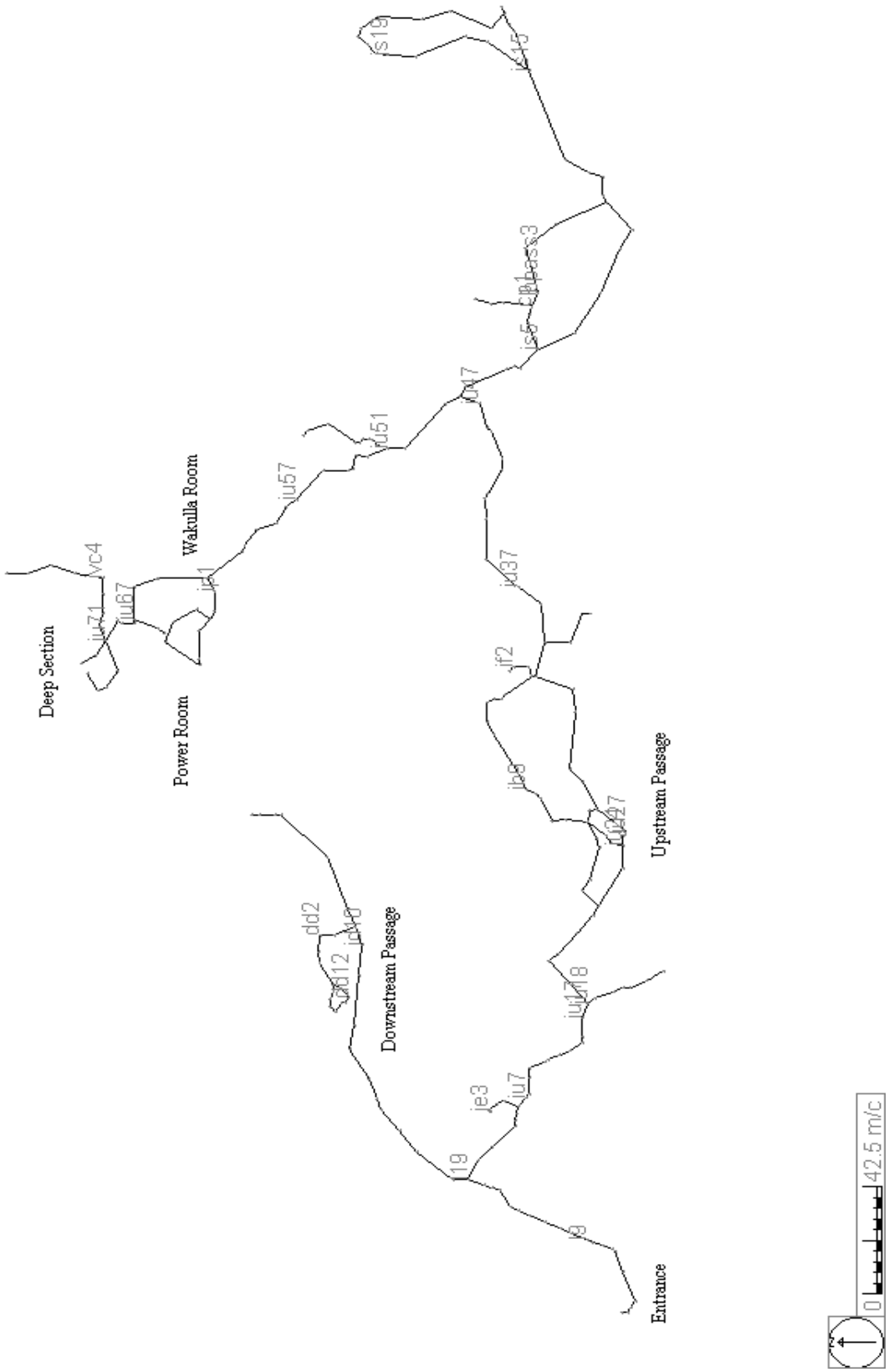

Figure A.7. Indian Springs Cave plan view. Horizontal scale is ~42 m/cm.

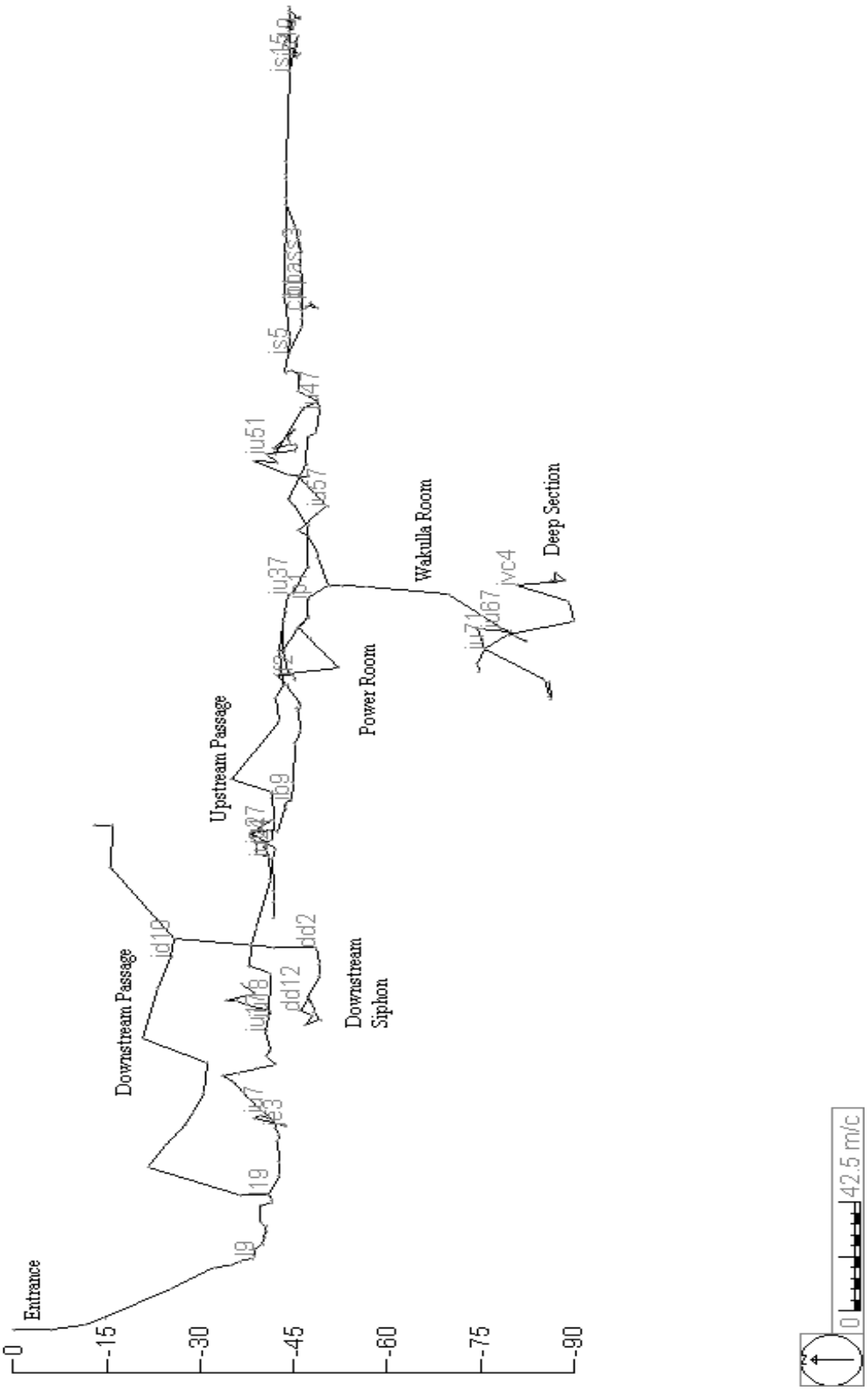

Figure A.8. Indian Springs Cave profile view. Horizontal scale is ~42 m/cm with depth in meters. The vertical exaggeration is 4X.

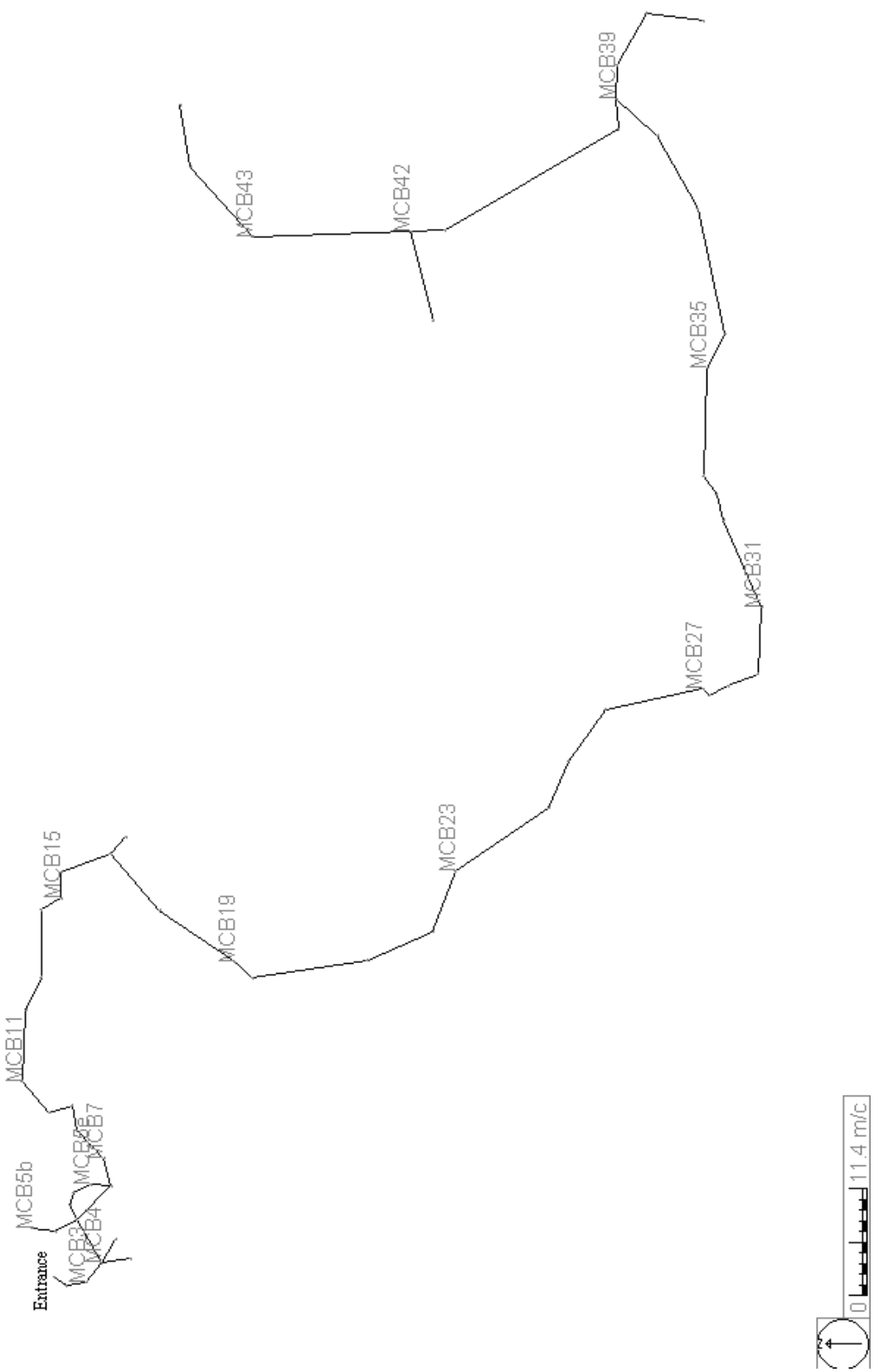

Figure A.9. McBride's Slough Cave plan view. Horizontal scale is ~ 11 m/cm.

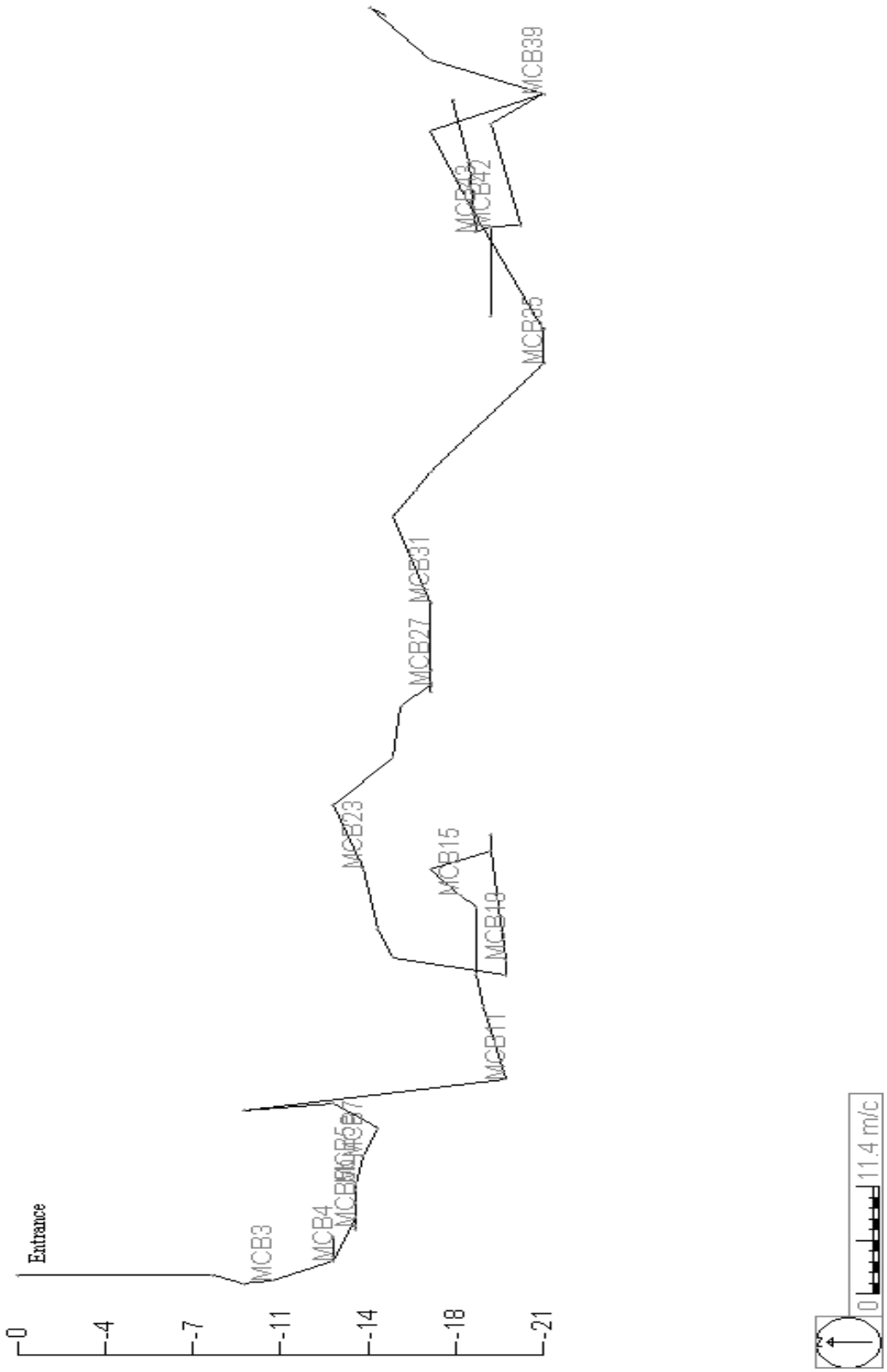

Figure A.10. McBride's Slough Cave profile view. Horizontal scale is ~ 11 m/cm with depth in meters. The vertical exaggeration is 4X.

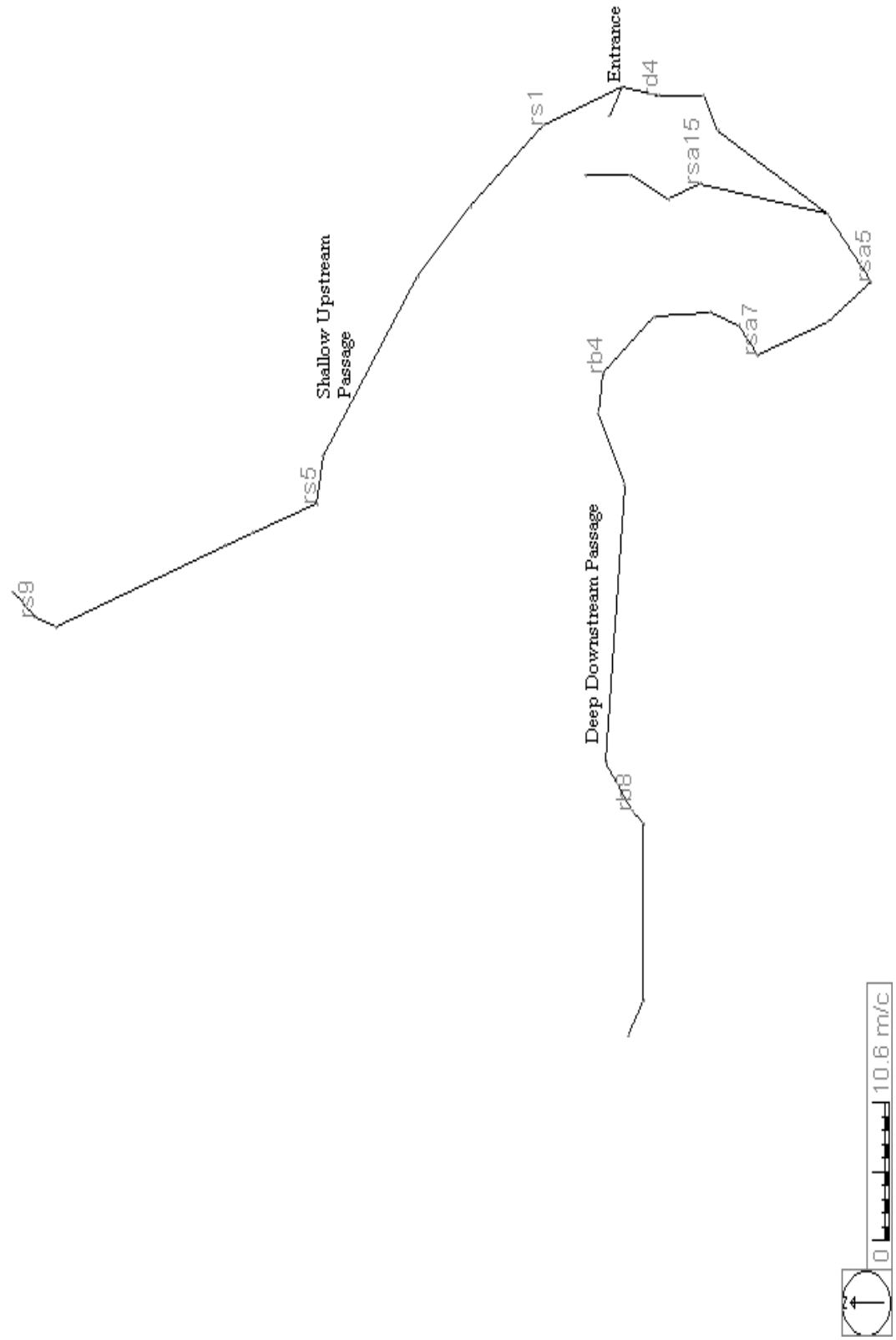

Figure A.11. Rat Sink Cave plan view. Horizontal scale is ~11 m/cm.

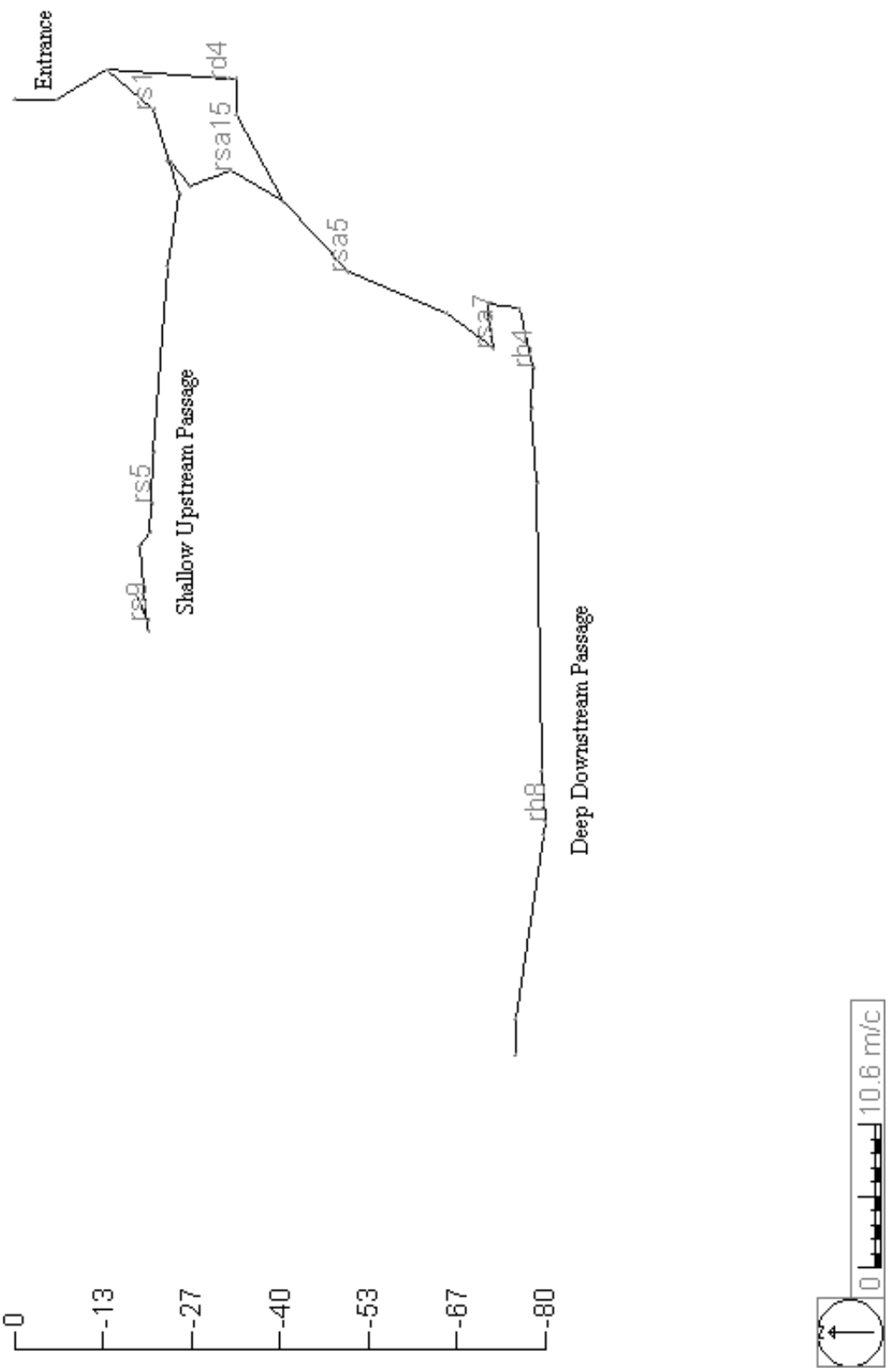

Figure A.12. Rat Sink Cave profile view. Horizontal scale is ~11 m/cm with depth in meters. The vertical exaggeration is 1X.

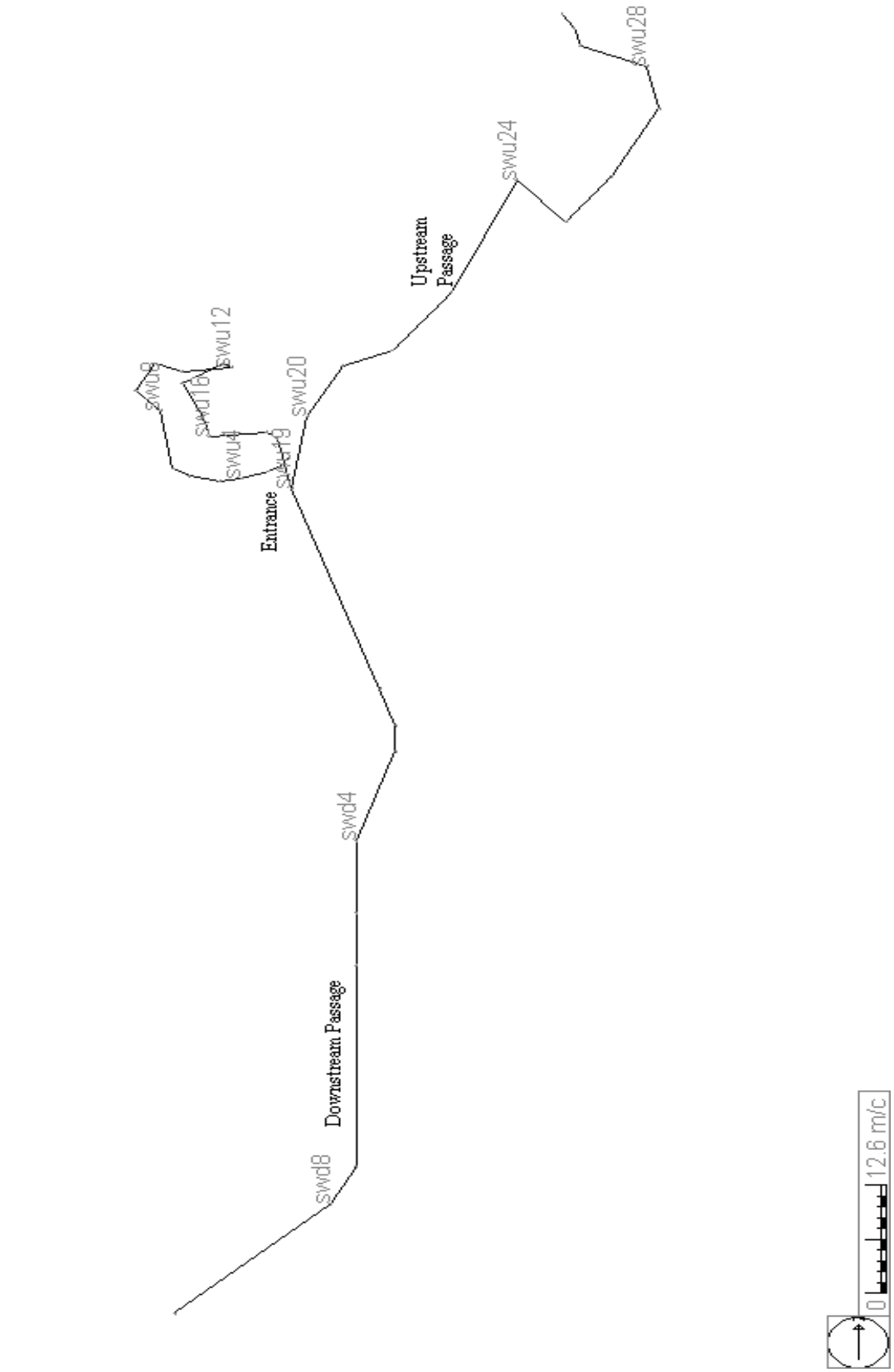

Figure A.13. Sally Ward Spring Cave plan view. Horizontal scale is ~13 m/cm.

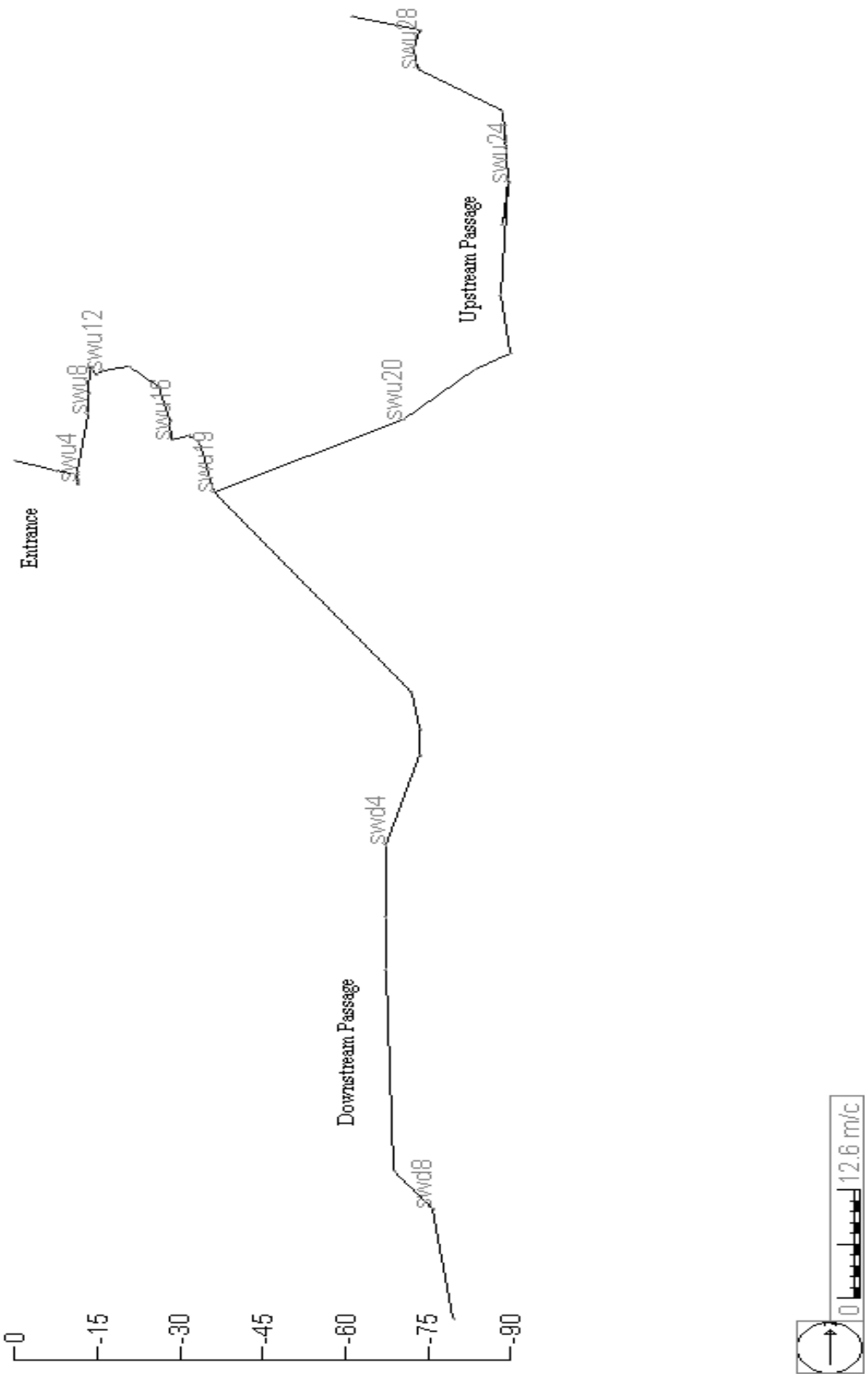

Figure A.14. Sally Ward Spring Cave profile view. Horizontal scale is ~13 m/cm with depth in meters. The vertical exaggeration is 1X.

Figure A.15. Shepherd Spring Cave plan view. Horizontal scale is ~51 m/cm.

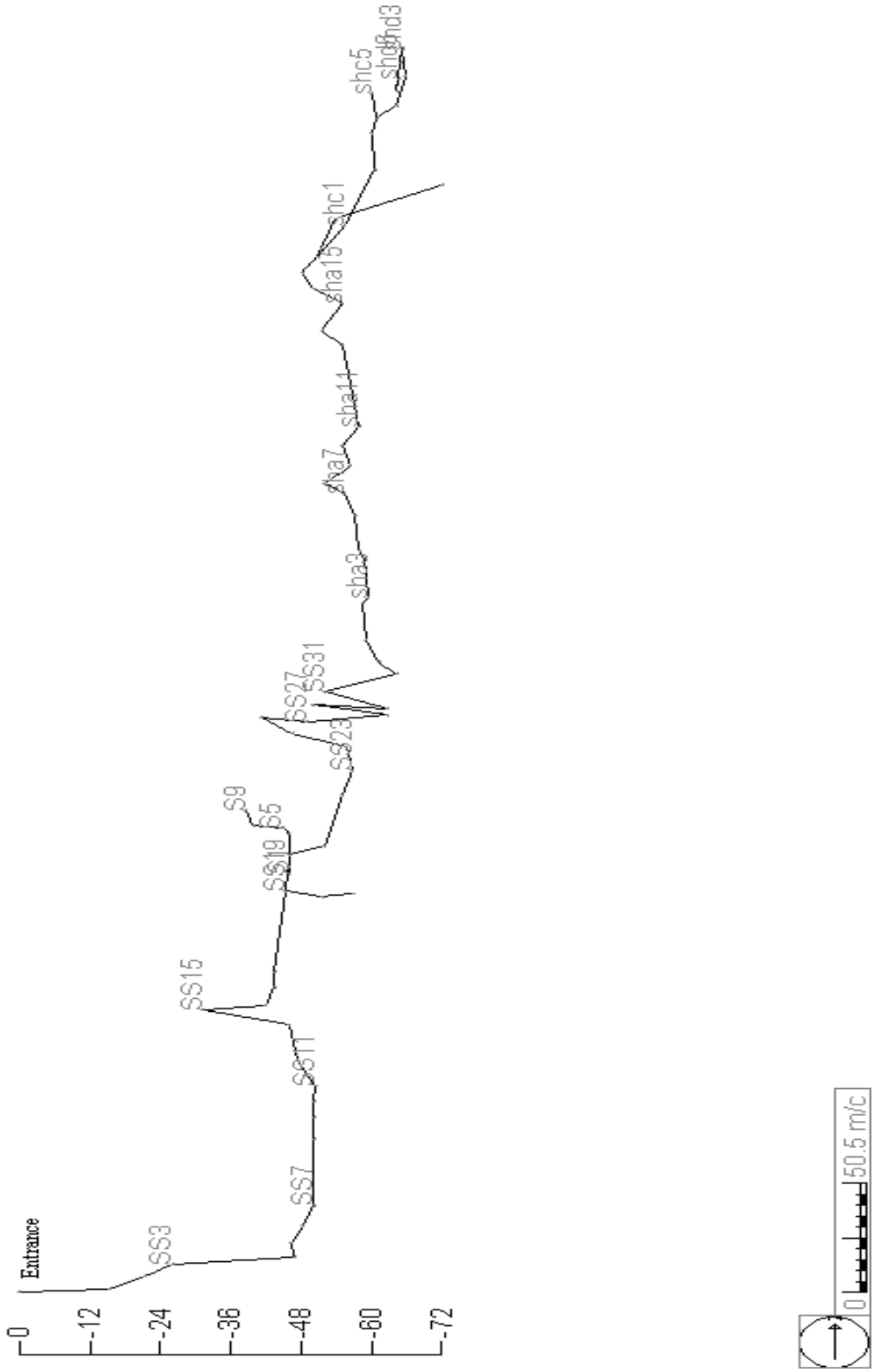

Figure A.16. Shepherd Spring Cave profile view. Horizontal scale is ~51 m/cm with depth in meters. The vertical exaggeration is 4X.

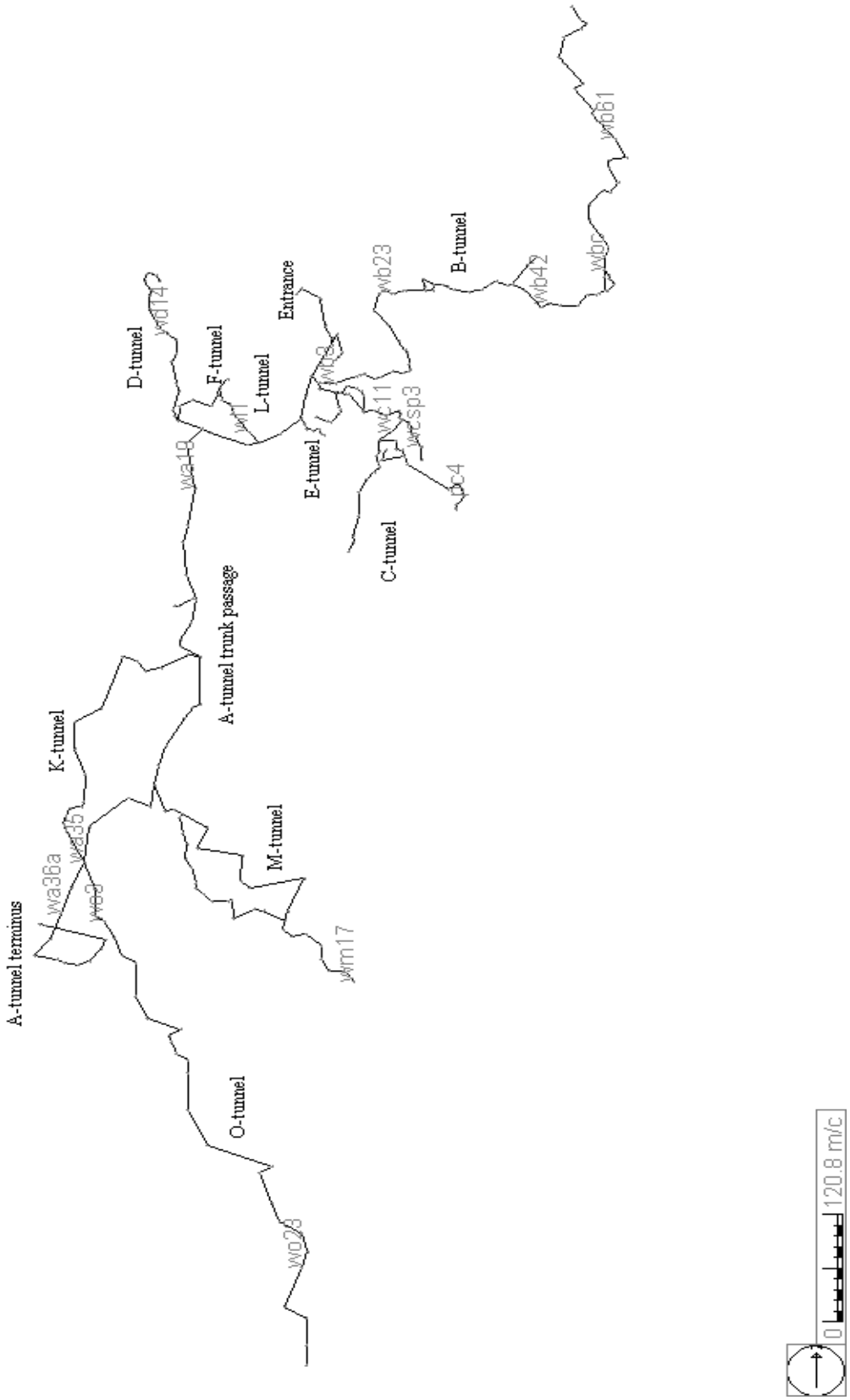

Figure A.17. Wakulla Springs Cave System plan view. Horizontal scale is ~121 m/cm.

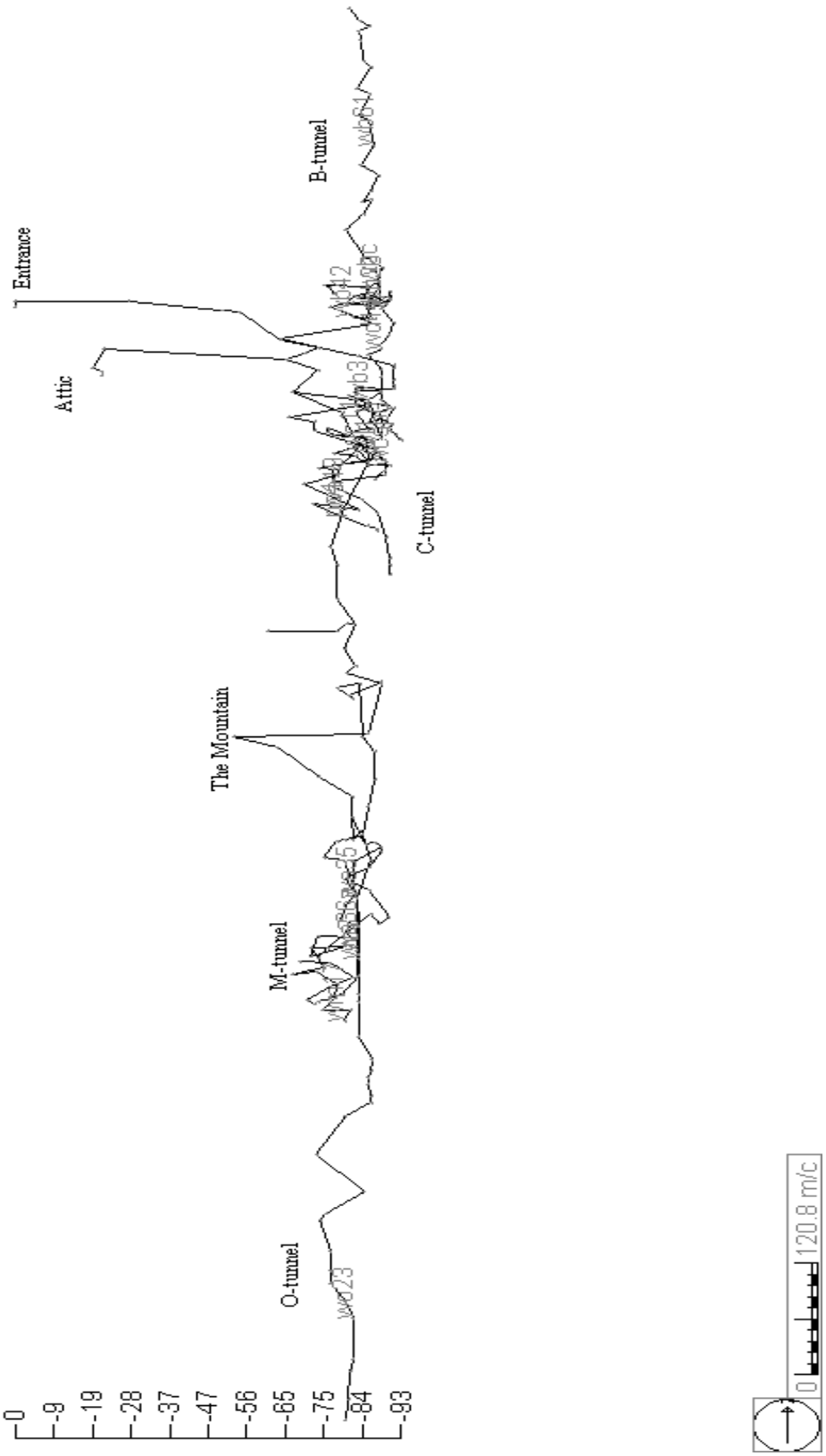

Figure A.18. Wakulla Springs Cave System profile view. Horizontal scale is ~121 m/cm with depth in meters. Vertical exaggeration is 7X.

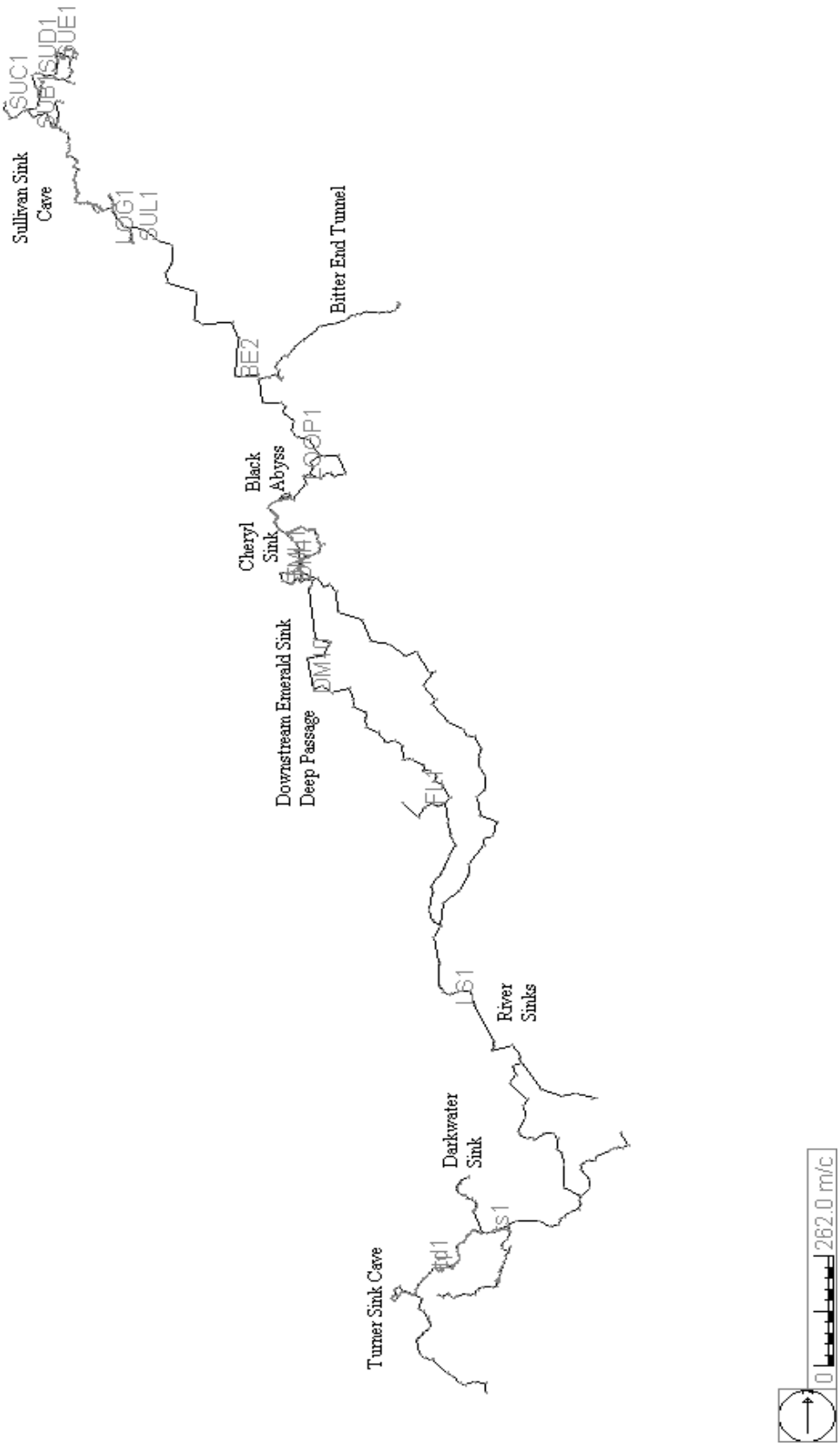

Figure A.19. Leon Sinks Cave System plan view.

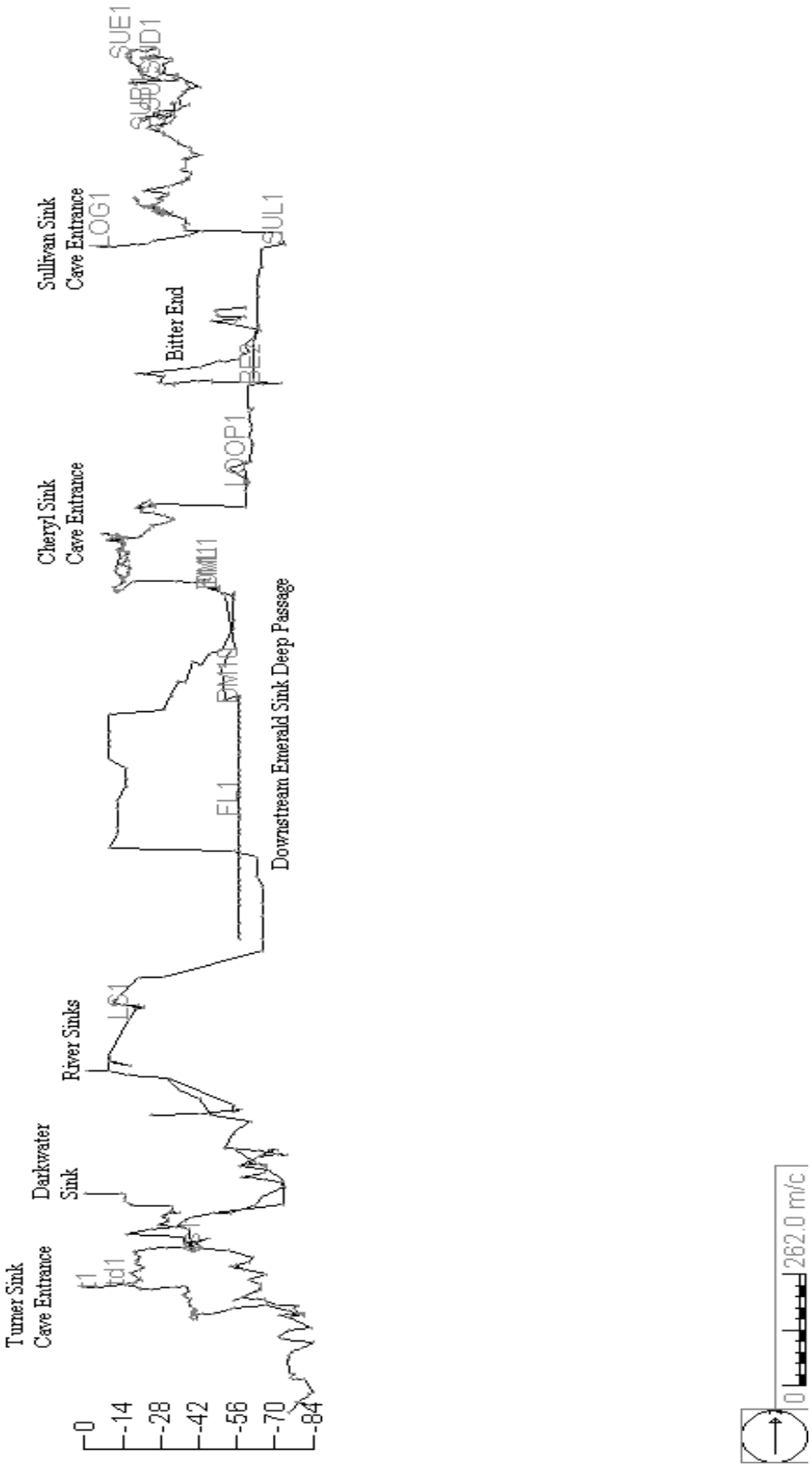

Figure A.20. Leon Sinks Cave System profile view with depth in meters. Vertical exaggeration is 12X.

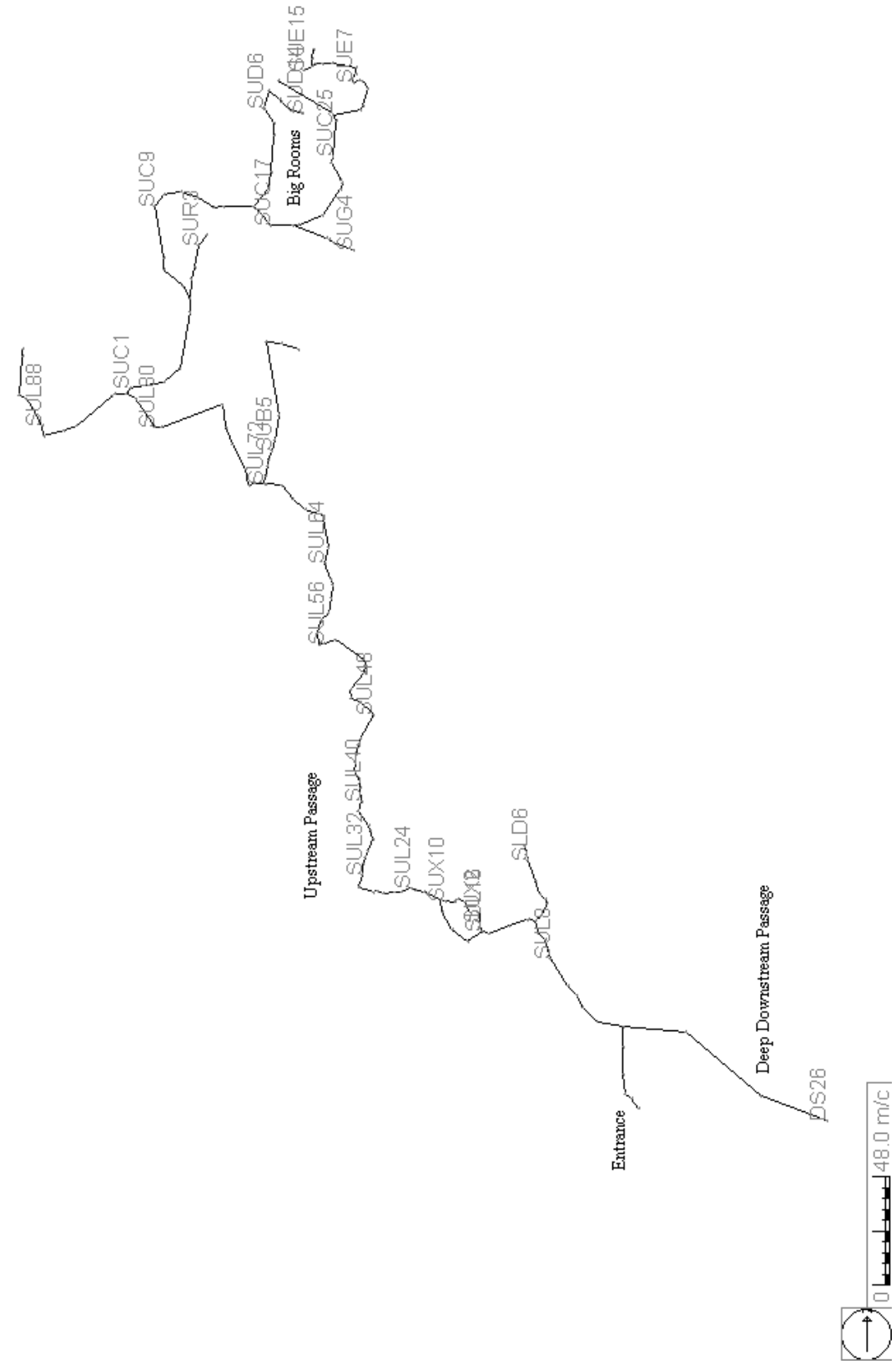

Figure A.21. Sullivan Sink Cave plan view. Horizontal scale is ~48 m/cm.

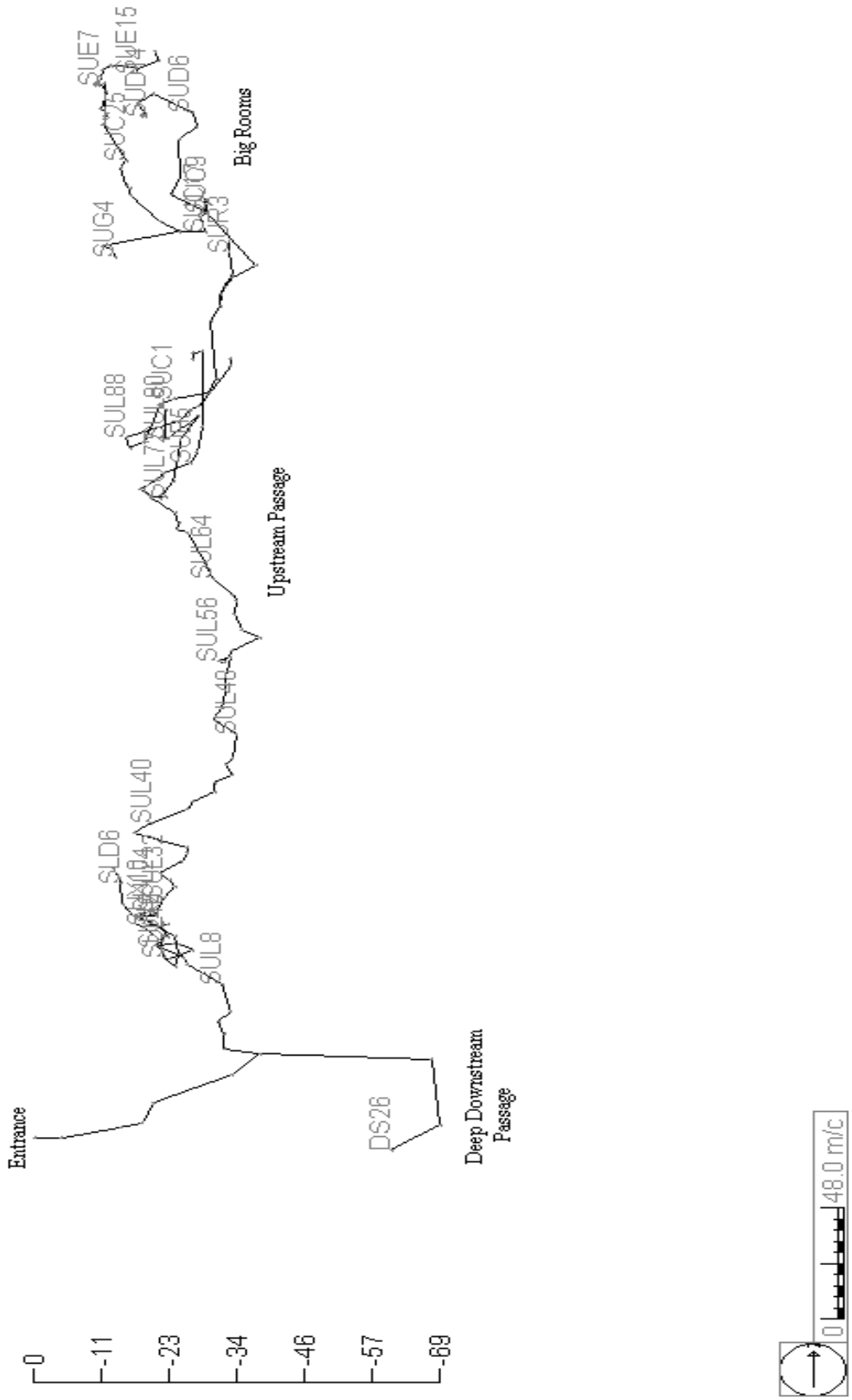

Figure A.22. Sullivan Sink Cave profile view. Horizontal scale is ~48 m/cm with depth in meters. Vertical exaggeration is 4X.

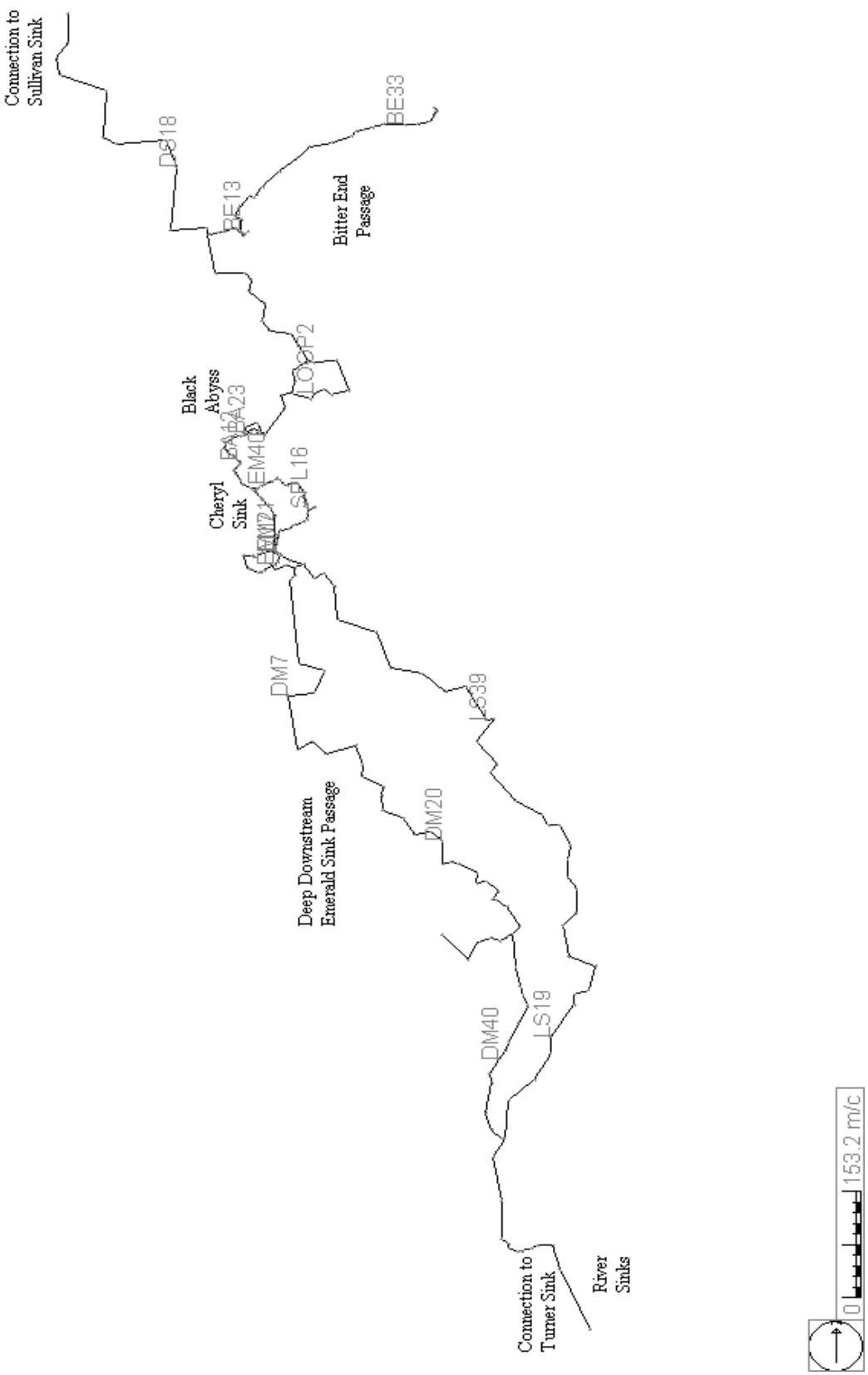

Figure A.23. Cheryl Sink Cave plan view. Horizontal scale is ~153 m/cm.

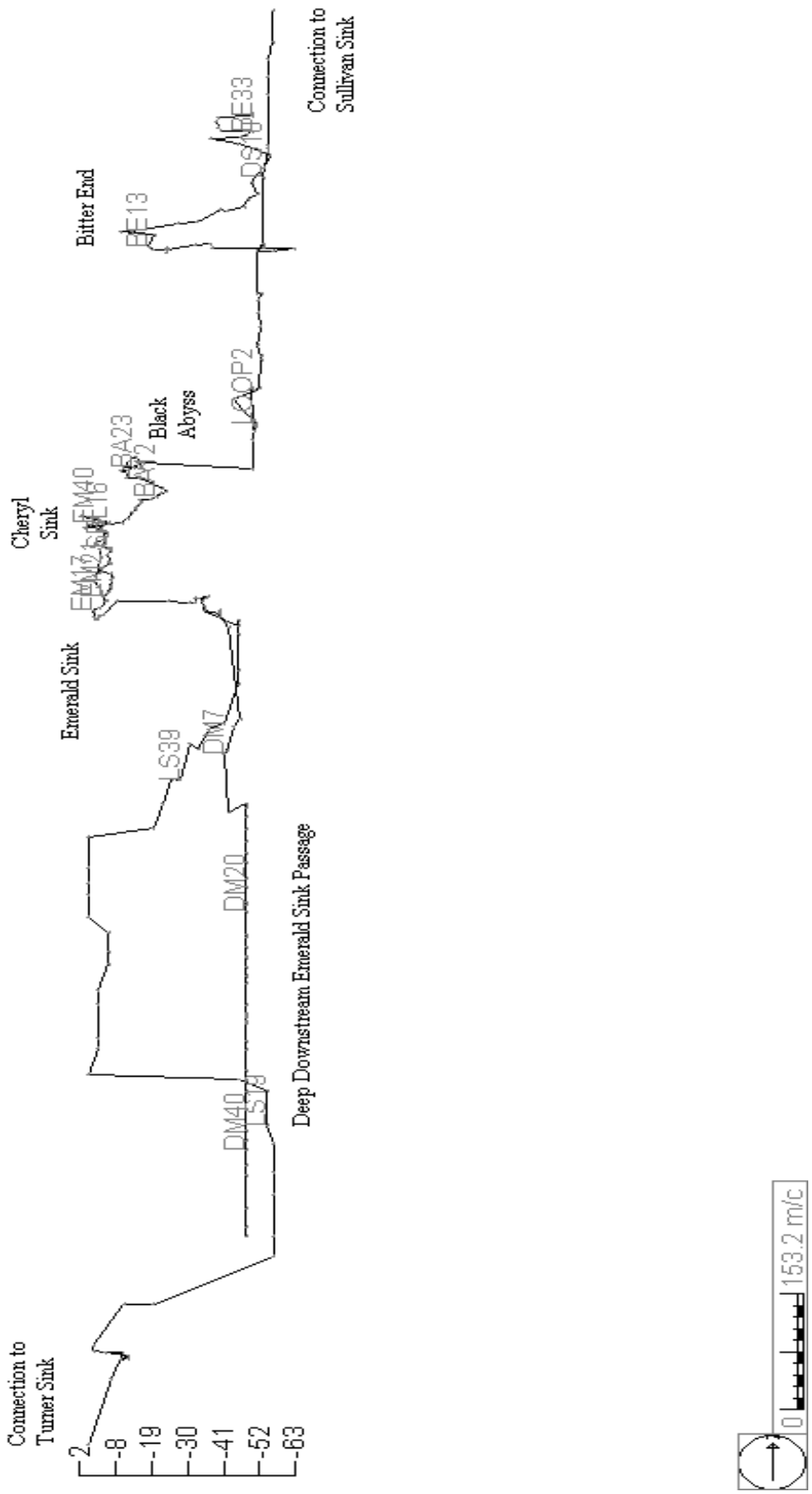

Figure A.24. Cheryl Sink Cave profile view. Horizontal scale is ~153 m/cm with depth in meters. Vertical exaggeration is 7X.

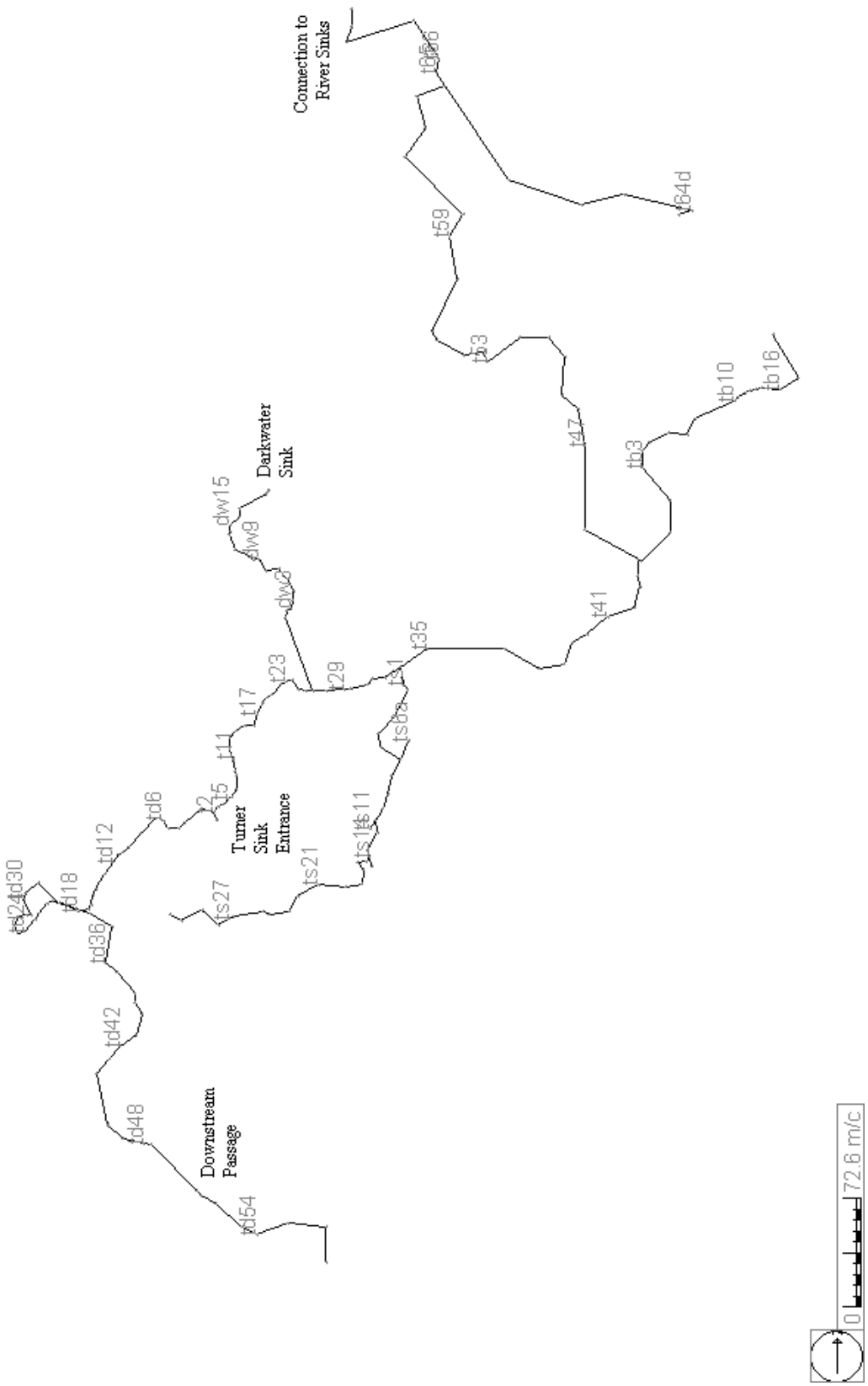

Figure A.25. Turner Sink Cave plan view. Horizontal scale is ~73 m/cm.

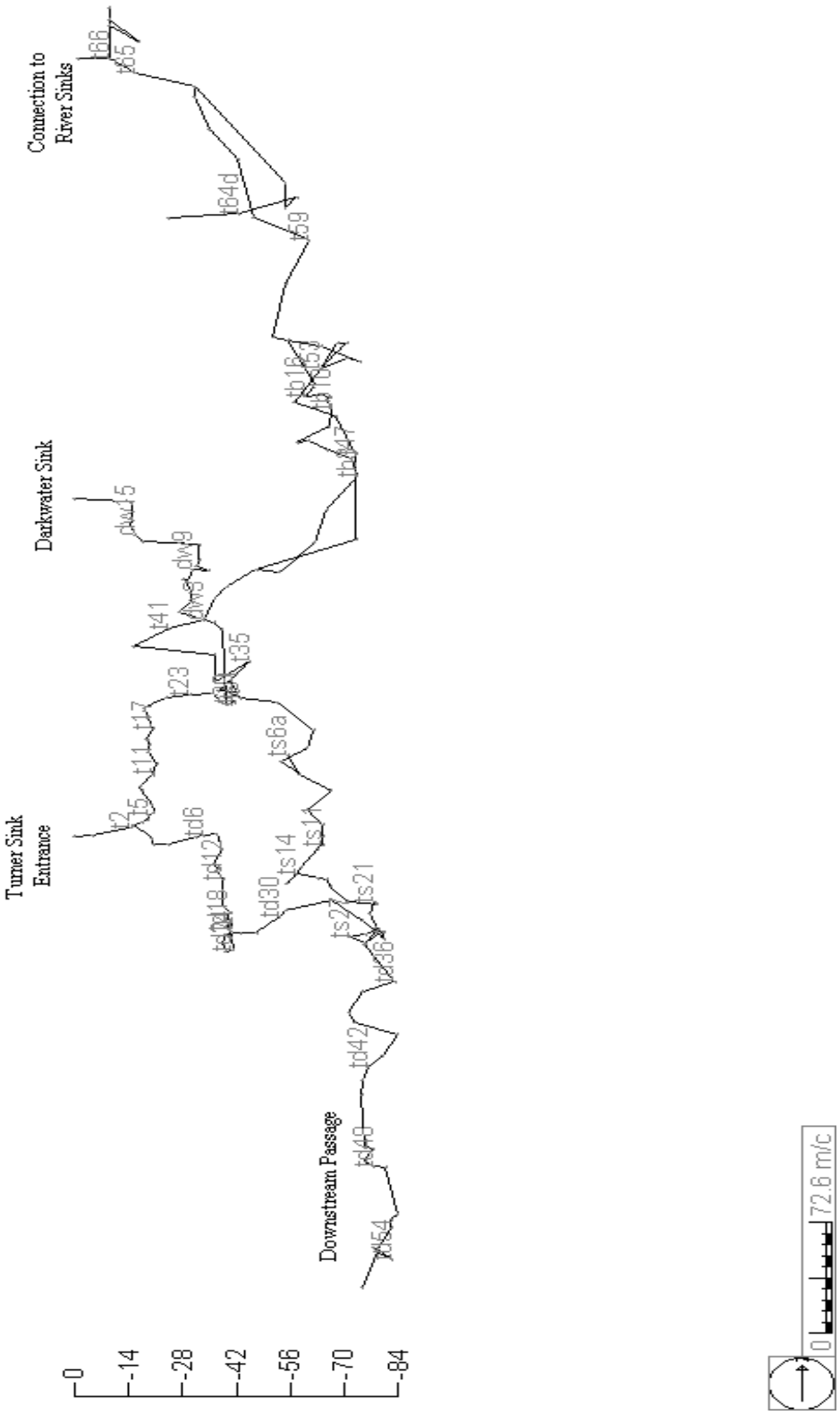

Figure A.26. Turner Sink Cave profile view. Horizontal scale is ~73 m/cm with depth in meters. Vertical exaggeration is 4X.

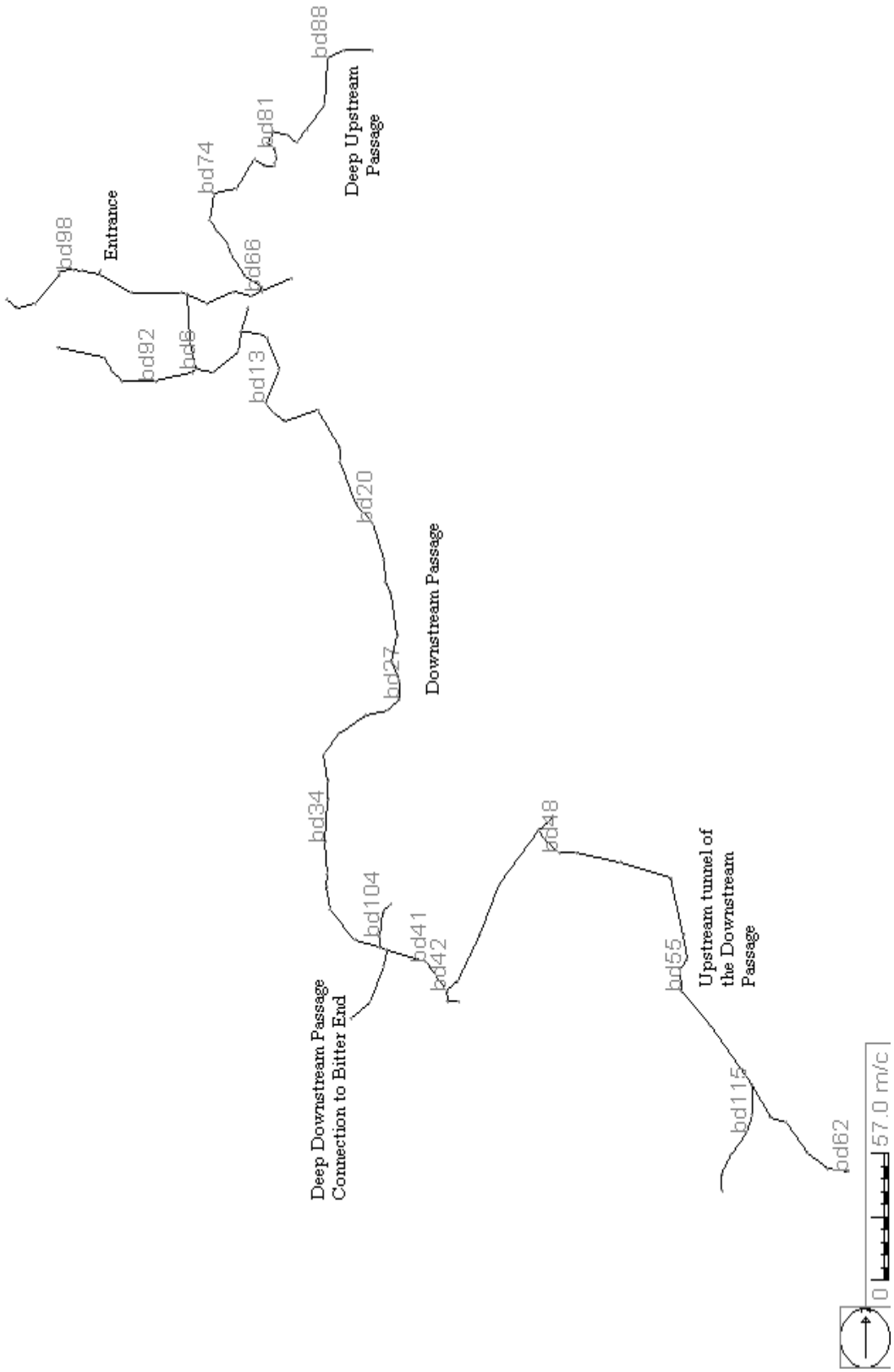

Figure A.27. Big Dismal Sink Cave plan view. Horizontal scale is ~57 m/cm.

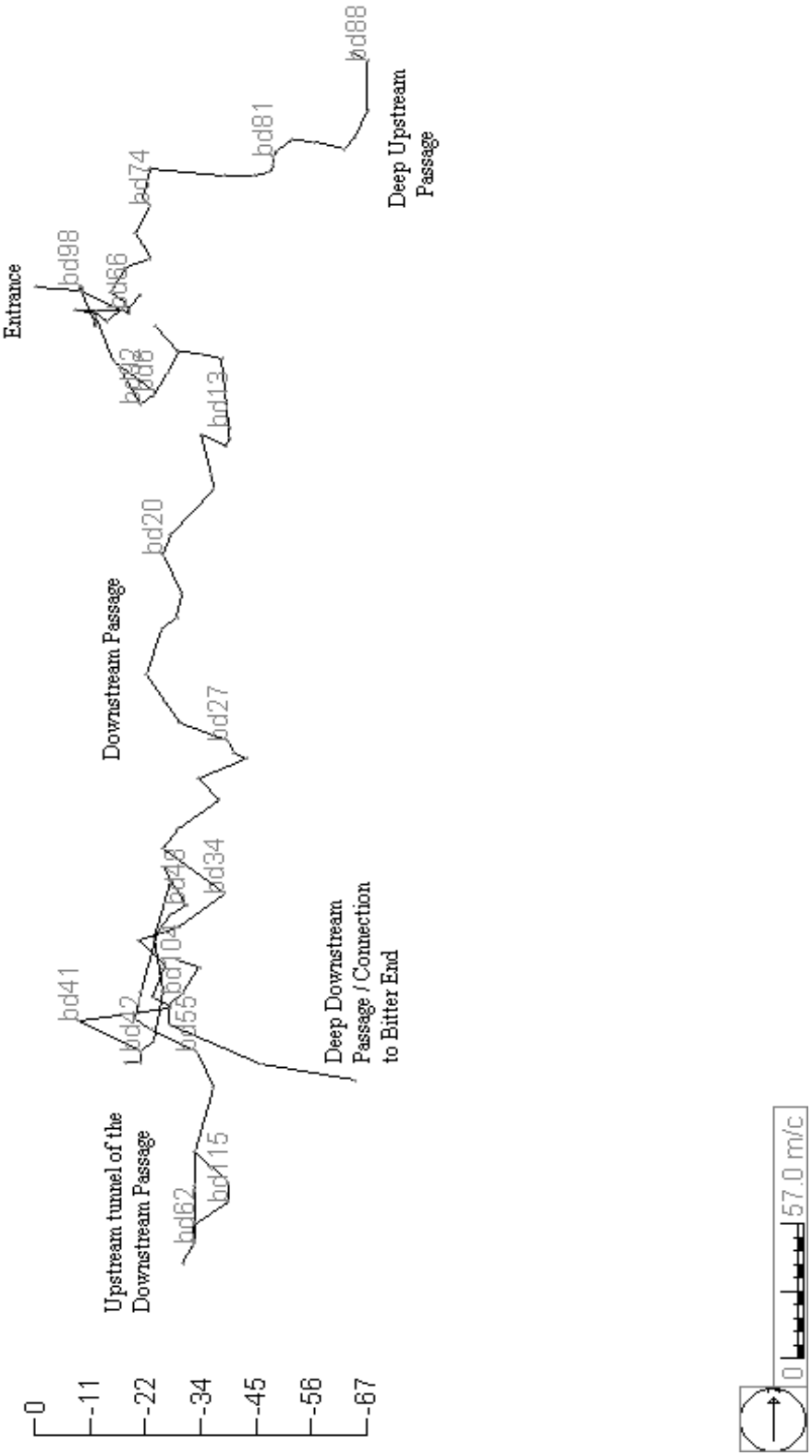

Figure A.27. Big Dismal Sink Cave profile view. Horizontal scale is ~57 m/cm with depth in meters. Vertical exaggeration is 4X.

APPENDIX B

This appendix contains the 14 sea level elevation figures considered in this study. Figures B.4 and B.10 were not utilized due to a lack of data points and in the case of Figure B.4, no clear conversion factor to depth below present mean sea level existed. The figures included in this appendix are as follows: Barbados coral U/Th dating (Fig. B.1) modified and smoothed from Bard *et. al.* (1990), Core DSDP 502b (Fig. B.2) modified from Imbrie *et. al.* (1984), SPECMAP (Fig. B.3) modified from Imbrie *et. al.* (1984), Sr isotopes from Core V28-238 (Fig. B.4) modified from Dia *et. al.* (1992), Benthonic $\delta^{18}O$ Core V28-238 (Fig. B.5) modified from Dia *et. al.* (1992), modified seawater curve (Fig. B.6) from Labeyrie *et. al.* (1987), Huon Province corals and Core V19-30 (Fig. B.7) modified from Chappell and Shackleton (1986), Haiti corals and Core Meteor 12392 (Fig. B.8) modified from Dodge *et. al.* (1983), Haiti corals and Core V19-29 (Fig. B.9) modified from Dodge *et. al.* (1983), New Guinea terraces (Fig. B.10) modified from Shackleton (1987), Core RC17-177 (Fig. B.11) modified from Shackleton (1987), Core V19-30 (Fig. B.12) modified from Shackleton (1987), Stacked curve of Cores RC17-177 and V19-30 (Fig. B.13) modified from Shackleton (1987) and Core V30-40 (Fig. B.14) modified from Imbrie *et. al.* (1984). Many of the figures were modified from the original publication in order to better illustrate concepts consistent with this study. Additionally, the modifications of all figures provided a consistent dataset from which to work. The data from these figures, consistent with other data in this study, were used in the statistical correlation procedure described in Chapter 3.

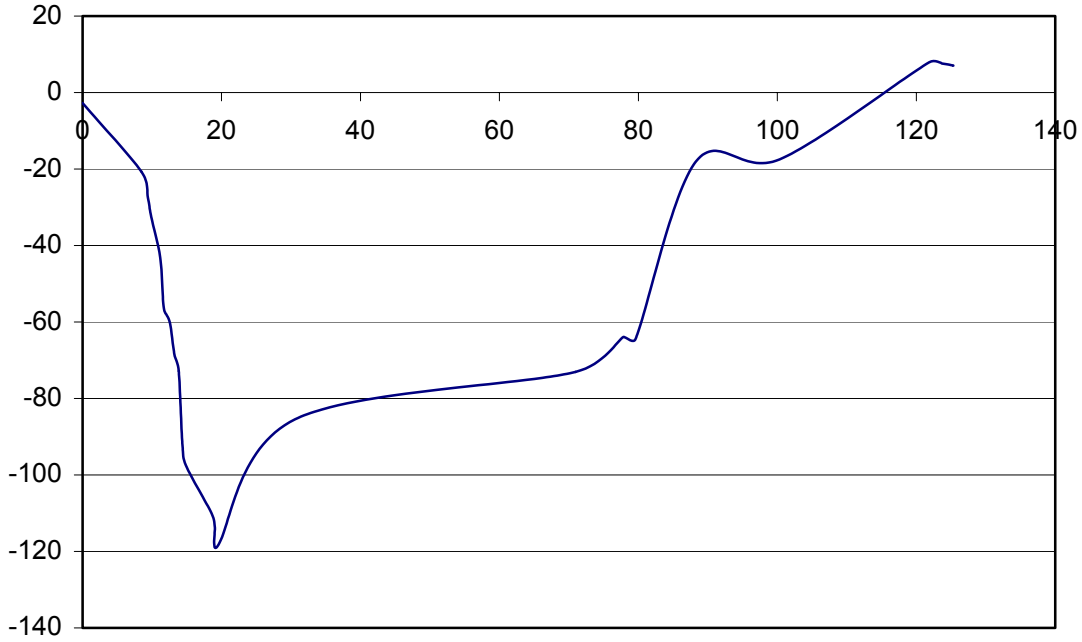

Figure B.1. Barbados coral U-Th dating modified and smoothed from Bard et. al. (1990, fig. 1), with ordinate depth in meters relative to present mean seal level and abscissa the time in Ka BP.

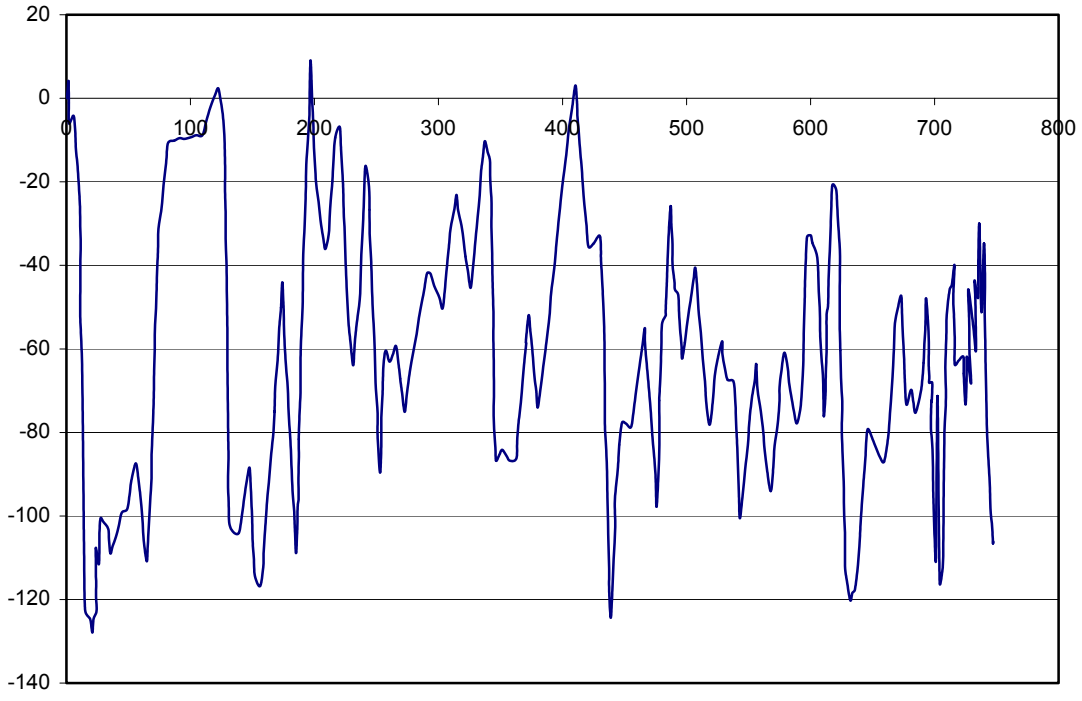

Figure B.2. $\delta^{18}O$ record of Core DSDP 502b modified from Imbrie *et. al.* (1984, fig. 5), with ordinate in meters derived from the $\delta^{18}O‰$ variations in *Globigerinoides sacculifer* and abscissa the time in Ka BP.

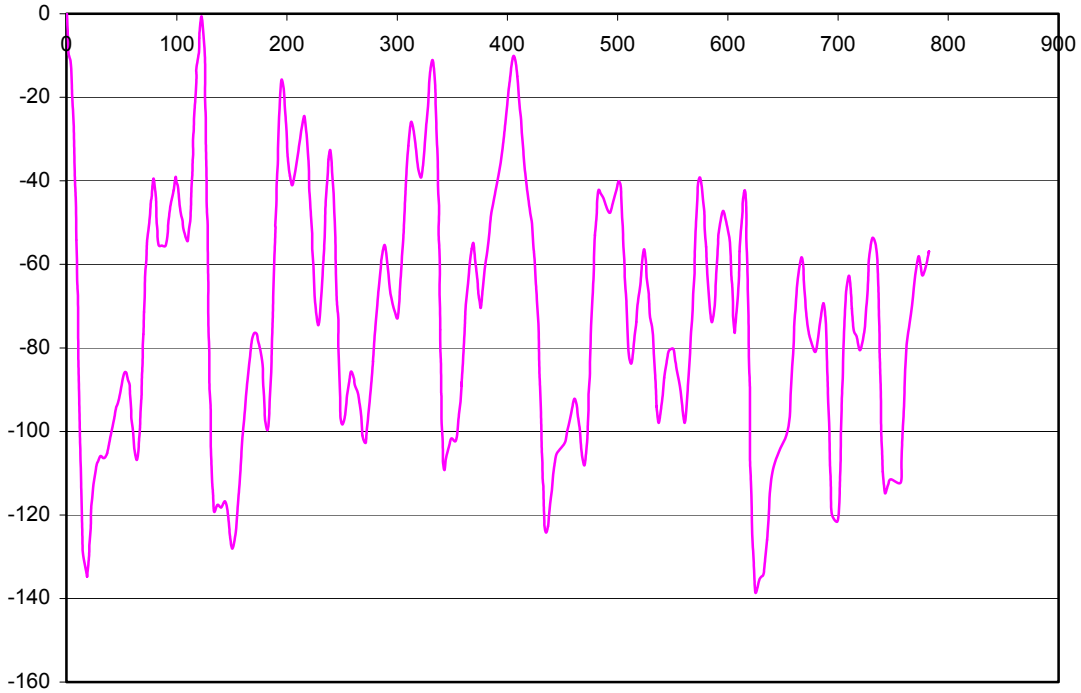

Figure B.3. $\delta^{18}O$ variation smoothed stack record on SPECMAP time scale modified from Imbrie *et. al.* (1984, fig. 8), with ordinate depth in meters below present mean sea level and abscissa the time in Ka BP.

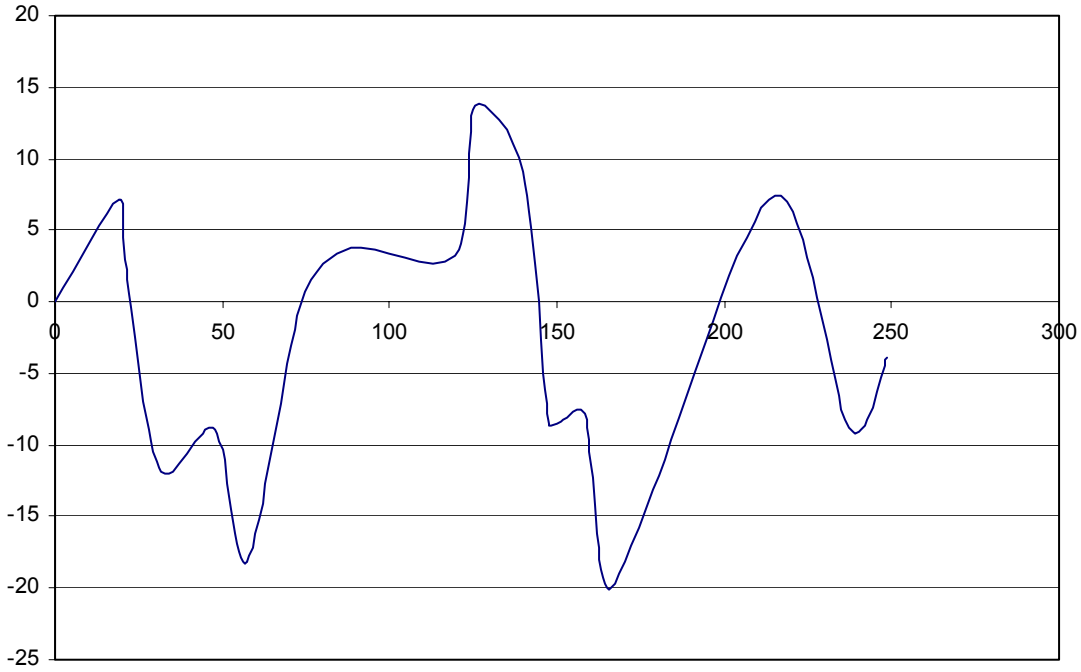

Figure B.4. Sr isotopes of foraminifera from Core V28-238 modified from Dia *et. al.* (1992, fig. 1b), with ordinate in Sr87 isotope composition and abscissa the time in Ka BP.

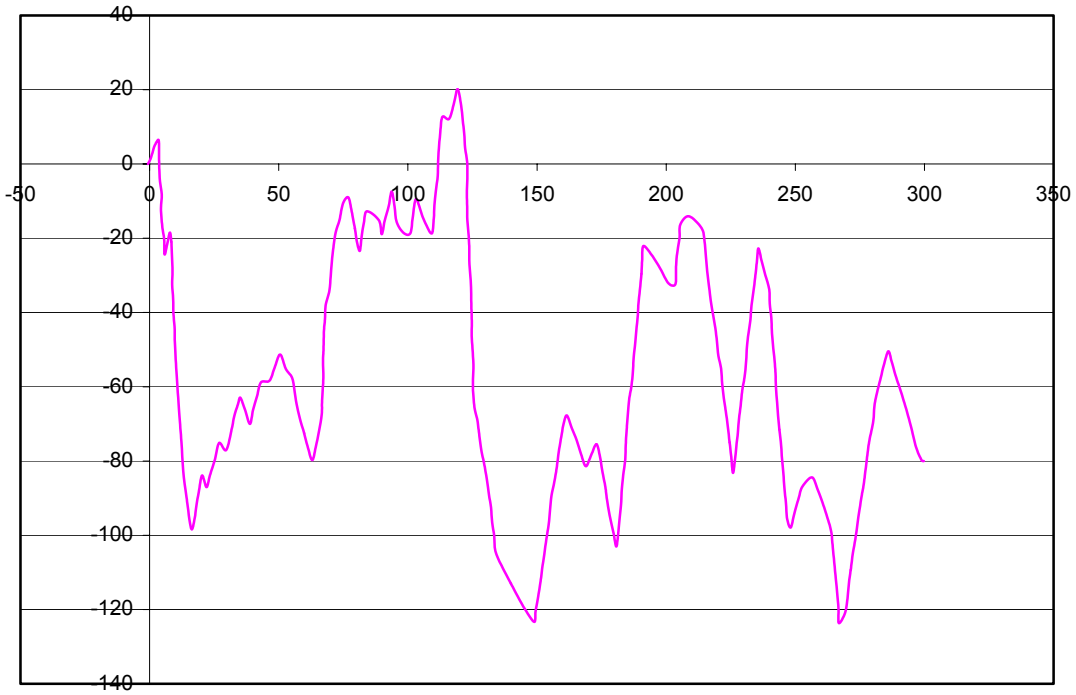

Figure B.5. Benthonic $\delta^{18}O$ from Core V28-238 modified from Dia *et. al.* (1992, fig. 1b), with ordinate depth in meters below present mean sea level and abscissa the time in Ka BP.

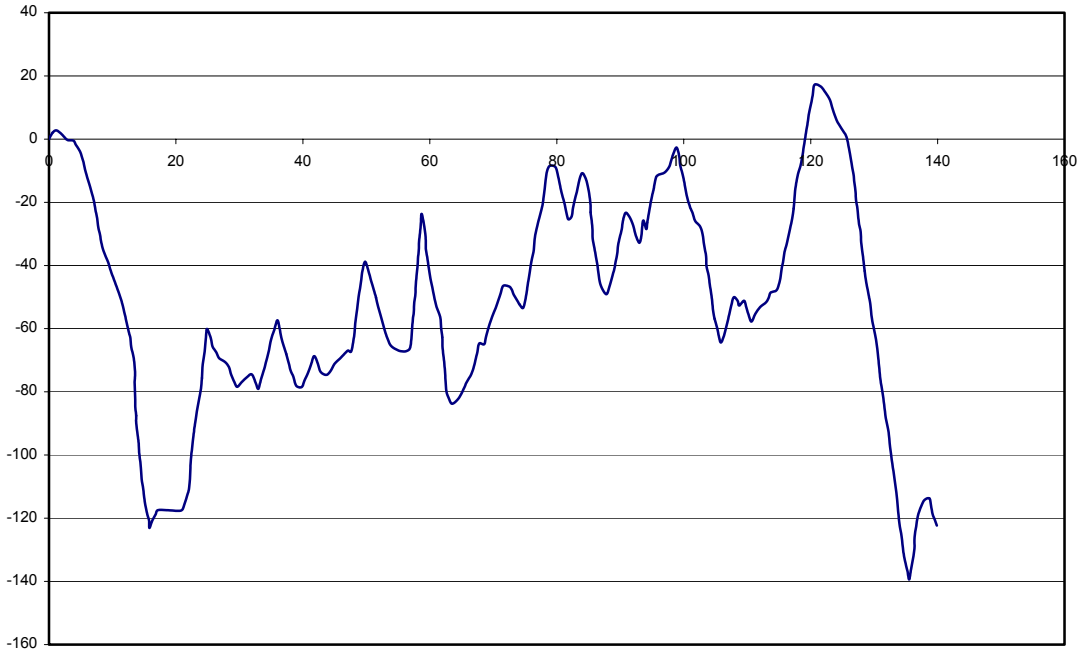

Figure B.6. Normalized $\delta^{18}O$ mean seawater curve of Labeyrie *et. al.* (1987, fig. 5) modified from Bard *et. al.* (1990, fig. 1), with ordinate depth in meters below present mean sea level and abscissa the time in Ka BP.

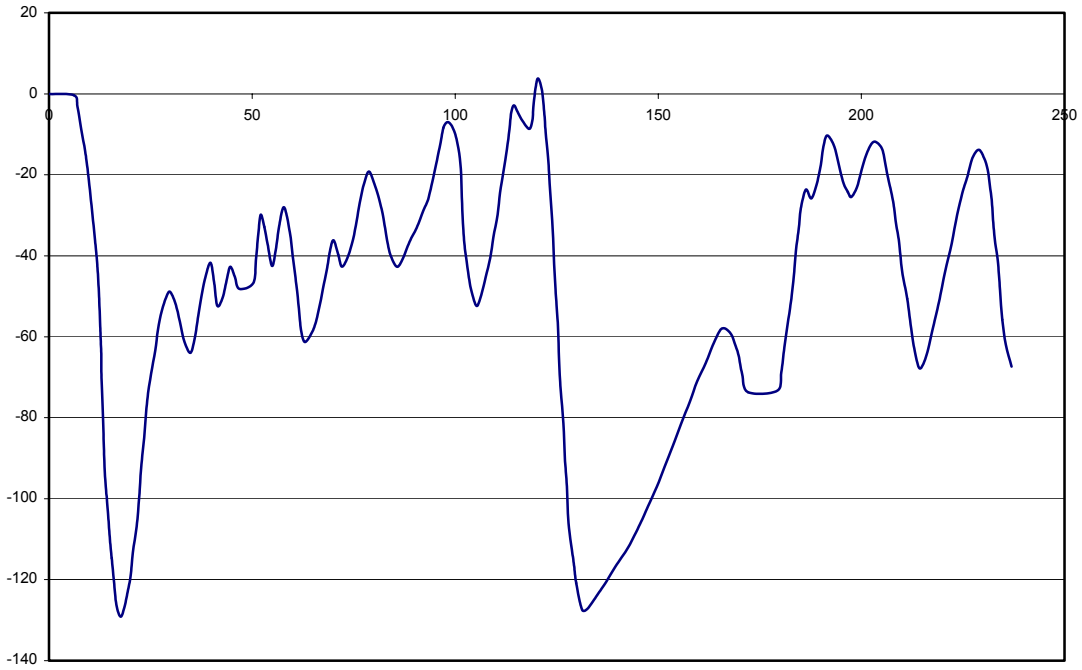

Figure B.7. Huon Province raised coral terraces recalculated with $\delta^{18}O$ foraminifera from Core V19-30, modified from Chappell and Shackleton (1986, fig. 1c), with ordinate depth in meters below present mean sea level and abscissa the time in Ka BP.

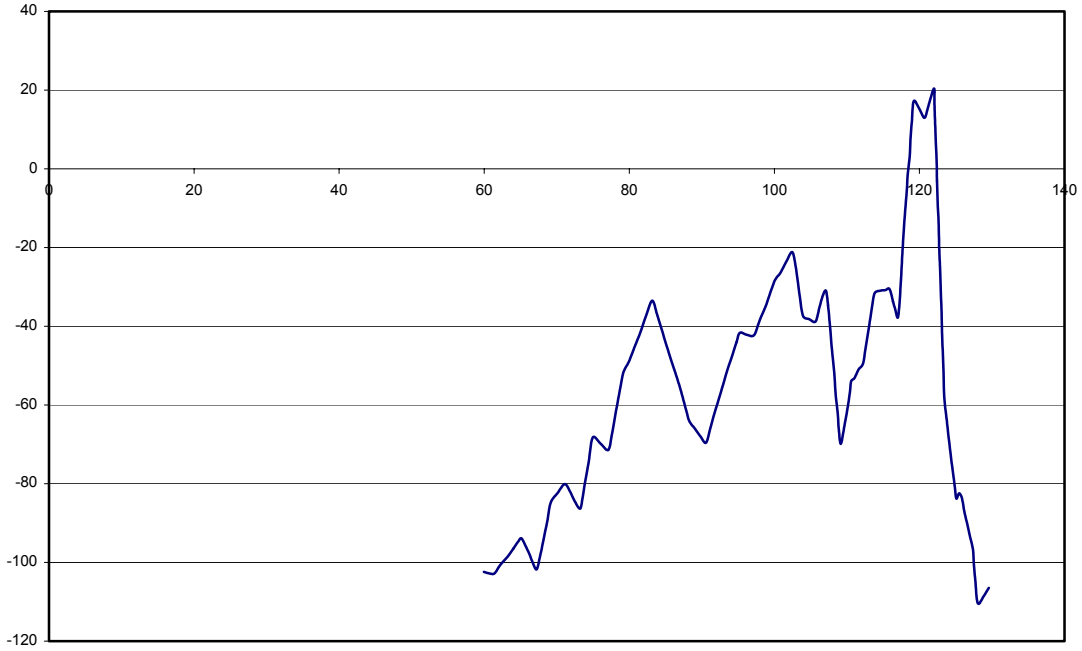

Figure B.8. Haiti raised coral terraces corresponding to U/Th ages in Barbados and $\delta^{18}O$ benthic foraminifera record of Core Meteor 12392 modified from Dodge *et. al.* (1983, fig. 1d), with ordinate depth in meters below present mean sea level and abscissa the time in Ka BP.

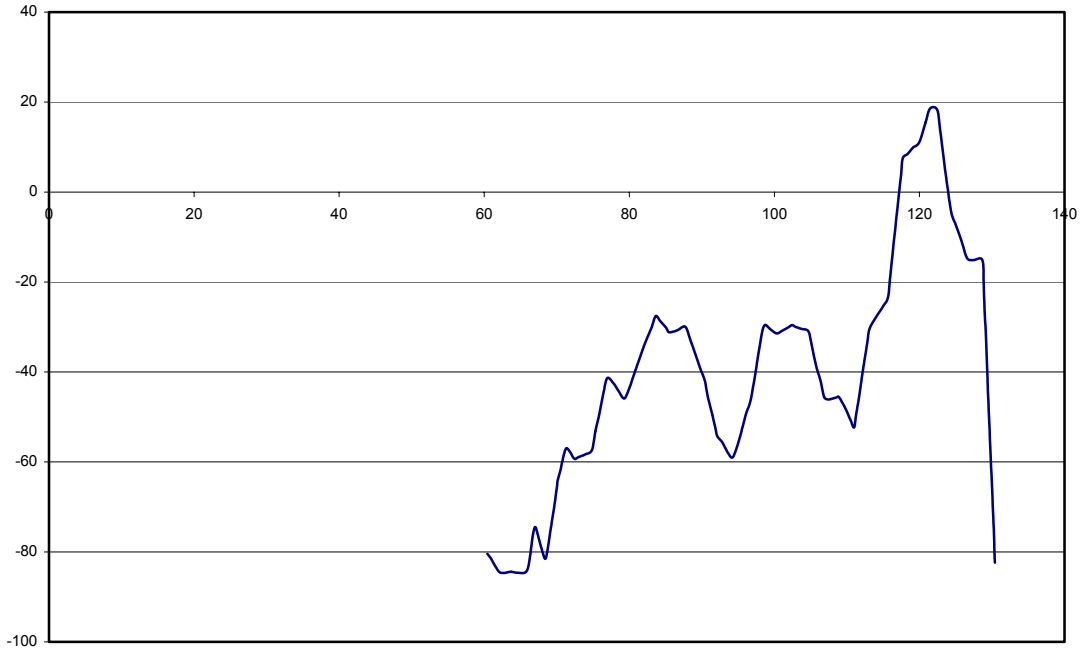

Figure B.9. Haiti raised coral terraces corresponding to U/Th ages in Barbados and $\delta^{18}O$ benthic foraminifera record of Core V19-29 modified from Dodge *et. al.* (1983, fig. 1d), with ordinate depth in meters below present mean sea level and abscissa the time in Ka BP.

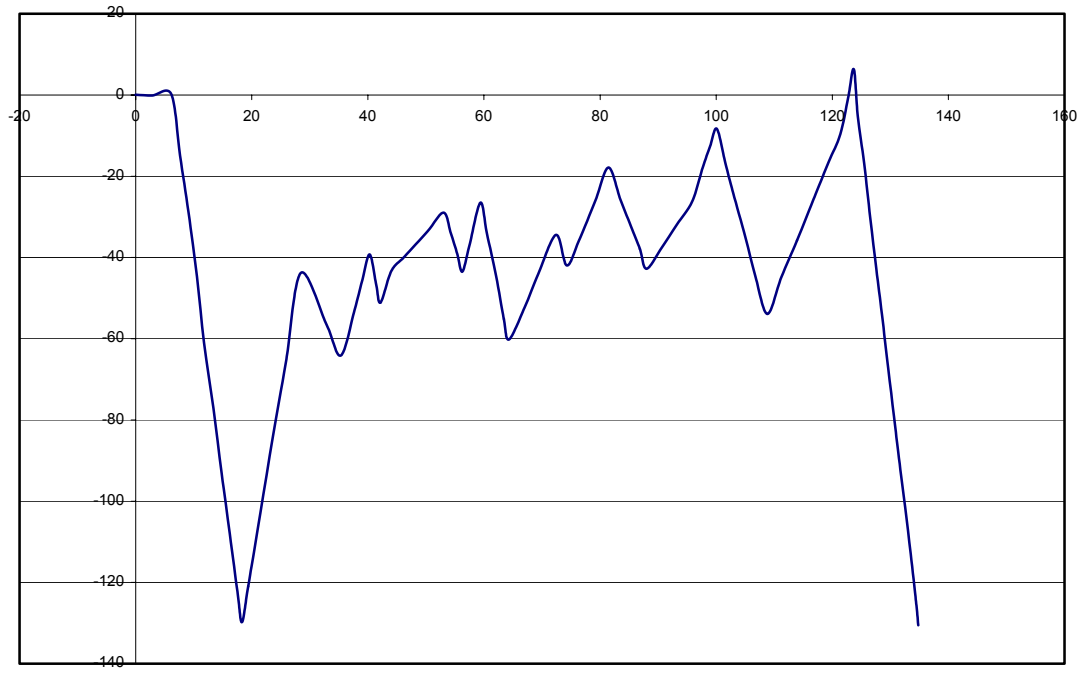

Figure B.10. Second approximation of sea level estimated from New Guinea terraces modified from Shackleton (1987, fig. 5 dashed line), with ordinate depth in meters below present mean sea level and abscissa the time in Ka BP.

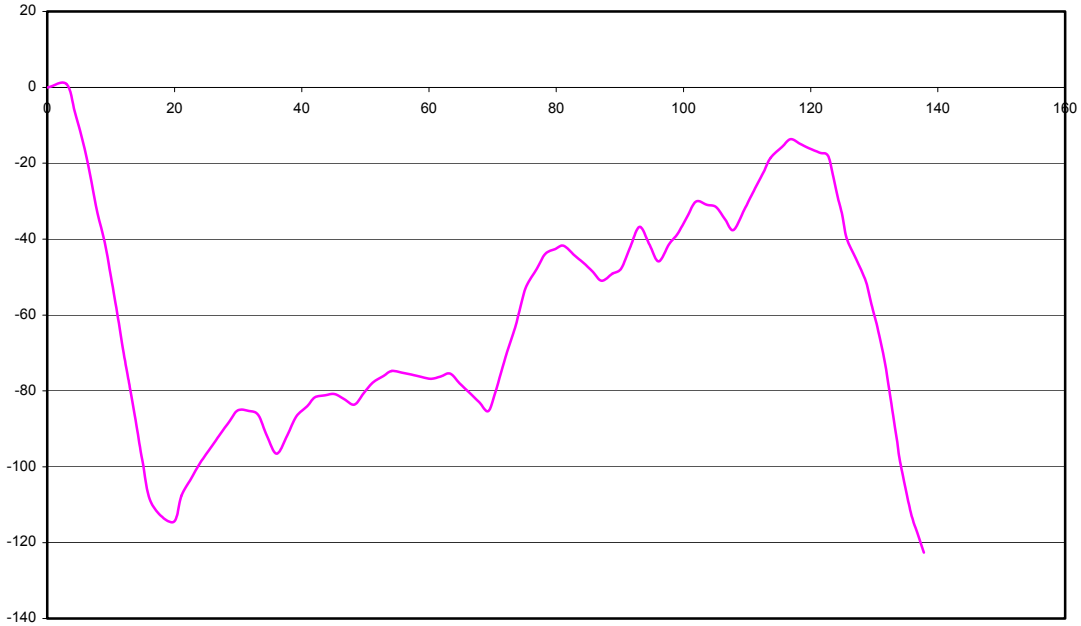

Figure B.11. Smoothed $\delta^{18}O$ planktonic foraminifera record of Core RC17-177 modified from Shackleton (1987, fig. 2 solid line), with ordinate depth in meters below present mean sea level and abscissa the time in Ka BP.

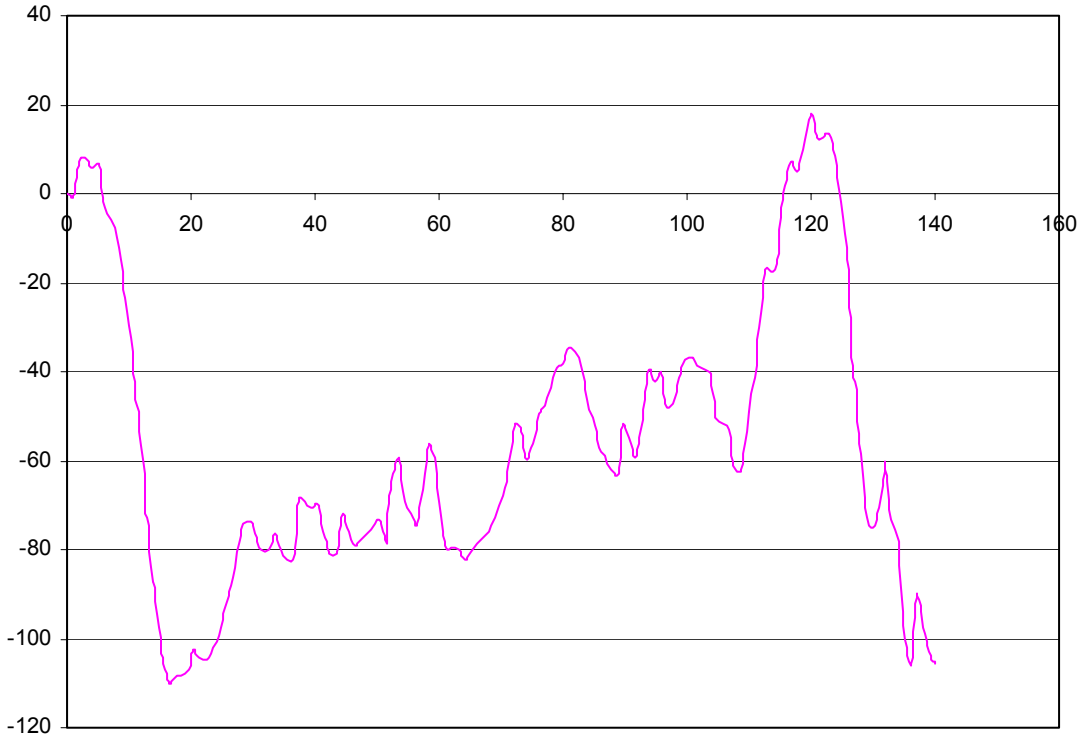

Figure B.12. Smoothed $\delta^{18}O$ benthonic foraminifera record of Core V19-30 modified from Shackleton (1987, fig. 1 solid line), with ordinate depth in meters below present mean sea level and abscissa the time in Ka BP.

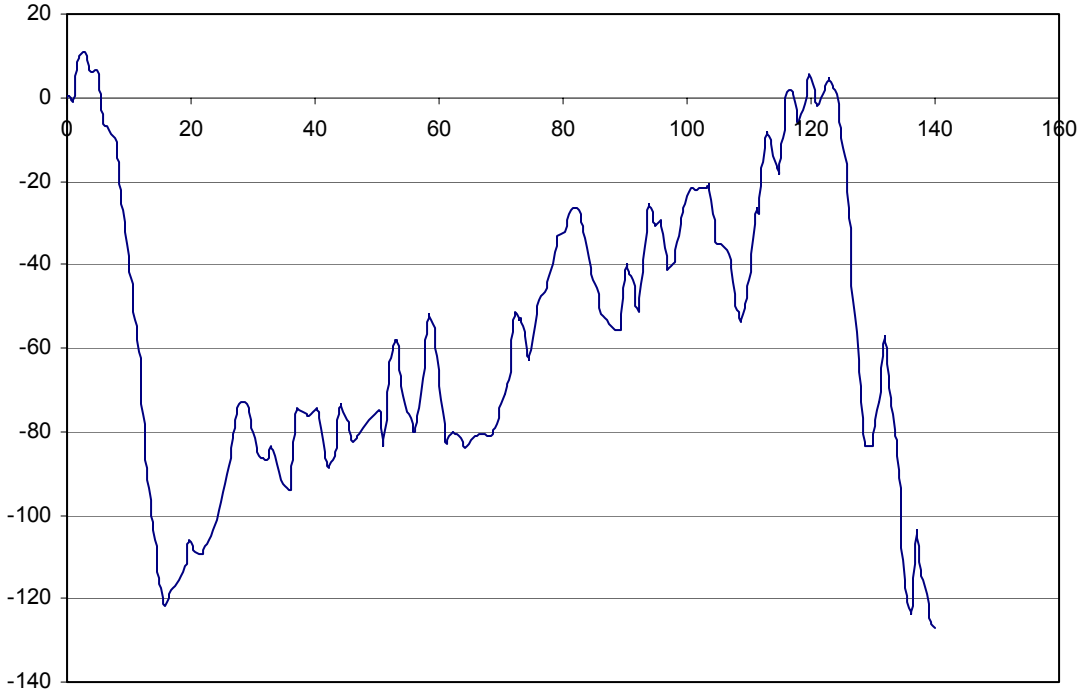

Figure B.13. $\delta^{18}O$ planktonic and benthonic foraminifera data from Cores RC17-177 and V19-30, respectively, modified from Shackleton (1987, fig. 5 solid line), with ordinate depth in meters below present mean sea level and abscissa the time in Ka BP.

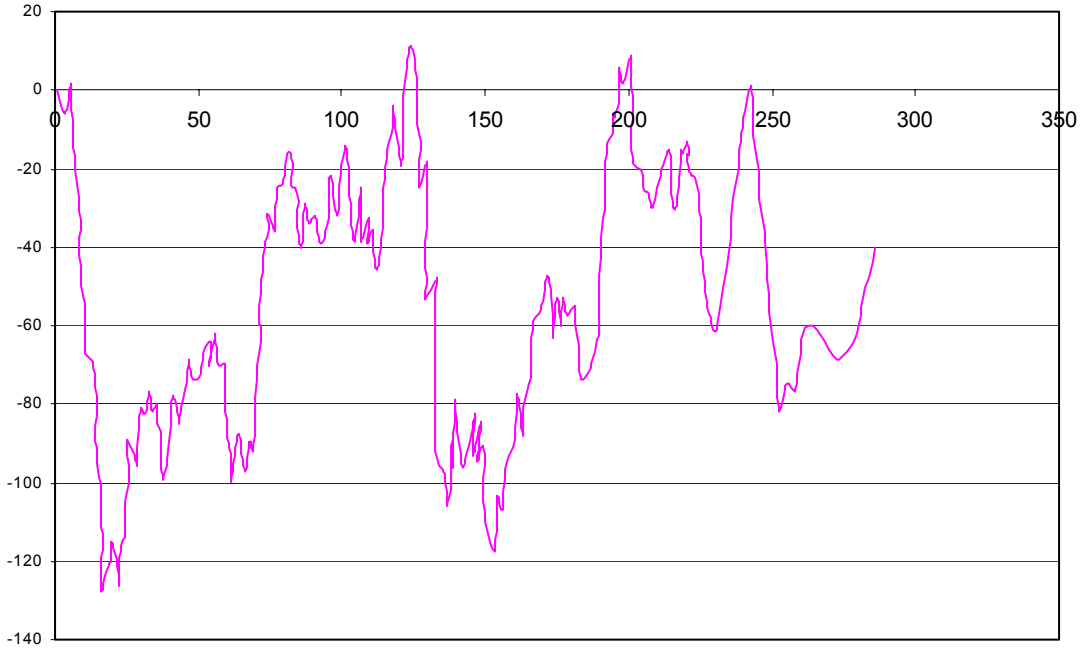

Figure B.14. $\delta^{18}O$ benthonic foraminifera data from Atlantic Core V30-40 modified from Imbrie et. al. (1984, fig. 6), with ordinate depth in meters below present mean sea level and abscissa the time in Ka BP.

APPENDIX C

Each of the 12 sea level height (elevation) figures (Appendix B) used in this study were summed over 2 m, 3 m and 4 m intervals, respectively. The smoothing analysis provided distributions of sea level duration per depth below present mean sea level. The sea level duration distribution figures included in this appendix are as follows: Core DSDP 502b (Fig. C.1 to C.3) modified from Imbrie *et. al.* (1984), SPECMAP (Fig. C.4 to C.6) modified from Imbrie *et. al.* (1984), Core V28-238 (Fig. C.7 to C.9) modified from Dia *et. al.* (1992), modified seawater curve (C.10 to C.12) from Labeyrie *et. al.* (1987), Huon Province and Core V19-30 (C.13 to C.15) modified from Chappell and Shackleton (1986), Haiti corals and Core Meteor 12392 (C.16 to C.18) modified from Dodge *et. al.* (1983), Haiti corals and Core V19-29 (C.18 to C.21) modified from Dodge *et. al.* (1983), New Guinea terraces (C.22 to C.24) modified from Shackleton (1987), Core RC17-177 (C.25 to C.27) modified from Shackleton (1987), Core V19-30 (C.28 to C.30) modified from Shackleton (1987), Stacked curve of Cores RC17-177 and V19-30 (C.31 to C.33) modified from Shackleton (1987) and Core V30-40 (C.34 to C.36) modified from Imbrie *et. al.* (1984). The smoothing analysis was undertaken to allow direct calculations of the correlations coefficient for each of the various intervals of the smoothed sea level duration figures with the passage length distribution figures of Appendix D.

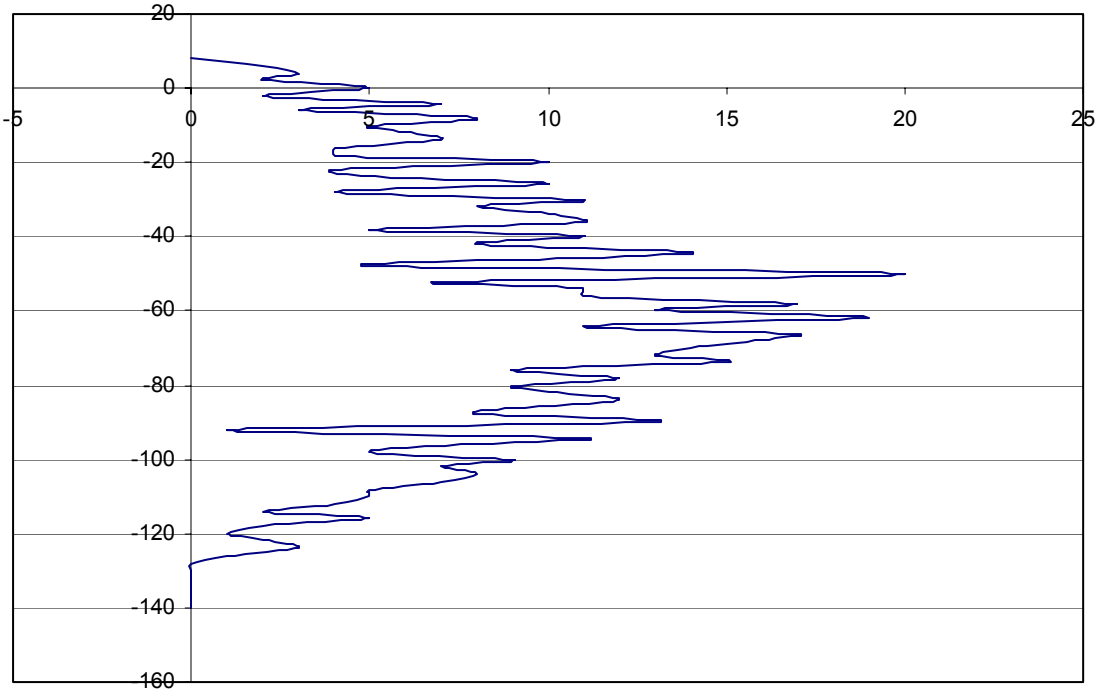

Figure C.1. $\delta^{18}O$ record of Core DSDP 502b sea level elevation duration distribution summed over a 2 m interval with ordinate depth in meters relative to present mean sea level and abscissa an arbitrary duration magnitude.

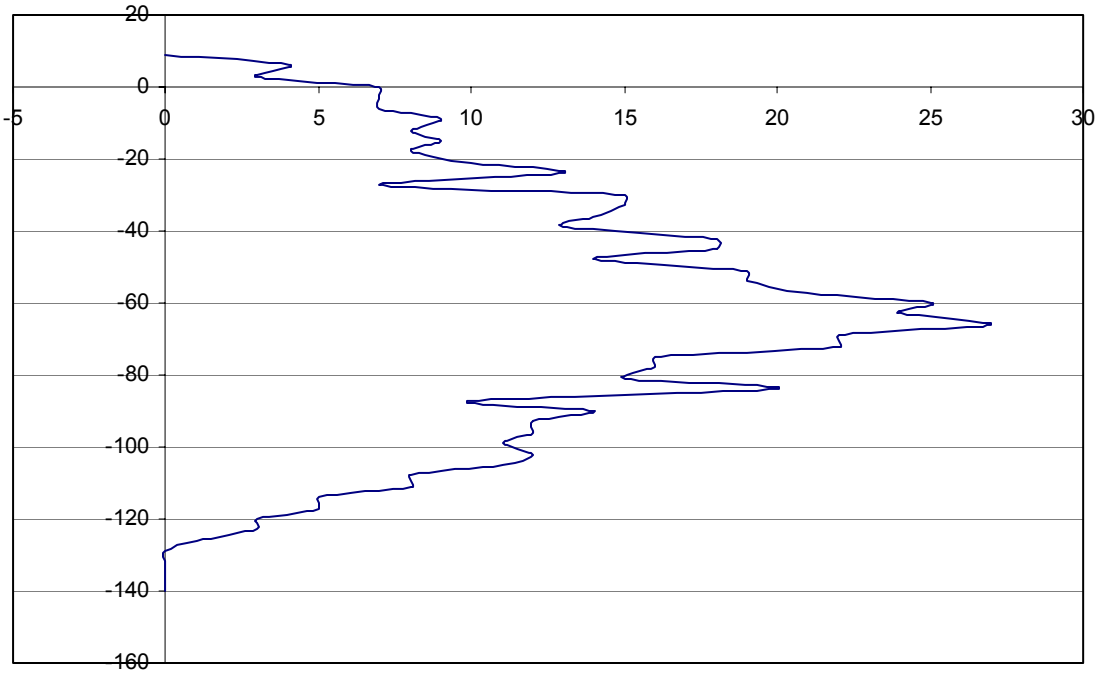

Figure C.2. $\delta^{18}O$ record of Core DSDP 502b sea level elevation duration distribution summed over a 3 m interval with ordinate depth in meters relative to present mean sea level and abscissa an arbitrary duration magnitude.

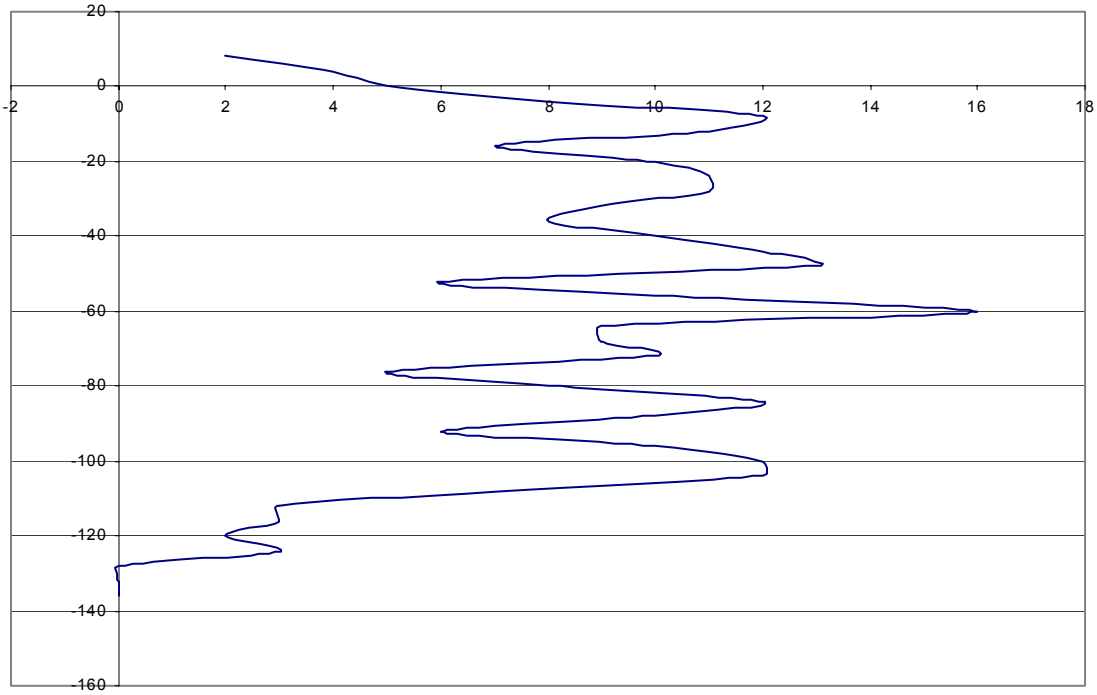

Figure C.3. $\delta^{18}O$ record of Core DSDP 502b sea level elevation duration distribution summed over a 4 m interval with ordinate depth in meters relative to present mean sea level and abscissa an arbitrary duration magnitude.

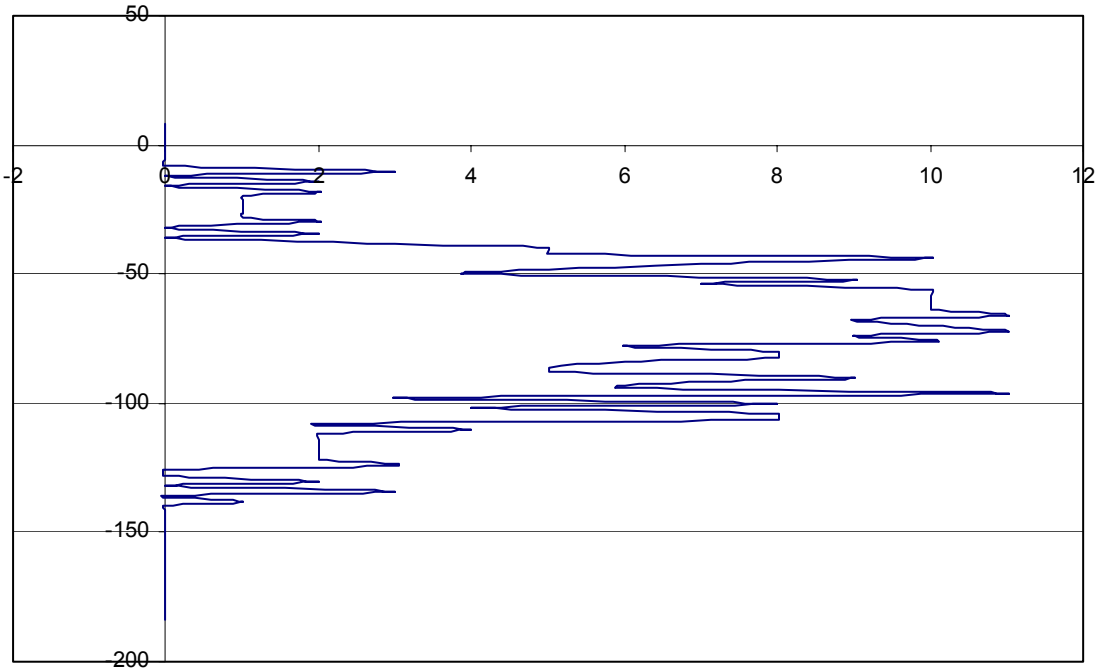

Figure C.4. $\delta^{18}O$ variation of smoothed stack SPECMAP sea level elevation duration distribution summed over a 2 m interval with ordinate depth in meters relative to present mean sea level and abscissa an arbitrary duration magnitude.

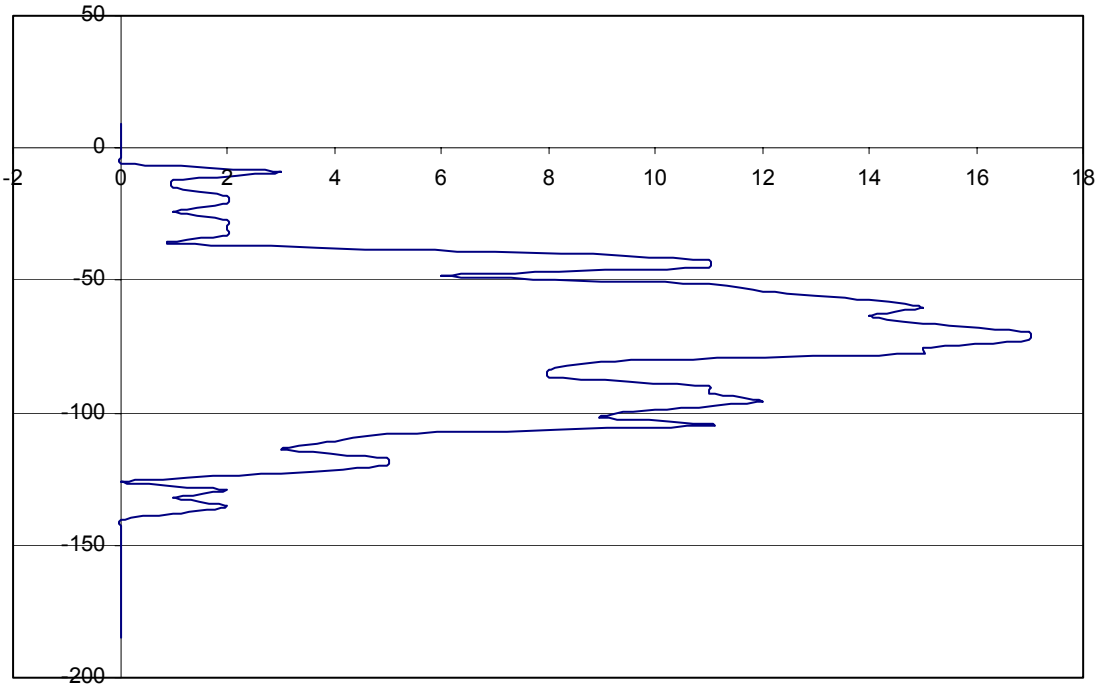

Figure C.5. $\delta^{18}O$ variation of smoothed stack SPECMAP sea level elevation duration distribution summed over a 3 m interval with ordinate depth in meters relative to present mean sea level and abscissa an arbitrary duration magnitude.

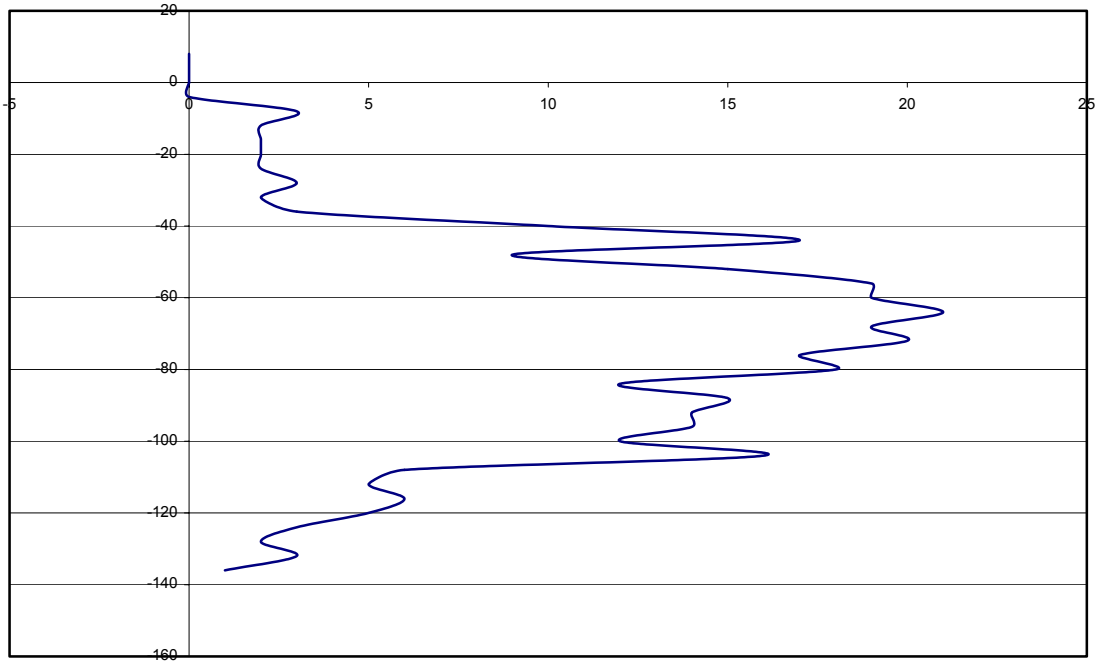

Figure C.6. $\delta^{18}O$ variation of smoothed stack SPECMAP sea level elevation duration distribution summed over a 4 m interval with ordinate depth in meters relative to present mean sea level and abscissa an arbitrary duration magnitude.

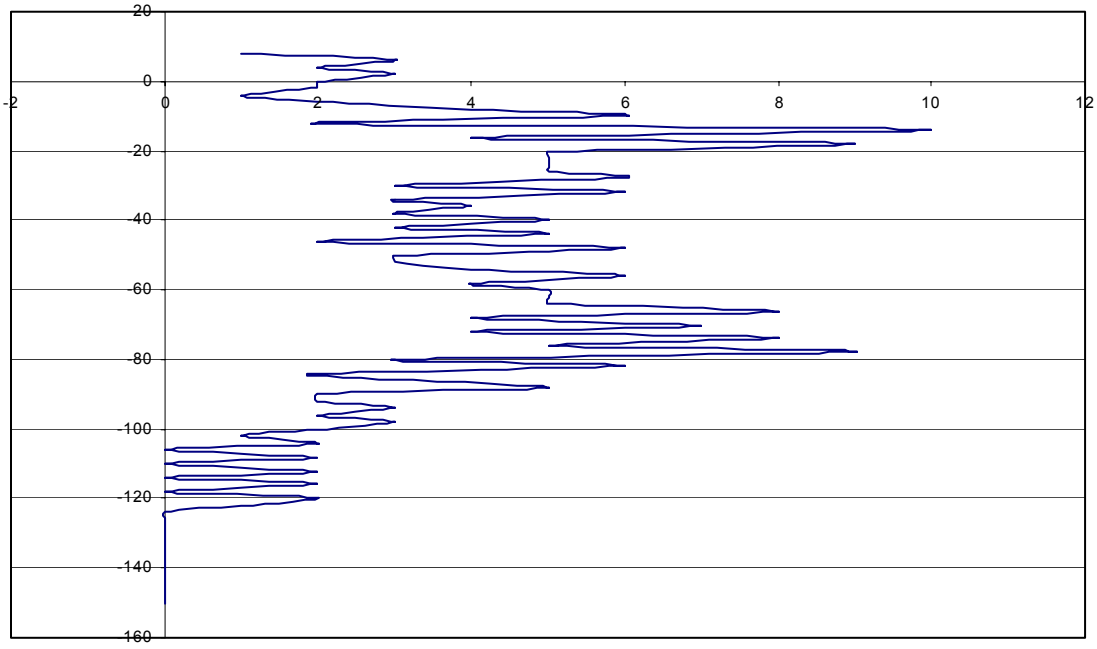

Figure C.7. Benthonic $\delta^{18}O$ from Core V28-238 sea level elevation duration distribution summed over a 2 m interval with ordinate depth in meters relative to present mean sea level and abscissa an arbitrary duration magnitude.

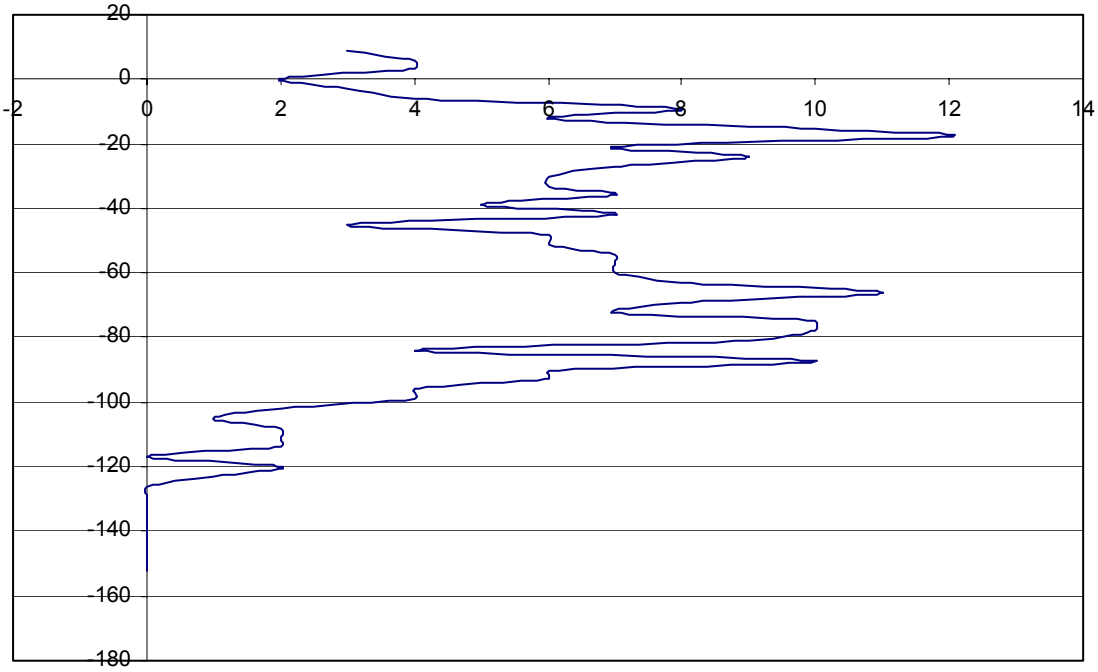

Figure C.8. Benthonic $\delta^{18}O$ from Core V28-238 sea level elevation duration distribution summed over a 3 m interval with ordinate depth in meters relative to present mean sea level and abscissa an arbitrary duration magnitude.

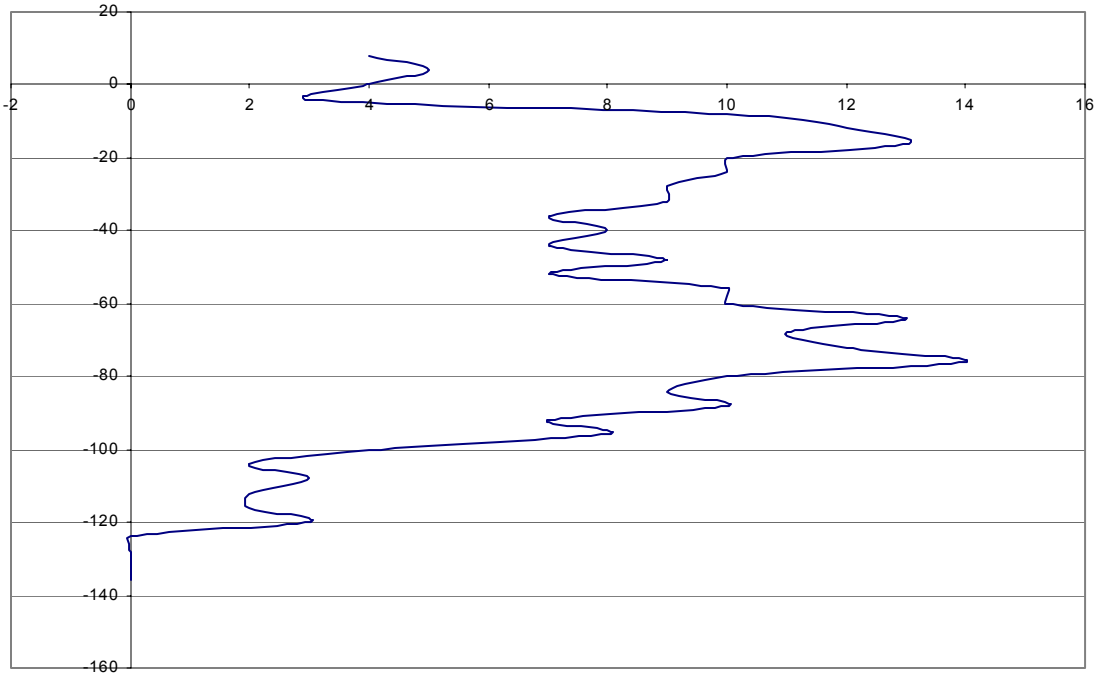

Figure C.9. Benthonic $\delta^{18}O$ from Core V28-238 sea level elevation duration distribution summed over a 4 m interval with ordinate depth in meters relative to present mean sea level and abscissa an arbitrary duration magnitude.

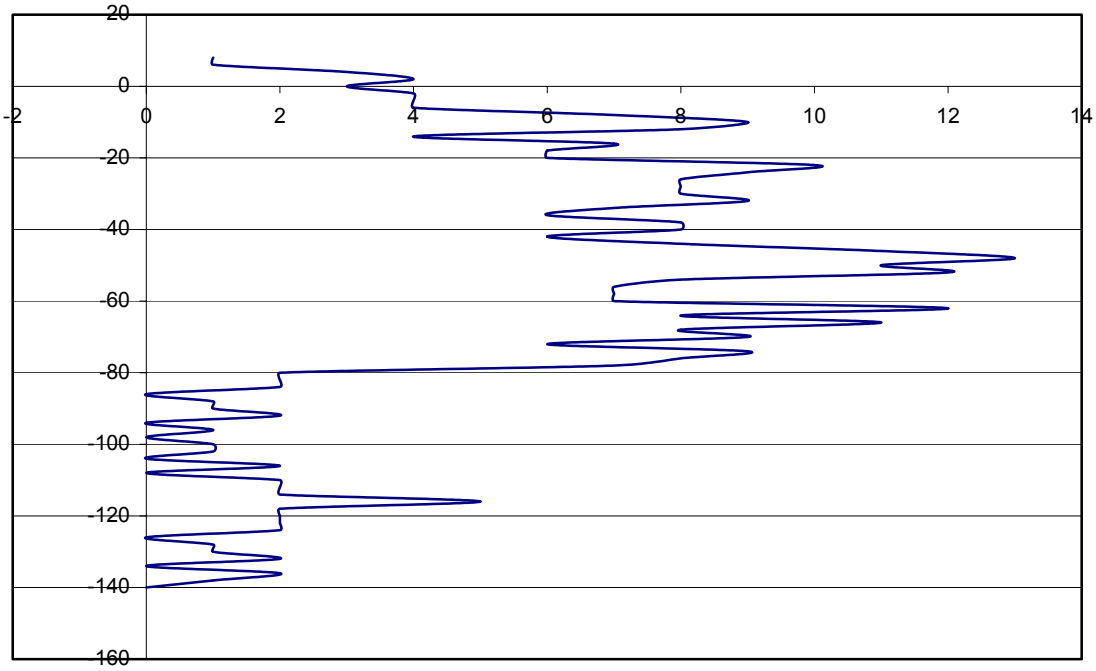

Figure C.10. Normalized $\delta^{18}O$ mean seawater curve of Labeyrie *et. al.* (1987) sea level elevation duration distribution summed over a 2 m interval with ordinate depth in meters relative to present mean sea level and abscissa an arbitrary duration magnitude.

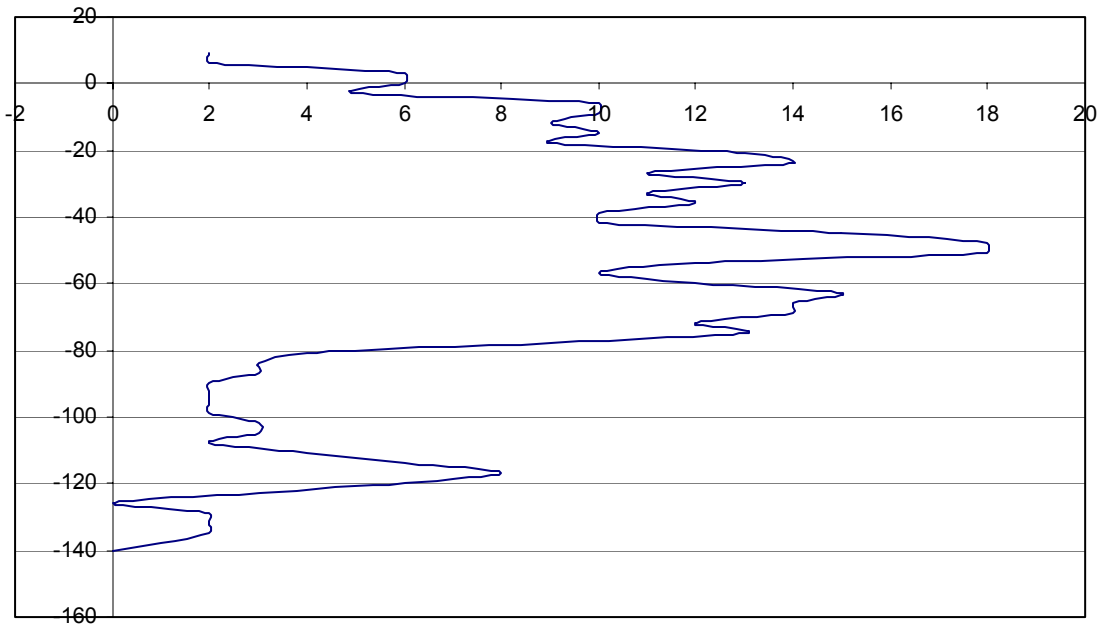

Figure C.11. Normalized $\delta^{18}O$ mean seawater curve of Labeyrie *et. al.* (1987) sea level elevation duration distribution summed over a 3 m interval with ordinate depth in meters relative to present mean sea level and abscissa an arbitrary duration magnitude.

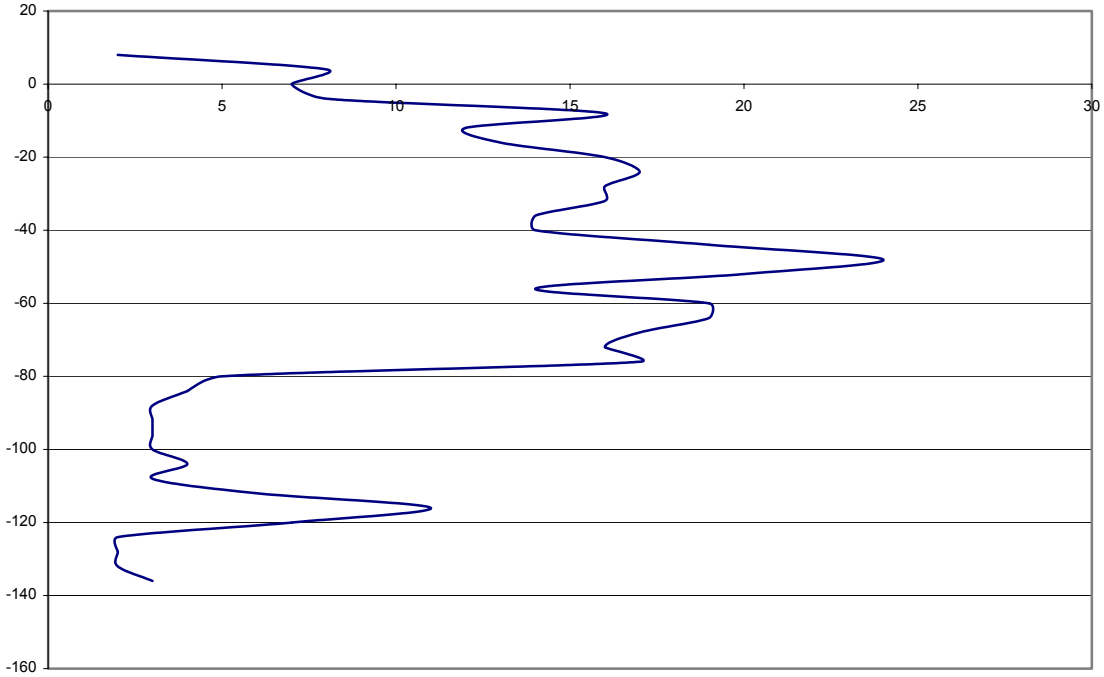

Figure C.12. Normalized $\delta^{18}O$ mean seawater curve of Labeyrie *et. al.* (1987) sea level elevation duration distribution summed over a 4 m interval with ordinate depth in meters relative to present mean sea level and abscissa an arbitrary duration magnitude.

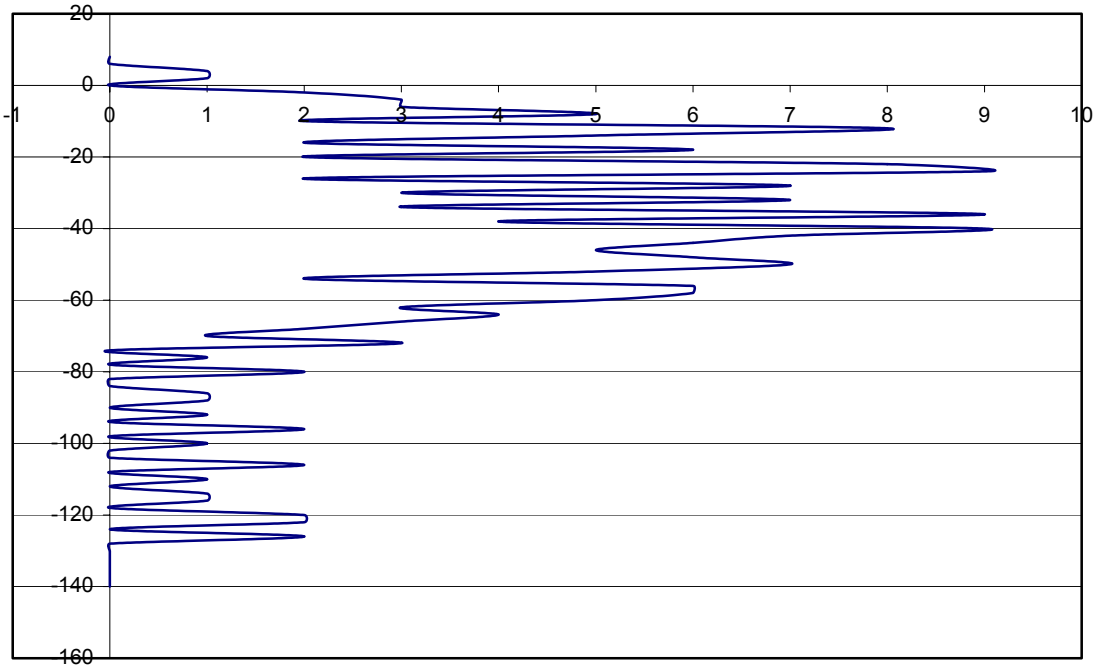

Figure C.13. Huon Province raised coral terraces recalculated with $\delta^{18}O$ foraminifera from Core V19-30 sea level elevation duration distribution summed over a 2 m interval with ordinate depth in meters relative to present mean sea level and abscissa an arbitrary duration magnitude.

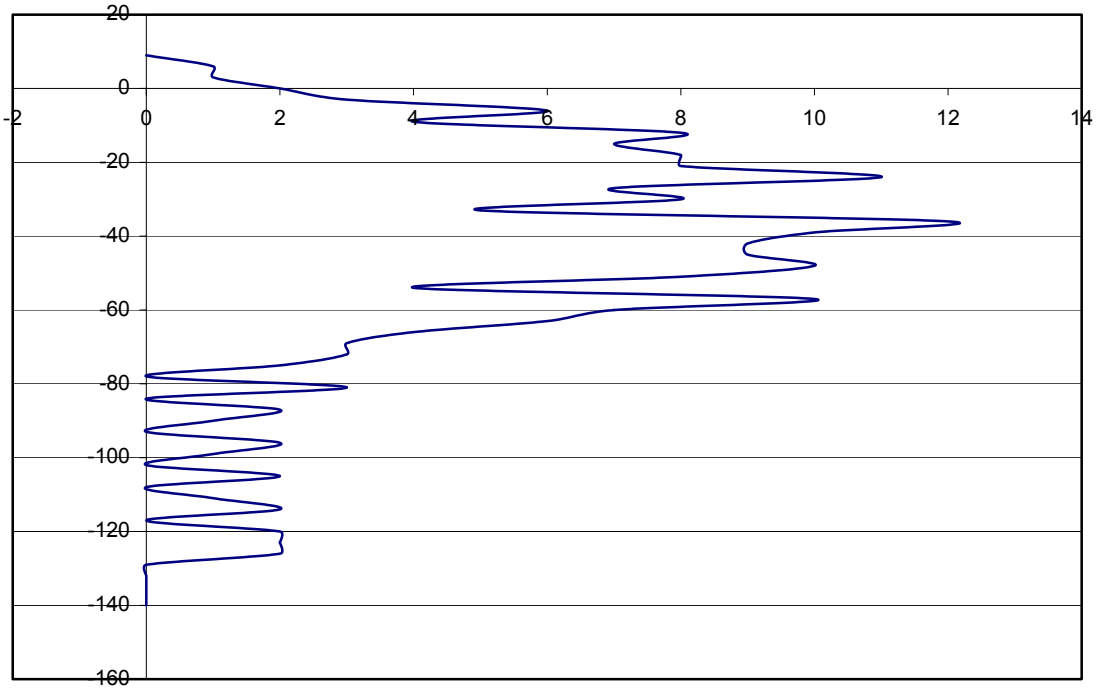

Figure C.14. Huon Province raised coral terraces recalculated with $\delta^{18}O$ foraminifera from Core V19-30 sea level elevation duration distribution summed over a 3 m interval with ordinate depth in meters relative to present mean sea level and abscissa an arbitrary duration magnitude.

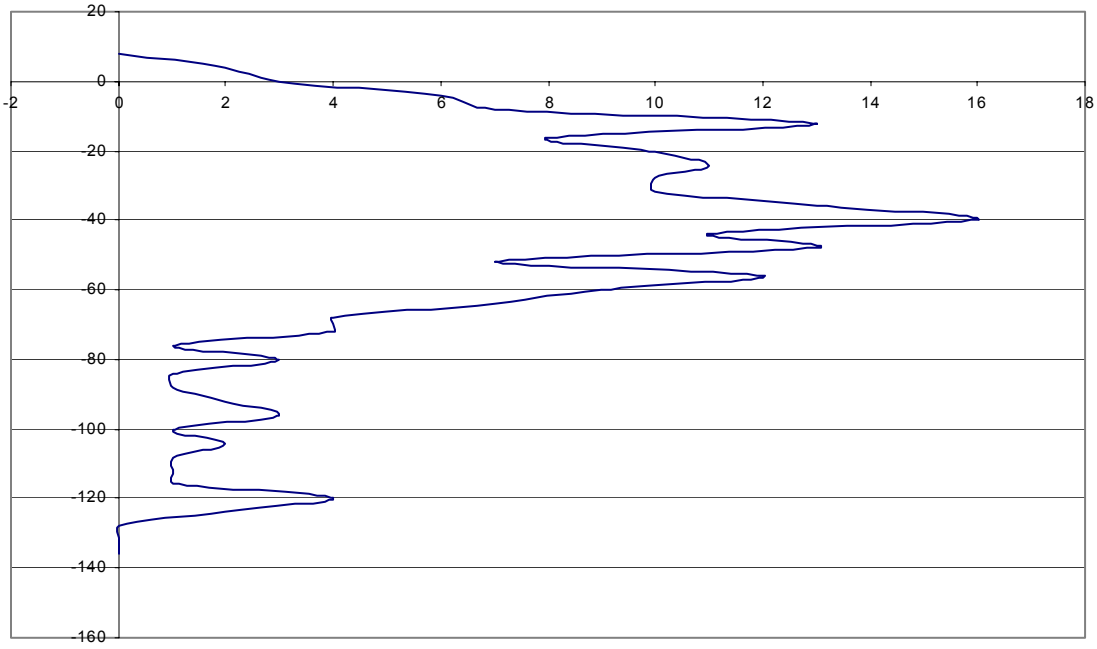

Figure C.15. Huon Province raised coral terraces recalculated with $\delta^{18}O$ foraminifera from Core V19-30 sea level elevation duration distribution summed over a 4 m interval with ordinate depth in meters relative to present mean sea level and abscissa an arbitrary duration magnitude.

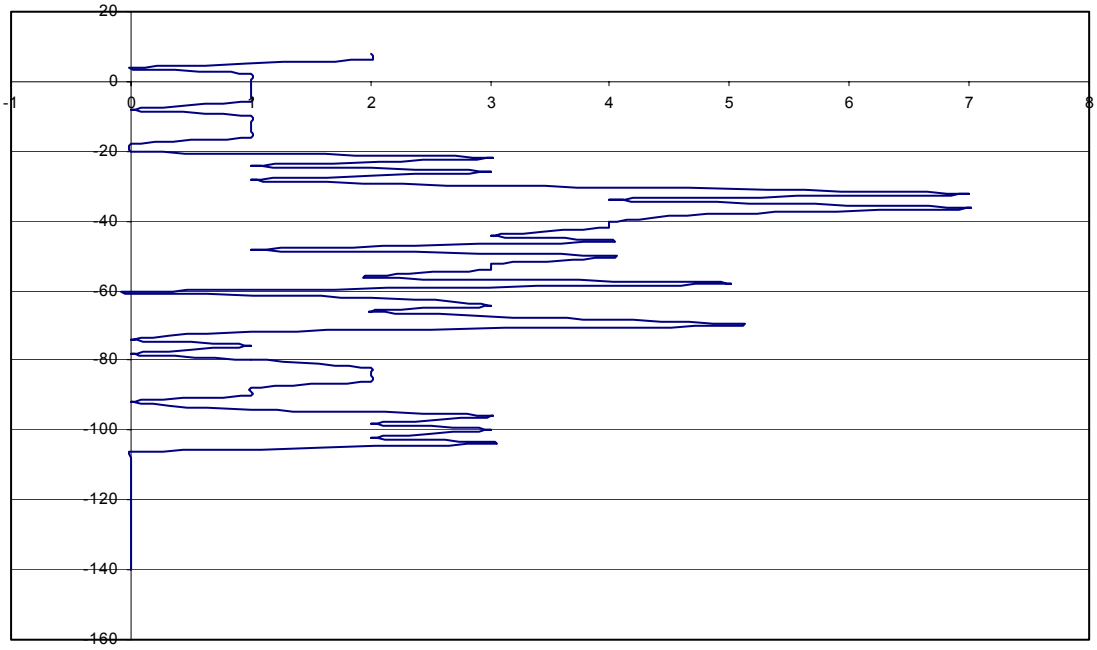

Figure C.16. Haiti raised coral terraces corresponding to U/Th ages in Barbados and $\delta^{18}O$ benthic foraminifera record of Core Meteor 12392 sea level elevation duration distribution summed over a 2 m interval with ordinate depth in meters relative to present mean sea level and abscissa an arbitrary duration magnitude.

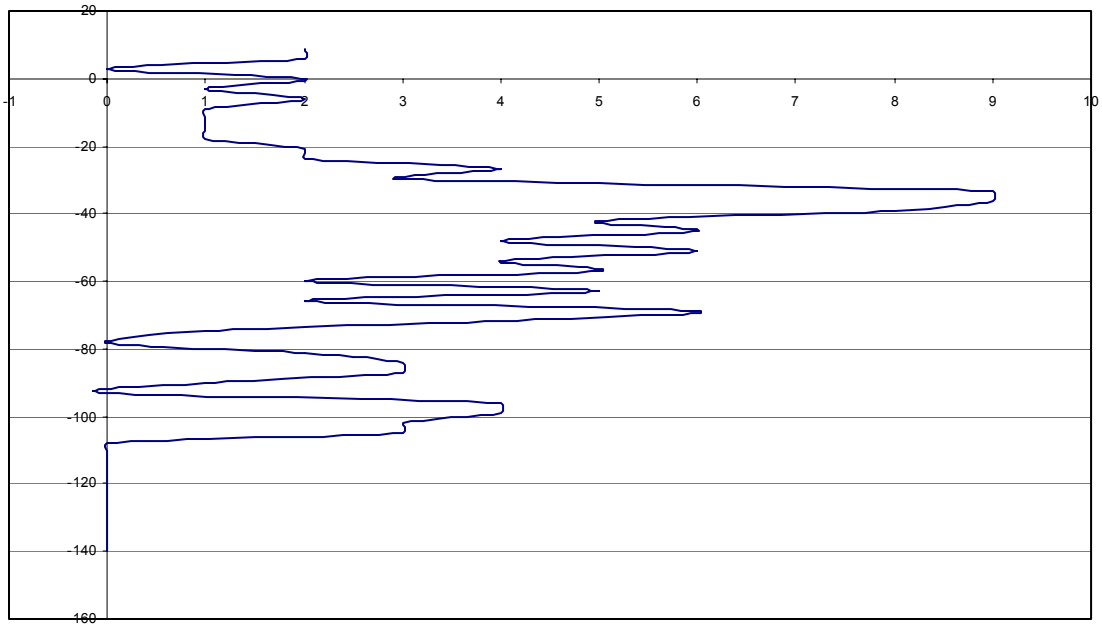

Figure C.17. Haiti raised coral terraces corresponding to U/Th ages in Barbados and $\delta^{18}O$ benthic foraminifera record of Core Meteor 12392 sea level elevation duration distribution summed over a 3 m interval with ordinate depth in meters relative to present mean sea level and abscissa an arbitrary duration magnitude.

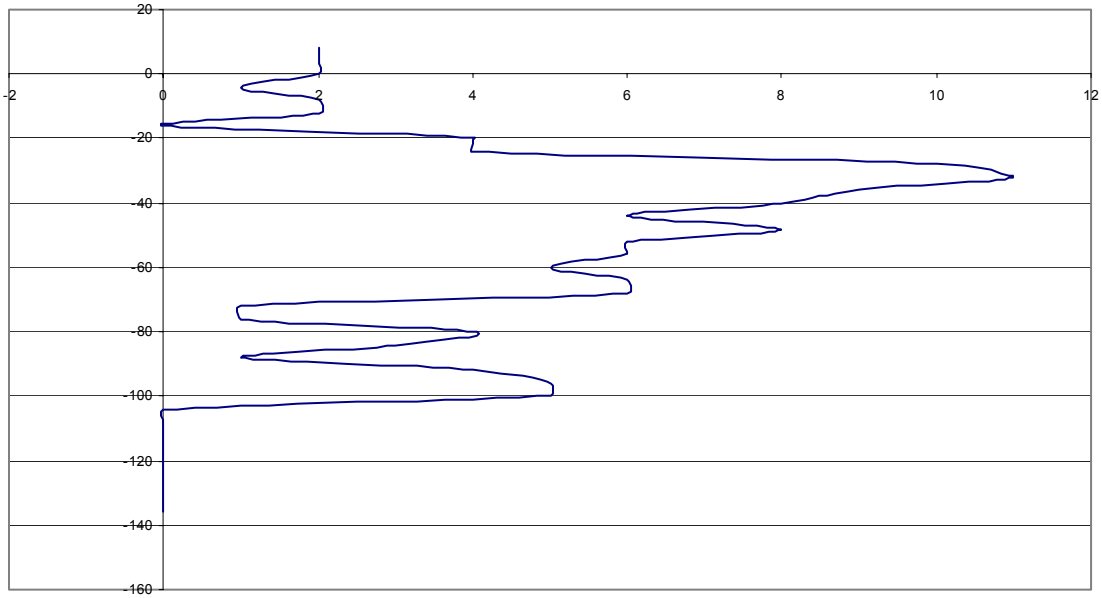

Figure C.18. Haiti raised coral terraces corresponding to U/Th ages in Barbados and $\delta^{18}O$ benthic foraminifera record of Core Meteor 12392 sea level elevation duration distribution summed over a 4 m interval with ordinate depth in meters relative to present mean sea level and abscissa an arbitrary duration magnitude.

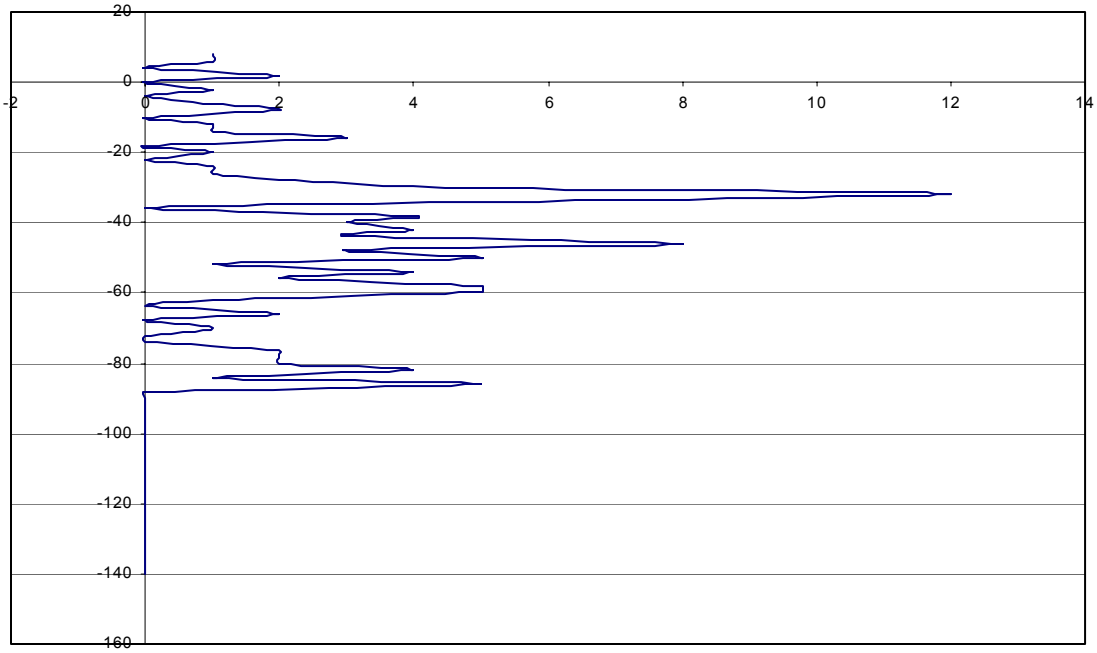

Figure C.19. Haiti raised coral terraces corresponding to U/Th ages in Barbados and $\delta^{18}O$ benthic foraminifera record of Core V19-29 sea level elevation duration distribution summed over a 2 m interval with ordinate depth in meters relative to present mean sea level and abscissa an arbitrary duration magnitude.

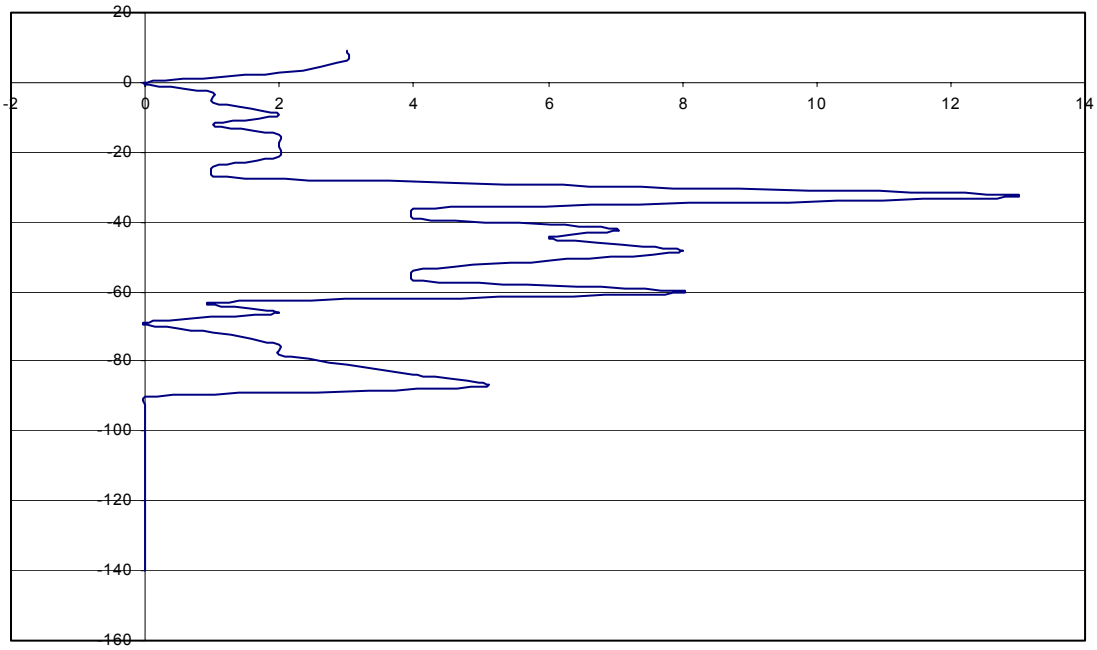

Figure C.20. Haiti raised coral terraces corresponding to U/Th ages in Barbados and $\delta^{18}O$ benthic foraminifera record of Core V19-29 sea level elevation duration distribution summed over a 3 m interval with ordinate depth in meters relative to present mean sea level and abscissa an arbitrary duration magnitude.

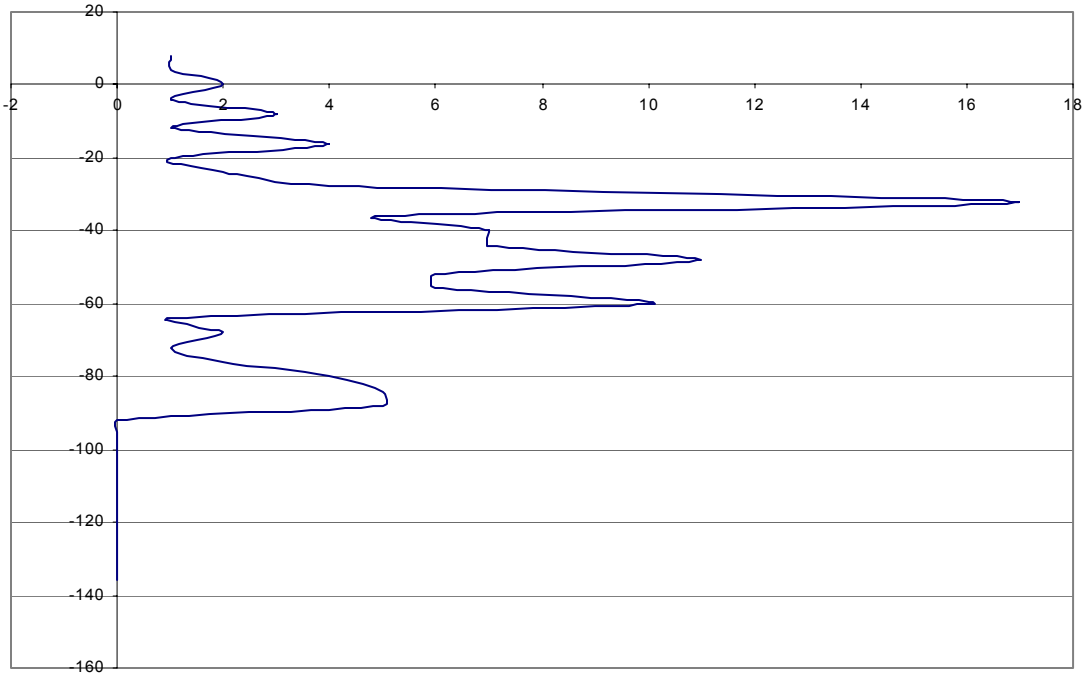

Figure C.21. Haiti raised coral terraces corresponding to U/Th ages in Barbados and $\delta^{18}O$ benthic foraminifera record of Core V19-29 sea level elevation duration distribution summed over a 4 m interval with ordinate depth in meters relative to present mean sea level and abscissa an arbitrary duration magnitude.

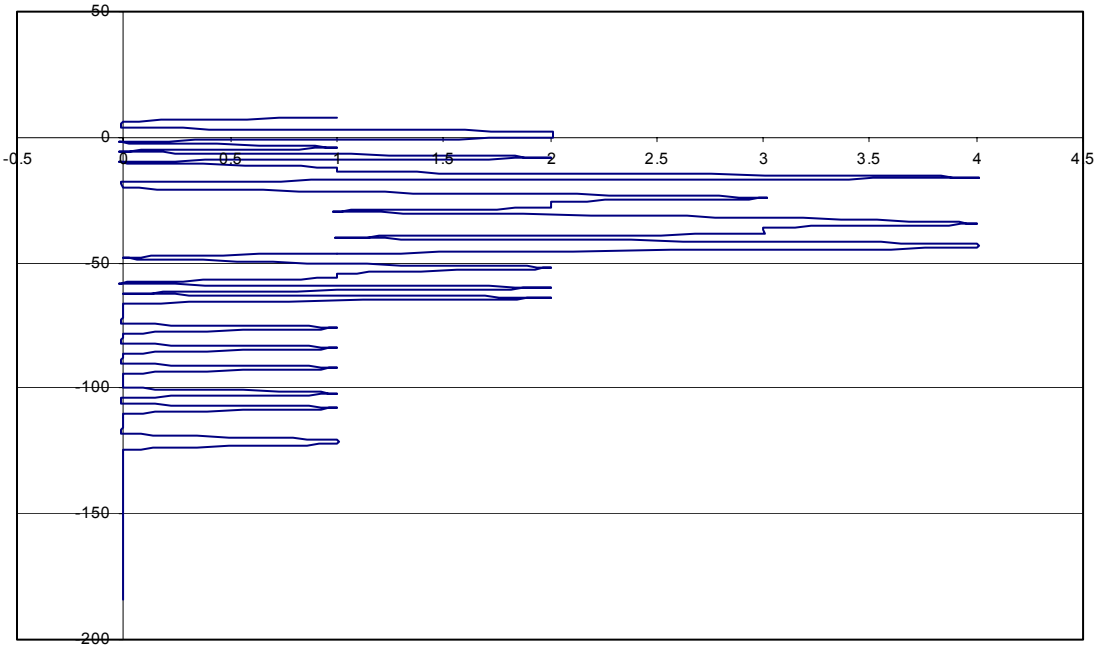

Figure C.22. Second approximation of sea level estimated from New Guinea terraces modified from Shackleton (1987) sea level elevation duration distribution summed over a 2 m interval with ordinate depth in meters relative to present mean sea level and abscissa an arbitrary duration magnitude.

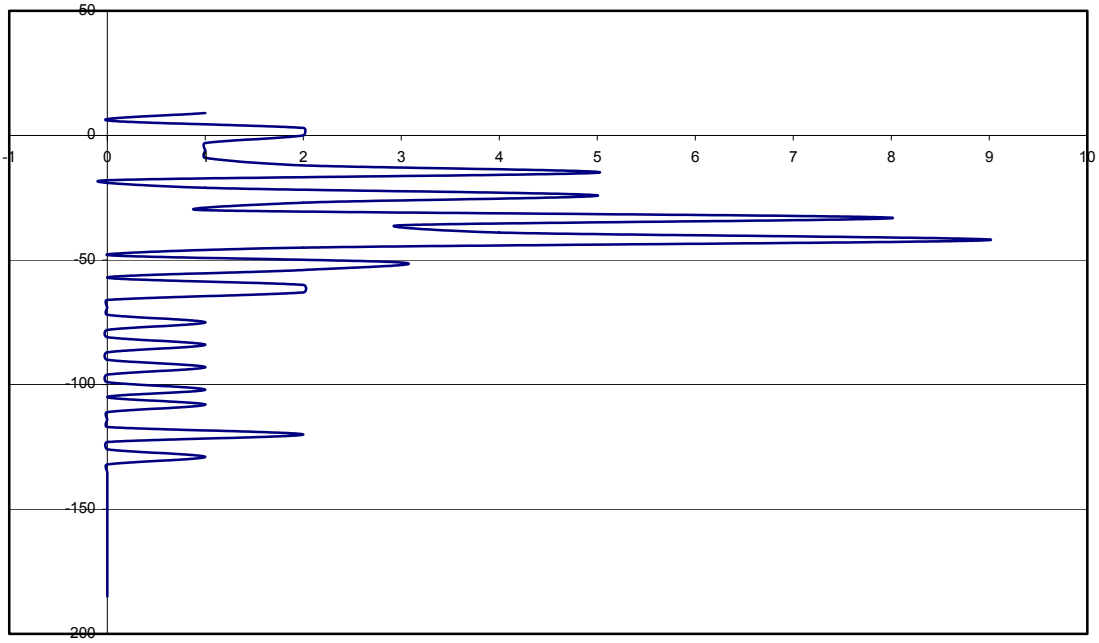

Figure C.23. Second approximation of sea level estimated from New Guinea terraces modified from Shackleton (1987) sea level elevation duration distribution summed over a 3 m interval with ordinate depth in meters relative to present mean sea level and abscissa an arbitrary duration magnitude.

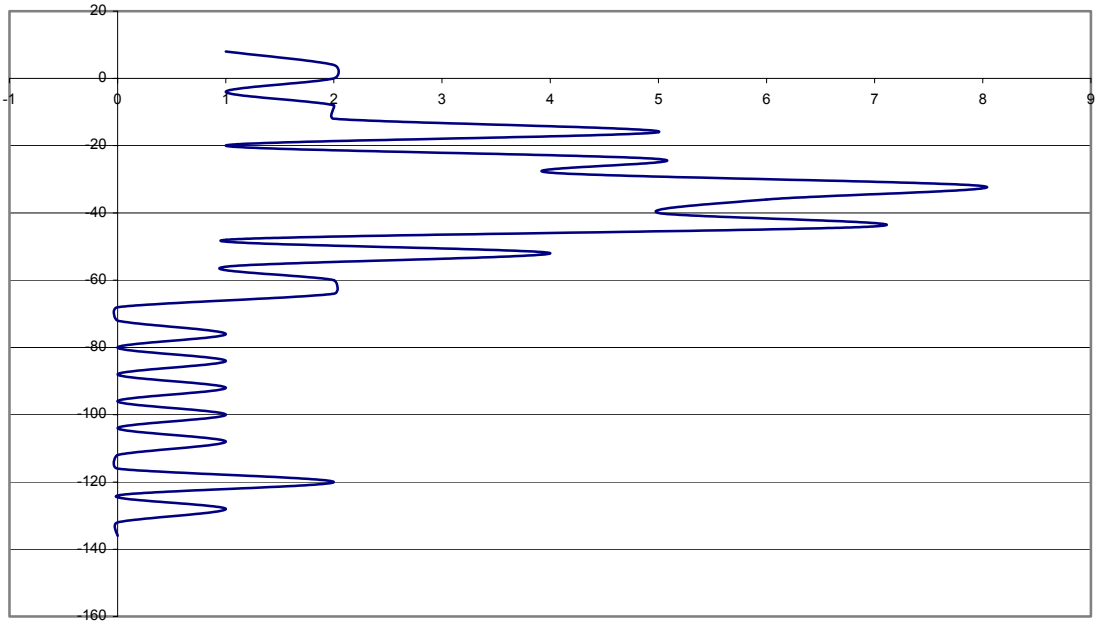

Figure C.24. Second approximation of sea level estimated from New Guinea terraces modified from Shackleton (1987) sea level elevation duration distribution summed over a 4 m interval with ordinate depth in meters relative to present mean sea level and abscissa an arbitrary duration magnitude.

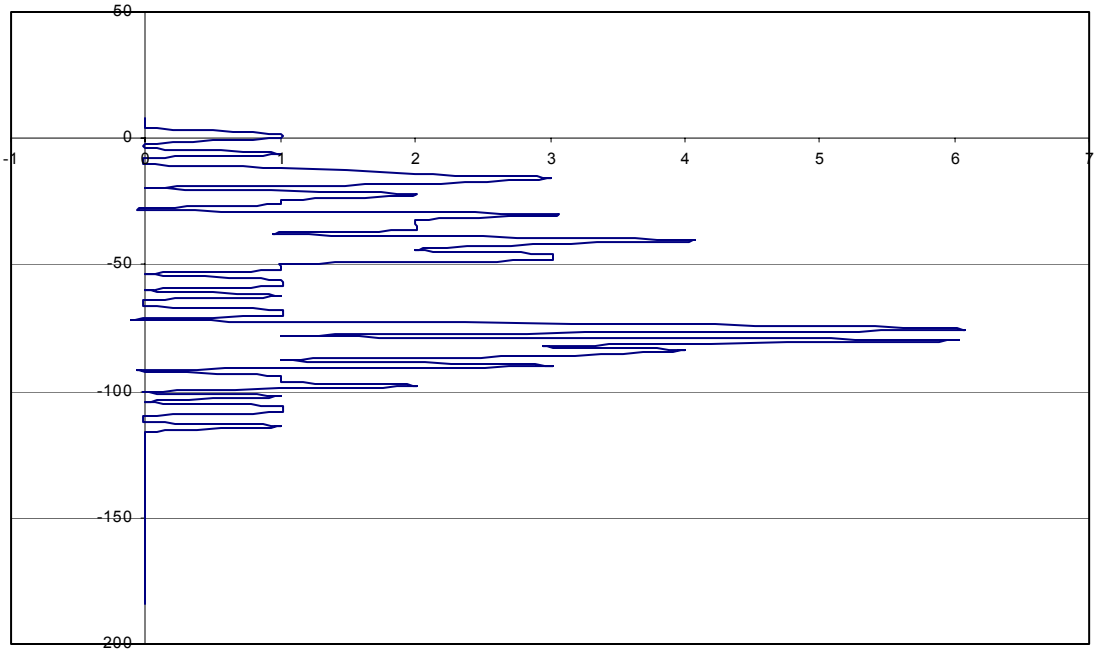

Figure C.25. Smoothed $\delta^{18}O$ planktonic foraminifera record of Core RC17-177 sea level elevation duration distribution summed over a 2 m interval with ordinate depth in meters relative to present mean sea level and abscissa an arbitrary duration magnitude.

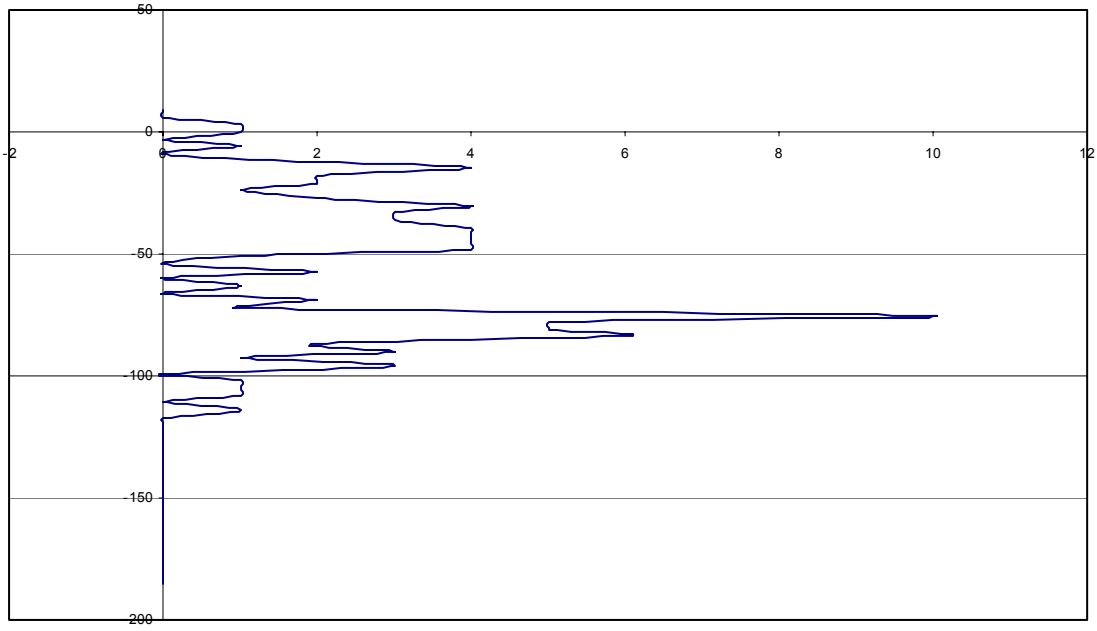

Figure C.26. Smoothed $\delta^{18}O$ planktonic foraminifera record of Core RC17-177 sea level elevation duration distribution summed over a 3 m interval with ordinate depth in meters relative to present mean sea level and abscissa an arbitrary duration magnitude.

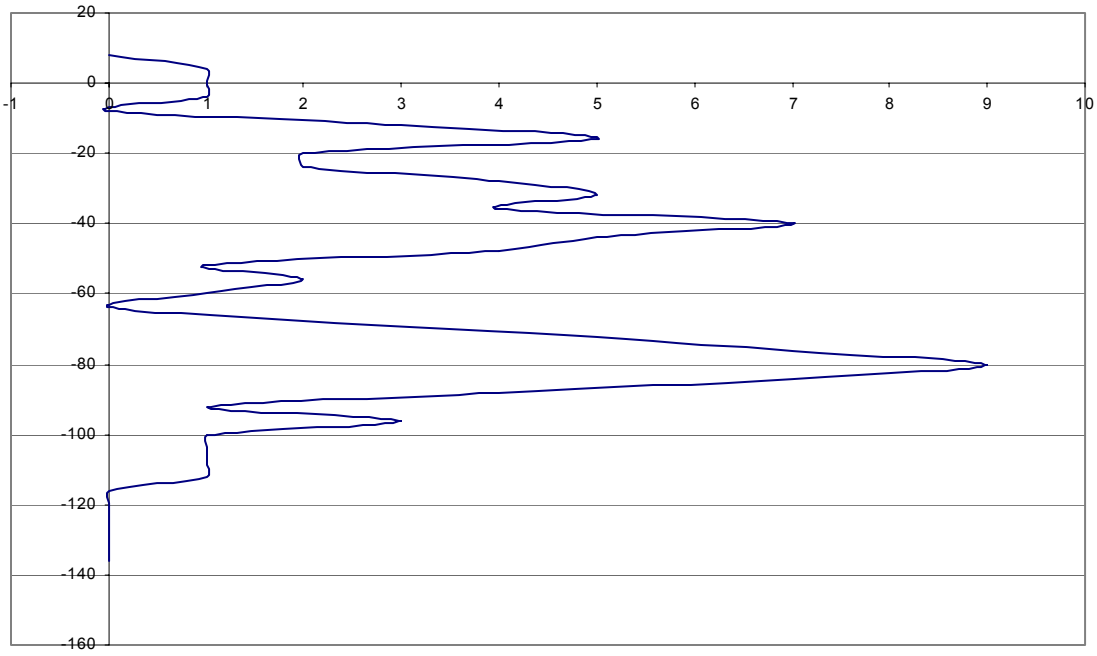

Figure C.27. Smoothed $\delta^{18}O$ planktonic foraminifera record of Core RC17-177 sea level elevation duration distribution summed over a 4 m interval with ordinate depth in meters relative to present mean sea level and abscissa an arbitrary duration magnitude.

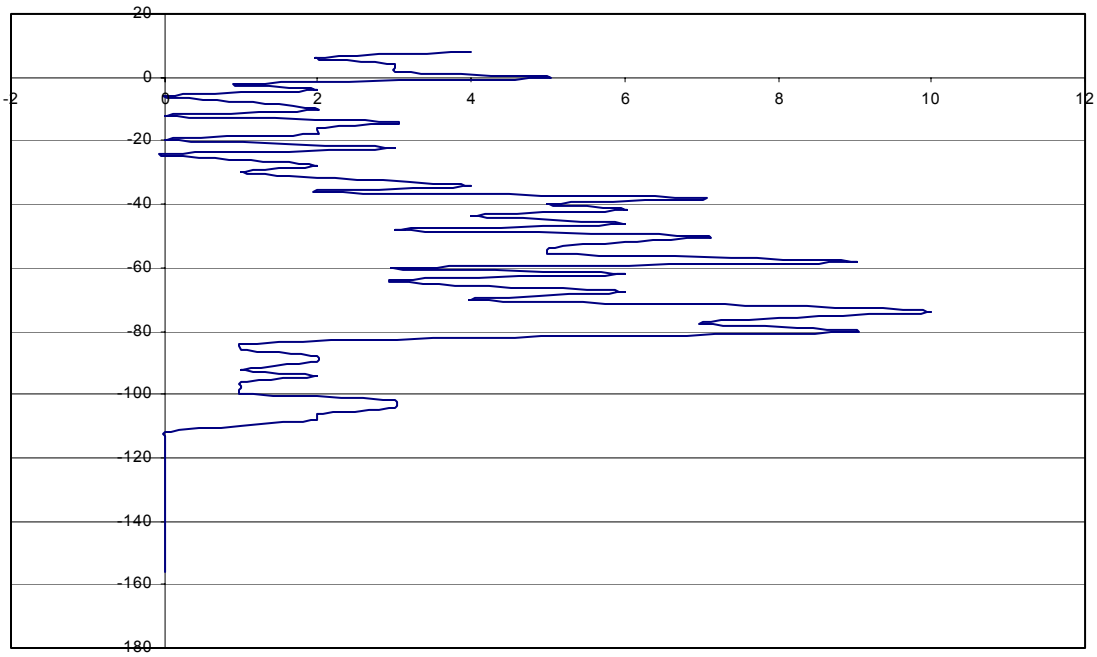

Figure C.28. Smoothed $\delta^{18}O$ benthonic foraminifera record of Core V19-30 sea level elevation duration distribution summed over a 2 m interval with ordinate depth in meters relative to present mean sea level and abscissa an arbitrary duration magnitude.

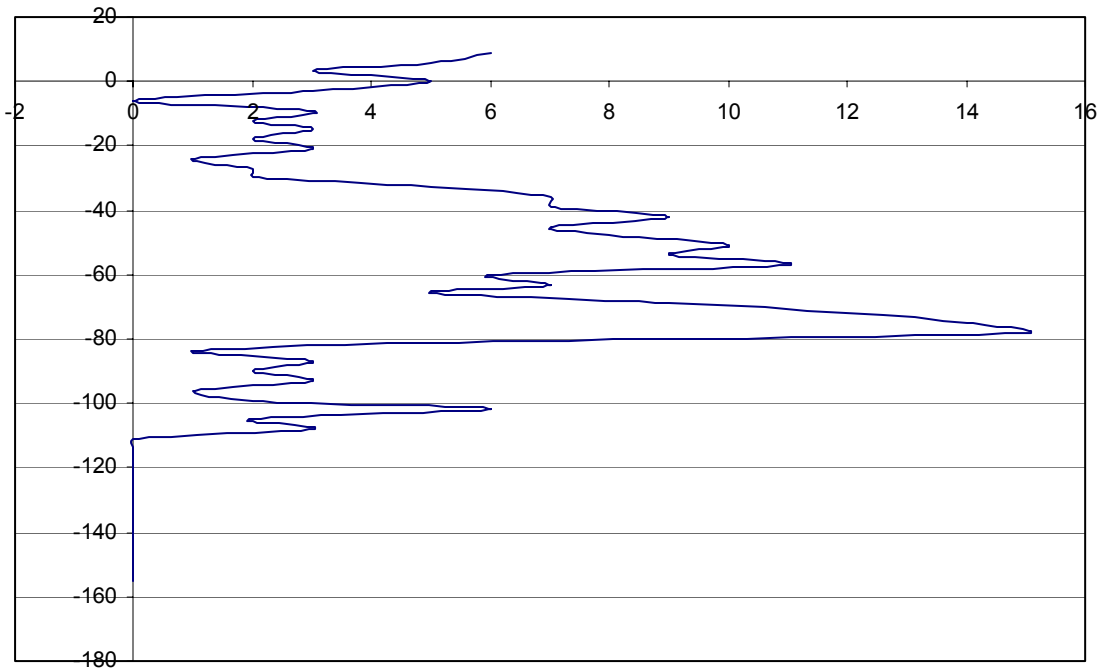

Figure C.29. Smoothed $\delta^{18}O$ benthonic foraminifera record of Core V19-30 sea level elevation duration distribution summed over a 3 m interval with ordinate depth in meters relative to present mean sea level and abscissa an arbitrary duration magnitude.

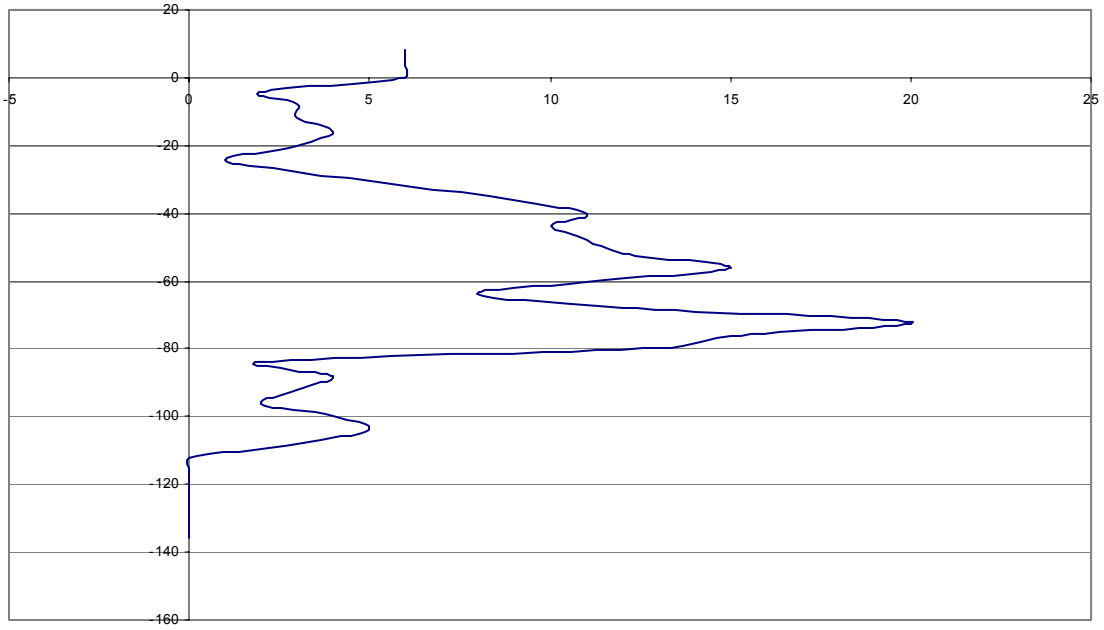

Figure C.30. Smoothed $\delta^{18}O$ benthonic foraminifera record of Core V19-30 sea level elevation duration distribution summed over a 4 m interval with ordinate depth in meters relative to present mean sea level and abscissa an arbitrary duration magnitude.

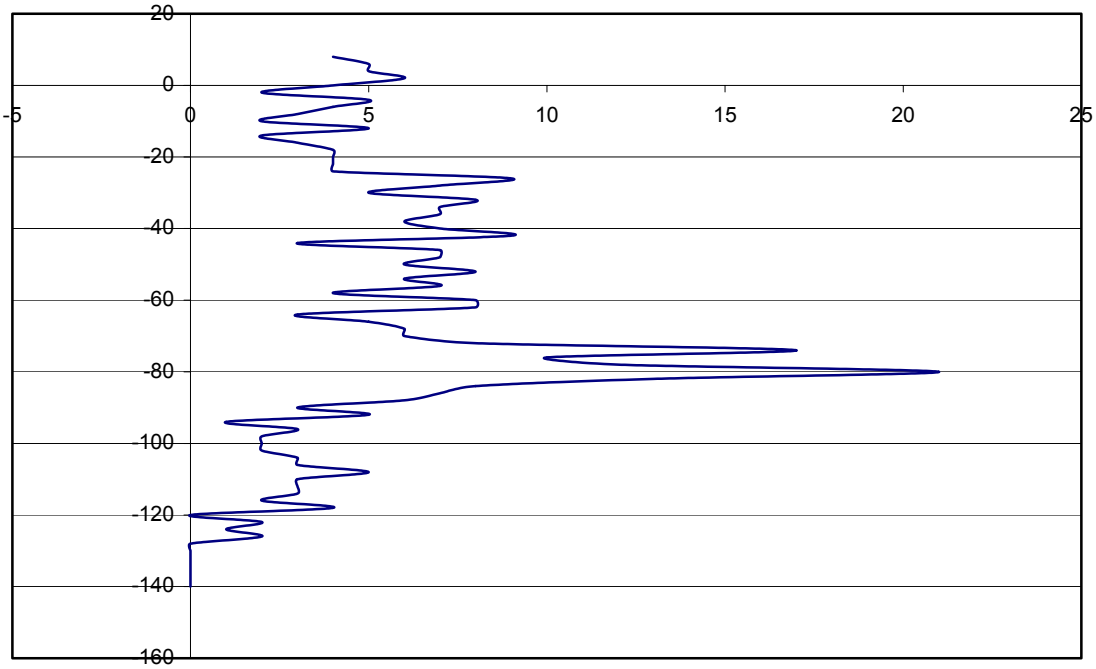

Figure C.31. $\delta^{18}O$ planktonic and benthonic foraminifera data from Cores RC17-177 and V19-30, respectively, sea level elevation duration distribution summed over a 2 m interval with ordinate depth in meters relative to present mean sea level and abscissa an arbitrary duration magnitude.

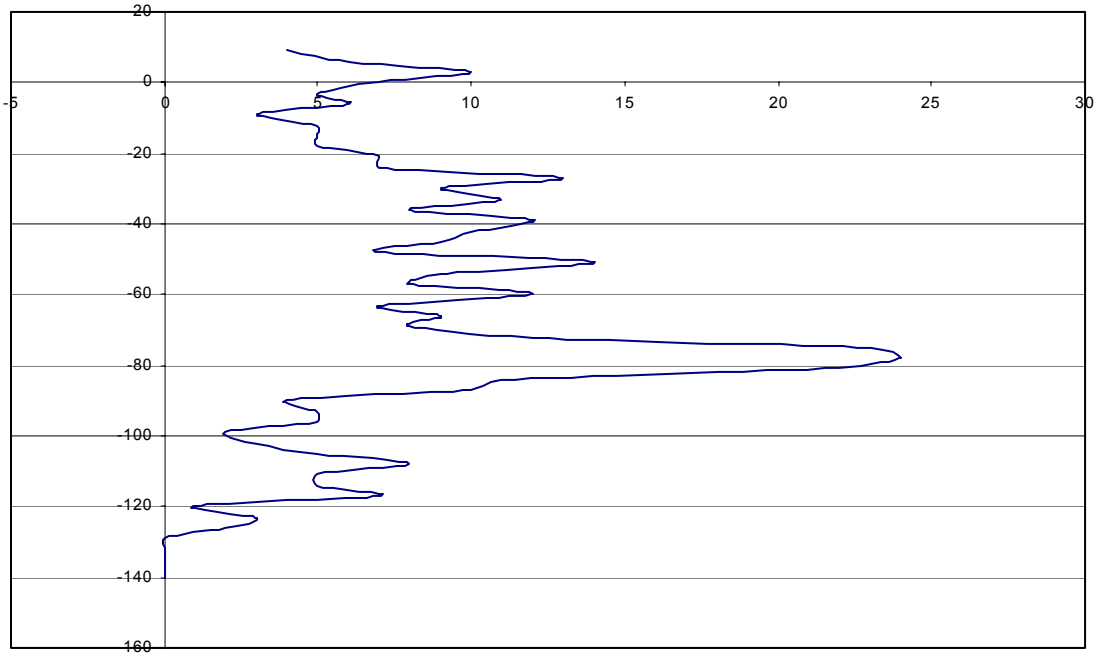

Figure C.32. $\delta^{18}O$ planktonic and benthonic foraminifera data from Cores RC17-177 and V19-30, respectively, sea level elevation duration distribution summed over a 3 m interval with ordinate depth in meters relative to present mean sea level and abscissa an arbitrary duration magnitude.

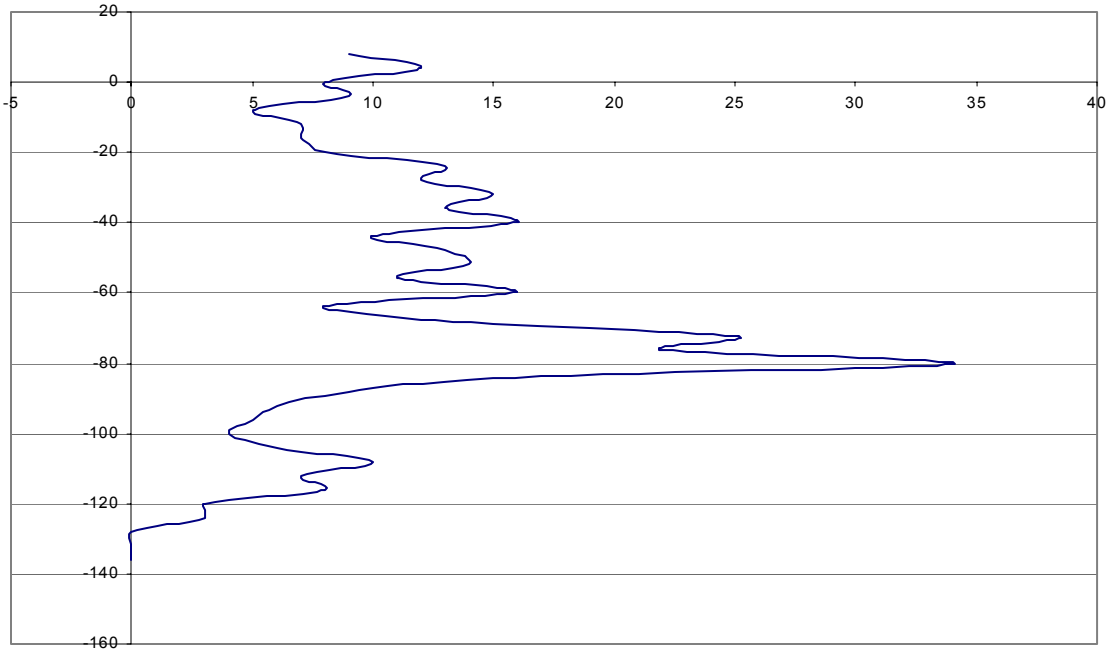

Figure C.33. $\delta^{18}O$ planktonic and benthonic foraminifera data from Cores RC17-177 and V19-30, respectively, sea level elevation duration distribution summed over a 4 m interval with ordinate depth in meters relative to present mean sea level and abscissa an arbitrary duration magnitude.

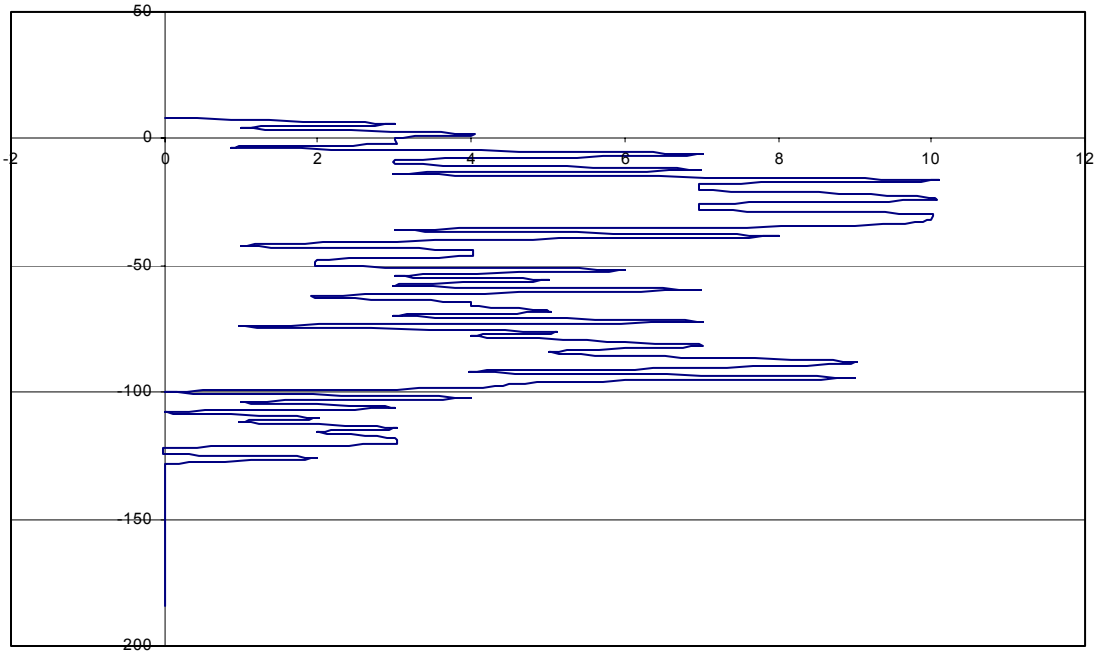

Figure C.34. $\delta^{18}O$ benthonic foraminifera data from Atlantic Core V30-40 sea level elevation duration distribution summed over a 2 m interval with ordinate depth in meters relative to present mean sea level and abscissa an arbitrary duration magnitude.

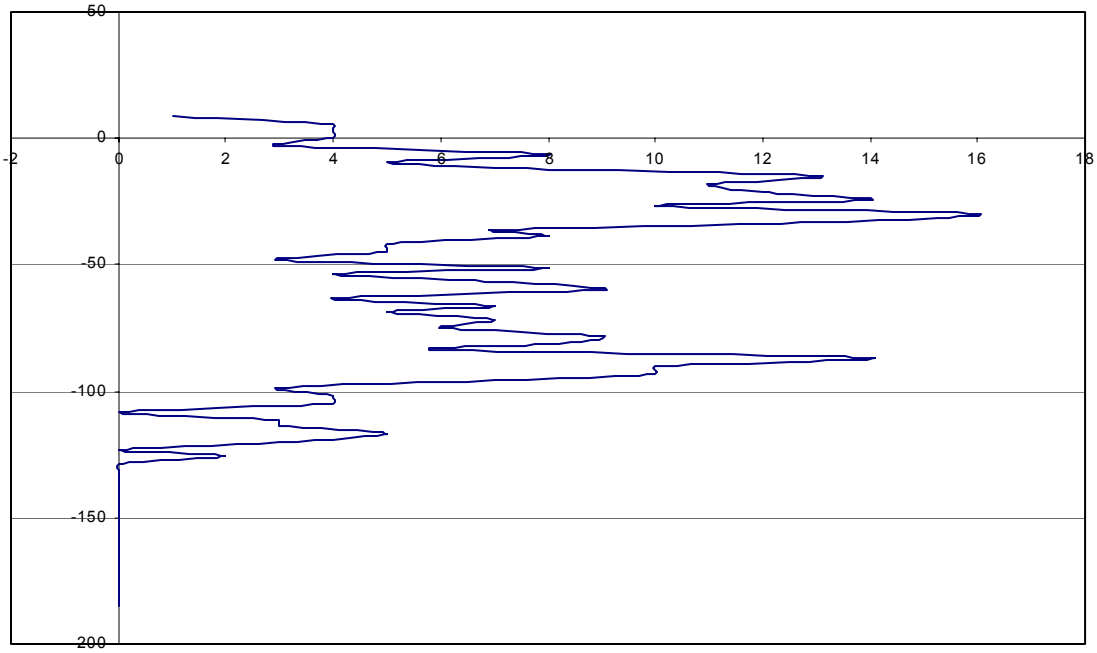

Figure C.35. $\delta^{18}O$ benthonic foraminifera data from Atlantic Core V30-40 sea level elevation duration distribution summed over a 3 m interval with ordinate depth in meters relative to present mean sea level and abscissa an arbitrary duration magnitude.

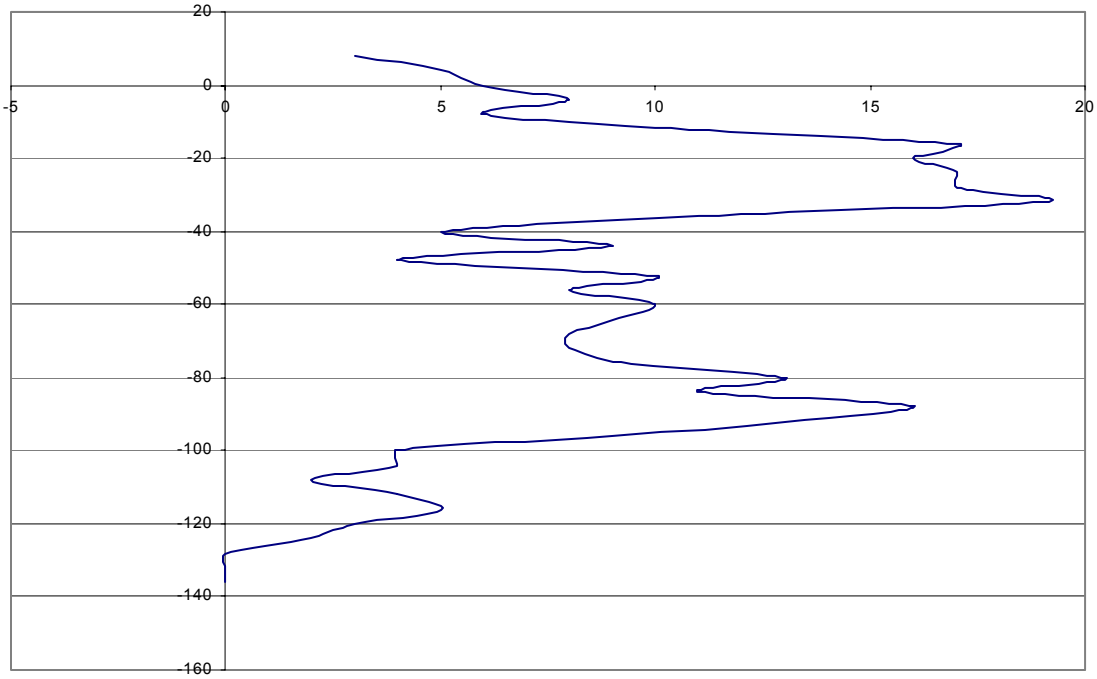

Figure C.36. $\delta^{18}O$ benthonic foraminifera data from Atlantic Core V30-40 sea level elevation duration distribution summed over a 4 m interval with ordinate depth in meters relative to present mean sea level and abscissa an arbitrary duration magnitude.

APPENDIX D

This appendix contains figures of the cave passage distribution lengths compiled for this study. Each figure displays the mean depth of total passage development below the water table surface. The first five figures (D.1 to D.5) contain the actual passage lengths of measured cave passage at depth summed over the intervals ~1/3 m, 1 m, 2 m, 3 m and 4 m, respectively. The subsequent figures (D.6 to D.21) contain the smoothed distribution of total cave passage lengths per depth summed over a 1 m, 2 m, 3 m and 4 m interval using a straight and weighted running-three mean and a straight and weighted running-five mean.

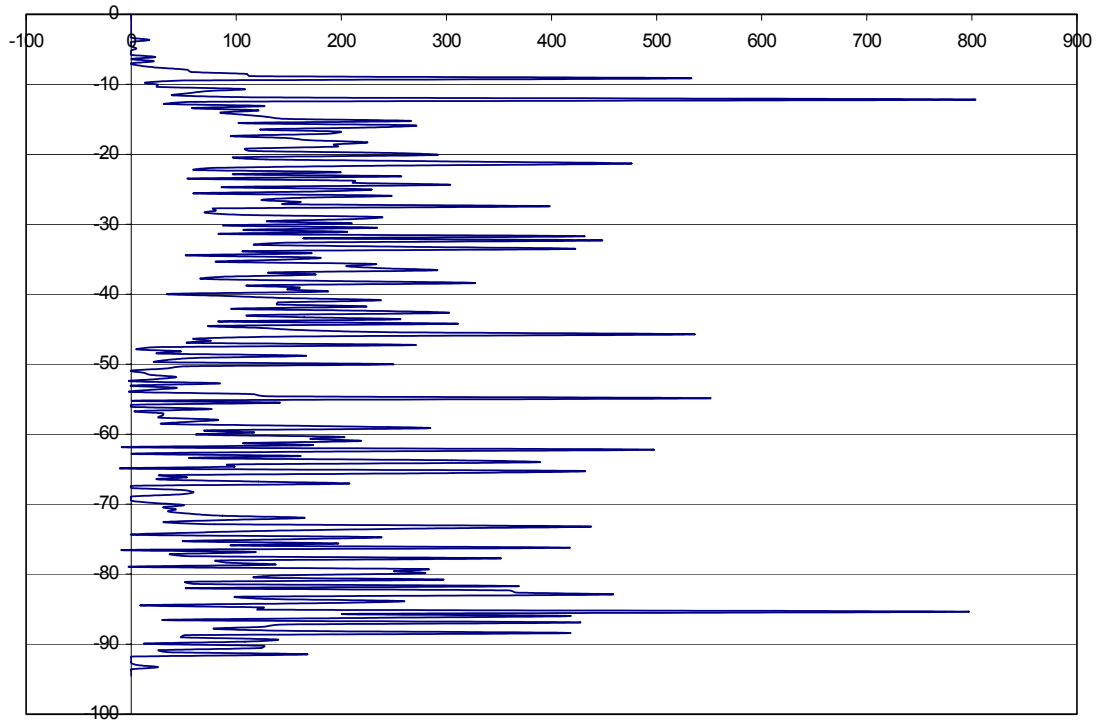

Figure D.1. Depth below water table on ~1/3 meter interval vs. Total passage length. Ordinate axis is depth in meters and abscissa is total length in meters.

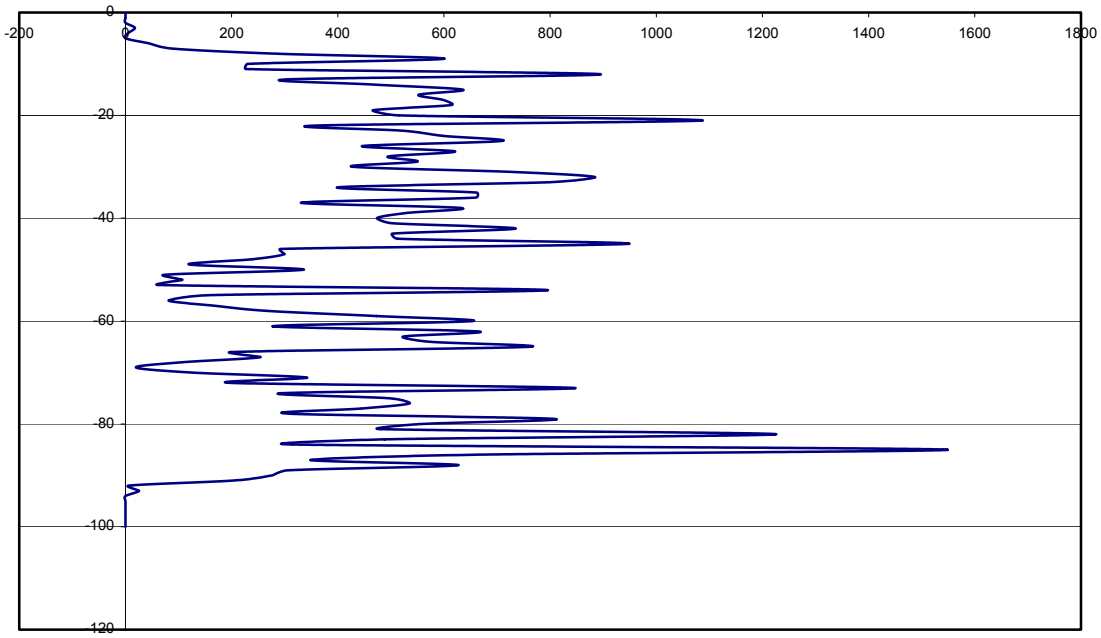

Figure D.2. Depth below water table on 1 meter interval vs. Total passage length. Ordinate axis is depth in meters and abscissa is total length in meters.

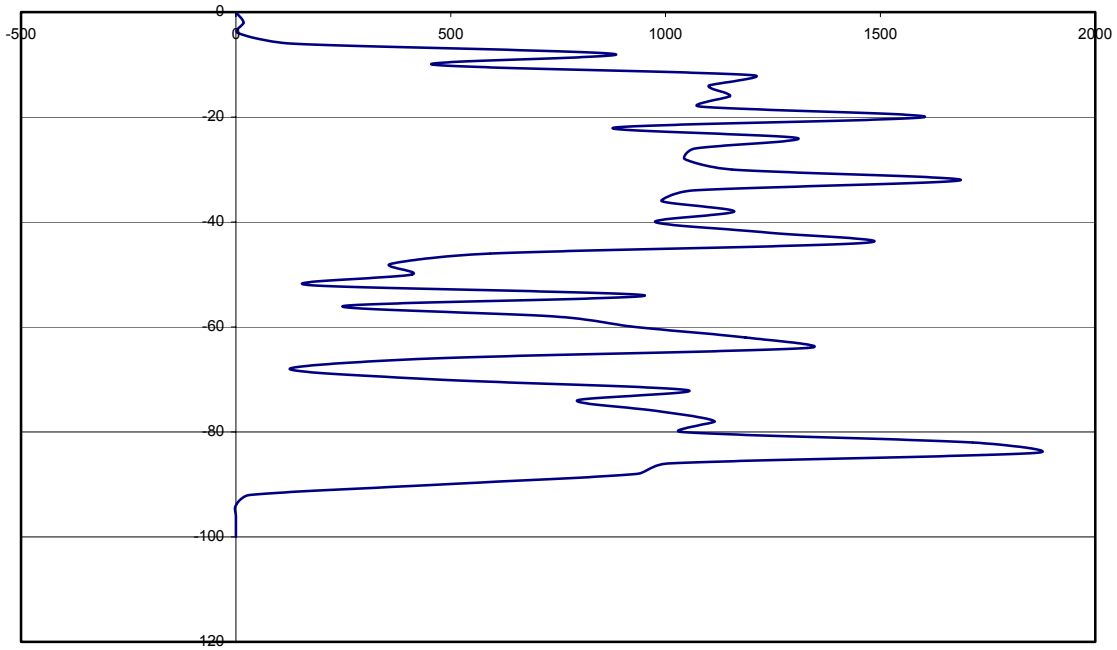

Figure D.3. Depth below water table on 2 meter interval vs. Total passage length. Ordinate axis is depth in meters and abscissa is total length in meters.

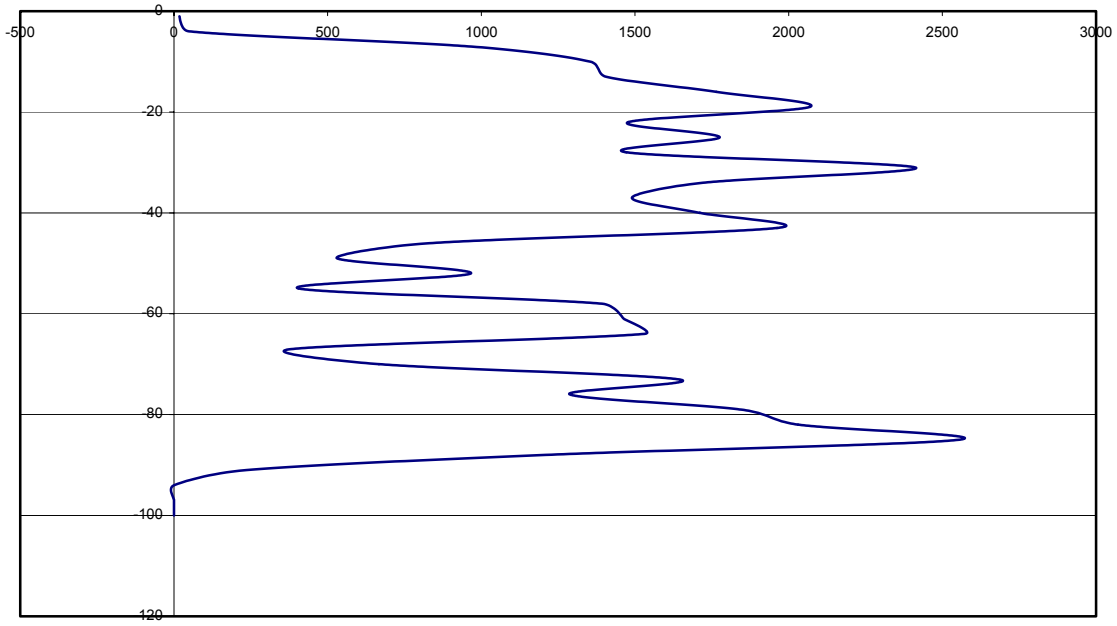

Figure D.4. Depth below water table on 3 meter interval vs. Total passage length. Ordinate axis is depth in meters and abscissa is total length in meters.

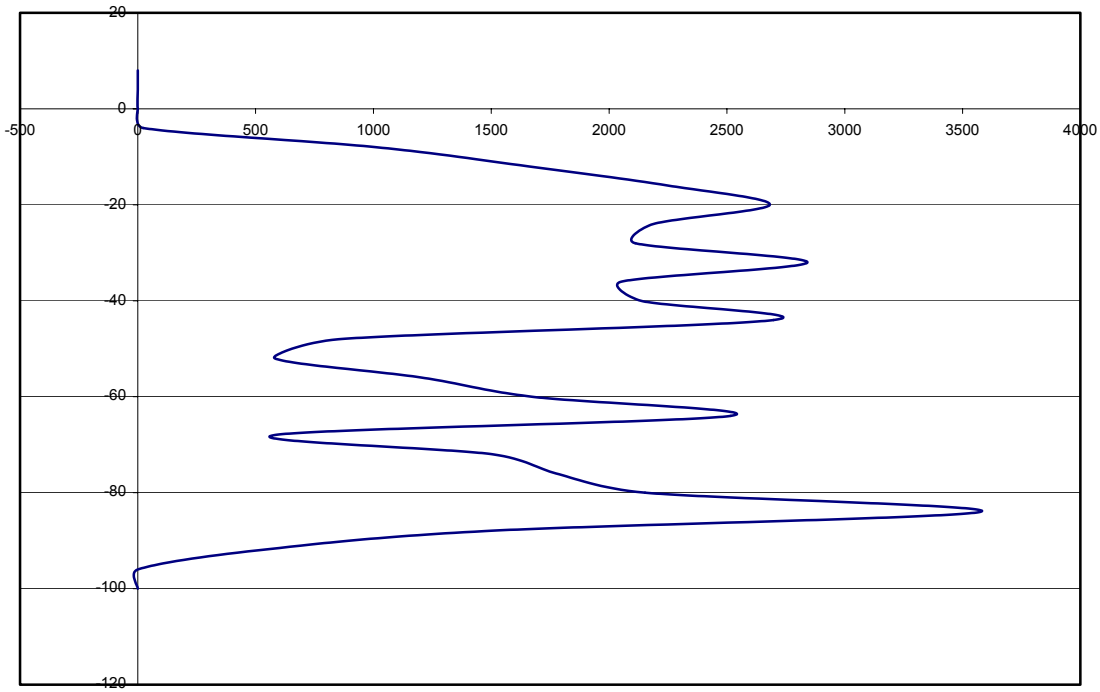

Figure D.5. Depth below water table on 4 meter interval vs. Total passage length. Ordinate axis is depth in meters and abscissa is total length in meters.

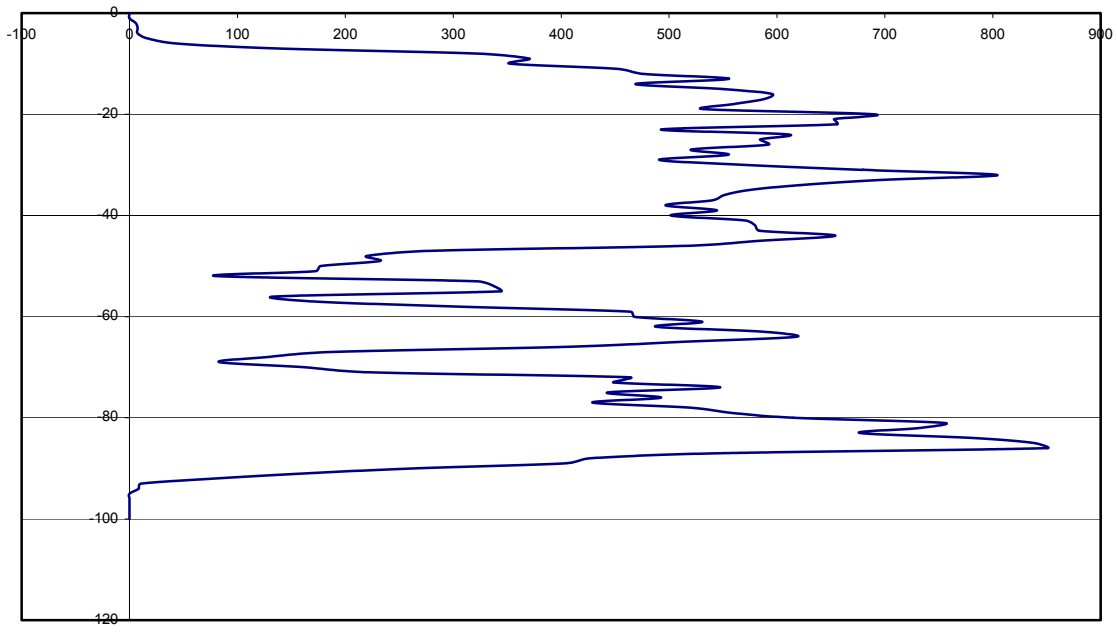

Figure D.6. Depth below water table on 1 meter interval using a straight running-three mean vs. Total passage length. Ordinate axis is depth in meters and abscissa is total length in meters.

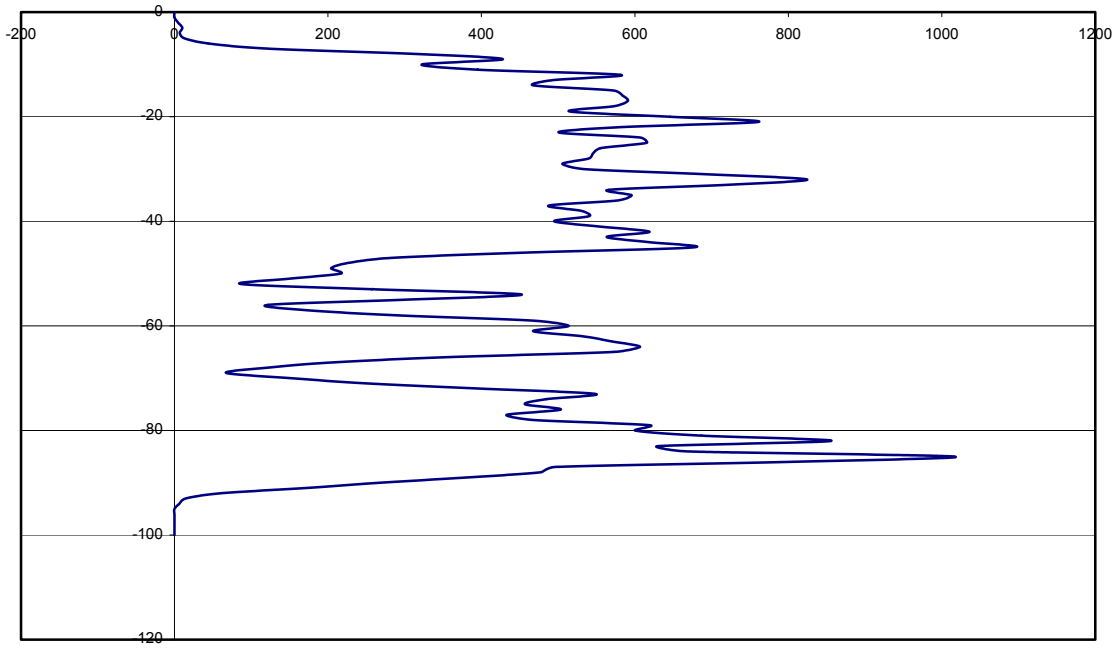

Figure D.7. Depth below water table on 1 meter interval using a weighted running-three mean vs. Total passage length. Ordinate axis is depth in meters and abscissa is total length in meters.

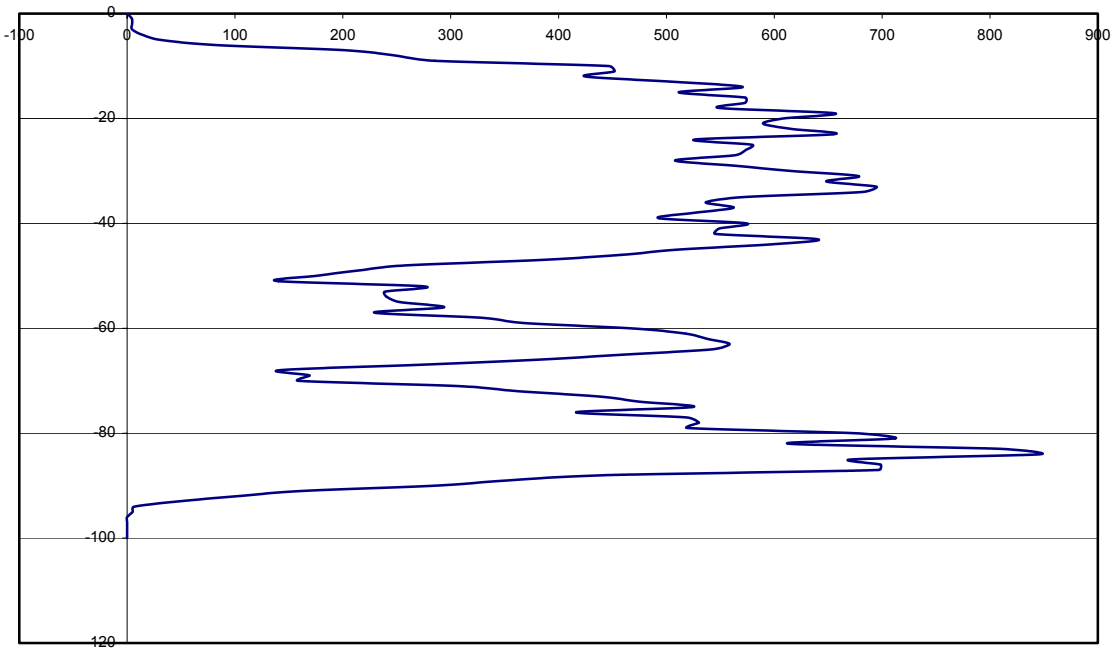

Figure D.8. Depth below water table on 1 meter interval using a straight running-five mean vs. Total passage length. Ordinate axis is depth in meters and abscissa is total length in meters.

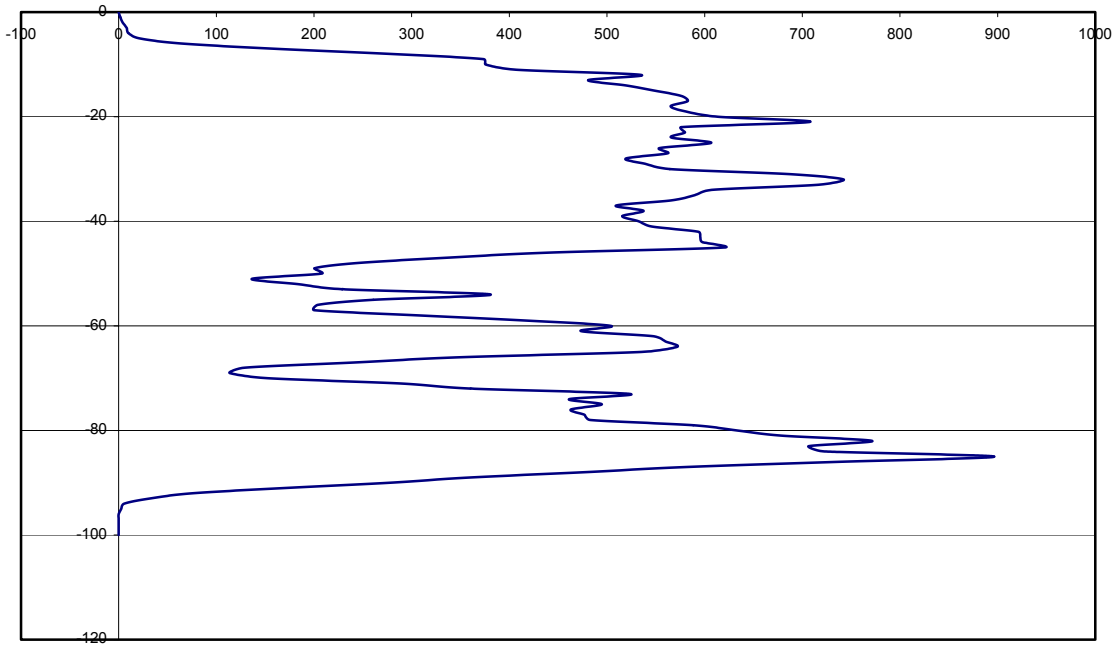

Figure D.9. Depth below water table on 1 meter interval using a weighted running-five mean vs. Total passage length. Ordinate axis is depth in meters and abscissa is total length in meters.

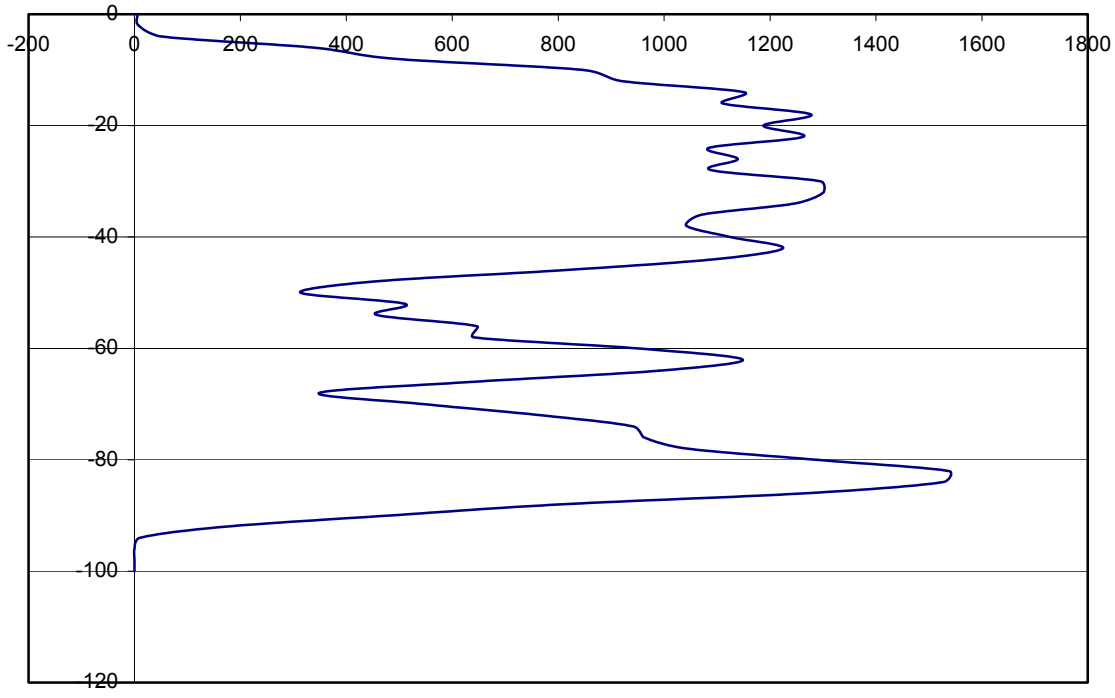

Figure D.10. Depth below water table on 2 meter interval using a straight running-three mean vs. Total passage length. Ordinate axis is depth in meters and abscissa is total length in meters.

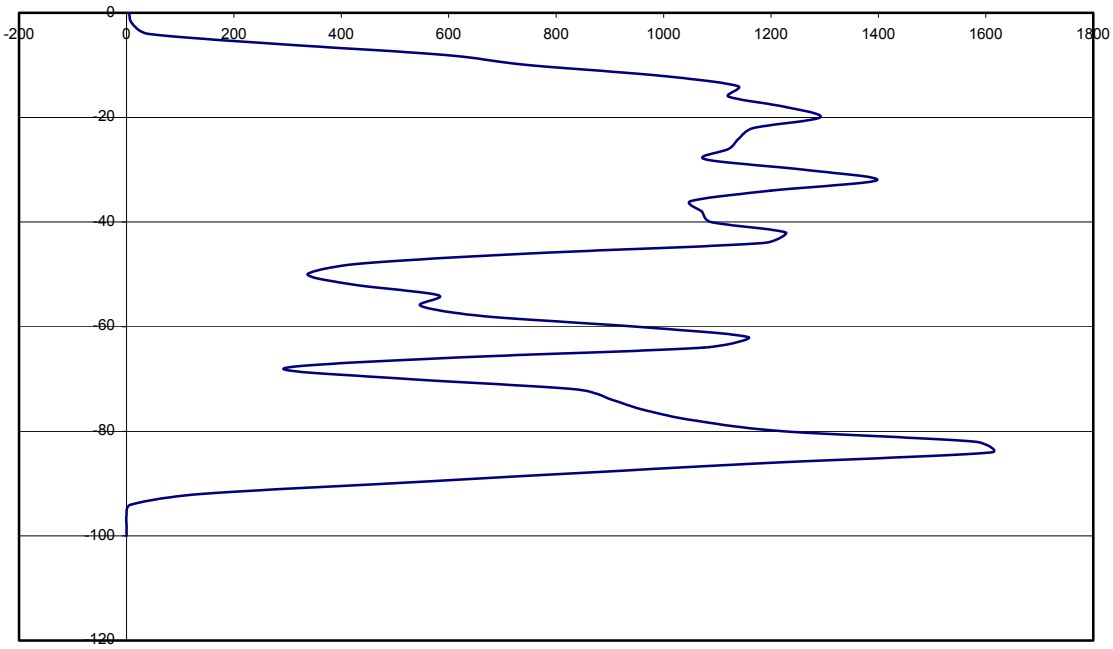

Figure D.11. Depth below water table on 2 meter interval using a weighted running-three mean vs. Total passage length. Ordinate axis is depth in meters and abscissa is total length in meters.

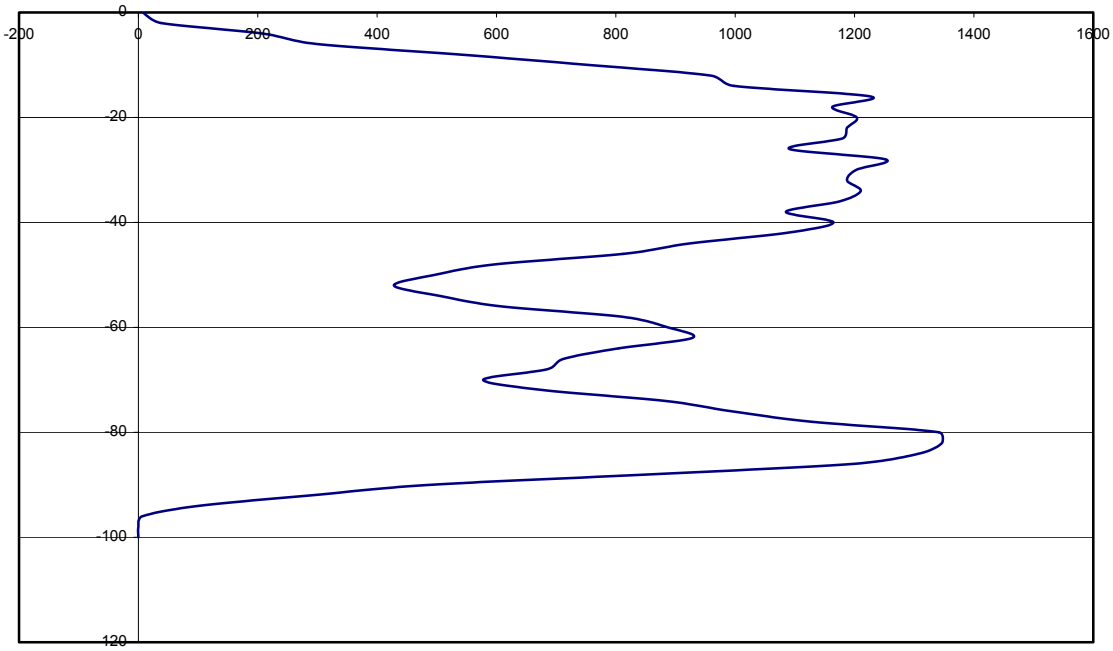

Figure D.12. Depth below water table on 2 meter interval using a straight running-five mean vs. Total passage length. Ordinate axis is depth in meters and abscissa is total length in meters.

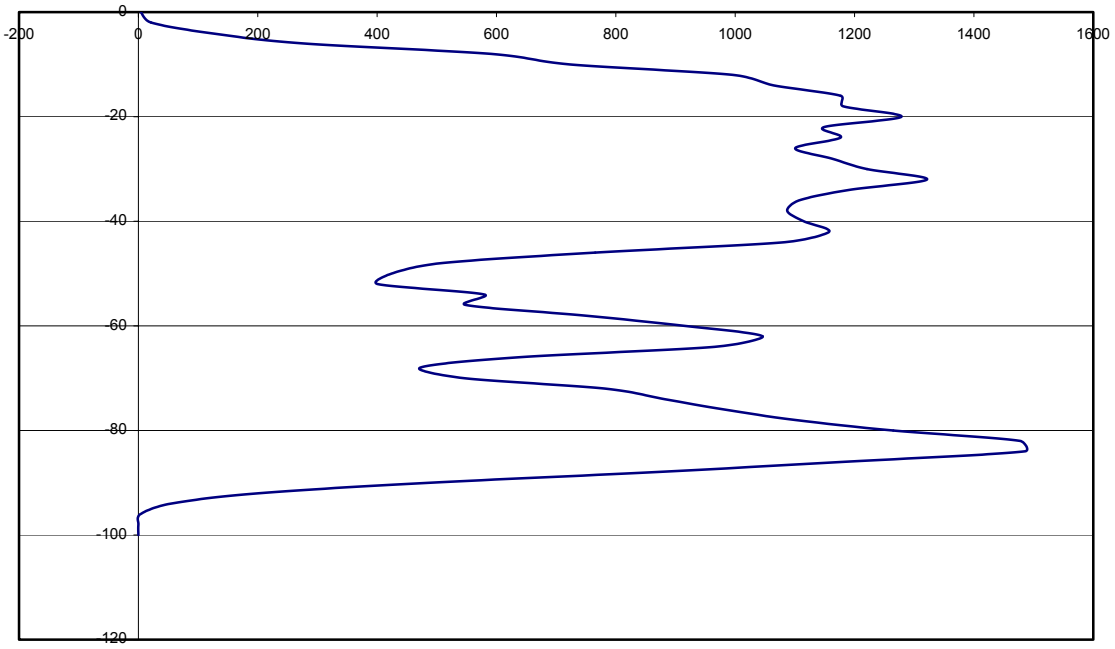

Figure D.13. Depth below water table on 2 meter interval using a weighted running-five mean vs. Total passage length. Ordinate axis is depth in meters and abscissa is total length in meters.

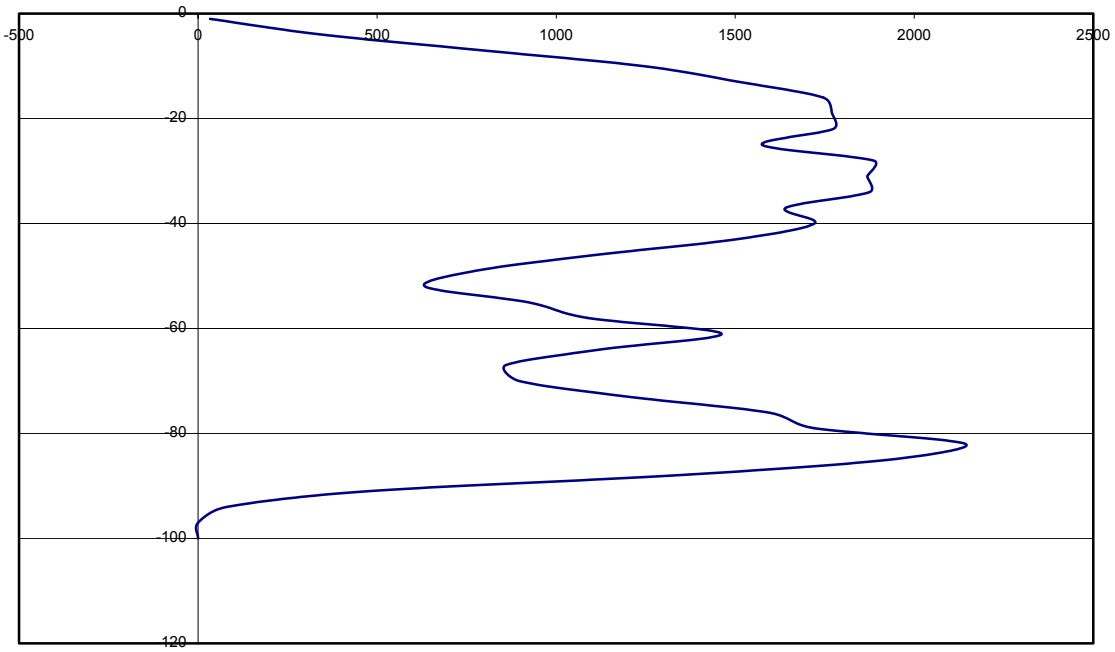

Figure D.14. Depth below water table on 3 meter interval using a straight running-three mean vs. Total passage length. Ordinate axis is depth in meters and abscissa is total length in meters.

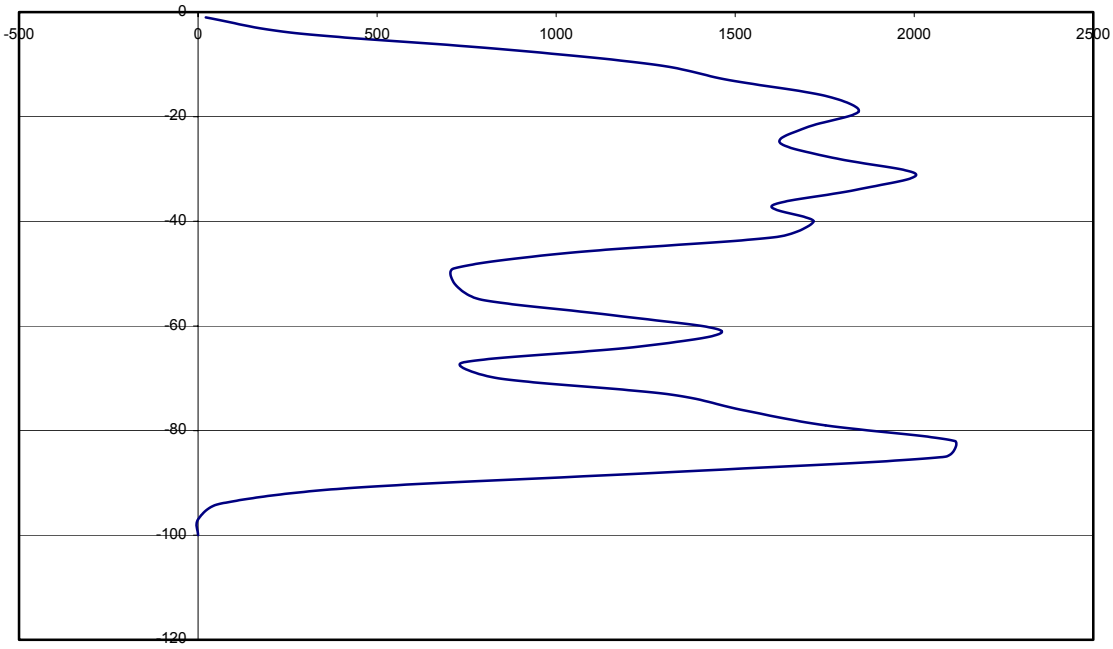

Figure D.15. Depth below water table on 3 meter interval using a weighted running-three mean vs. Total passage length. Ordinate axis is depth in meters and abscissa is total length in meters.

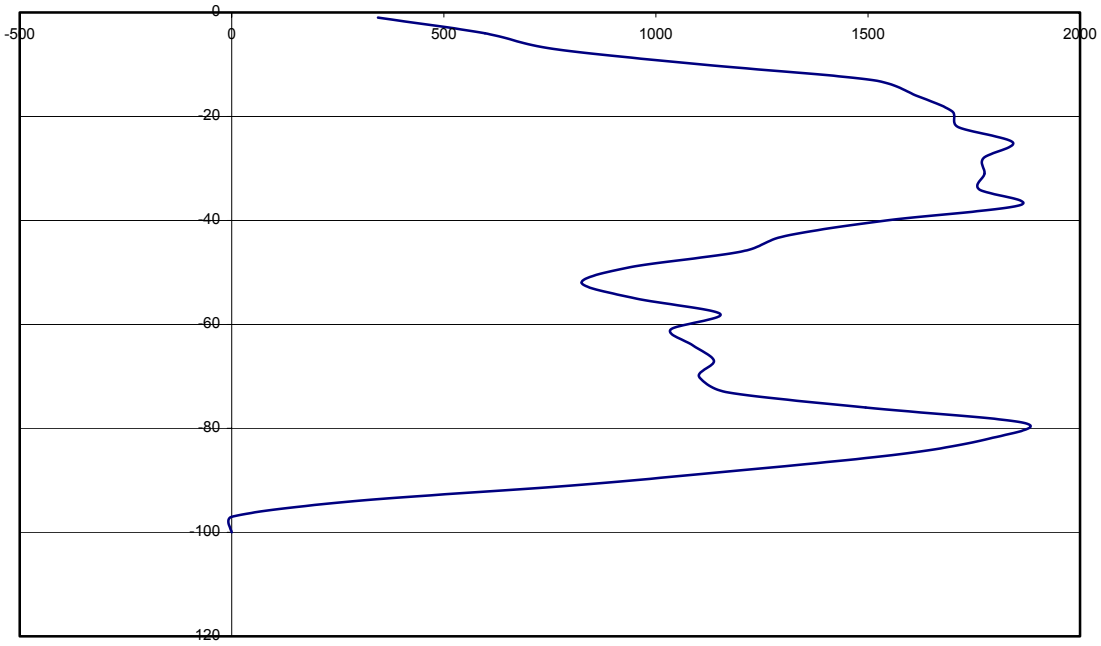

Figure D.16. Depth below water table on 3 meter interval using a straight running-five mean vs. Total passage length. Ordinate axis is depth in meters and abscissa is total length in meters.

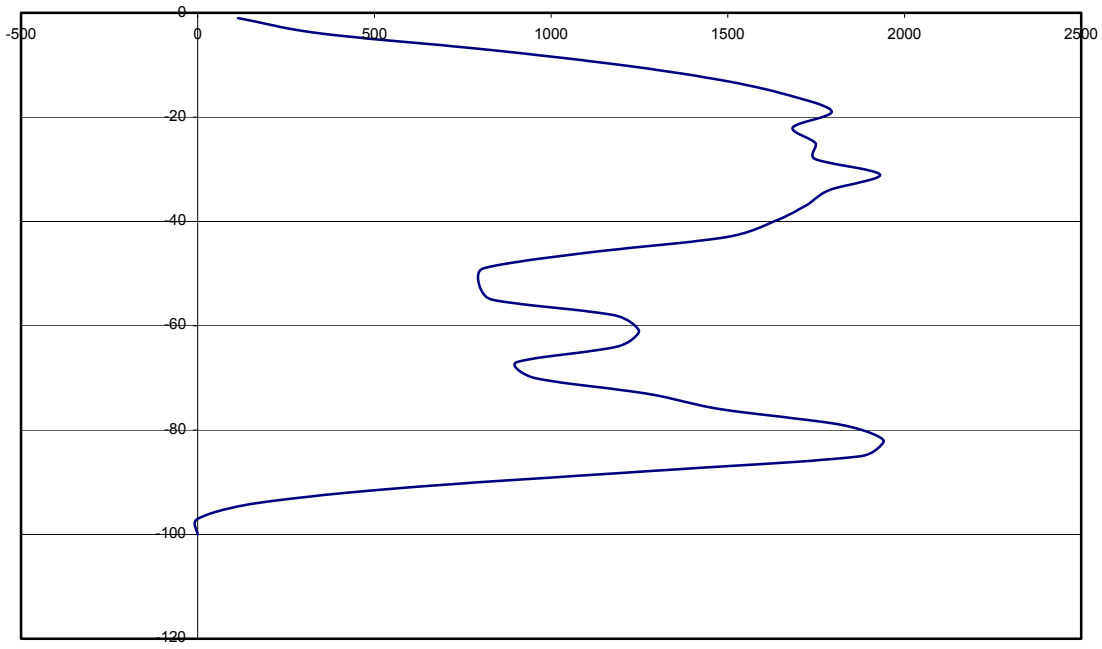

Figure D.17. Depth below water table on 3 meter interval using a weighted running-five mean vs. Total passage length. Ordinate axis is depth in meters and abscissa is total length in meters.

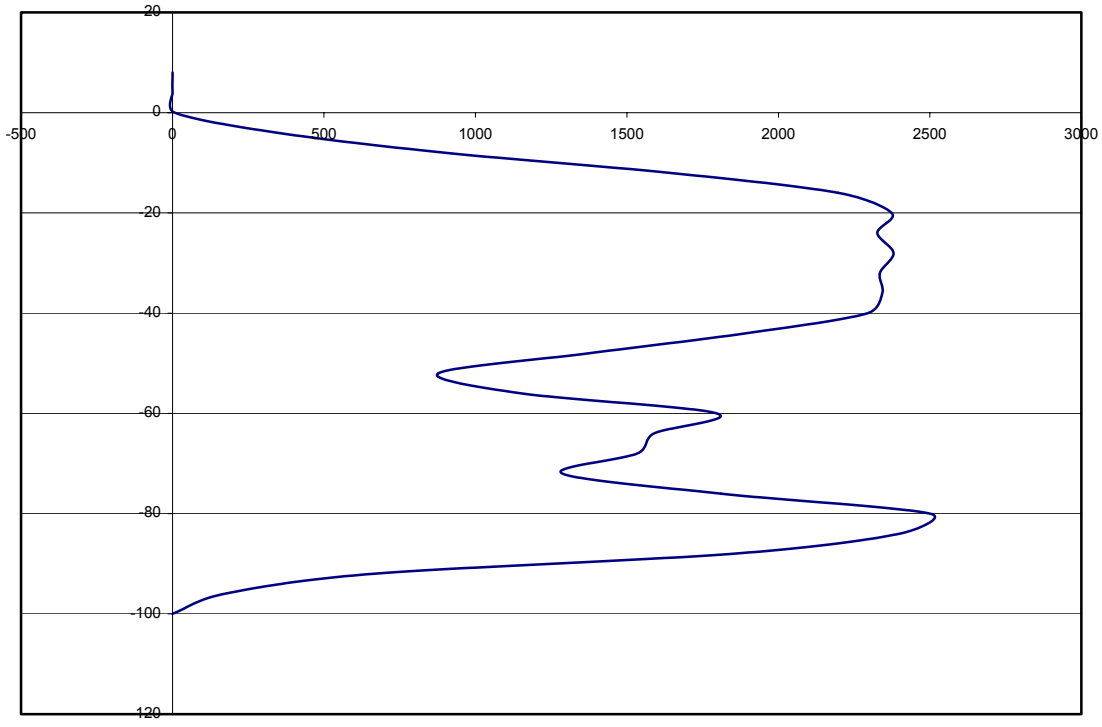

Figure D.18. Depth below water table on 4 meter interval using a straight running-three mean vs. Total passage length. Ordinate axis is depth in meters and abscissa is total length in meters.

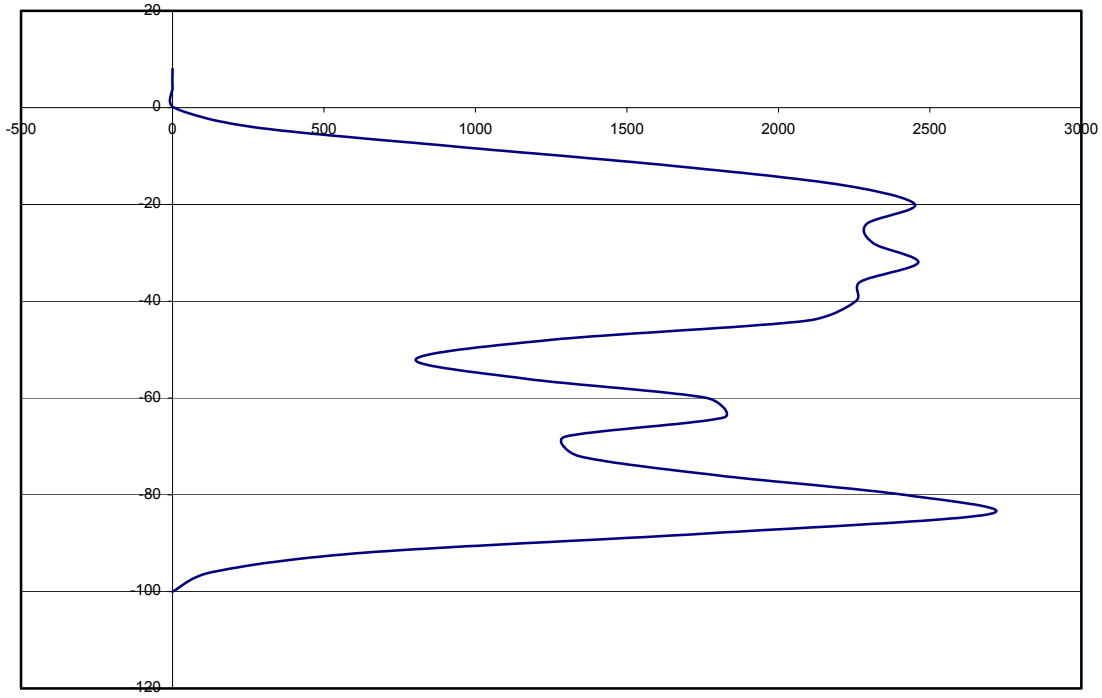

Figure D.19. Depth below water table on 4 meter interval using a weighted running-three mean vs. Total passage length. Ordinate axis is depth in meters and abscissa is total length in meters.

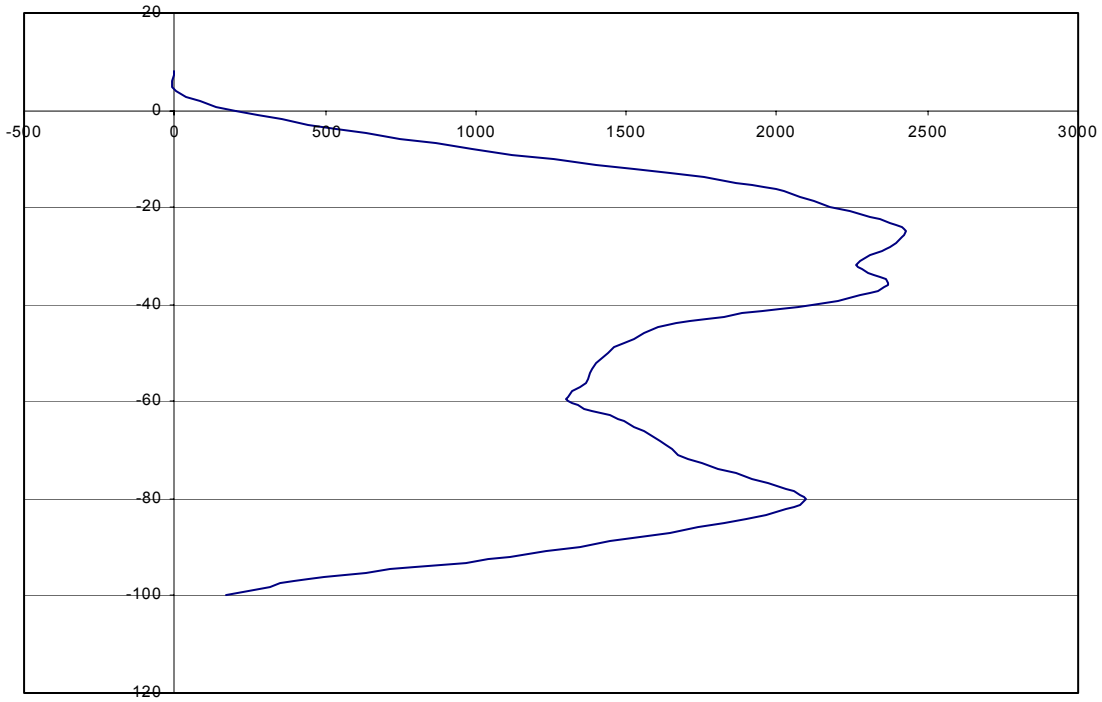

Figure D.20. Depth below water table on 4 meter interval using a straight running-five mean vs. Total passage length. Ordinate axis is depth in meters and abscissa is total length in meters.

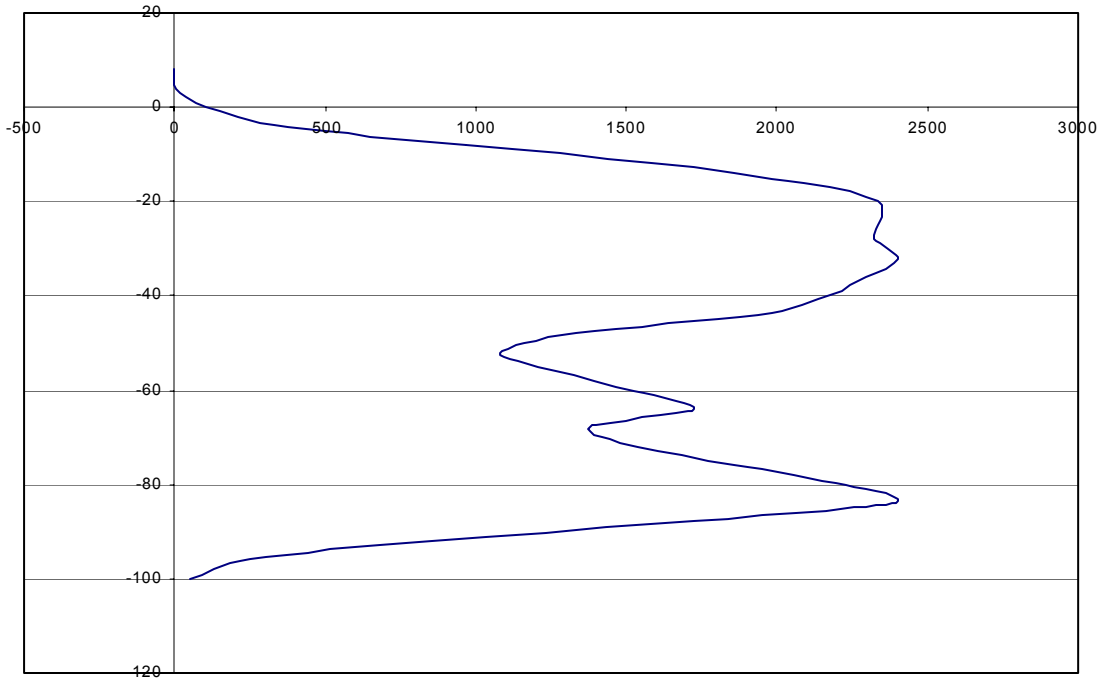

Figure D.21. Depth below water table on 4 meter interval using a weighted running-five mean vs. Total passage length. Ordinate axis is depth in meters and abscissa is total length in meters.

APPENDIX E

This appendix contains 13 figures illustrating correlation between sea level elevation durations with the passage length distribution over select intervals. The figures included contain the some of the highest correlation coefficient from Tables 3.2, 3.3, 3.4 and 3.5. Those included are as follows: (E.1) Haiti corals and Core V19-29 modified from Dodge *et. al.* (1983) plotted with actual passage length summed over 1 m interval, (E.2) New Guinea terraces modified from Shackleton (1987) plotted with actual passage length summed over 2 m interval, (E.3) Core V30-40 modified from Imbrie *et. al.* (1984) plotted with passage length using a running three mean summed over 2 m interval, (E.4) Core DSDP 502b modified from Imbrie *et. al.* (1984) plotted with actual passage length summed over a 3 m interval, (E.5) Core V30-40 modified from Imbrie *et. al.* (1984) plotted with passage length using a running three mean summed over 3 m interval, (E.6) Core V30-40 modified from Imbrie *et. al.* (1984) plotted with passage length using a running five mean summed over 3 m interval, (E.7) Core V28-238 modified from Dia *et. al.* (1992) plotted with passage length using a running five mean summed over 3 m interval, (E.8) Core RC17-177 modified from Shackleton (1987) plotted with passage length using a weighted running five mean summed over 3 m interval, (E.9) SPECMAP modified from Imbrie *et. al.* (1984) plotted with passage length using a running five mean summed over 3 m interval, (E.10) Core V28-238 modified from Dia *et. al.* (1992) plotted with passage length using a running five mean summed over 4 m interval, (E.11) Core RC17-177 modified from Shackleton (1987) plotted with passage length using a running three mean summed over 4 m interval, (E.12) Core V30-40 modified from Imbrie *et. al.*

(1984) plotted with passage length using a running five mean summed over 4 m interval , (E.13) Core V30-40 modified from Imbrie *et. al.* (1984) plotted with passage length using a running three mean summed over 4 m interval.

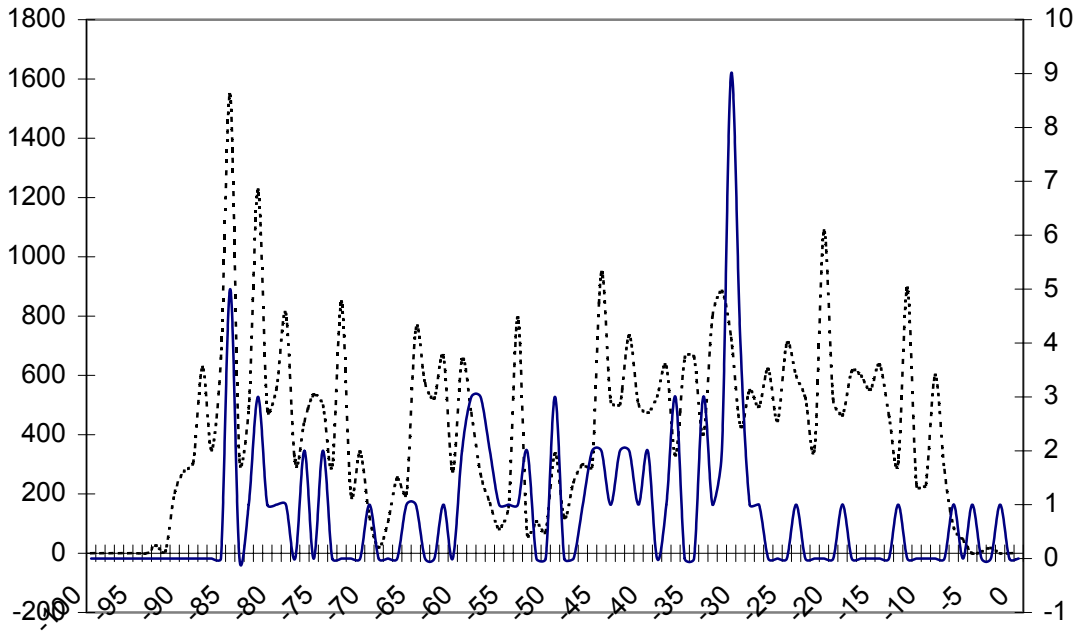

Figure E.1. Actual length of passage (dotted line), left ordinate in meters, and duration of sea level height, right ordinate arbitrary, for Core V19-29 (solid line) summed over 1 m interval, abscissa in meters below mean sea level.

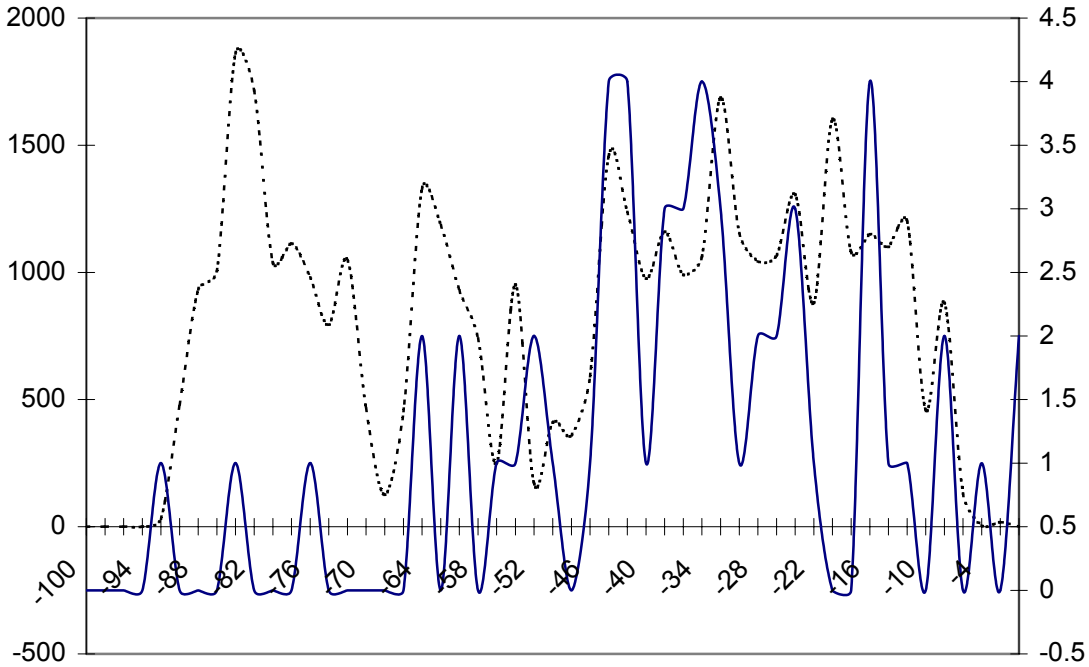

Figure E.2. Actual length of passage (dotted line), left ordinate in meters, and duration of sea level height, right ordinate arbitrary, for New Guinea terraces (solid line) summed over 2 m interval, abscissa in meters below mean sea level.

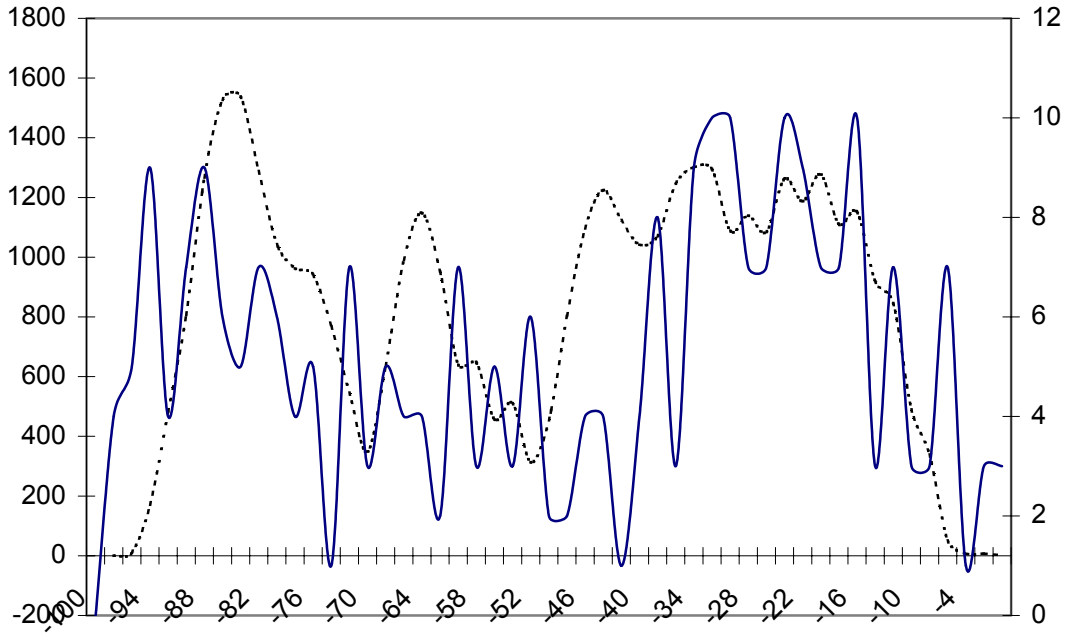

Figure E.3. Straight running three-mean of passage length (dotted line), left ordinate in meters, and duration of sea level height, right ordinate arbitrary, for Core V30-40 (solid line) summed over 2 m interval, abscissa in meters below mean sea level.

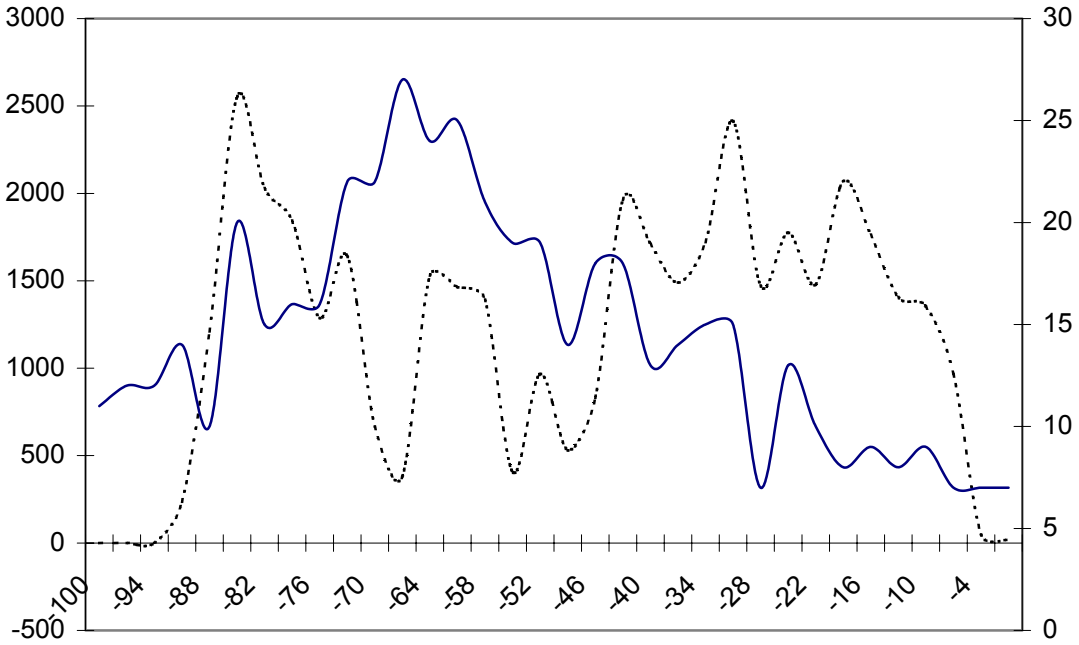

Figure E.4. Actual length of passage (dotted line), left ordinate in meters, and duration of sea level height, right ordinate arbitrary, for Core DSDP502b (solid line) summed over 3 m interval, abscissa in meters below mean sea level.

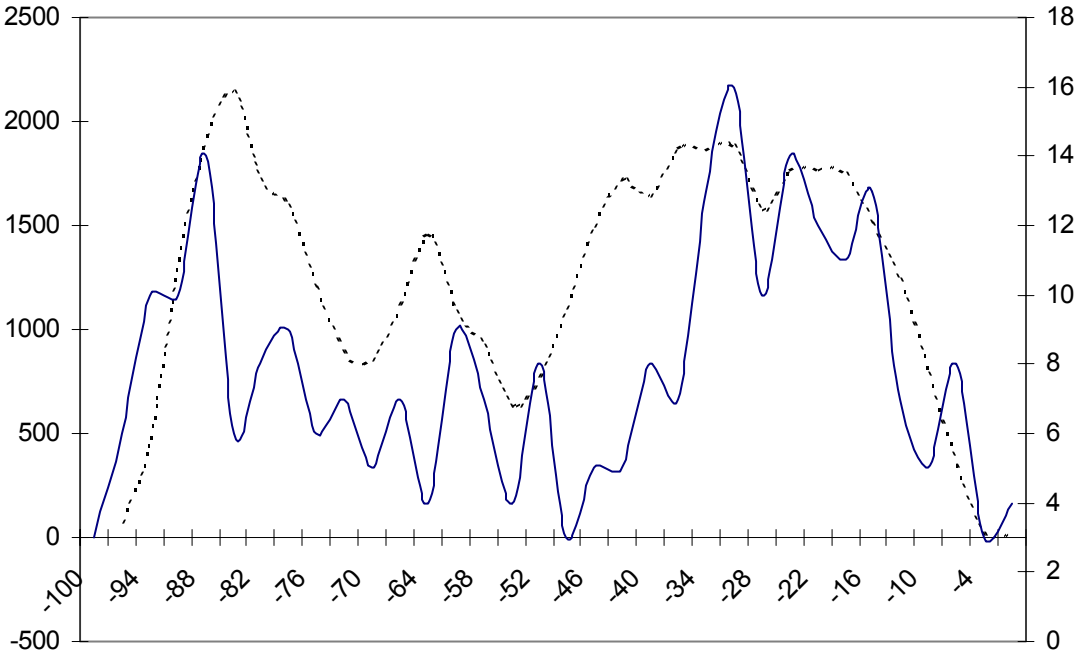

Figure E.5. Straight running three-mean of passage length (dotted line), left ordinate in meters, and duration of sea level height, right ordinate arbitrary, for Core V30-40 (solid line) summed over 3 m interval, abscissa in meters below mean sea level.

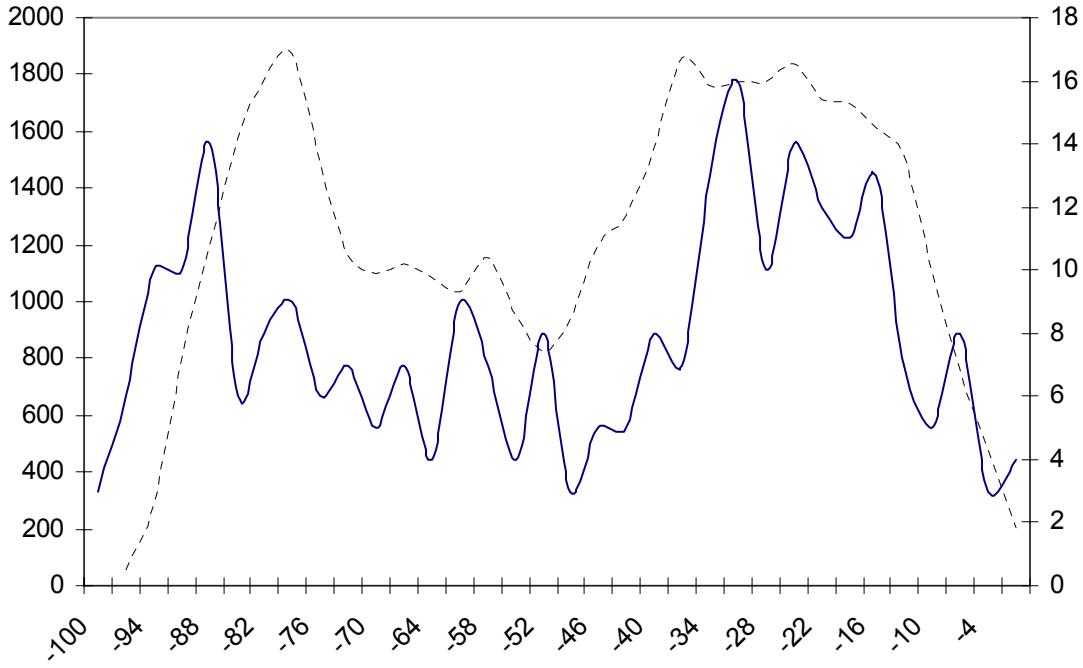

Figure E.6. Straight running five-mean of passage length(dotted line), left ordinate in meters, and duration of sea level height, right ordinate arbitrary, for Core V30-40 (solid line) summed over 3 m interval, abscissa in meters below mean sea level.

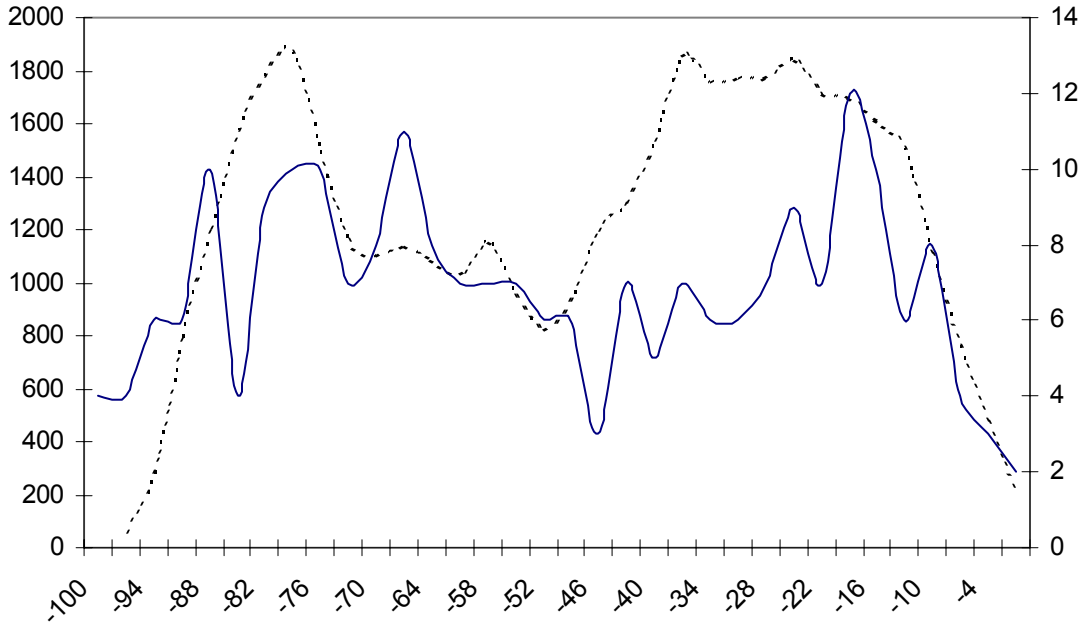

Figure E.7. Straight running-five mean of passage length (dotted line), left ordinate in meters, and duration of sea level height, right ordinate arbitrary, for $\delta^{18}O$ record of Core V28-238 (solid line) summed over 3 m interval, abscissa in meters below mean sea level.

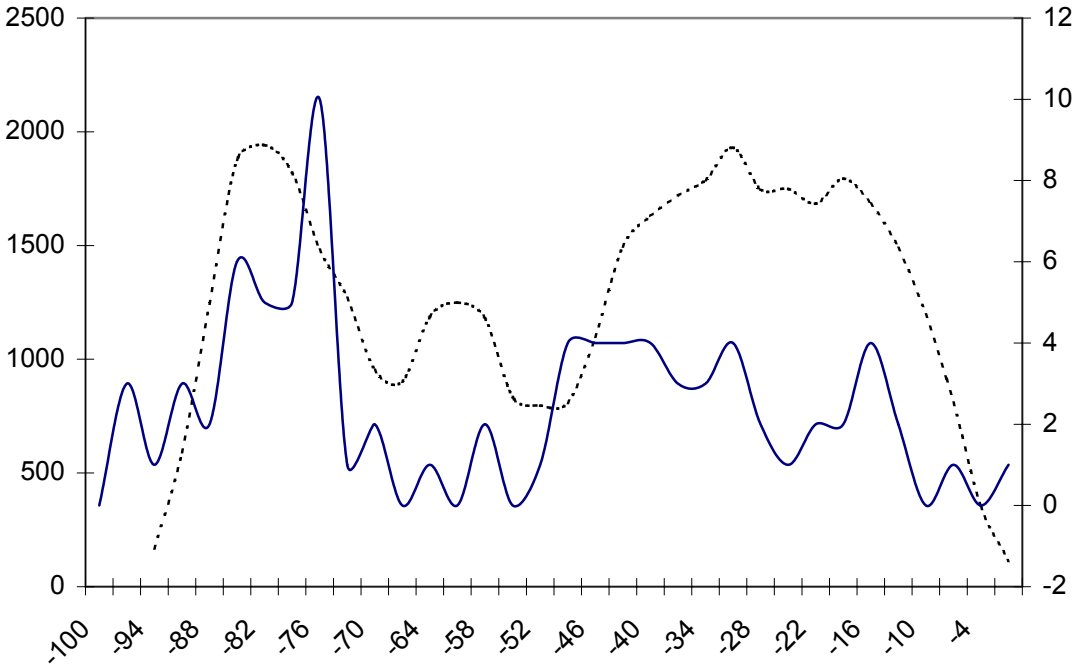

Figure E.8. Weighted running-five mean of passage length (dotted line), left ordinate in meters, and duration of sea level height, right ordinate arbitrary, for Core RC17-177 (solid line) summed over 3 m interval, abscissa in meters below mean sea level.

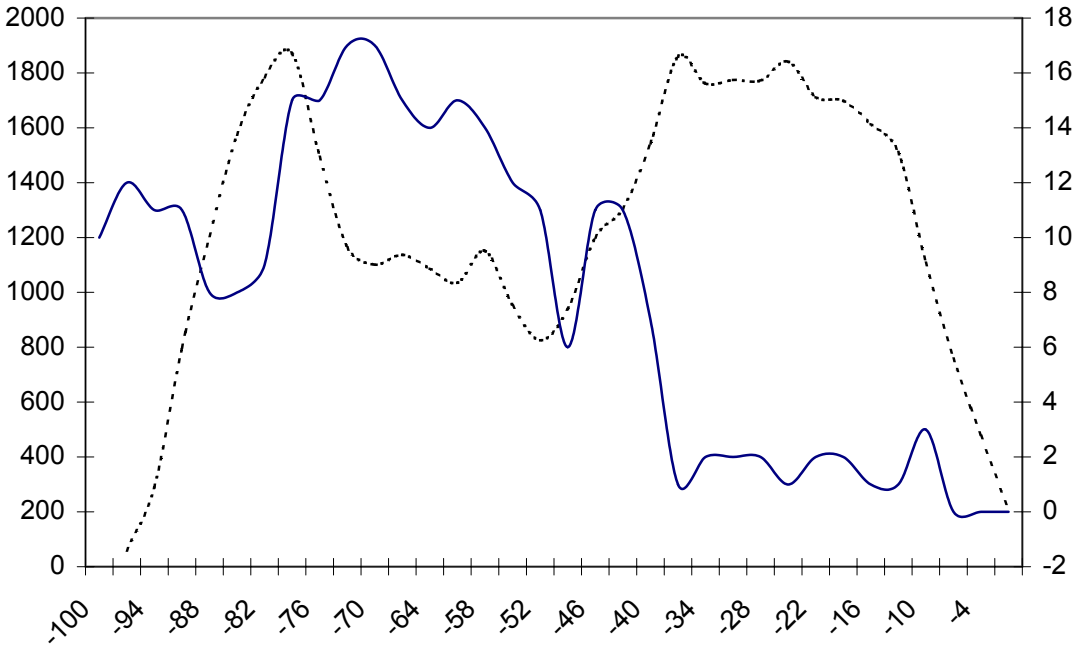

Figure E.9. Straight running-five mean of passage length (dotted line), left ordinate in meters, and duration of sea level height, right ordinate arbitrary, for smoothed stack SPECMAP (solid line) summed over 3 m interval, abscissa in meters below mean sea level.

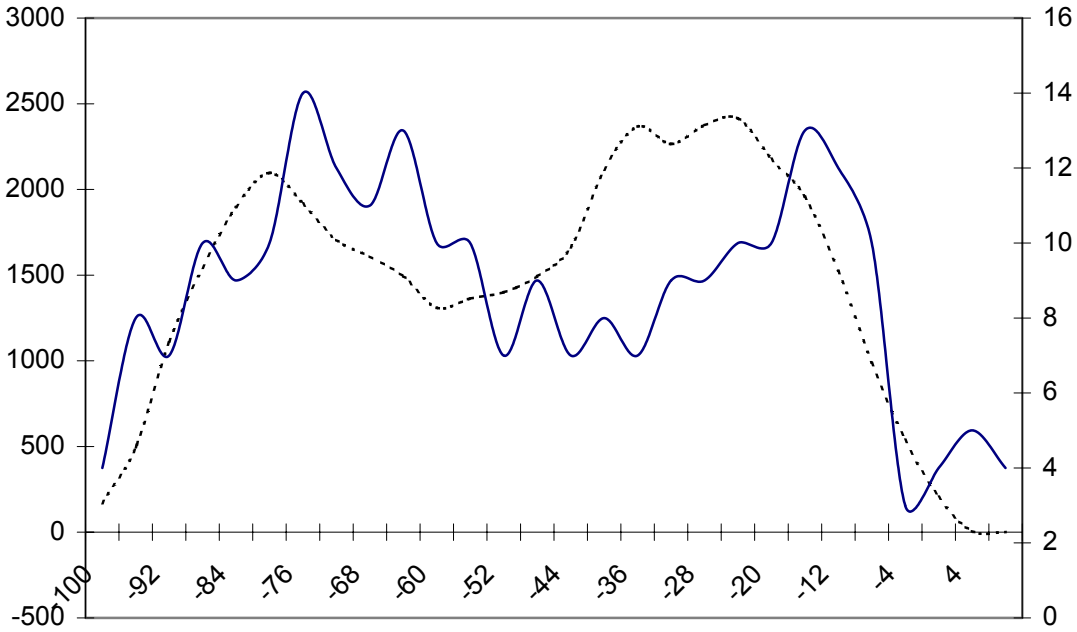

Figure E.10. Straight running-five mean of passage length (dotted line), left ordinate in meters, and duration of sea level height, right ordinate arbitrary, for $\delta^{18}O$ record of Core V28-238 (solid line) summed over 4 m interval, abscissa in meters below mean sea level.

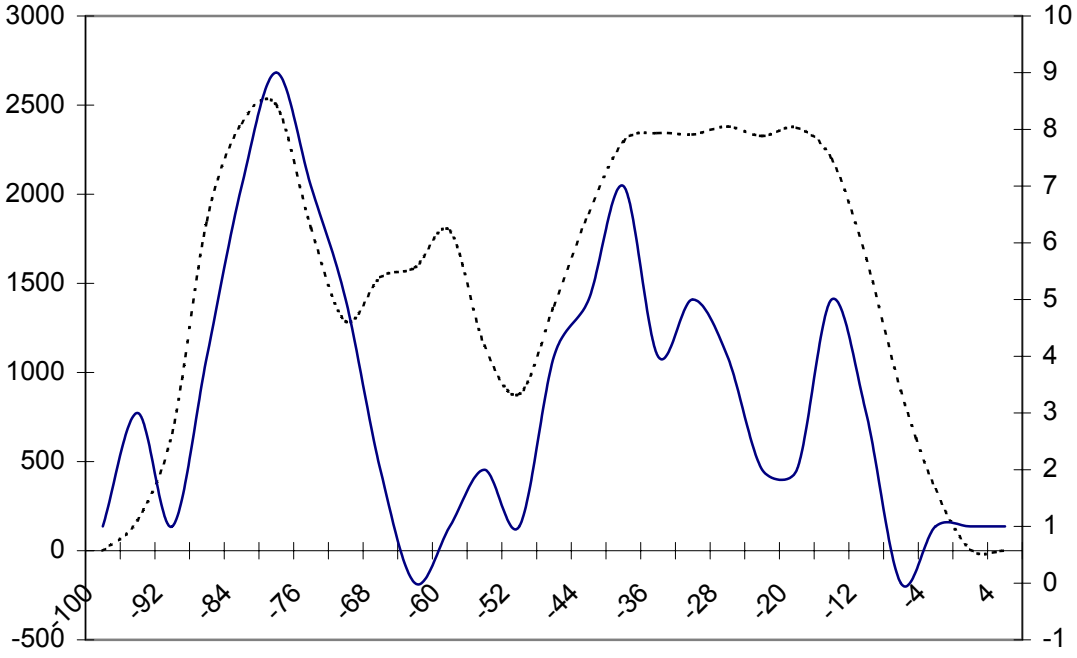

Figure E.11. Straight running-five mean of passage length (dotted line), left ordinate in meters, and duration of sea level height, right ordinate arbitrary, for Core RC17-177 (solid line) summed over 4 m interval, abscissa in meters below mean sea level.

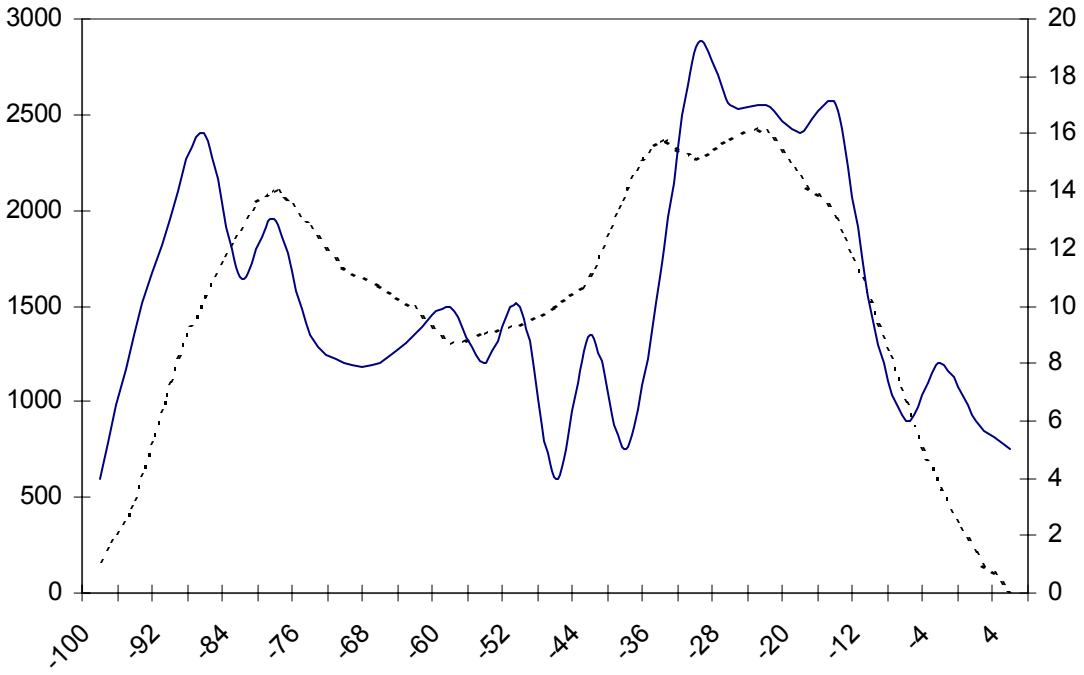

Figure E.12. Straight running five-mean of passage length (dotted line), left ordinate in meters, and duration of sea level height, right ordinate arbitrary, for Core V30-40 (solid line) summed over 4 m interval, abscissa in meters below mean sea level.

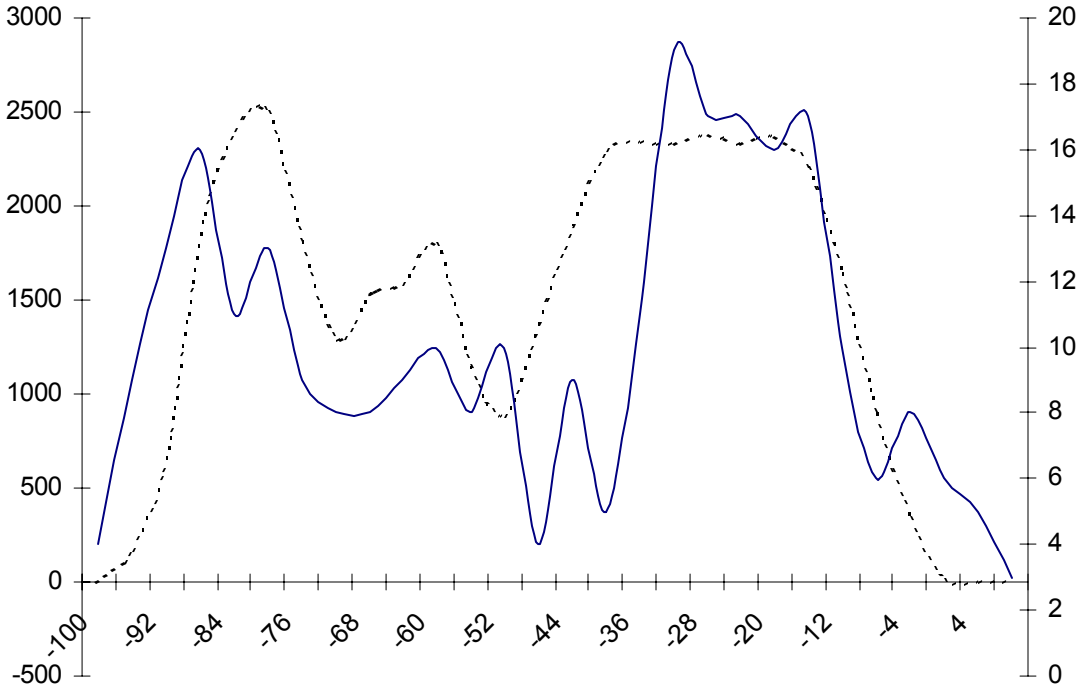

Figure E.13. Straight running three-mean of passage length (dotted line), left ordinate in meters, and duration of sea level height, right ordinate arbitrary, for Core V30-40 (solid line) summed over 4 m interval, abscissa in meters below mean sea level.

APPENDIX F

This appendix contains 10 figures illustrating correlation between sea level elevation durations with the passage length distribution over 1 m, 2 m and 3 m intervals. The figures included contain the some of the highest correlation coefficient from Tables 3.6, 3.7 and 3.8. for the limited time durations of the two longest sea level elevation records. Those included are as follows: (F.1) 475 Ka BP duration record of Core DSDP 502b modified from Imbrie *et. al.* (1984) plotted with a weighted running three mean of passage length summed over a 2 m interval, (F.2) 450 Ka BP duration record of SPECMAP modified from Imbrie *et. al.* (1984) plotted with passage length using a running three mean summed over 2 m interval, (F.3) 425 Ka BP duration record of Core DSDP 502b modified from Imbrie *et. al.* (1984) plotted with a straight running three mean of passage length summed over a 3 m interval, (F.4) 450 Ka BP duration record of Core DSDP 502b modified from Imbrie *et. al.* (1984) plotted with a straight running three mean of passage length summed over a 3 m interval, (F.5) 450 Ka BP duration record of Core DSDP 502b modified from Imbrie *et. al.* (1984) plotted with a straight running five mean of passage length summed over a 3 m interval, (F.6) 400 Ka BP duration record of SPECMAP modified from Imbrie *et. al.* (1984) plotted with passage length using a running three mean summed over 3 m interval, (F.7) 425 Ka BP duration record of Core DSDP 502b modified from Imbrie *et. al.* (1984) plotted with a straight running three mean of passage length summed over a 4 m interval, (F.8) 425 Ka BP duration record of Core DSDP 502b modified from Imbrie *et. al.* (1984) plotted with a straight running five mean of passage length summed over a 4 m interval, (F.9) 425 Ka BP duration record of

SPECMAP modified from Imbrie *et. al.* (1984) plotted with passage length using a running five mean summed over 4 m interval, and (F.10) 450 Ka BP duration record of SPECMAP modified from Imbrie *et. al.* (1984) plotted with passage length using a running five mean summed over 4 m interval.

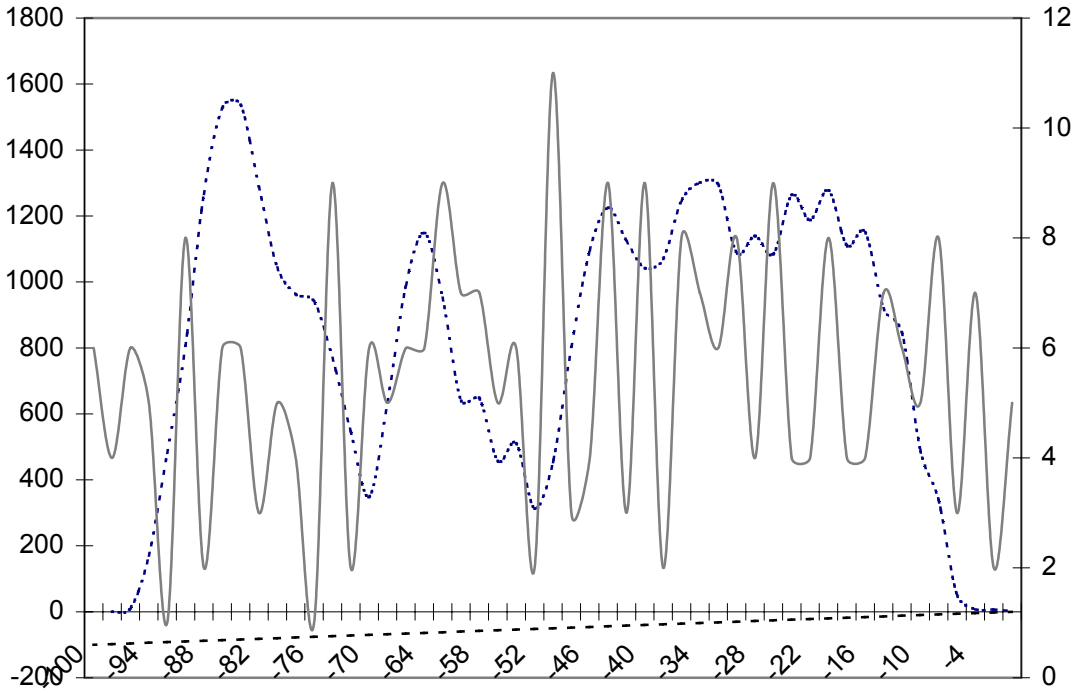

Figure F.1. Weighted running three mean of passage length passage (dotted line), left ordinate in meters, and duration of sea level height for 475 Ka BP, right ordinate arbitrary, for Core DSDP 502b (solid line) summed over 2 m interval, abscissa in meters below mean sea level.

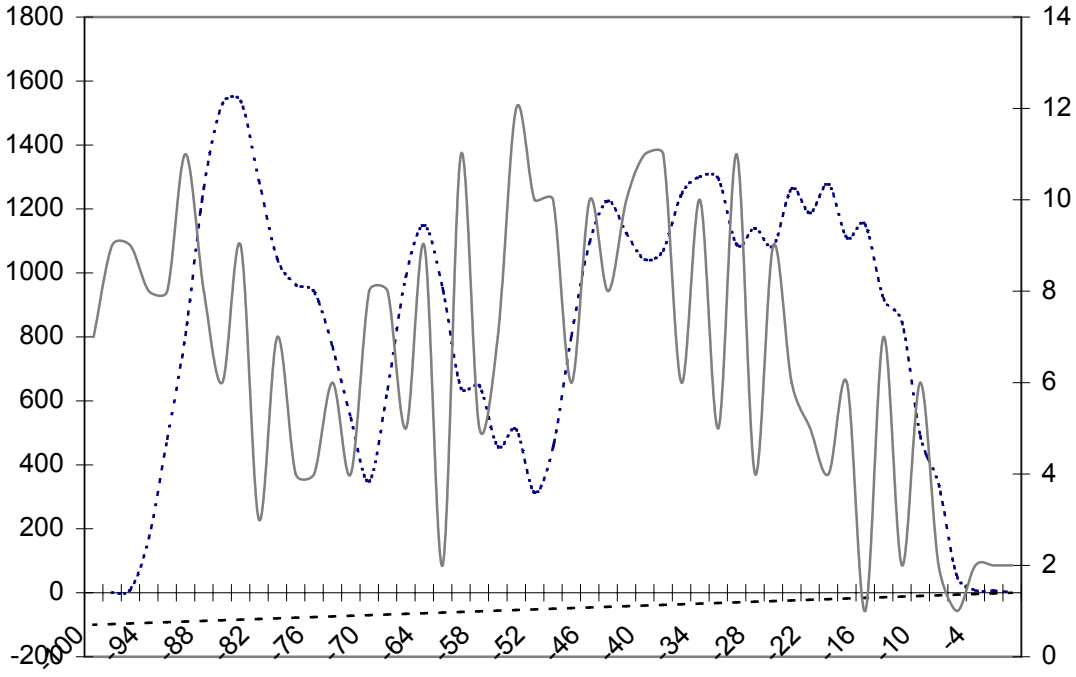

Figure F.2. Straight running-three mean of passage length (dotted line), left ordinate in meters, and duration of sea level height for 450 Ka BP, right ordinate arbitrary, for smoothed stack SPECMAP (solid line) summed over 2 m interval, abscissa in meters below mean sea level.

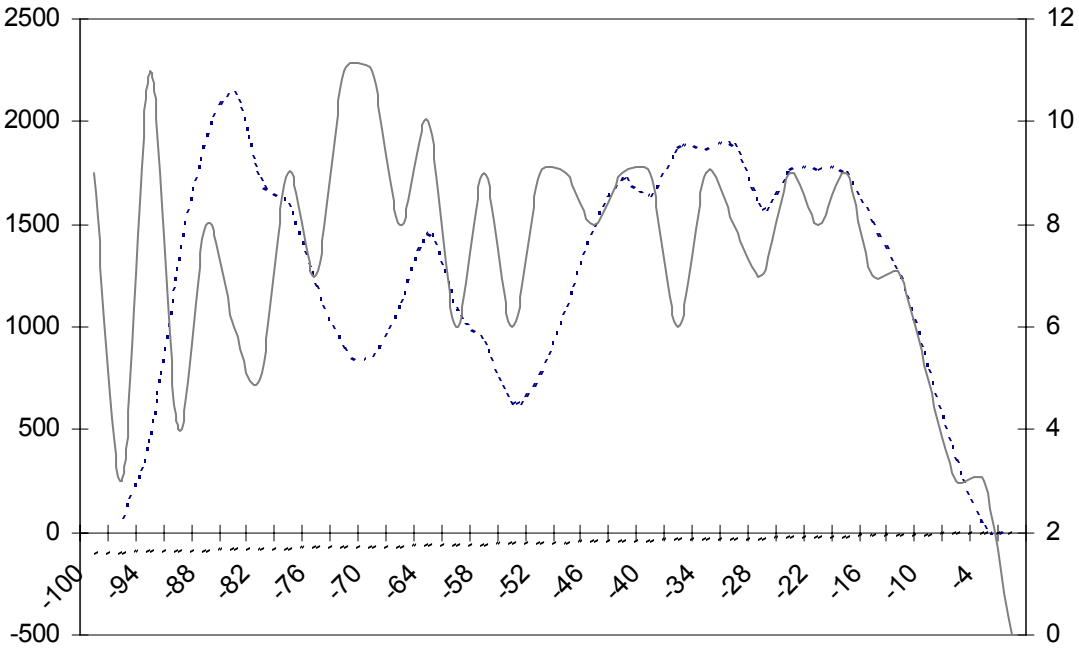

Figure F.3. Straight running three mean of passage length passage (dotted line), left ordinate in meters, and duration of sea level height for 425 Ka BP, right ordinate arbitrary, for Core DSDP 502b (solid line) summed over 3 m interval, abscissa in meters below mean sea level.

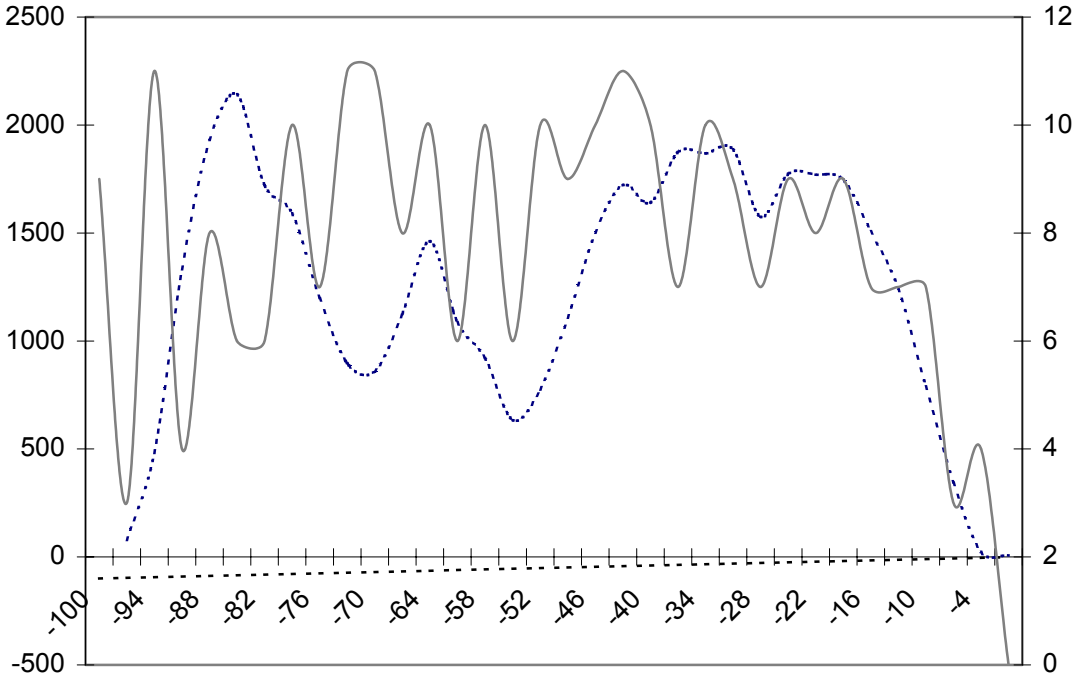

Figure F.4. Straight running three mean of passage length passage (dotted line), left ordinate in meters, and duration of sea level height for 450 Ka BP, right ordinate arbitrary, for Core DSDP 502b (solid line) summed over 3 m interval, abscissa in meters below mean sea level.

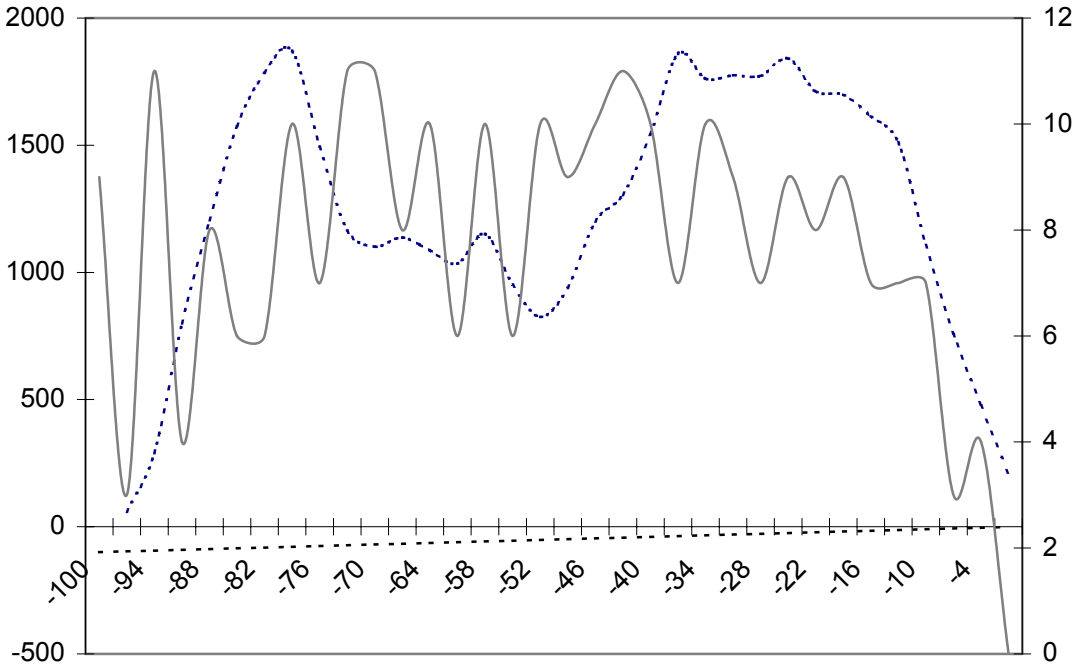

Figure F.5. Straight running five mean of passage length passage (dotted line), left ordinate in meters, and duration of sea level height for 450 Ka BP, right ordinate arbitrary, for Core DSDP 502b (solid line) summed over 3 m interval, abscissa in meters below mean sea level.

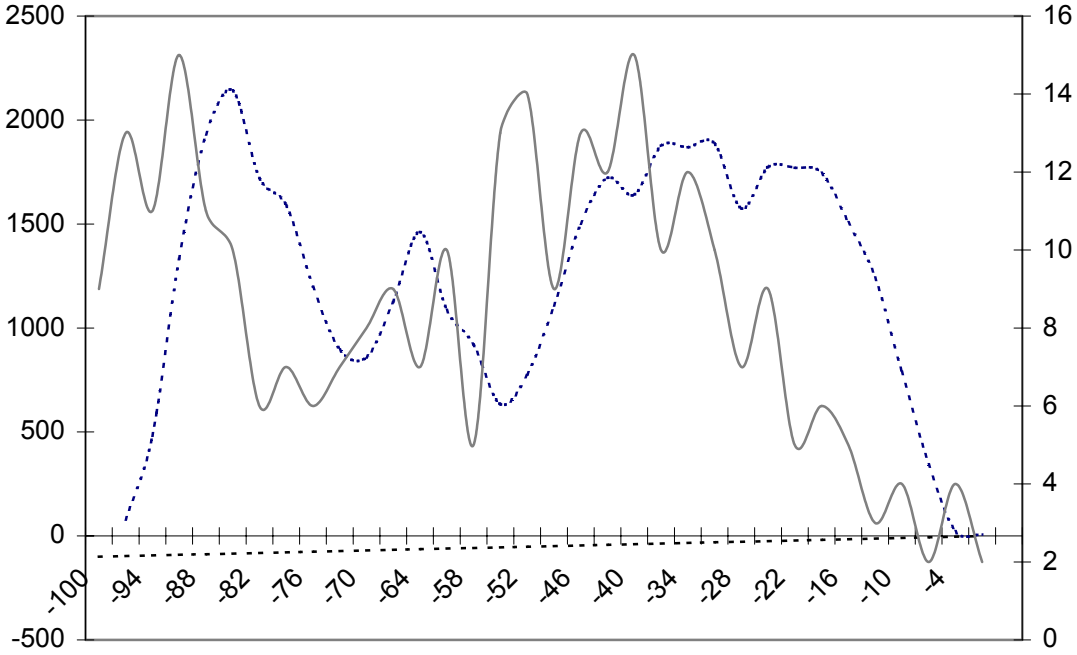

Figure F.6. Straight running-three mean of passage length (dotted line), left ordinate in meters, and duration of sea level height for 400 Ka BP, right ordinate arbitrary, for smoothed stack SPECMAP (solid line) summed over 3 m interval, abscissa in meters below mean sea level.

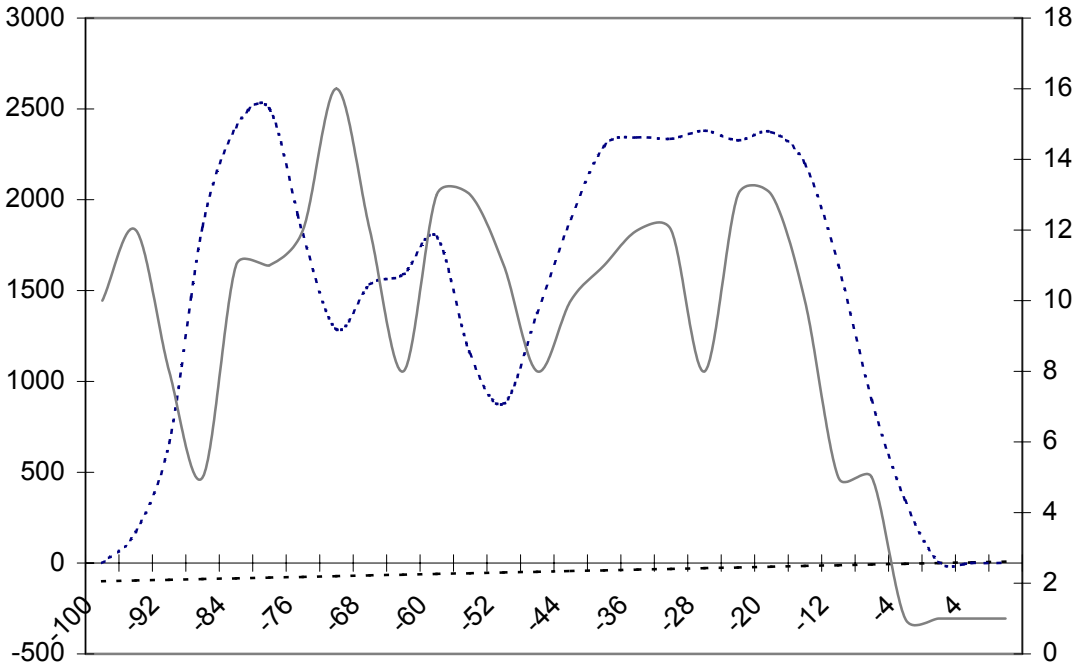

Figure F.7. Straight running three mean of passage length passage (dotted line), left ordinate in meters, and duration of sea level height for 425 Ka BP, right ordinate arbitrary, for Core DSDP 502b (solid line) summed over 4 m interval, abscissa in meters below mean sea level.

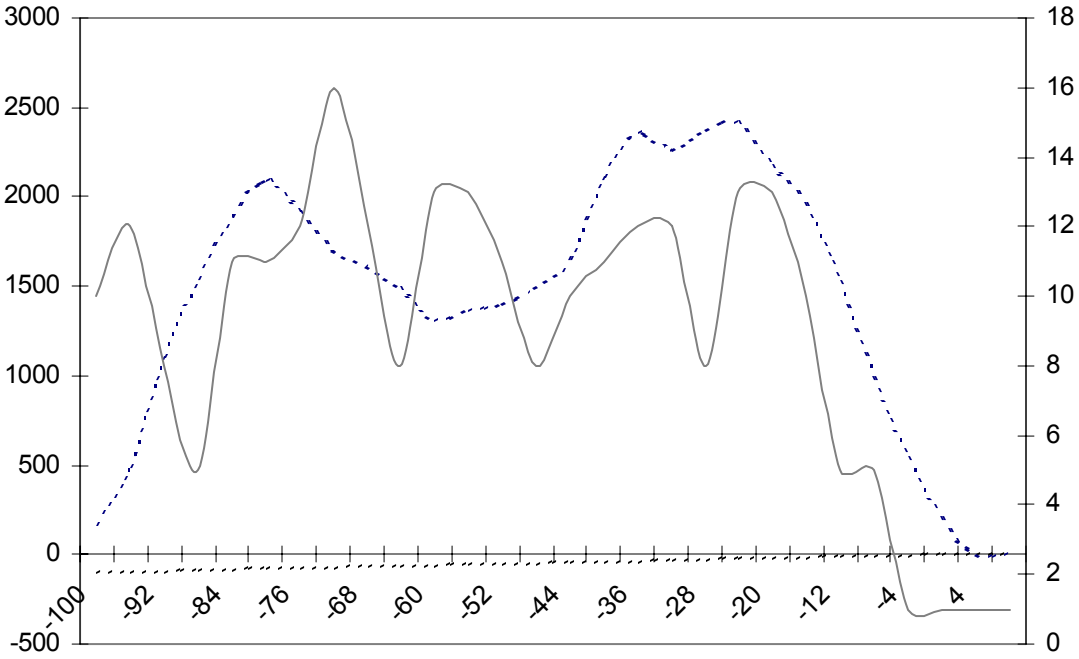

Figure F.8. Straight running five mean of passage length passage (dotted line), left ordinate in meters, and duration of sea level height for 425 Ka BP, right ordinate arbitrary, for Core DSDP 502b (solid line) summed over 4 m interval, abscissa in meters below mean sea level.

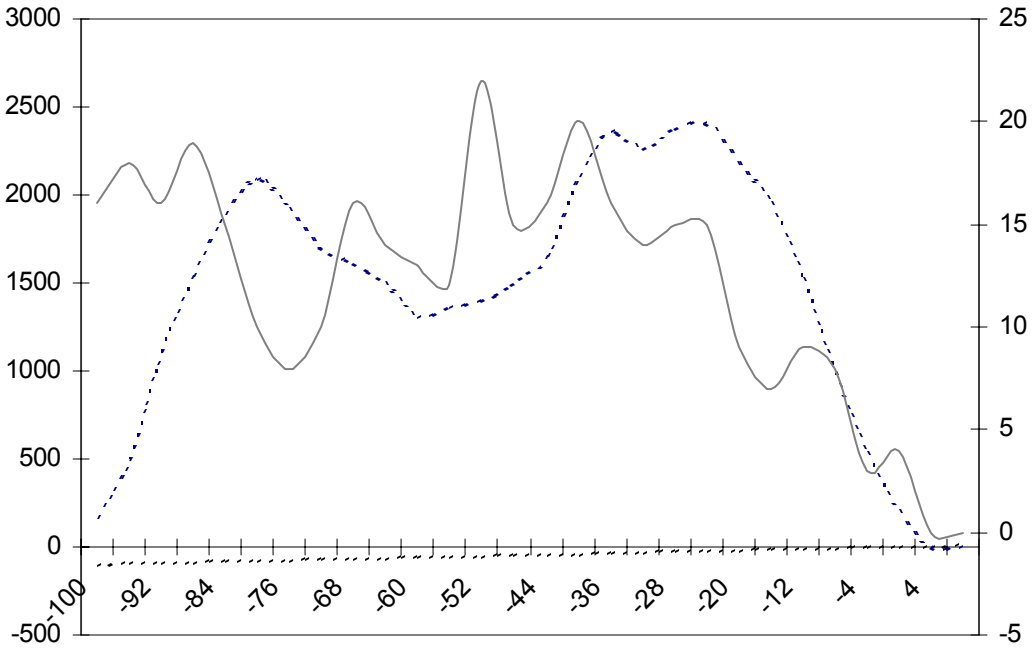

Figure F.9. Straight running five mean of passage length (dotted line), left ordinate in meters, and duration of sea level height for 425 Ka BP, right ordinate arbitrary, for smoothed stack SPECMAP (solid line) summed over 4 m interval, abscissa in meters below mean sea level.

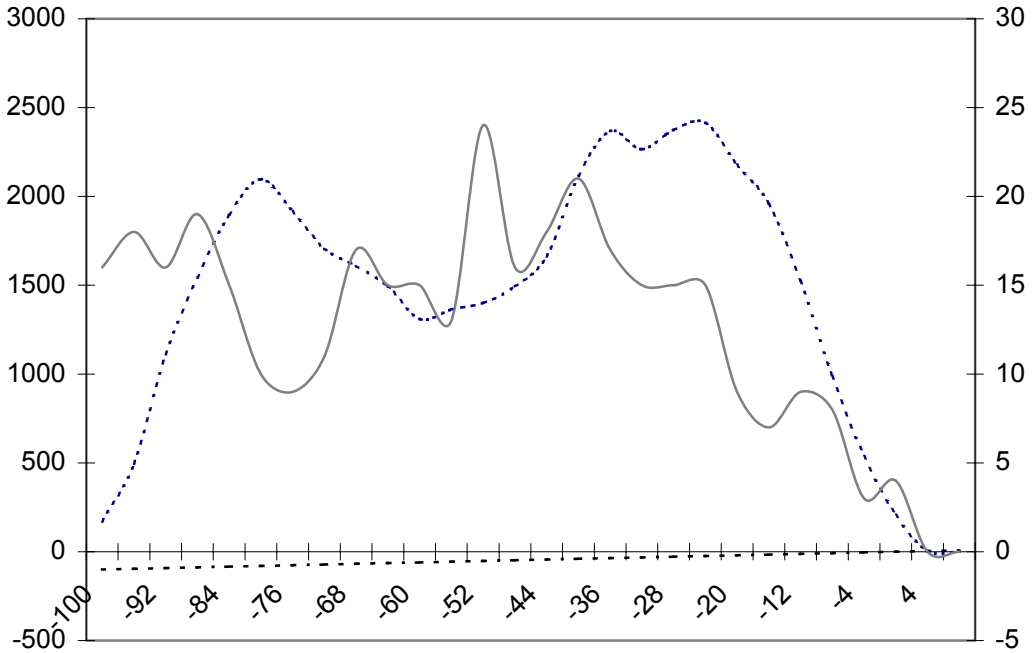

Figure F.10. Straight running five mean of passage length (dotted line), left ordinate in meters, and duration of sea level height for 450 Ka BP, right ordinate arbitrary, for smoothed stack SPECMAP (solid line) summed over 4 m interval, abscissa in meters below mean sea level.

APPENDIX G

This appendix contains 6 figures illustrating the correlation coefficients calculated for the timeline of formation analysis conducted in Chapter 3. The figures are a graphical representation of the correlation coefficients from Tables 3.6, 3.7 and 3.8. Those included are as follows: (G.1) 400 – 500 Ka BP correlation coefficients over a 2 m interval of Core DSDP 502b, (G.2) 400 – 500 Ka BP correlation coefficients over a 2 m interval of SPECMAP, (G.3) 400 - 500 Ka BP correlation coefficients over a 3 m interval of Core DSDP 502b, (G.4) 400 – 500 Ka BP correlation coefficients over a 3 m interval of SPECMAP, (G.5) 400 – 500 Ka BP correlation coefficients over a 4 m interval of Core DSDP 502b, (G.6) 400 – 500 Ka BP correlation coefficients over a 4 m interval of SPECMAP.

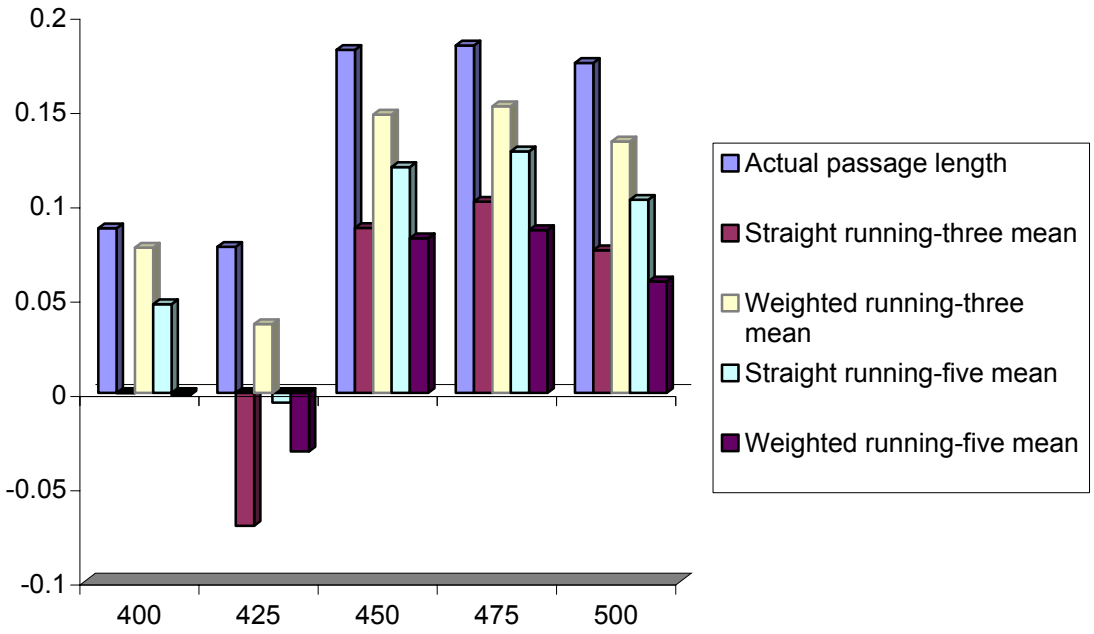

Figure G.1. Correlation coefficients for Core DSDP 502b summed over 2 m interval. Ordinate is correlation coefficient and abscissa is time in Ka.

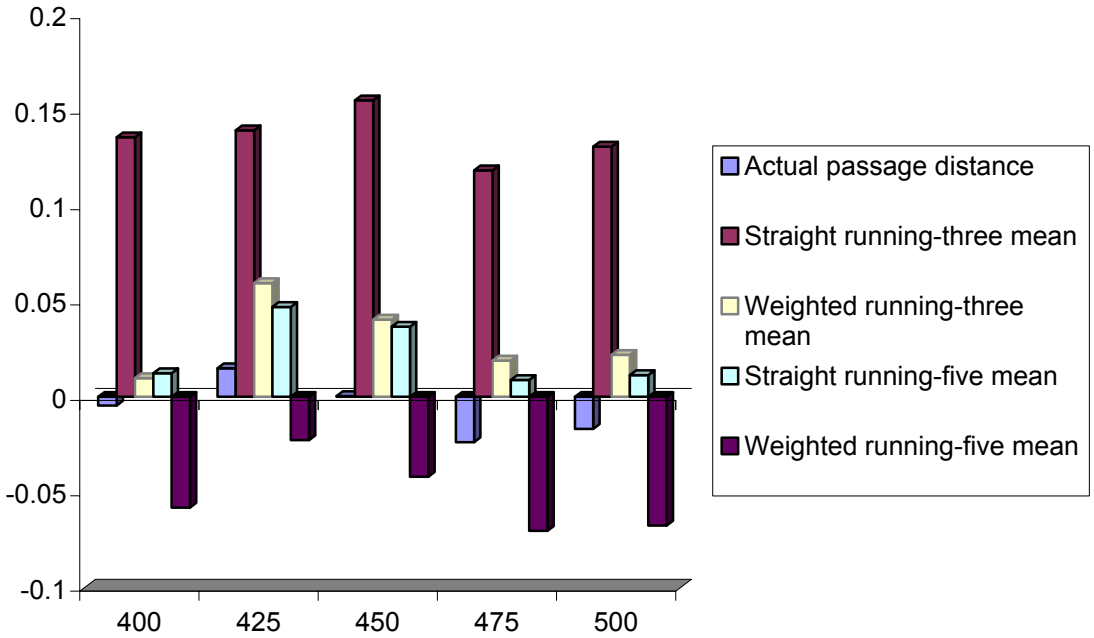

Figure G.2. Correlation coefficients for smoothed stack SPECMAP summed over 2 m interval. Ordinate is correlation coefficient and abscissa is time in Ka.

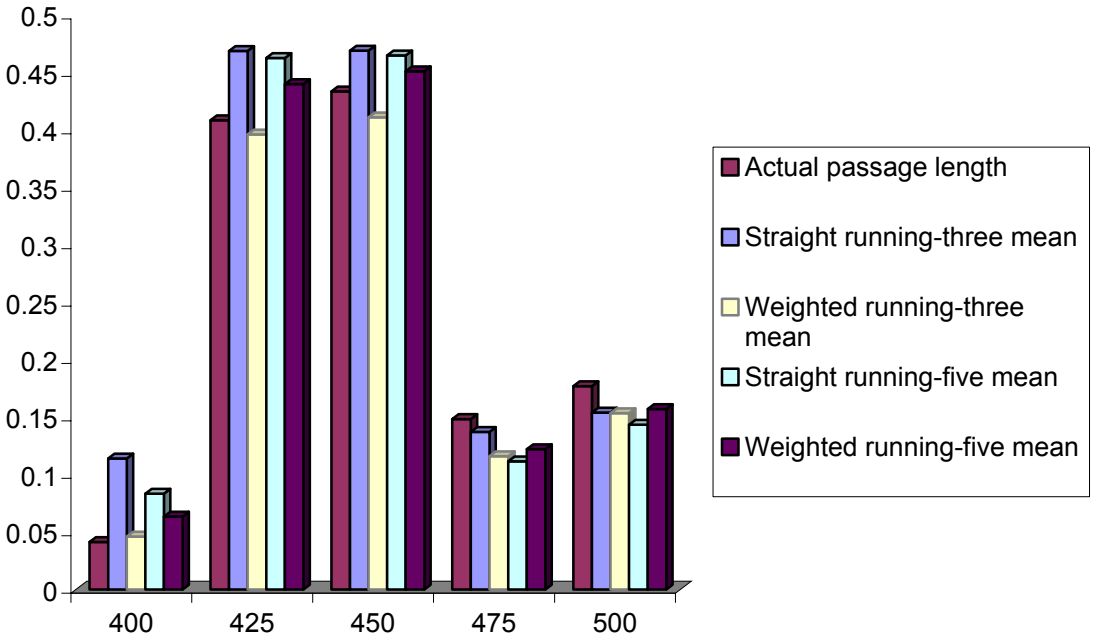

Figure G.3. Correlation coefficients for Core DSDP 502b summed over 3 m interval. Ordinate is correlation coefficient and abscissa is time in Ka.

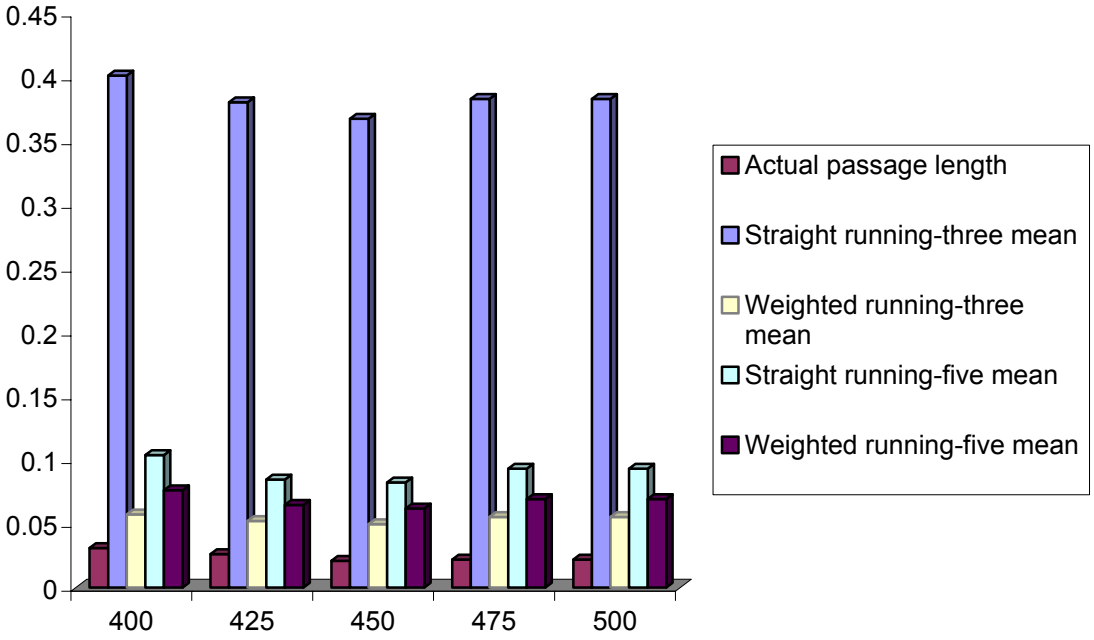

Figure G.4. Correlation coefficients for smoothed stack SPECMAP summed over 3 m interval. Ordinate is correlation coefficient and abscissa is time in Ka.

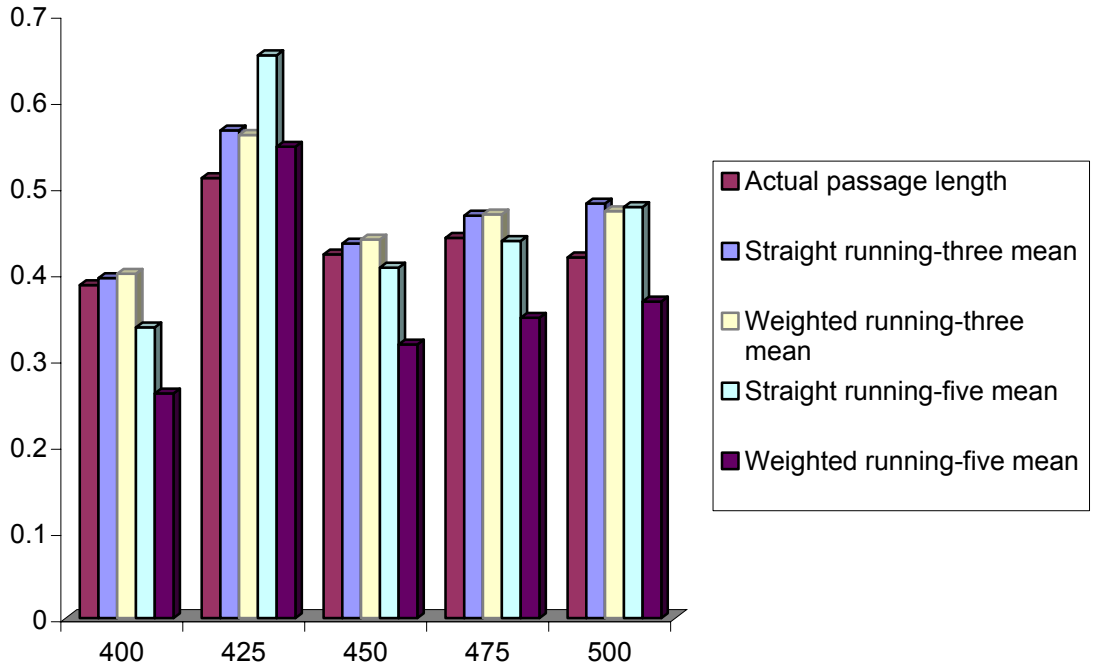

Figure G.5. Correlation coefficients for Core DSDP 502b summed over 4 m interval. Ordinate is correlation coefficient and abscissa is time in Ka.

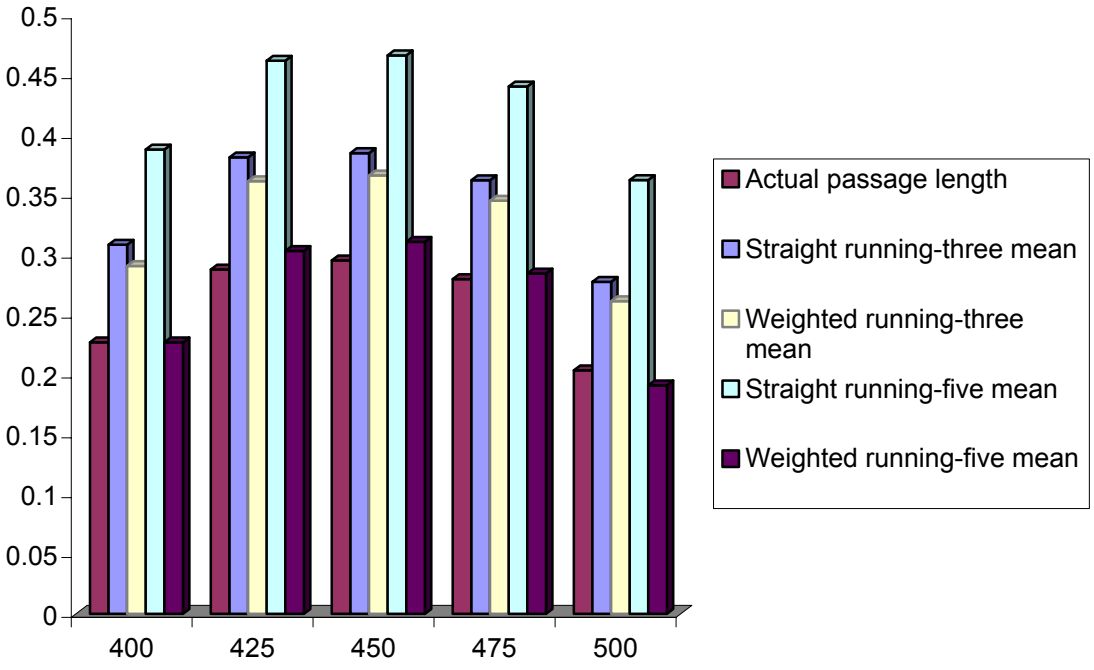

Figure G.6. Correlation coefficients for smoothed stack SPECMAP summed over 4 m interval. Ordinate is correlation coefficient and abscissa is time in Ka.

REFERENCES

Aharanov, E., Whitehead, J. A., Keleman, P. B. and M. Spiegelman, 1995, Channeling instability of upwelling melt in the mantle, *Journal of Geophysical Research*, v. 100, p. 20,433.

Aharanov, E., Spiegelman, M. and P. Keleman, 1997, Three-dimensional flow and reaction in porous media: Implications for the Earth's mantle and sedimentary basins, *Journal of Geophysical Research*, v. 103, p. 14,821.

Bard, E., Hamelin, B, Fairbanks, R. and A. Zindler, 1990a, Calibration of the ^{14}C timescale over the past 30,000 years using mass spectrometric U-Th ages from Barbados corals, *Nature*, v. 345, p. 405

Bard, E., Hamelin, B, and R. Fairbanks, 1990b, U-Th ages obtained by mass spectrometry in corals from Barbados: sea level during the past 130,000 years, *Nature*, v. 346, p. 456.

Bear, J., 1988, *Dynamics of Fluids in Porous Media*, New York: Dover.

Bogli, A. 1964, Mischungskorrosion-ein beitrag zum verkarstungsprblem, *Erdkunde* 18(2) Bonn, 83-92. Translation presented in Mixture Corrosion – A contribution to the Karstification Problem, *Cave Geology* v. 1, n. 10, p. 393, (1985).

Bretz, J. H., 1955, Cavern making in part of the Mexican Plateau, *Journal of Geology*, v. 63, p. 364.

Brooks, H. K., 1967, *Rate of solution of limestone in the karst terrane of Florida, Florida Water Resources Research Center Publ. No. 6*.

Chadam, J., Hoff, D., Merino, E., Ortoleva, P., and A. Sen, 1986, Reactive Infiltration Instabilities, *IMA Journal of Applied Mathematics*, v. 36, p. 207.

Chappel, J. & Shackleton, N. J., 1986, Oxygen isotopes and sea level, *Nature*, v. 324, p.137.

Davies, W. M., 1930, Origin of limestone caverns, *Geological Society of America Bulletin*, v. 41, p. 475.

Davies, W. E., 1960, Origin of caves in folded limestone, *National Speleological Society Bulletin*, v. 22, p. 5.

Davis, H., 1996, *Hydrogeologic Investigation and Simulation of Ground-Water Flow in the Upper Floridan Aquifer of North-Central Florida and Delineation of Contributing Areas for Selected City of Tallahassee, Florida, Water Supply Wells: USGS Water-Resources Investigation Report 95-4296*.

Dia, A., Cohen, A., O'Nions, R, and N. Shackleton, 1992, Seawater Sr isotope variation over the past 300 Kyr and influence of global climate cycles, *Nature*, v. 356, p. 786.

Diment, G. A. and K. K. Watson, 1983, Stability Analysis of Water Movement in Unsaturated Porous Materials 2. Numerical Studies, *Water Resources Research*, v. 19, n. 4, p. 1002.

Diment, G. A. and K. K. Watson, 1985, Stability Analysis of Water Movement in Unsaturated Porous Materials 3. Experimental Studies, *Water Resources Research*, v. 21, n. 7, p. 979.

Dogde, R., Fairbanks, R., Benninger, L., and F. Maurrasse, 1983, Pleistocene Sea Levels from Raised Coral Reefs of Haiti, *Science*, v. 219, p. 1423.

Domineco, P. A. and F. W. Schwartz, 1990, *Physical and Chemical Hydrogeology*, John Wiley & Sons, Inc., New York.

Dreybrodt, W., 1996, Principles of early development of karst conduits under natural and man-made conditions revealed by mathematical analysis of numerical models, *Water resources Research* v. 32, n. 9, p. 2923.

Dreybrodt, W., 1988, *Processes in karst systems: physics, chemistry, and geology*, Springer-Verlag, New York.

Dreybrodt, W. et. al., 1999, Dynamics of the early evolution of karst, *Karst Modeling: Karst Waters Institute SP5*, p. 106.

Droppa, A., 1957, *Demanovske Jaskyne*, Slovak Academy of Science, Bratislava.

Ewers, R. O., 1982, *An analysis of solution cavern development in dimensions of length and breadth, Ph. D. Thesis*, Geography, McMaster University, Hamilton, Ontario.

Ford, D. C., 1968, Features of cavern development in Central Mendip, *Trans. Cave Research Group Great Britain*, v. 10, p. 11.

Ford, D. C., 1971, Geologic structure and a new explanation of limestone cavern genesis, *Trans. Cave Research Group Great Britain*, v. 13. p. 81.

Ford, D. C. and Ewers, R. O., 1978, The development of limestone cave systems in the dimensions of length and depth, *Canadian Journal of Earth Sciences*, v. 15, p. 1783.

Ford, D. C. and Williams, P. W., 1989, *Karst geomorphology and hydrology*, Unwin Hyman, London.

Furbish, D. J., 1997, *Fluid Physics in Geology: An introduction to fluid motions on Earth's surface and within its crust*, Oxford University Press, New York.

Furbish, D. J., 1998, Irregular bed forms is steep, rough channels: 1. stability analysis, *Water Resources Research*, v. 34, p. 3635.

Gabrovsek, F. and W. Dreybrodt, 2000, Role of mixing corrosion in calcite-aggressive H_2O-CO_2-$CaCO_3$ solutions in the early evolution of karst aquifers in limestone, *Water Resources Research*, v. 36, n. 5, p. 1179.

Glass, R. J., Parlange, J-Y. and T. S. Steenhuis, 1989a, Wetting Front Instability 1. Theoretical and Dimensional Analysis, *Water Resources Research*, v. 25, n. 6, p. 1187.

Glass, R. J., Steenhuis, T. S., and J-Y. Parlange, 1989b, Wetting Front Instability 2. Experimental Determination of Relationships Between System Parameters and Two-Dimensional Unstable flow Field Behavior in Initially Dry Porous Media, *Water Resources Research*, v. 25, n. 6, p. 1195.

Groves, C. G. and A. D. Howard, 1994a, Minimum hydrochemical conditions allowing limestone cave development, *Water Resources Research*, v. 30, p. 607.

Groves, C. G. and A. H. Howard, 1994b, Early development of karst system 1. Preferential flow path enlargement under laminar flow, *Water Resources Research*, v. 30, p. 2837.

Hays, J., Imbrie, J. and N. Shackleton, 1976, Variations in the Earth's Orbit: Pacemaker of the Ice Ages, *Science*, v. 194, n. 4270, p. 1121.

Healy, H., 1982, Potentiometric surface of the Floridan Aquifer in Florida, May 1982, *Florida Geological Survey Map Series n. 104.*

Hendry, C. W., and Sproul, C. R., 1966, *Geology and groundwater resources of Leon County, Florida: Florida Geologic Survey Bulletin 47*.

Hoefner, M. L. and H. S. Fogler, 1988, Pore Evolution and Channel Formation During Flow and Reaction in Porous Media, *AIChE Journal*, v. 34, n. 1, p. 45.

Howard, A. H. and C. G. Groves, 1995, Early development of karst systems 2. Turbulent flow, *Water Resources Research*, v. 31, p. 19.

Hughes, G. H., 1967, *Analysis of the water-level fluctuations of Lake Jackson near Tallahassee, Florida: Florida Geological Survey Report of Investigation No. 48.*

Huddlestun, P. H., 1993, A Revision of the Lithostratigraphic Units of the Coastal Plain of Georgia: The Oligocene, *Georgia Geologic Survey Bulletin 105*.

Imbrie, J., Hays, J., Martinson, D., McIntyre, A., Mix, A., Morley, J., Pisias, N., Prell, W., and N. Shackleton, 1984, The orbital theory of Pleistocene climate: support from a revised chronology of the marine O record, *Milankovitch and Climate, Part I*, Berger, A. *et. al.*, Eds., D. Reidel Publishing Co., p. 269.

Imbrie, J., McIntyre, A., and A. Mix, 1989, Oceanic response to orbital forcing in the Late Quqternary: observational and experimental strategies, *Climate and Geo-Sciences*, Berger, A. *et. al.*, Eds., D. Reidel Publishing Co., p. 121.

Irvine, G., 1999, Woodville Karst Plain Project, http://www.wkpp.org/, personal communication.

Irving, S., 1997, Woodville Karst Plain Project, http://www.wkpp.org/ ,personal communication.

Izumi, N. and G. Parker,1995, Inception of channelization and drainage basin formation: pstream-driven theory, Journal of Fluid Mechanics, v. 283, p. 341.

Labeyrie, L. D., Duplessy, J. C., and P. Blanc, 1987, Variations in mode of formation and temperature of oceanic deep waters over the past 125,000 years, *Nature*, v. 327, p. 477.

Lowenherz, D. S., 1991, Stability and the initiation of channelized surface drainage: a reassessment of the short wavelength limit, *Journal of Geophysical Research*, v. 96, n. B5, p. 8453.

Mahon, G., A. Sepulveda and A. Choquette, 1997, Potentiometric surface of the Upper Floridan Aquifer in Florida, May and June 1995, *Florida Geological Survey Map Series n. 140.*

Miller, James A., 1986, *Hydrologic framework of the Floridan aquifer system in Florida and in parts of Georgia, Alabama and South Carolina: U. S. Geologic Survey Professional Paper 1403-B*.

Miotke, F. D. and Palmer, A. N., 1972, Genetic relationship between caves and landforms in the Mammoth Cave National Park Area, Bohler, Wurzburg.

Palmer, A., 1981, *A geological guide to Mammoth Cave National Park*, Zephyrus Press, Teaneck, NJ.

Palmer, A., 1991, Origin and morphology of limestone caves, *Geological Society of America Bulletin*, v. 103, p.1.

Parlange, J.-Y. and D. E. Hill, 1976, Theoretical analysis of wetting front instability in soils, *Soil Science*, v. 122, n. 4, p. 236.

Plummer, L. and T. Wigley, 1976, The dissolution of calcite in CO_2-saturated solutions at 25C and 1 atmosphere total pressure*, Geochimica et Cosmochimica Acta* v. 40, p. 191.

Plummer, L., T. Wigley and D. Parkhurst, 1978, The kinetics of calcite dissolution in CO_2-water systems at 5 to 60 C and 0.0 to 1.0 atm. CO_2, *Am. J. Sci.*, v. 278, p. 179.

Puri, H. S. and R. O. Vernon, 1964, *Summary of the Geology of Florida and a Guidebook to the classic Exposures, Florida Geological Survey Special Publication 5*.

Rhoades , R. and M. Sinacori, 1941, Pattern of ground-water flow and solution, *J. Geol.*, v. 49, p. 785.

Rupert, F., 1988, *The Geology of Wakulla Springs: Florida Geological Survey Open File Report 22*.

Rupert, F. and S. Spenser, 1988, *Geology of Wakulla County, Florida: Florida Geological Survey Bulletin 60.*

Scott, T. M., Lloyd, J. M. and G. Maddox, Eds., 1991, *Florida's Ground Water Quality monitoring Program Hydrogeological Framework: Florida Geological Survey Special Publication No. 32.*

Scott, T. M. (compiler), 2000, *Geologic Map of the State of Florida, Florida Geological Survey Map Series*, in preparation.

Schmidt, W., 1984, *Neogene stratigraphy and geologic history of the Apalachicola Embayment, Florida, Florida Geological Survey Bulletin 58*.

Shakleton, N. J., 1987, Oxygen isotopes, ice volumes and sea level, *Quaternary Science Reviews*, v. 6, p. 183.

Siemers J. and W. Dreybrodt, 1998, Early development of karst aquifers on persolation networks of fractures in limestone, *Water Resources Research*, v. 34, n. 3, p. 409.

Smith, T. R. and F. P. Bretherton, 1972, Stability and the conservation of mass in drainage basin evolution, *Water Resources Research*, v. 8, n. 6, p. 1506.

Sprinkle, C. L., 1985, *Geochemistry of the Floridan aquifer system in Florida and in parts of Georgia, South Carolina, and Alabama, U. S. Geologic Survey Professional Paper 1403-I*.

Swinnerton, A. C., 1932, Origin of limestone caverns, *Geological Society of America Bulletin*, v. 43, p. 663.

Sweeting, M. M., 1950, Erosion cycles and limestone caverns in the Ingleborough District, *Geograph. Journal*, v. 115, p. 63.

Werner, C. L., 1998, Groundwater flow pattern analysis from cave exploration in the Woodville Karst Plain, Florida, *Proceeding of the Wakulla Springs Woodville Karst Plain Symposium, October, 9, 1998,* Schmidt, W., J. Lloyd and C. Collier, Eds., *Florida Geological Survey Special Publication Series no. 46*, p. 37-43.

White, W. B., 1988, *Geomorphology and hydrology of karst terrains*, Oxford University Press, New York.

White, W. B. and White, E. L., 1974, Base level control of underground drainage in the Potomac River Basin, *Proceeding of the 4th Conference on Karst Geology and Hydrology*, H. W. Rauch and E. Werner, Eds., West Virginia Geological Survey, p. 41.

White, W. B. and White, E. L. eds., 1989, *Karst hydrology: Concepts from the Mammoth Cave Area*, Van Nostrand Reinhold, New York.

White, W. B., 1999, Groundwater flow in karstic aquifers, *Handbook of Groundwater Engineering*, CRC Press LLC, p. 18-1.

Winsberg, M. D., 1990, *Florida Weather*, University of Central Florida Press, Orlando.

Wisenbaker, M., 1999, Woodville Karst Plain Project, http://www.wkpp.org/, personal communication.

BIOGRAPHICAL SKETCH

Christopher Lee Werner was born on March 16, 1969 in Pittsburgh, Pennsylvania. He graduated with honors receiving a B. S. in Earth and Planetary Science and minor in Physics from the University of Pittsburgh in August, 1996. He received the American Minerologist Undergraduate Award in 1992. His professional experience includes a work study position at the University of Pittsburgh in 1992. He has been an Assistant Geologist with the Florida Geological Survey from February 1997 to the present.

He is an avid dry cave explorer, having originally explored and surveyed several kilometers of dry caves in Pennsylvania, West Virginia and Kentucky. He served as Vice-Chairman of the Pittsburgh Grotto of the National Speleological Society in 1993 and a joint-venturer with the Cave Research Foundation from 1994 to 1996.

Having moved to Tallahassee, Florida in 1996 to attend graduate school at the Florida State University, he became a member of the Woodville Karst Plain Project cave diving team. He has successfully completed more than 1400 dives, over 800 being in underwater caves, more than 1000 using mixed-gases other than air, over 900 involving decompression and over 350 involving deep exceptional-exposure decompression profiles. He has originally explored and surveyed several tens of kilometers of underwater cave passage in Florida. He is member of the Board of Directors and currently serves as the Science Director for the Woodville Karst Plain Project.